Universidad de Valladolid

Escuela de Doctorado Universidad de Valladolid

PROGRAMA DE DOCTORADO EN QUÍMICA

DOCTORAL THESIS / *TESIS DOCTORAL*:

Non-Covalent Interactions in Thiol Aggregates and Nucleoside-Amino Acid Binding Models

Presented by / *Presentada por*
Rizalina Tama Saragi
in fulfillment for the Degree of / *para optar al grado de*
Doctor / *Doctora*
from the / *por la*
Universidad de Valladolid

Supervised by / *Dirigida por:*
Prof. Alberto Lesarri Gómez
Prof. Judith Millán Moneo

This thesis was possible thanks to the funding of the following institutions:

Esta tesis ha sido posible gracias a la financiación de las instituciones siguientes:

Project: PGC2018-098561-B-C22,
Ministerio de Ciencia, Innovación y Universidades

Project: CTQ2015-68148-C2-2-P,
Ministerio de Economía y Competitividad

Convocatoria de Contratos Predoctorales de la Universidad de Valladolid Nº. E-47-2017-0186492

This thesis is dedicated to my late father, thank you for making me stronger, better, and optimistic. I am forever grateful and proud of you.

Table of Contents

Non-Covalent Interactions in Thiol Aggregates and Nucleoside-Amino Acid Binding Models

Abstract

This thesis contains an experimental and computational investigation of non-covalent interactions in different thiol dimers and DNA-amino acid model complexes. The experiments used chirped-pulse broadband Fourier transform microwave spectroscopy in the cm-wave region (2-8 GHz), providing an accurate structural description of the target compounds. Several quantum mechanical methods including density-functional theory, energy decomposition by symmetry-adapted perturbation theory and topological analyses of the electronic density rationalized the experimental results. The studied thiol systems comprised the weakly-bound homodimers of thiophenol, benzyl mercaptan, 2-phenethyl mercaptan and 2-naphtalenethiol, which were generated *in situ* in the isolation conditions of a supersonic jet expansion. The thiol dimers were compared to their alcohol counterparts, offering insight into the electronic and structural characteristics of the non-covalent interactions to sulfur centers and, in particular, of the weak dispersive S-H···S hydrogen bond, seldom analysed in the gas phase. Additionally, several biologically relevant model clusters formed by nucleoside dimers and capped amino acids were investigated computationally, in order to improve our understanding of the DNA-amino acid interaction. These models illustrate the influence of sugar puckering in the amino acid conformation and the implication of the hydrogen bonds stabilizing the complexes. The results obtained in the thesis confirm the importance of the chemically specific reductionist approach and the benefits of a synergic combination of rotational data and computational calculations.

Interacciones No Covalentes en Agregados de Tioles y Modelos de Asociación Nucleósido-Aminoácido

Resumen

Esta Tesis contiene una investigación experimental y computacional de interacciones no covalentes en diferentes dímeros de tioles y complejos modelo ADN-aminoácido. Los experimentos han utilizado espectroscopía de microondas de banda ancha con excitación multifrecuencia y transformación de Fourier en la región centimétrica (2-8 GHz). Los resultados experimentales se han racionalizado utilizando diversos métodos mecanocuánticos, incluyendo teoría del funcional de la densidad, descomposición energética por teoría de perturbaciones adaptada en simetría y análisis topológicos de la densidad electrónica. Los tioles estudiados han comprendido los homodímeros débilmente enlazados de tiofenol, bencil mercaptano, 2-fenetil mercaptano y 2-naftalenotiol, que fueron generados *in situ* bajo condiciones de aislamiento en una expansión de chorro supersónico. Los dímeros de tioles fueron comparados a sus análogos con alcoholes, ofreciendo información sobre las características electrónicas y estructurales de las interacciones no covalentes a grupos de azufre y, en particular, sobre las interacciones dispersivas débiles del enlace de hidrógeno S-H···S, raramente analizado en fase gas. Adicionalmente, se han investigado computacionalmente varios modelos de agregación de relevancia biológica, formados por dímeros de nucleósidos y aminoácidos modelo, con objeto de mejorar nuestro entendimiento de las interacciones ADN-aminoácido. Estos modelos ilustran la influencia del plegamiento de los azúcares en la conformación de los aminoácidos, y la implicación de los enlaces de hidrógeno que estabilizan los complejos. Los resultados obtenidos en la Tesis confirman la importancia de una aproximación reduccionista químicamente selectiva y los beneficios de una combinación sinérgica de datos rotacionales y cálculos computacionales.

Interaksi Non-Kovalen dalam Agregat Tiol dan Model Pengikatan Nukleosida-Asam Amino

Abstrak

Penelitian ini berisi percobaan eksperimental dan komputasi terhadap interaksi non-kovalen pada beberapa dimer tiol dan pemodelan pada DNA-asam amino. Eksperimen dilakukan dengan spekstroskopi *broadband* gelombang mikro dengan eksitasi multi frekuensi dan transformasi Fourier pada frekuensi 2-8 GHz. Beberapa metode mekanika kuantum digunakan termasuk *density functional theory*, dekomposisi energi menggunakan *symmetry-adapted perturbation theory* dan analisis topologi kerapatan elektron untuk verifikasi data eksperimen yang dihasilkan. Homodimer dari tiofenol, benzil mercaptan, 2-fenil etil mercaptan, dan 2-naftalentiol terbentuk dari sebuah ekspansi jet supersonik yang dihasilkan secara *in situ* pada kondisi terisolasi. Perbandingan antara dimer tiol dan pasangan analog alkoholnya memberikan informasi elektronik dan struktur pada interaksi non-kovalen dari senyawa-senyawa sulfur, khususnya, pada ikatan hidrogen S-H···S yang lemah dan bersifat dispersif yang jarang diteliti pada fase gas. Selain itu, untuk meningkatkan pemahaman terhadap interaksi sistem yang lebih relevan secara biologis seperti interaksi DNA dan asam amino, maka penelitian terhadap model dimer nukleosida dan asam amino dilakukan secara komputasi. Model ini menggambarkan pengaruh pengerutan molekul gula pada konformasi asam amino dan implikasinya terhadap ikatan hidrogen pada kestabilan kompleks yang terbentuk. Hasil yang diperoleh dalam penelitian ini mengkonfirmasi pentingnya pendekatan reduksionis pada model yang dipelajari dan manfaat kombinasi sinergis antara data rotasi dan kalkulasi komputasi.

Acknowledgements

I am thankful for everyone who has helped me during the Ph.D. program. I would first to express the highest appreciation to Alberto Lesarri, who has given so much effort to help me for completing this thesis. Thank you for your patience and kindness. I am deeply grateful to Judith Millán for her guidance and support and to Rodrigo Martínez for his advice and invaluable insight into computational part and during my visit at Universidad de La Rioja. My sincere thanks to the member of Group of Spectroscopy and Plasmas and Supersonic Jets (GEPCS). I would also like to thank to Melanie Schnell for the precious collaborations and the group members for the hospitality during my stay at DESY including Amanda and Cristobal who are now here in Valladolid, I thank you for sharing your knowledge and expertise with me.

Many others have been helpful during this journey. I appreciate the kind assistance from administrative staff from *Escuela de Doctorado* and *Casa de Estudiante*. Without the financial support from the Universidad de Valladolid, the completion of this degree would not have been possible.

A special thank you to my friend, Marcos, for continuous help and care inside and outside the lab. I also had great pleasure of working with Isabel and Wenqin, who have provided a supportive and cheerful environment.

As an Indonesian, I am privileged to do a PhD and that is mainly because of my hardworking and loving parents, Bapak Burhan dan Mamak Ani. I cannot begin to show my gratitude to them for your endless love and prayers, I hope that I have made you proud. I must thank my sisters (Kakak Indi, Mariana, and Annisa) with whom I shared laughter, frustration, and sisterhood. Thanks should go to Vicky and Dina for cheering me up when I am sad and for your kind and beautiful friendship.

Chapter 1.

Introduction

This thesis is dedicated to the characterization of intermolecular interactions in the gas phase, in particular in weakly-bound dimers and hydrates, using a combination of rotational spectroscopy and molecular orbital calculations.

In this chapter, we present an introduction to the objectives and methods used in the thesis. We divided this chapter into two parts: the first part reviews non-covalent interactions, especially the concepts of hydrogen bond and π-stacking. The second part reviews the methods used in the thesis, including both experimental and theoretical techniques. The experimental section will focus on rotational spectroscopy and microwave instrumentation, while the theoretical section will be dedicated to the computational methods and analysis tools used during this work.

1. NON-COVALENT INTERACTIONS

The term non-covalent interaction (NCI) is used to categorize molecular interactions that do not imply the formation of a chemical bond, which are conventionally labelled either as (electrostatically dominated) hydrogen bonds or (dispersive) van der Waals forces. However, scientists are aware that the NCI definition is not straightforward and unambiguous since these categories are extensive. The term non-covalent interaction is recent,[1] but the effects of intermolecular interactions were first addressed by van der Waals around the end of the XIXth century to explain the macroscopic properties of gases. A microscopic interpretation of the intermolecular forces was only possible later with the advent of quantum mechanics.[2,3]

The covalent bond dominates the description of a molecule when it is considered isolated from any perturbations. However, once a molecule is surrounded by other molecules, such as in solution or in bulk, these environments disturb the molecular orbital distribution, and the perturbation modifies its electronic properties, affecting the

molecular structure, functionality, and, eventually, reactivity. This perturbation differs on the strength and level of the non-covalent interactions, with the most noticeable changes occurring in ionic and H-bonded systems, which may promote the initiation of chemical reactions. Typically, non-covalent interactions are considerably weaker than covalent bonds (by about 1-3 orders of magnitude), especially for neutral molecules like those considered here. Yet, non-covalent interactions play a delicate and critical role in nature.

The investigation of aggregation and solvation is the main concern of the studies of non-covalent interactions, including how the role of water influences molecular functionality. Many studies have analysed the hydrogen bond formation and the proton donor/acceptor amphoteric role of the water, using different experimental techniques. Therefore, hydrogen bonding also became the most widely investigated non-covalent interaction, both theoretically and experimentally.[4–8] Not limited to the hydration or solvation effects, hydrogen bonding is also used to describe the interaction between many hosts and guest molecules in supramolecular Chemistry or Biology. Experiments in the gas phase provide a reductionist approach in which non-covalent interactions can be individually selected and isolated. This thesis will present different examples of the generation and characterization in the gas phase of dimers and trimers of neutral model compounds in Chapters 2-5. The weak binding energies pose a problem for structural investigations, as many of these interactions would be blurred at room temperature. For this reason, specific experimental methods like supersonic jet expansions[9] are used to generate and isolate weakly-bound aggregates. Our studies combine jet-cooled rotational spectroscopy with computational predictions appropriate for small-size (<600-800 u) molecular models.

The importance of non-covalent interactions is especially noticeable in biological systems since they are responsible for the structure of key macromolecules such as DNA, RNA, and proteins (Figure 1.1).[1,10–12] Bring to mind that the double helix structure of DNA, which controls the transmission of genetic information, relies on the formation of nucleic bases pairs by non-covalent interactions. The nucleic bases are polar, aromatic heterocycles that interact either via H-bonds or π–π interactions, resulting in two structural motifs, planar H-bonding and vertical π–stacking.[13,14] Both interactions are important in determining the architecture and functionality of nucleic acids. Non-covalent interactions also determine many other biochemical processes, including molecular recognition and signal transduction, which also require a transmission of information between molecules.

The critical role of non-covalent interactions in bio disciplines is largely associated with the easy formation and breakdown of intermolecular complexes. For example, DNA should be stiff enough to store genetic information, yet simultaneously soft enough to

allow, after receiving enzymatic information, to unwind and thus to reproduce genetic information. Furthermore, the opening and closing of the molecule should be perfectly reproducible. Thus, nature has probably selected non-covalent interactions over the too strong covalent bonds because of their specificity and weak character. However, large biological systems cannot be easily studied in the gas phase. Therefore, we also used purely theoretical methods to understand the importance of non-covalent interactions in biomolecules, as illustrated in Chapter 6 of this thesis, where we explored a simplified model of DNA-protein interaction.

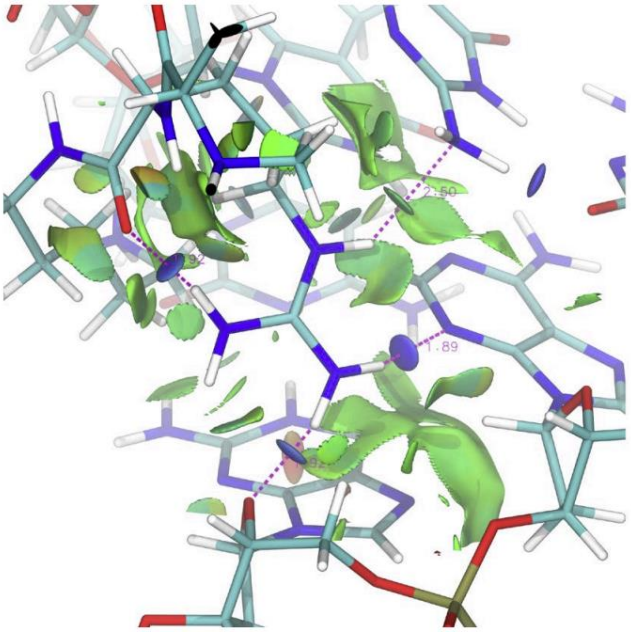

Figure 1.1. An illustration of the extensive influence of non-covalent interactions in biological molecules, using an NCI representation of the H3K9 system and arginine, discussed in ref. 12.

The understanding of non-covalent interactions has grown from decades of experimental work and theoretical calculations.[15] In the last decade, the concept of non-covalent interactions extended significantly beyond the conventional R-H···Y hydrogen bond, [4,8] including new donor-acceptor interactions in other formally analog R-A···Y bridging interactions. As part of this effort, the hydrogen bond was redefined in 2011 by IUPAC[16] to include weak interactions involving aliphatic donors (C-H···O, C-H···N, etc.),[17] π acceptors (C-H···π, N-H···π, etc.),[18] low-electronegativity donors (S-H, P-H, etc.)[19] or H acceptors.[20] Later, IUPAC defined the halogen bond (XB) in 2013[21] and several new interactions were introduced, such as chalcogen bonds,[22] pnictogen bonds,[23,24] or tetrel

bonds,[25,26] involving atoms of groups 14, 15, 16,[27] or even coinage-metals.[28] The diversity of non-covalent interactions makes them more attractive to be studied.

This thesis will focus on hydrogen bonds between neutral molecules mostly involving thiols* and alcohols to examine the effect of the lower electronegativity of sulfur and to compare the different roles of oxygen and sulfur on dimerization. A few additional studies will be summarized at the end of the thesis.

1.1. Hydrogen Bonding

The concept of the hydrogen bond has evolved considerably since the 1920's when it was introduced by Latimer and Rodebush[29] and popularized by Pauling.[4,30] The progress of knowledge on hydrogen bonding has been enormous, and scientists feel that there is always a necessity for updating and revising the definition of hydrogen bonding. In 2011, the IUPAC revised the criteria to consider an interaction as a hydrogen bond, accommodating some previously unnoticed weak interactions. According to IUPAC, the hydrogen bond is *"an attractive interaction between a hydrogen atom from a molecule or a molecular fragment X–H in which X is more electronegative than H, and an atom (Y) or a group of atoms in the same or a different molecule in which there is evidence of bond formation."*[16]

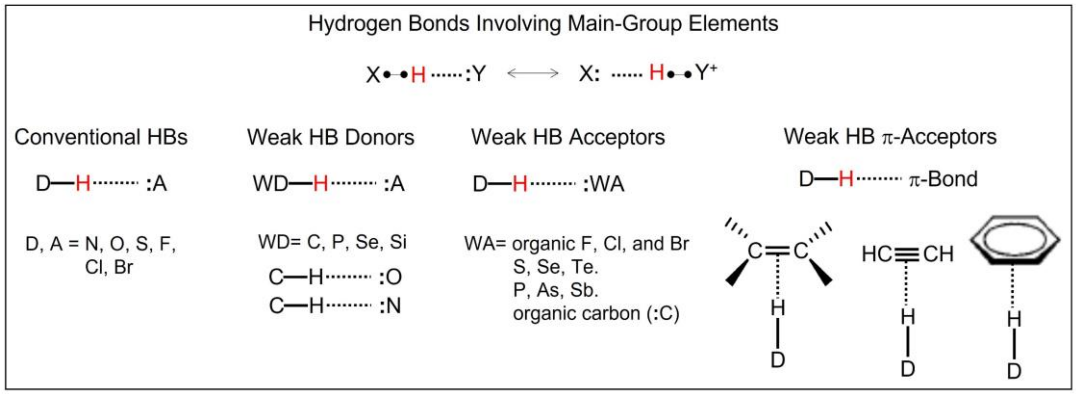

Figure 1.2. Classification of hydrogen bonds with main-group elements (adapted from ref. 4).

In the hydrogen bond, a proton-sharing interaction is the key feature distinguishing hydrogen bonds from other donor-acceptor interactions. The opposite, however, may not be true, and not all the shared proton interactions inevitably conform to the hydrogen bond definition. A diversity of hydrogen bonds involving the main-group

*Throughout this thesis, thiols are sometimes referred to as mercaptans.

elements is illustrated in Figure 1.2, following Gili and Gili.[4] According to the initial definitions of Pauling or Pimentel[8,30] the H atom is bonded to very electronegative atoms (X) such as N, O, F, etc., while Y is either a nucleophilic region or a region of electron excess.[5–7,30] However, many other atoms have been observed to participate in hydrogen bonds.

As mentioned before, the electronegativities of donor and acceptor in Figure 1.3 are the first factor to describe the strength and characteristics of hydrogen bonds. Third-row and fourth-row atoms with lower electronegativity such as S and Se can behave as weak hydrogen bond acceptors and, in some cases, also as hydrogen bond donors. However, they generally present longer hydrogen bond distances and geometries deviating from linearity. Nevertheless, the experimental and theoretical results reveal that even C–H aliphatic groups can be involved in hydrogen bonds as weak donors. In comparison, π electrons can act as proton acceptors to stabilize weak hydrogen bonding interaction in many chemical systems.[6,7] In consequence, the conditions of hydrogen bonds along the periodic table are highly diverse.

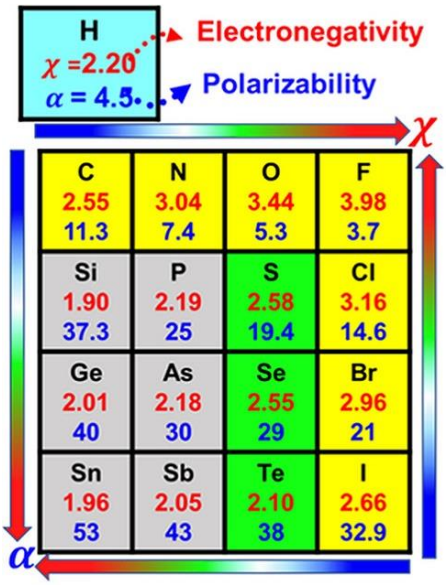

Figure 1.3. Table of Pauling's dimensionless electronegativities (χ) and polarizabilities (atomic units, see *Mol. Phys*. 2019, 117, 1200-1225) for elements of groups 14-17 (adapted from ref. 31).

In the conventional point of view, the hydrogen bond is highly electrostatic and only partly covalent. From a rigorous theoretical consideration, the hydrogen bond is not a simple interaction. It includes contributions from electrostatic interactions (acid/base), polarization (hard/soft) effects, van der Waals (dispersion/repulsion: intermolecular

electron correlation) interactions, and covalency (charge transfer).[32] There is also a diversity of hydrogen bonds with regard to their bond energies, changing considerably from strong (60-160 kJ mol^{-1}), moderate (16-60 kJ mol^{-1}), or weak (2-16 kJ mol^{-1}). The characteristic of a strong hydrogen bond is mostly covalent, where there is an electrostatic contribution to the bond. In a moderate and weak hydrogen bond, this electrostatic contribution changes. In brief, hydrogen bonds encompass a wide and continuous scale of bonding energies. The strongest hydrogen bonds are very similar to covalent bonds, and the weakest bonds are barely distinguishable from pure van der Waals interactions.

However, there are no specific geometric criteria for the Y···H atoms specified in the IUPAC definition, exception made of its directional character. In Chapters 2-5, the geometry of the hydrogen bonds will be determined experimentally and/or through computational calculations. In the computational study of Chapter 6, we will set specific hydrogen bonding thresholds to classify different types of hydrogen bonds. In the following, we discuss the general characteristics of the hydrogen bonds encountered in this thesis.

1.1.1. Conventional hydrogen bonds

The name *conventional hydrogen bonds* has been used to address all the interactions called 'hydrogen bonds' or 'hydrogen bridges'[4–8,32] from the early times of hydrogen bond studies. This group includes the bonds formed by main-group elements with electronegativities greater than 3.0 (N, O, F, Cl, and Br). Consequently, donors and acceptors are strong enough to show the full spectrum of hydrogen bond energies and geometries. Hydrogen bonds formed by sulfur (S) as donor or acceptor are generally considered to be conventional as well, despite the relatively lower electronegativity of the sulfur atom. However, due to their different exciting features and relevance in this thesis, they will be explained specifically in a separate section below. Conventional hydrogen bonds include practically all cases of strong hydrogen bonds so far known and, to some extent, all the other weak hydrogen bond groups listed in Figure 1.2.

Some of the most recognizable conventional hydrogen bonds are those involving one or two oxygen centers, such as O-H···O, O-H···N or N-H···O. The O-H···O hydrogen bond is very significant because of its impact on solvation or molecular packing in biological compounds and macromolecules, like carbohydrates, amino acids, nucleosides, and others. These hydrogen bonds are the most studied because of their abundance in nature and their presence in various compounds, whether in solutions (i.e., using NMR or IR spectroscopy), crystals (using X-ray or neutron diffraction and reported in CCDC Cambridge structural database), and in the gas-phase (typically by molecular

spectroscopy). Consequently, more structural and spectroscopic data are available for these hydrogen bonds.

Some typical structural features of the O-H···O hydrogen bonds obtained from experimental data and theoretical calculation are displayed in Table 1.1. The hydrogen bonds have wide ranges for the distances and angles of the O-H···O link, covering differences of 0.2-0.6 Å for the distances and 140-180° for the angles.[4,5] Carboxylic acid hydrates typically have stronger hydrogen bond properties, shortening the bond distances.[5] In carbohydrates, where the donor and acceptors are alcohol or ether groups, the hydrogen bond distances maintain a shorter interval of $r_{OH\cdots O}$ =1.74-1.96 Å. [5]

Table 1.1. A selection of O-H···O hydrogen bond lengths (Å) from different classes of small molecules based on neutron diffraction analyses.

	Carboxylic acids	Amino acids	Carbohydrates	Inorganic salt hydrates	Purines and pyrimidines	Organic hydrates	Nucleosides and nucleotides
Number of data[a]	26	26	255	296	66	46	322
min	1.40	1.44	1.74	1.74	1.60	1.60	1.55
max	2.01	2.06	1.96	2.26	2.46	2.25	2.18
mean	1.71	1.74	1.82	1.82	1.83	1.90	1.92

[a]Data according to Jeffrey, ref. 5.

Numerous O−H···O hydrogen bonds have been investigated in the form of homodimers or heterodimers (for instance, monohydrates) using experimental methods and ab initio or density functional (DFT) electronic structure methods.[5–7] The structure of the water dimer, the prototypic O−H···O interaction, was soon analysed by a molecular beam electric resonance experiment[33,34] and extended to other clusters, up to the water decamer.[35,36] Wide-ranging work on the hydrogen bonds in dimers is presented in many original articles and reviews containing different functional groups (aliphatic, acid, amide, aromatic, etc.). Alcohol clusters like those of methanol, ethanol, phenol, benzyl alcohol, etc., have been studied using various quantum chemical methods combined with gas-phase spectroscopy. These dimers constitute small-size model systems to understand the hydrogen bonding interactions in biomolecules. Specific reviews on rotational investigations of hydrogen bonds are also available.[11,37,38]

1.1.2. Hydrogen bonds of sulfur centers

Most of the information concerning hydrogen bonds involving sulfur centers has emerged from protein and crystal structures database analysis and, more recently, from electronic and vibrational laser spectroscopy. Sulfur is considered a weak actor

compared to oxygen, but analogously to the alcohol group, the thiol group can donate to O, N, S, and even π-acceptors. However, compared to more conventional hydrogen bonds like O-H···O, O-H···N or N-H···O, sulfur hydrogen bonds have been conventionally dismissed as weak interactions with dispersive character,[6–8] characterized by longer interaction distances and deviations from linearity. The first studies associated these characteristics to the smaller electronegativity (2.58) compared to oxygen (3.44) and the larger sizes of the higher chalcogens. However, as shown in Figure 1.3, the polarizability of sulfur is also larger (19.4 a.u.) than in oxygen (5.3 a.u.), increasing the dispersive forces and contributing to intermolecular interactions not purely electrostatic.

Studies by Biswal[39] and Wategaonkar[40] concluded that sulfur hydrogen bonds are multifaceted interactions where sulfur can form σ and π hydrogen bonds as a donor (S-H···O, S-H···S, S-H···π, etc.) and acceptor (O-H···S, N-H···S, etc.). They also confirmed that sulfur hydrogen bonds could be as strong as conventional hydrogen bonds and may display considerable electrostatic character. In consequence, these interactions offer all characteristics of conventional hydrogen bonds. As one of the main elements in protein and organic compounds, sulfur and its interactions are indeed very motivating, especially considering the small number of gas-phase studies.

To fully understand the diverse hydrogen bonds and non-covalent interactions involving sulfur, we require molecular studies on the structure, physical properties, and balance of electrostatic and dispersive contributions in model clusters. Especially, the observation of weakly-bound intermolecular clusters in the gas phase is useful to validate and benchmark the theoretical models and complement the crystal data. Vibrational evidence of sulfur hydrogen bond generally originates from IR,[41,42] and double-resonance (UV–UV or UV–IR) laser spectroscopy,[39,43–53] but is typically of low resolution (cm^{-1}) and not always structurally unambiguous. Moreover, high-resolution rotationally-resolved[11,37] studies are still scarce. As a matter of fact, the hydrogen sulfide dimer was reported only in 2018.[45] Up to the present time, rotational spectroscopy has addressed only a few intra-[54–57] and intermolecular[58,59] interactions in hydrogen sulfide dimers or sulfur-containing complexes. One of the objectives of this thesis is to extend the rotational data available on sulfur hydrogen bonding.

Several thiols were selected in this thesis because they are available commercially and may be combined with different chemical groups. Molecular studies on sulfur hydrogen bond have mostly observed thiols as proton acceptors, especially in O-H···S,[46,47,50,60] N-H···S,[43] F-H···S,[61] and C-H···S[62] hydrogen bonds. The description of thiol as proton donors in S-H···S[45,49] and other weak sulfur interactions like S-H···O,[51] S-H···N,[63] and S-H···π[64] has been far less explored. The S-H···S bond (2.778(9) Å in the H_2S dimer) is much longer than the equivalent O-H bond in Table 1.1.[45,52] Some structures

also reflect the change in acceptor directionality associated with the larger inter *n*-pair angle at S than O in thiols and thioethers (i.e., 85(3)° in tetrahydrothiophene···water or values close to 90°).[46]

As the physical interaction components may be different from those of oxygen centers, computational methods like the energy decomposition analysis are helpful to confirm the presence of hydrogen bonds and describe the contributions from electrostatic, polarization, exchange repulsion, charge transfer, and dispersion forces. The information collected so far supports that hydrogen-bonding interactions involving sulfur as acceptor are largely dominated by dispersive interactions, in some cases accounting for more than half of the total binding energy.[44,52,53] In addition, it is observed that they are not much weaker than the interactions involving oxygen, which have a stronger electrostatic component.[39,50]

In this thesis, the structural influence of the scarcely studied S–H···S hydrogen bond has been observed in the homodimers of several molecules, including aromatic and saturated five- and six-membered rings like (thiophenol)$_2$ in Chapter 2, (benzyl mercaptan)$_2$ in Chapter 3, (2-phenethyl mercaptan)$_2$ in Chapter 4 and (2-naphthalenethiol)$_2$ in Chapter 5. In some of these cases, a comparison is included with the equivalent oxygen compounds. Other systems studied during the thesis period are briefly mentioned in the final chapter.

1.2. π–Stacking

π-Stacking interactions involving aromatic rings like those of Figure 1.4 are indeed exciting and important non-covalent interactions in molecular/biomolecular assembly and engineering. These interactions play a crucial role in defining the structure of biomacromolecules like DNA and RNA.[65–67] A decisive role is also observed in proteins, despite there are only four aromatic sidechains (tryptophan, histidine, tyrosine, and phenylalanine) in the twenty essential amino acids. π-Stacking interactions also influence the intermolecular interactions in other areas of chemistry, including the packing of polycyclic systems in synthetic organic and organometallic molecules,[68,69] protein and crystal design,[70] functional materials design,[71] supramolecules,[69] and organocatalytic activity and selectivity.[72,73]

π-Stacking interactions were initially explained by Hunter and Sander[74] with a polar electrostatic model in which the aromatic rings are viewed as a collection of atom-centered local quadrupole moments. This model then developed to an intuitive physical image of the impact of the substituent effect in π-stacking interactions, which recognized the aromatic ring as a positively charged σ framework and a negatively charged π cloud. However, in 2006, Sinnokrot and Sherill[75] studied the prototypical stacked dimer of

benzene dimer and substituted benzenes and found that the substituent effects are not driven solely by electrostatic effects but result from other effects (dispersion, induction, etc.).

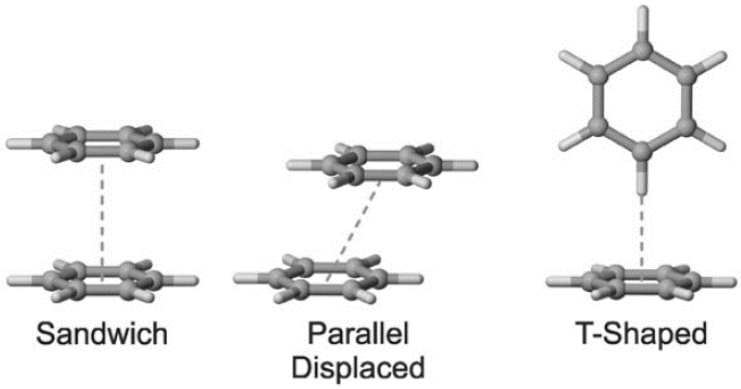

Figure 1.4. Prototypical configurations of the benzene dimer. Of these, only the parallel-displaced and T-shaped dimers are energy minima. The parallel displaced and T-shaped dimers are bound by about 11.7 kJ mol^{-1} in the gas phase, whereas the sandwich dimer is bound by 7.5 kJ mol^{-1}, see ref. 76.

Wheeler and Houk studied the dimers of several substituted and unsubstituted aromatic rings. They found that there are direct electrostatic interactions between the substituents and the unsubstituted ring, with the additional dispersive interactions between the substituents and the other ring preferentially stabilizing most substituted benzene dimers in stacked configurations.[77] Other recent calculations have explained the physical origin of π–π stacking stabilization as dispersion forces ($1/r^6$ dependence), promoted by the close near-parallel biplanar arrangement.[78,79] The quadrupolar electrostatic potential of unsaturated rings actually favors stacking of saturated rings, but a reduced Pauli exchange repulsion counterbalances this factor for arene-arene stacking. However, Grimme concluded that at least for aromatic systems smaller than anthracene, there does not appear to be anything "special" about aromatic π–π interactions and wondered if they really exist.[78]

In this sense, Martinez and Iverson also mentioned that the term π–stacking or π–π stacking could be misleading since they only recall a preferred face-to-face geometry and might even indicate to some the presence of large, dominating dispersion interactions between aromatic molecules.[79] In consequence, the terms "π–stacking" and "π–π interactions" should only be used as geometric descriptors. The term "stacking" summons a relatively clear physical picture of planar molecules in roughly parallel, overlapping orientations, devoid of the added implications of the widely-used terms.[76]

2. METHODS

As previously mentioned, the experimental studies of non-covalent interactions have been done primarily in condensed phases, either in crystal structures or liquids, while the investigations in the gas phase are still growing. In the gas phase, a molecule is a nearly isolated system with no influences from the solvent or the packed crystal structure. Since the introduction of the supersonic jet techniques in the 1980s, it has been possible to generate weakly-bound intermolecular complexes with specific sizes and functional groups. [9,80,81] Hence, more detailed and diverse non-covalent interactions can be studied using gas-phase molecular models. A great benefit of this technique is the direct comparison of the isolated molecules or complexes with theoretical calculations. High-resolution rotational or vibrational studies are some of the spectroscopic methods offering more detailed structural data in the gas phase.[37,38]

Since the rotational spectrum of a polyatomic molecule is directly connected to the geometric distribution of atomic masses through the moments of inertia, it is suitable and sensitive for the study of molecular structures. Pure rotational spectra are observed mainly in the frequency ranges from the centimeter to the millimeter and submillimeter-wavelengths (1 GHz to 1 THz), depending on the molecular size and temperature. Specifically, the investigations presented in this thesis have been conducted in the cm-wave region of 2-18 GHz. In this section, we will review some fundamentals of rotational spectroscopy from its historical evolution to the techniques used today, as well as the methodological approaches. More specific details can be found in the bibliography, including experimental techniques,[82,83] theory of rotational spectroscopy,[84–86] supersonic jets expansions,[9] or the quantum mechanical molecular orbital methods.[87]

2.1. Rotational Spectroscopy

Rotational spectroscopy utilizes the information obtained from the absorption or emission of electromagnetic radiation associated to changes in molecular rotational energy, typically in the microwave region of the electromagnetic spectrum. The only condition for an allowed rotational spectrum is that the molecule had a permanent electric dipole moment. For most molecules, the rotational motion is generally uncoupled from other molecular degrees of freedom, or in some cases, the couplings can be evaluated perturbatively. By itself, the rotational spectrum of a molecule is often absent of vibrational perturbations and only requires a relatively simple effective Hamiltonian to achieve a quantitative experimental fit.[84,86] In the presence of large-

amplitude motions and Coriolis effects, an explicit vibrational-rotational Hamiltonian is required, as in the cases of inversion, torsion or internal rotation.

Since the first study in 1934[88] to date, rotational spectroscopy has evolved greatly, developing different complementary techniques and incorporating time-domain detection and supersonic jet expansions. The development of radar and introduction of Wilson's Stark modulation direct-absorption techniques in the cm-wave range were the initials experimental milestones leading to routinely operational spectrometers. These experiments were done in a static gas cell using frequency scanning techniques, where monochromatic radiation passes through a sample cell, and the transmitted intensity is registered versus the frequency. The technique progressed around 1975 with the introduction of time-domain rotational spectroscopy[89–91] or Fourier-transform microwave spectroscopy (FTMW) techniques by Flygare. The FTMW technique uses a short (μs) MW pulse to produce a transient excitation polarizing the sample, subsequently recording in the time-domain the molecular relaxation signal or free-induction-decay. Then, in 1981 Flygare combined the time-domain spectroscopic techniques with a supersonic jet expansion,[92] using a high-quality tuneable Fabry-Pérot resonator[93,94] to couple the radiation to the sample. This spectrometer is known as Balle-Flygare or molecular beam (MB-FTMW) cavity spectrometer.

The Balle-Flygare FTMW spectrometer has been intensively used in many laboratories since they are relatively affordable to build and operate. In particular, since the introduction of the coaxial orientation of the beam and the resonator (COBRA set-up) by Grabow[95] in 1996, the spectrometer produces sub-Doppler resolution (FWHM linewidths of 10 kHz) and very high sensibility. The downside is the limited bandwidth (1 MHz), which requires slow mechanical scanning. In 2006, Pate developed the revolutionary chirped-pulse (CP) excitation spectroscopy,[96] a broadband FTMW spectrometer which has a bandwidth limit that is only imposed by the technical limitations of high-speed digitizers and microwave power amplifiers.[97] This instrument uses a fast-passage technique based on a frequency modulated (chirped pulse) excitation, simultaneously exciting the full operating bandwidth.

The CP-FTMW technique allowed to exponentially reduce the spectral acquisition time and the amount of sample while increasing the frequency operation bandwidth four orders of magnitude.[82] Other designs for broadband spectroscopy have been contributed by Grabow, considerably improving the spectral linewidth and other characteristics (In-phase/quadrature-phase-modulation passage-acquired-coherence technique, IMPACT).[98] In 2013, Patterson introduced the detection of molecular chirality by using a triple resonance or three-wave-mixing, which is currently progressing in a few laboratories.[99]

As mentioned before, molecular rotation is the fundamental idea in rotational spectroscopy. Therefore, the basic theory of quantum molecular rotation is essential to understand the rotational spectra and will be briefly reviewed in the following section. The purpose of the section is not to give a full and detailed explanation of the theory and the fundamental mathematics but rather to provide a general outline of the basic tools to understand rotational analysis. More specific details of molecular rotation theory can be found in the literature.[84–86]

2.1.1. Molecular rotation

The first approach to molecular rotation assumes that the molecule is a rigid rotor, where bond angles and distances adopt constant values. A rigid rotor can be defined by its inertial tensor (a symmetric 3×3 matrix). Using the principal axes system, the tensor is diagonal (moments of inertia I_a, I_b, I_c) and the Hamiltonian for molecular rotation can be written as:

$$H_{rot} = A\,{J_a}^2 + B\,{J_b}^2 + C\,{J_c}^2 \tag{1}$$

where J_i $(i = a, b, c)$ are the angular momentum operators along the principal axes of inertia a, b, and c, while A, B, C are the rotational constants, inversely proportional to their moment of inertia (usually expressed in MHz):

$$A = \left(\frac{h^2}{8\pi^2 I_a}\right)\ B = \left(\frac{h^2}{8\pi^2 I_b}\right)\ C = \left(\frac{h^2}{8\pi^2 I_c}\right) \tag{2}$$

The values of the moments of inertia differ depending on the type of molecular rotor. The molecules can be divided into the following groups: linear molecules ($I_a = 0 < I_b = I_c$), spherical tops ($I_a = I_b = I_c$), prolate symmetric tops ($I_a < I_b = I_c$), oblate symmetric tops ($I_a = I_b < I_c$) and asymmetric tops ($I_a < I_b < I_c$).

In linear and symmetric top molecules, the energy levels can be expressed in a closed form, as follows:

$$E(J) = BJ(J+1) \text{ Linear} \tag{3}$$

$$E(J,K) = BJ(J+1) + (A-B)K^2 \text{ Symmetric Prolate} \tag{4}$$

$$E(J,K) = BJ(J+1) + (C-B)K^2 \text{ Symmetric Oblate} \tag{5}$$

where $J = 0, 1, 2, 3, \ldots$ is the quantum number associated to total angular momentum (J, with $J^2 = {J_a}^2 + {J_b}^2 + {J_c}^2$) and $K = 0, \pm1, \pm2, \ldots, \pm J$ is the quantum number associated with the projection of the angular momentum along with one of the symmetry axes (J_i with $i = a$ for prolate and c for oblate).

Most of the molecules targeted in microwave studies belong to the group of asymmetric tops, like the molecules investigated in this thesis. However, in some cases, their structure may be close to that of a symmetric top (near-prolate or near-oblate). Only in a few cases, the system is a symmetric rotor, for example, the trimer of thiophenol in Chapter 2. The Ray's asymmetry parameter, κ, is often used to measure the degree of asymmetry:

$$\kappa = \frac{2B - A - C}{A - C} \tag{6}$$

The values of κ lie between -1 (prolate case) and +1 (oblate case).

The solution of the molecular rotation Hamiltonian is more complicated for asymmetric rotors, and the energy levels cannot be solved analytically. Since none of the angular momentum components is a constant of motion, the J_i operators do not commute with the rotational Hamiltonian (H_{rot}) and therefore K is no longer a good quantum number. In the molecular rotor, each J level gives rise to $J + 1$ distinct energy sublevels in a symmetric top (degeneracy in $|K|$), while it generates $2J + 1$ sublevels in an asymmetric top or K splitting. Then the energy levels are approached by a correlation diagram between the prolate and oblate symmetric top limits. Thus, rotational energy levels are expressed as (J, K_{-1}, K_{+1}), where K_{-1} represents the K value corresponding to the limiting prolate top and K_{+1} the one for the oblate top.

For two rotational levels defined by the wavefunctions $\psi(J, K_{-1}, K_{+1})$ and $\psi(J', K'_{-1}, K'_{+1})$, the transition dipole moment is given by the integral:

$$R = \int \psi^*(J, K_{-1}, K_{+1})\, \boldsymbol{\mu}\, \psi(J', K'_{-1}, K'_{+1})\, dt \tag{7}$$

where $\boldsymbol{\mu}$ is the electric dipole moment operator. The intensity of a rotational transition is proportional to the square of the transition moment. Hence, the condition for transitions between rotational energy levels to be allowed is that R adopts non-zero values. In symmetry terms, the direct product of the symmetry species of the integrand must be totally symmetric.

$$R \neq 0 \Longrightarrow \Gamma[\psi(J, K_{-1}, K_{+1})] \otimes \Gamma[\boldsymbol{\mu}] \otimes \Gamma[\psi(J', K'_{-1}, K'_{+1})] = A \tag{8}$$

This imposes a suite of restrictions on the values of J, K_{-1}, and $K_{+1}$of the two energy levels. Since the wavefunctions of the asymmetric rotor can be expressed as linear combinations of the symmetric rotor, the selection rules for J are the same as in a symmetric rotor:

$$\Delta J = 0, \pm 1 \tag{9}$$

where transitions with $\Delta J = -1$, $\Delta J = 0$, and $\Delta J = +1$ are designated as P, Q, and R branches, respectively. The selection rules for the pseudo quantum numbers K_{-1}, K_{+1} may be obtained from the symmetry of the ellipsoid of inertia and are summarized in Table 1.2.

Table 1.2. Selection rules for the pseudo quantum numbers of the asymmetric rotor.

μ-type transition	ΔK_{-1}	ΔK_{+1}
a $(\mu_a \neq 0)$	$0,\ \pm 2, .. (\pm even)$	$\pm 1, \pm 3, .. (\pm odd)$
b $(\mu_b \neq 0)$	$\pm 1, \pm 3, .. (\pm odd)$	$\pm 1, \pm 3, .. (\pm odd)$
c $(\mu_c \neq 0)$	$\pm 1, \pm 3, .. (\pm odd)$	$0, \pm 2, .. (\pm even)$

The rigid rotor model is approximately valid for asymmetric tops when *J* values are low and can be used to predict the molecular levels and transitions. Otherwise, the three ground-state experimental rotational constants can be calculated by fitting of a set of observed pure rotational transitions. For larger quantum numbers, however, perturbative corrections to the rigid rotor are necessary. Classically these corrections are interpreted as vibrational distortions of the molecular rotating structure, known as centrifugal distortion, and are expressed in the Hamiltonian as follows:

$$H_{rot} = H_{rigid\ rotor} + H_{centrifugal\ distortion} \tag{10}$$

The centrifugal distortion corrections are several orders of magnitude smaller than the rotational constants, but they are necessary for a proper assignment or prediction of the spectrum. The centrifugal terms were deduced by Watson, [100–102] using two different formalisms, either the symmetrically- or asymmetrically-reduced semi-rigid rotor Hamiltonian. These models use five centrifugal distortion parameters up to quartic order in the angular momenta and are precise enough for the quantitative assignment of pure rotational spectra into the millimeter-wave range.

In this thesis, we mostly used the Watson's S-reduction Hamiltonian of Equation (11), which uses the centrifugal distortion constants $D_J, D_{JK}, D_K, d_1, d_2$:

$$H_{rot} = \underbrace{A{J_a}^2 + B{J_b}^2 + C{J_c}^2}_{rigid\ rotor} \underbrace{-D_J J^4 - D_{JK} J^2 J_c^2 - D_K J_c^4 + d_1 J^2 (J_+^2 + J_-^2) + d_2 J^2 (J_+^4 + J_-^4)}_{quartic\ centrifugal\ distortion\ terms} \tag{11}$$

with J_+ and $J_- = (J_a \pm i\, J_b)$. The A-reduction set of distortion constants $(\Delta_J, \Delta_{JK}, \Delta_K, \delta_1, \delta_2)$ was originally intended for asymmetric rotors. However, for near-prolate molecules, Watson also noticed that the A-reduction sometimes fails since δ_K depends on $(B - C)$ in the denominator,[84,102] which does not happen for the S-reduced equivalent constant d_2. In this situation, the S reduction may give a better numerical description of the centrifugal forces.

In some molecular systems, the presence of large-amplitude motions like inversion, torsion, or puckering may produce additional complications in the spectrum, requiring two-state vibrational-rotational Hamiltonians. These cases are often associated to double-minimum potential functions, where the introduction of a small barrier produces a doubling of the ground vibrational state (Figure 1.5). As a consequence, two ladders of rotational states are built on top of each vibrational sublevel. These kinds of effects are equivalent to symmetry operations inverting all atomic coordinates and have important consequences in the determination of selection rules and statistical weight. Tunnelling across the barrier causes a doubling of rotational states with opposite (0^+ and 0^-) parities, and transitions can be observed between the corresponding symmetric and antisymmetric rovibrational states. Symmetry-inverting inter-state ($0^+ \leftrightarrow 0^-$) transitions occur for dipole-inverting (antisymmetric) motions so that the moment of transition integral remains totally symmetric. The reverse is true for non-inverting intra-state ($0^+ \leftrightarrow 0^+$ or $0^- \leftrightarrow 0^-$) transitions. The overall torsion-rotation Hamiltonian can be written as follows:

$$H = \begin{pmatrix} H_{rot}^{0^+} & H_{rot-vib} \\ H_{rot-vib} & H_{rot}^{0^-} + \Delta E_{0^\pm} \end{pmatrix} \tag{12}$$

where $H_{rot}^{0^+}$ and $H_{rot}^{0^-}$ are rotational Hamiltonians like those of equation (10) and $H_{rot-vib}$ represents the interactions terms.[103]

As an example, in the dimers with one water molecule and small reorientation barriers, the internal rotation of water around its internal axis produces two equivalent minima along a double-minimum potential energy function. As the motion connecting the two minima inverts two half spin fermions, the two tunnelling component lines have a 1:3 (=antisymmetric:symmetric) statistical weight, which corresponds to 0^+ (symmetric) and 0^- (antisymmetric) sublevels of the ground state, respectively.

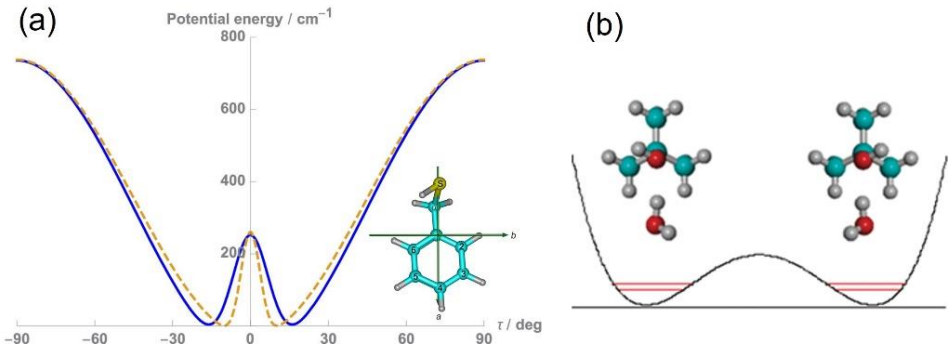

Figure 1.5. (a) Flexible model calculation for the torsional motion along the coordinate τ in benzyl mercaptan (continuous trace) compared to the ab initio potential (dashed), ref. 104. (b) The tunnelling motion of tert-butylalcohol-water, associated to the internal rotation of the hydroxyl group accompanied by structural relaxation and inversion in the monomer, ref. 105.

2.1.2. Microwave spectroscopy techniques

Fourier Transform Microwave (FTMW) spectroscopy exploits the information from resonant frequencies of rotational transitions of a molecule or cluster, allowing a very precise structural derivation. This technique is based on the excitation of the rotational energy levels in the microwave region, followed by the emission detection in the time domain (Free Induction Decay, FID) and the Fourier transformation to the frequency domain to obtain the rotational spectrum. In particular, the combination of supersonic jets[9] and Fourier transform microwave spectroscopy (FTMW)[89,90] is considered one of the most advanced experimental techniques to investigate the molecular structure in the gas phase.[106] Isomers, tautomers, and isotopologues can be identified with high spectral resolution using this technique.

Two different spectrometers at the *Group of Spectroscopy of Plasmas and Supersonic Jets* of the Universidad de Valladolid were used to collect the information and experimental data presented in this thesis:

1. A Balle-Flygare FTMW cavity spectrometer (8-18 GHz) and
2. A Chirped-Pulse FTMW spectrometer (2-8 GHz).

These spectrometers employ supersonic jet expansions and will be briefly explained in two separate sections.

The features and advantages of jet expansions for spectroscopy are described elsewhere,[107] but quickly summarized here. Supersonic jets are generated using a near-adiabatic gas expansion through a pin-hole nozzle (*ca*. 0.5-1.5 mm) into an expansion chamber. The pressurized region and the expansion chamber maintain a huge pressure difference, so the expanding molecules pass from a high-pressure (1-10 bar) random

thermal motion to a directed motion in the low-pressure region (10^{-5}-10^{-7} mbar). The sudden change in the kinetic conditions converts the broad velocity distribution into a narrow distribution centered around the terminal speed. This process converts the internal molecular energies into kinetic energy, producing considerable molecular freezing. However, since the different internal motions cannot equilibrate, the translational, rotational, and vibrational temperatures are different. The effective rotational temperatures are 2-3 K, while vibrational temperatures reach 100-150 K, moving the molecular population to the lower rotational levels of the vibronic ground-state and simplifying the spectrum.

Supersonic jet also reduced the intermolecular collisions, avoiding any mechanism of chemical reaction or decomposition. Therefore, the supersonic jets are used as a source of intermolecular clusters. Many-body collisions create the clusters in the first instants of the expansion, which are then stabilized by the absence of collisions. For this reason, jet expansions are the most effective way to study weak intermolecular complexes.[92] Furthermore, the reduction of intermolecular collisions also contributes to the spectral linewidth reduction, hence, to a very high spectral resolution (~5kHz, ~10^{-7}cm^{-1}). These features make this type of expansion a valuable tool for spectroscopy investigations characterizing molecular structures in the gas phase (in particular, rotational, vibrational, and electronic spectroscopy).

2.1.2.1. Balle-Flygare FTMW spectrometer

The Balle-Flygare FTMW spectrometer used here is a non-commercial instrument based on the Balle-Flygare design[94] (Figures 1.6 and 1.7). The sample can be prepared as a gaseous mixture (typically 0.1-0.5%) in a carrier gas or located in a reservoir nozzle if it is liquid or solid for thermal vaporization. The spectrometer uses circular nozzles (diameters ϕ=0.8-1.2 mm) and may be heated to ca. 373 K depending on molecular properties such as melting and boiling point, vapor pressure, etc. The sample is dragged by a carrier gas (He, Ne, or Ar) at pressures of 1-5 bar and expanded through a solenoid valve, creating a pulsed supersonic jet along the axis of a Fabry-Perot MW resonator.

The resonator consists of two spherical mirrors located near the confocal position (radius=33 cm), at the center of which there are two (¼ wavelength) L-shaped dipole antennas. The microwave radiation is introduced in the chamber by one of the antennas and is reflected in the resonator, while the injection valve is positioned off-axis near the center of one of the mirrors. The collinear arrangement of the jet and resonator axis[95,108] doubles each transition into two Doppler components. This radiation interacts with the supersonic expansion and produces a molecular excitation. The gas pulses extend for 500-1000 μs and are followed by short microwave impulses (~1 μs, < 100 mW) at a fixed

frequency, which allow the molecules to be polarized. Typically, up to 4 microwave pulses may be used per gas pulse.

After a few microseconds, the molecular emission (FID) is collected with the second antenna, amplified, down-converted to 30 MHz, and recorded for about 400 μs. A Fourier transformation finally produces the rotational spectrum in the frequency domain. The resulting signal is processed with the FTMW++ software developed by Grabow.[109] All frequency oscillators in the system are referenced to a 10 MHz rubidium standard, providing frequency accuracies of the rotational transitions below 5 kHz. This spectrometer allows us to work at higher frequencies that cannot be achieved using a CP-FTMW spectrometer. In addition, a better spectral resolution is provided, which is very useful to determine rotational transitions split into different component lines in case of hyperfine and/or tunneling effects.

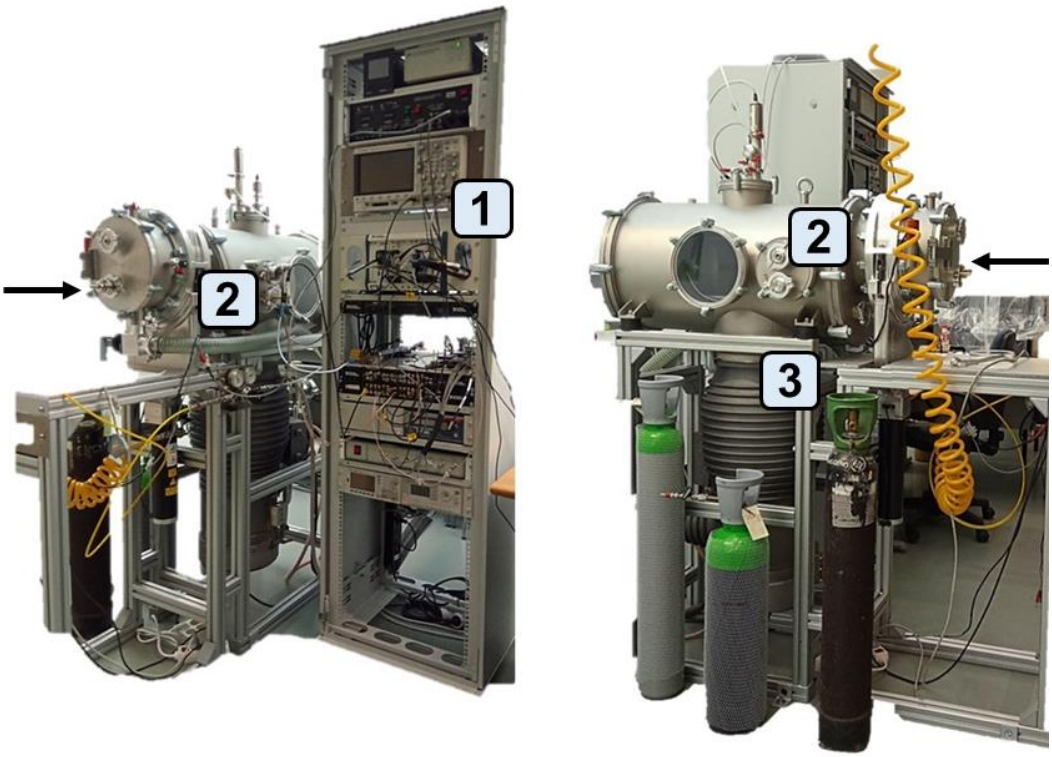

Figure 1.6. Two different views of the Balle-Flygare FTMW spectrometer at the Universidad de Valladolid (UVa) with the numbering of main components: electronic rack (1), expansion chamber (2), and diffusion pump (3). The arrow shows the gas inlet.

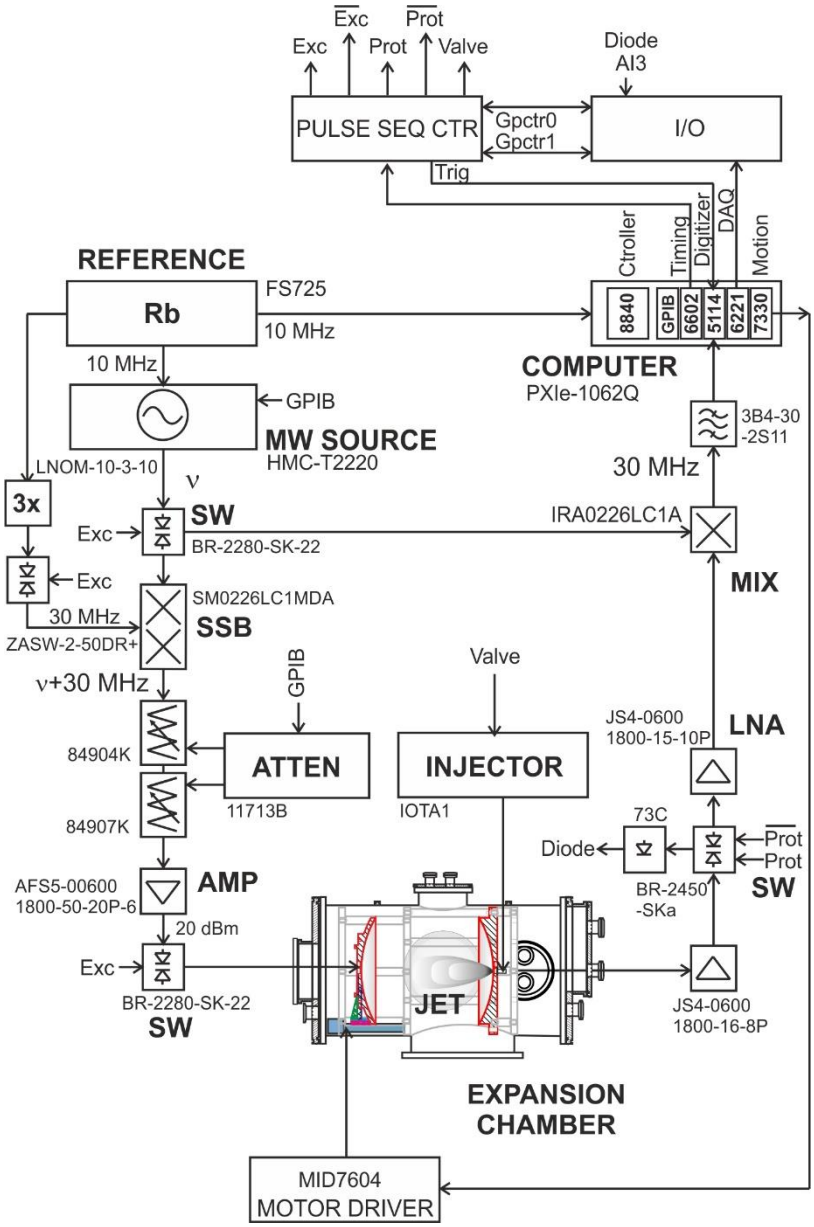

Figure 1.7. Functional diagram of the Balle-Flygare FTMW cavity spectrometer used in the thesis.

2.1.2.2. Chirped-Pulse FTMW spectrometer

The chirped-pulse FTMW spectrometer located at Universidad de Valladolid was purchased commercially from BrightSpec company and has been the main instrument used for this thesis. This instrument follows Pate's direct-digital design and covers the 2-8 GHz frequency region[110] (Figures 1.8, 1.9, and 1.10). In this spectrometer, the fast-passage technique has been implemented using a digital frequency sweep carried out with an arbitrary waveform generator (AWG), sweeping at a rate much faster than the dephasing time of the molecular coherence.[111] The sample is excited by a short microwave pulse implementing a very fast linear frequency sweep (6 GHz/μs) or "chirped" pulse so that this technique is known as chirped-pulse Fourier Transform Microwave (CP-FTMW) spectroscopy. The chirped pulse covers all molecular transitions within the frequency range of the sweep, allowing for simultaneous excitation and recording of a large swath of molecular transitions in a single experiment.

In this spectrometer, the supersonic expansion occurs in a high-vacuum chamber, which holds two horn antennas: one to emit the polarization radiation and the other to receive the molecular FID emission signal. The sample injection is like in the FTMW spectrometer, using a solenoid valve attached to a pin-hole nozzle. Solid or liquid samples can be stored inside the heating nozzle in the vacuum chamber and vaporized thermally. The chirp-pulsed instrument has a perpendicular arrangement between the nozzle and the horn antennas; therefore, the transitions do not present Doppler splitting. Instead, the linewidth increases about an order of magnitude compared with the cavity spectrometer (about 150 kHz). The chirped pulse (1-4 μs) created by the AWG (25 GS/s in two-channel) is amplified with a solid-state power amplifier (20 W) and broadcasted into the excitation region. The weak FID signal is detected using a receiver horn antenna, then passed through a diode limiter, a PIN-diode switch (closed during excitation), and amplified by a low-noise amplifier. Finally, the signal is recorded in the time-domain by a digital oscilloscope (25 GS/s) and converted into the frequency domain by a fast Fourier transform procedure. The typical operation requires signal averaging and uses a repetition rate of 5 Hz. All frequencies are phase-locked to a 10 MHz Rb standard.

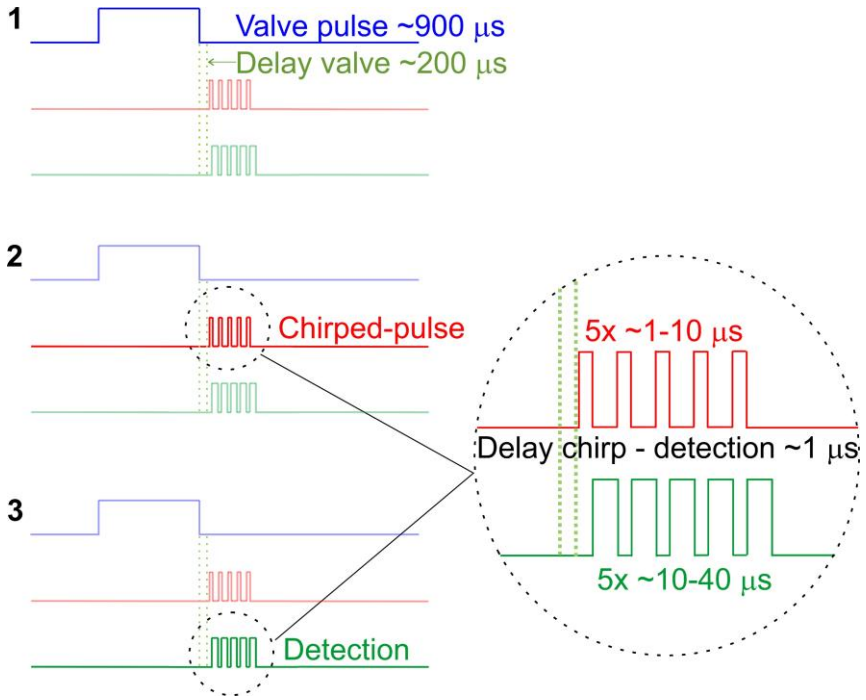

Figure 1.8. Scheme of the operation sequence in the CP-FTMW spectrometer, (1) valve pulse and supersonic expansion. (2) Chirped-pulse that causes the polarization and molecular excitation. (3) FID detection, then followed by a Fourier transform.

The pulse sequence of the CP-FTMW spectrometer is represented in Figure 1.8 and includes the following steps:

1) Formation of the supersonic expansion. In this step, the sample (either a gas mixture or a vaporized sample diluted in the carrier gas) is injected into the expansion chamber. The supersonic jet is formed by opening the valve for about 400-900 μs, depending on the carrier gas used. After the gas pulse, there is a delay of 100-300 μs to allow the expansion to reach the chamber.
2) Chirped-pulse excitation. A chirped pulse is generated (1-5 μs), and the sample is polarized, covering a maximum bandwidth of 6 GHz. These pulses are previously amplified with a 20 W pulsed solid-state unit. Then the polar molecular species in the supersonic expansion spontaneously emit coherent radiation at the resonant frequencies of the rotational transitions or FID. Several (5-8) excitation pulses can be used for each gas pulse, increasing the efficiency of the spectroscopic process.

3) FID acquisition. This FID molecular emission signal is amplified and detected in the time domain for ~40 μs, followed by a Fourier transformation into the frequency domain. A Kaiser-Bessel window is normally applied before the Fourier transformation for apodization.
4) Averaging. The excitation and detection process is averaged before being recorded and presented in the control computer.

A picture of the CP-FTMW spectrometer is presented in Figure 1.9. The electronic set-up is described in Figure 1.10 (the components in red are used for a perpendicular double-resonance).

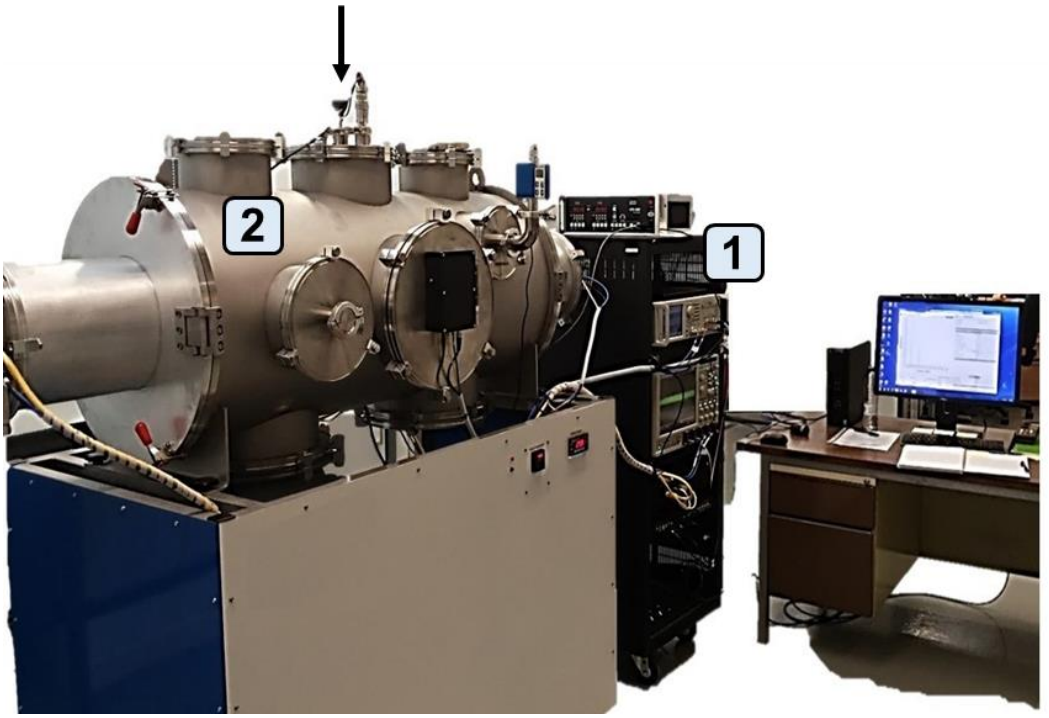

Figure 1.9. Broadband CP-FTMW spectrometer at UVa with the electronic rack (1) and the expansion chamber (2); the arrow displays the gas inlet.

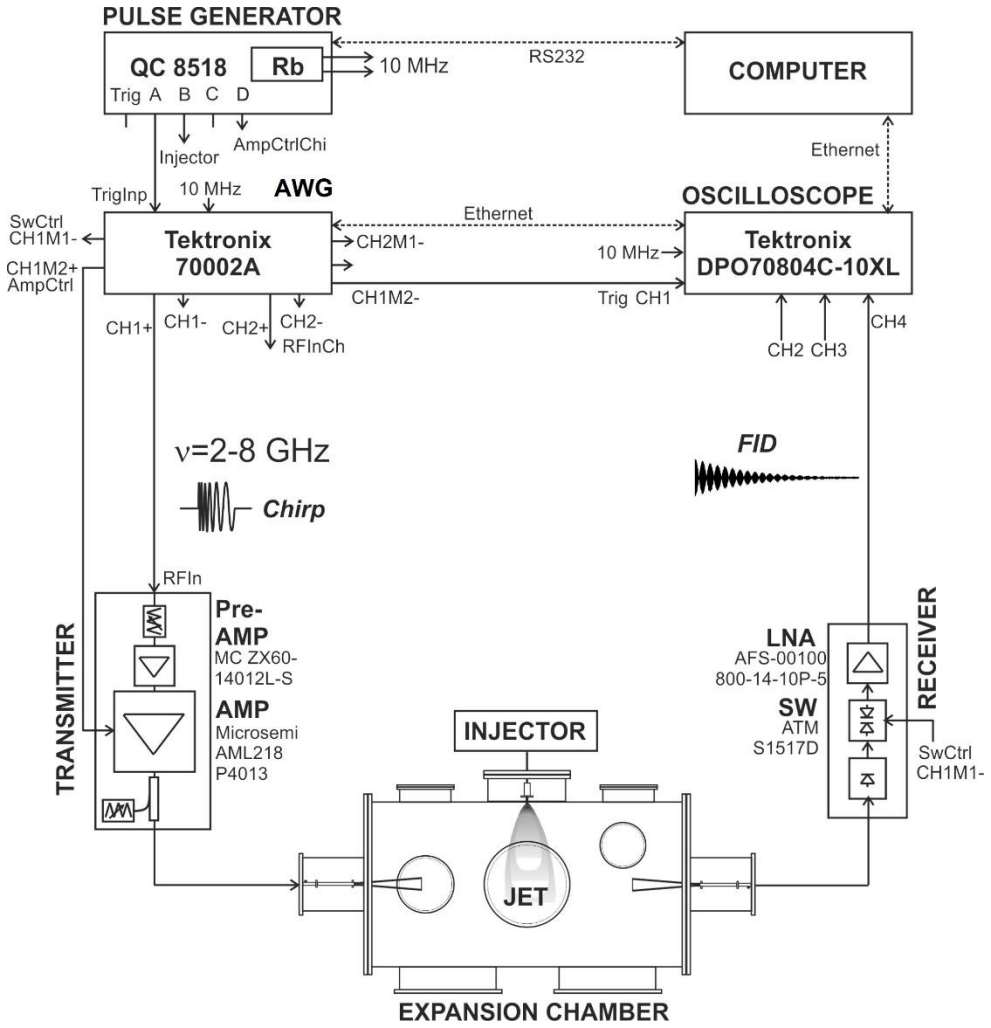

Figure 1.10. Functional diagram of the CP-FTMW spectrometer

2.2. Computational Methods

The development of new microwave techniques and instrumentation has broadened the scope of rotational spectroscopy and the size and complexity of the molecular systems that can be studied. At this moment, molecular systems up to 200-600 u can be analysed, as exemplified in the studies of organophosphorus compounds (PSP: 19 heavy atoms, 276 u),[112] the oxadiamantyl dimer[113] (28 heavy atoms, 378 u), or an intermolecular system like the 2-adamantanol dimer (22 heavy atoms, 304 u). The development of computational methods plays an essential role in spectroscopic

advances to predict and rationalize those different systems. In the larger molecules or clusters, several degrees of freedom define their conformation, making them conformationally complicated systems. Therefore, unlike dealing with small molecules, the chemical intuition is sometimes not enough to predict the most stable conformations in the gas phase. The computational calculations then become a vital tool for predicting the most stable conformations and molecular properties. Besides, the computational calculations are also benefited by the comparison with experimental rotational spectra. In this thesis, ab initio and density-functional theory (DFT) calculations were mainly used to rationalize the experiments.

2.2.1. Conformational search

The conformational search is the first step in the theoretical calculations necessary to predict the structures and relative energies of the lowest-lying conformers, which are required to describe the potential energy surface of a molecule or cluster. Molecular mechanics[87] was used in this thesis to obtain a fast and unrestricted structural scan of the molecule, despite its known accuracy deficiencies. Molecular mechanics is a purely classical method describing the molecule as a mechanical collection of point masses and springs, and totally ignores the electronic structure or microscopic description. The potential energy or force field is based on empirical information and calculated as the sum of stretching, bending, torsional, and non-bonded interactions terms. Since molecular mechanics is a cheap method in terms of computational cost, the complete potential energy surface of a large molecular system can be explored without any restrictions in seconds. These calculations can give an overall idea of the conformational landscape, but they can also miss many local minima. The accuracy of the energy calculations is also a well-known weakness of molecular mechanics, but at the same time, it can provide a large number of structures for structural screening. The initial structures must always be reanalysed later with quantum mechanical methods, which provide reliable information based on the molecular orbital distribution and the potential energy surface. Typically, waveform-based ab initio methods or Kohn-Sham DFT calculations are used for the quantum predictions.

The molecular mechanics method used in this thesis was the Merck Molecular Force Field (MMFF), which was designed to treat bio-organic and pharmaceutical-related molecular systems. This force field was initially used to study receptor-ligand interactions involving proteins and nucleic acids as receptors where the conformational geometries and energies are carefully assessed.[114] Therefore, MMFF is also a good option for conformational search or organic compounds, as those investigated in this thesis.

In addition to the force field, a search algorithm is necessary to locate the conformational landscape. Here we used a combination of Monte Carlo (MC) and large-scale low-mode sampling (LLMOD),[115] implemented in MacroModel (Schrodinger, LLC). New conformations are generated by randomly changing the dihedral angles in rotatable bonds by the Monte Carlo method, whereas LLMOD computes the molecular vibrational modes and then amplifies them to create different structures. Normally, a conformational search is limited to relevant structures within an energy window of 20-30 kJ mol^{-1}.

2.2.2. Quantum chemical methods

In order to obtain accurate structures and energies, quantum mechanical methods are necessary. These methods simultaneously provide a description of the PES, the electronic distribution, the vibrational force field, and the structural properties, necessary for predicting spectroscopic parameters like the rotational constants. In this way, theory supports and complements the interpretation and analysis of the rotational spectra.

The quantum mechanical methods used in this thesis depended on several characteristics of the investigated systems, such as molecular size for individual molecules or a good description of intermolecular forces in weakly-bound clusters. Waveform-based perturbative ab initio methods like second-order Møller-Plesset perturbation theory (MP2)[116] is one of the most widely used methods in the rotational spectroscopy community. This method corrects Hartree-Fock[117] by calculating the sum of the amplitudes between all double combinations of occupied and virtual orbitals.[118] In addition, MP2 considers dispersive interactions, although this method may overestimate their strength in some cases. However, since MP2 has a high computational cost, this method may no longer be affordable in larger molecules or clusters.

The second method that is widely used is DFT. Currently, the use of DFT is increasing[119] compared to the other quantum mechanical methods. As a result, many density-functional approximations have been developed, each with its benefits and limitations. For this reason, it is crucial to choose the right functional, which may be highly parametrized based on different experimental parameters. Grimme and other authors have presented a categorization (or "Jacob's ladder" Figure 1.11) of DFT methods,[120] ranging from composite, meta-GGA (generalized gradient approximation), hybrid, and double-hybrid techniques. This thesis has tested different DFT methods to complete our experimental work, including the hybrid methods B3LYP[121] and ωB97XD,[122] and the double-hybrid B2PLYP.[123] Additionally, some calculations tried the meta-GGA functional MN15L and hybrid M06-2X[110] methods in a few cases, with worse

results. Although B3LYP is a common functional in the spectroscopy community, it has a major downside: it does not account for dispersion interaction. Therefore, to account for the dispersion correction, these methods are supplemented by Grimme's D3 dispersion correction[126] and Becke-Johnson damping functions.[127]

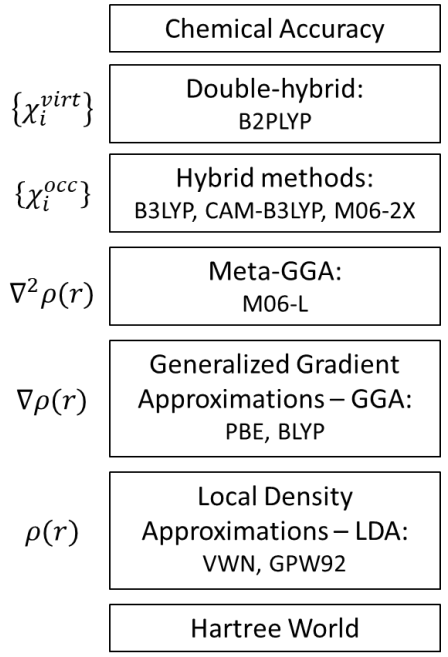

Figure 1.11. Jacob's ladder of density functional approximations, according to ref. 128.

Regarding the basis sets, we mainly used the triple-zeta quality with polarization and diffuse functions, most often the Ahlrich's polarized basis def2-TZVP.[129] For Chapter 6, we used the split-valence 6-311G basis set by Pople[130] augmented with polarization and diffuse functions or 6-311++G(d,p). The computational calculations were implemented mostly in Gaussian16.[131] All these theoretical methods will be further presented in the following chapters.

Geometry optimizations with quantum methods will give relatively accurate structures for spectroscopic work. These calculations are complemented with vibrational frequency calculations performed for each optimized geometry, normally within the harmonic approximation. Since geometry optimization sometimes provides a transition state structure, the frequency calculation allows the identification of stationary points as minima. Besides, the estimation of the zero-point energy correction and thermodynamic quantities can be achieved from the frequency calculations. Finally,

the centrifugal distortion constants can be obtained from the derived force field, which can be used to compare with the experiment. In the case of intermolecular clusters, the basis set superposition error is corrected with the counterpoise approximation.[132]

2.2.3. Additional computational tools

Although DFT and/or ab initio calculations are satisfactory methods for comparing to the experimental data, additional computational tools exploring the properties of the molecular electronic density can also give valuable information to understand bonding in intermolecular clusters. Two computational tools are used in this thesis with regard to the study of intermolecular interactions in molecular clusters: energy decomposition with symmetry-adapted perturbation theory (SAPT)[133] and electronic density topological analysis with NCIPlot.[134–136] Both tools will be briefly discussed.

2.2.3.1. SAPT

Symmetry-adapted perturbation theory is a theory of intermolecular interactions describing non-covalent interactions. SAPT typically computes the energy between two molecules directly via a perturbative approach without computing the total energy of the monomers or dimer. Additionally, the interaction energy calculated by SAPT decomposes into four physically meaningful components: electrostatic, exchange, induction, and dispersion terms.[137] In SAPT, the Hamiltonian of the dimer is partitioned into contributions from each monomer and the interaction. The simplest truncation of SAPT is called SAPT0 and defined in Equation 12, which captures the classical electrostatic interaction of two charge density and exchange at first order, and at second order the terms for electrostatic induction and dispersion appear, along with their exchange counterparts. The calculations may use different basis sets and were used as implemented in PSI4.[138]

$$E_{int}^{SAPT0} = E_{elst}^{(1)} + E_{exch}^{(1)} + E_{ind}^{(2)} + E_{exch-ind}^{(2)} + E_{disp}^{(2)} + E_{exch-disp}^{(2)} \quad (12)$$

2.2.3.2. NCI Plot

The non-covalent interactions plot characterizes the intermolecular interactions using a topological approach based on electron density. This approach allows both the analysis and mapping of a wide range of non-covalent interaction types. In a molecular system, the NCIs regions are identified by the isosurfaces of the reduced density gradient $s(r)$ in the DFT framework, [135,136,139]

$$s(r) = \frac{|\nabla\rho(r)|}{2k_F(r)\rho(r)} \quad (13)$$

where $k_F = (3\pi^2\rho(r))^{1/3}$ is a constant. The approach of NCI focuses on regions far from the nuclei where the interaction between nearby groups perturbs the electron density. This perturbation produces a change in its reduced density gradient, generating a density critical point between them. In the analysis of weak interactions, the NCI approach highlights the regions where the electron density is weak, and its reduced density gradient is close to zero. However, the representation of the electron density versus its reduced gradient displays those critical points as holes, and the attractive and repulsive interactions are indistinguishable. Hence, a 2D NCI plot is generated by using the sign of the second eigenvalue of the Hessian matrix of the electron density (λ_2) to discriminate those interactions. The reduced gradient (s) is plotted as a function of the electron density (ρ), multiplied by the sign of λ_2. Therefore, the critical points are separated based on the topology of the electron density and the nature of the interactions: strong attractive interactions (such as hydrogen bonds); strong repulsive interactions (such as steric crowding); and delocalized weak interactions (such as van der Waals interactions). These different interaction features are also summarized in Table 1.3.

Table 1.3. Classification of NCI interactions according to the reduced gradient of the electron density.

ρ approx. (a.u)	λ_2	Typical shape	Interaction type	Example
>0.015	$\lambda_2 < 0$	Lentils	Strongly attractive	Hydrogen bonds
>0.015	$\lambda_2 > 0$	Compact	Strongly repulsive	Steric Clash
>0.015	$\lambda_2 \approx 0$	Sheets	Very weak	van der Waals

The NCIplot method also permits the 3D mapping, which is the spatial representation of the non-covalent interactions obtained in the 2D plots. These plots generate the isosurfaces of the reduced gradient of density between the atoms, displaying all non-covalent interactions and categorizing them by a color code: blue for stabilizing (attractive) interactions; green for weak interactions, and red for destabilizing (repulsive) interactions. The intensity of the color tone indicates the strength of the interactions. For instance, hydrogen bonds presented in deep blue are stronger than those presented in light blue. These isosurfaces are generated by analysing local properties on a cubic grid constructed within the NCIPlot program.[134,135] The NCIplot method used in this thesis evaluated the nature of non-covalent interactions between the aggregates of several molecules (Chapter 2 to 5) and the nucleoside aggregates (deoxycytidine and deoxyguanosine) and between nucleoside dimer with an amino acid in Chapter 6.

References:

(1) Müller-Dethlefs, K.; Hobza, P. Noncovalent Interactions: A Challenge for Experiment and Theory. *Chem. Rev.* 2000, *100* (1), 143–167. https://doi.org/10.1021/cr9900331.

(2) Israelachvili, J. N. *Intermolecular and Surface Forces: Third Edition*, Third Edition.; Elsevier Inc.: Oxford, 2011.

(3) Stone, A. *The Theory of Intermolecular Forces*, Second Edi.; Oxford University Press: Oxford, 2013. https://doi.org/10.1093/ACPROF:OSO/9780199672394.001.0001.

(4) Gilli, G.; Gilli, P. *The Nature of the Hydrogen Bond*; Press, I.-O. U., Ed.; Oxford, 2009.

(5) Jeffrey, G. A. *An Introduction to Hydrogen Bonding*; Oxford University Press: Oxford, 1997.

(6) Desiraju, G. R.; Steiner, T. *The Weak Hydrogen Bond*; Oxford University Press: Oxford, 1999.

(7) Scheiner, S. *Hydrogen Bonding. A Theoretical Perspective*; Oxford University Press: Oxford, 1997.

(8) Pimentel, G. C.; McClellan, M. A. *The Hydrogen Bond*; Freeman, W. H., Ed.; San Francisco, 1960.

(9) Miller, D. R. Free Jet Sources. In *Atomic and Molecular Beam Methods vol. 1*; Scoles, G., Ed.; Oxford University Press: Oxford, 1988; pp 14–53.

(10) Meyer, E. A.; Castellano, R. K.; Diederich, F. Interactions with Aromatic Rings in Chemical and Biological Recognition. *Angewandte Chemie - International Edition*. John Wiley & Sons, Ltd March 17, 2003, pp 1210–1250. https://doi.org/10.1002/anie.200390319.

(11) Juanes, M.; Saragi, R. T.; Caminati, W.; Lesarri, A. *The Hydrogen Bond and Beyond: Perspectives for Rotational Investigations of Non-Covalent Interactions*; 2019; Vol. 25, pp 11402–11411. https://doi.org/10.1002/chem.201901113.

(12) Millan, J.; Lesarri, A.; Fernández, J. A.; Martínez, R. Exploring Epigenetic Marks by Analysis of Noncovalent Interactions. *ChemBioChem* 2021, *22* (2), 408–415. https://doi.org/10.1002/CBIC.202000380.

(13) Matta, C. F.; Castillo, N.; Boyd, R. J. Extended Weak Bonding Interactions in DNA: π-Stacking (Base-Base), Base-Backbone, and Backbone-Backbone Interactions. *J. Phys. Chem. B* 2006, *110* (1), 563–578. https://doi.org/10.1021/jp054986g.

(14) Černý, J.; Kabeláč, M.; Hobza, P. Double-Helical → Ladder Structural Transition in the B-DNA Is Induced by a Loss of Dispersion Energy. *J. Am. Chem. Soc.* 2008, *130* (47), 16055–16059. https://doi.org/10.1021/ja805428q.

(15) Al-Hamdani, Y. S.; Tkatchenko, A. Understanding Non-Covalent Interactions in Larger Molecular Complexes from First Principles. *J. Chem. Phys.* 2019, *150* (1). https://doi.org/10.1063/1.5075487.

(16) Arunan, E.; Desiraju, G. R.; Klein, R. A.; Sadlej, J.; Scheiner, S.; Alkorta, I.; Clary, D. C.; Crabtree, R. H.; Dannenber, J. J.; Hobza, P.; Kjaergaard, H. G.; Legon, A. C.; Mennucci, B.; Nesbitt, D. J. Definition of the Hydrogen Bond (IUPAC Recommendations 2011). *Pure Appl. Chem.* 2011, *83* (8), 1637–1641. https://doi.org/10.1351/PAC-REC-10-01-02.

(17) Desiraju, G. R. The C−H···O Hydrogen Bond: Structural Implications and Supramolecular Design. *Acc. Chem. Res.* 1996, *29* (9), 441–449. https://doi.org/10.1021/ar950135n.

(18) Nishio, M.; Hirota, M.; Umezawa, Y. *The CH···π Interaction*; Wiley: New York, 1998.

(19) Takahashi, O.; Kohno, Y.; Nishio, M. Relevance of Weak Hydrogen Bonds in the Conformation of Organic Compounds and Bioconjugates: Evidence from Recent Experimental Data and High-Level Ab Initio MO Calculations. *Chem. Rev.* 2010, *110* (10), 6049–6076. https://doi.org/10.1021/cr100072x.

(20) Bakhmutov, V. I. *Dihydrogen Bonds: Principles, Experiments, and Applications*; Wiley: New York, 2008.

(21) Desiraju, G. R.; Ho, P. S.; Kloo, L.; Legon, A. C.; Marquardt, R.; Metrangolo, P.; Politzer, P.; Resnati, G.; Rissanen, K. Definition of the Halogen Bond (IUPAC Recommendations 2013). *Pure Appl. Chem.* 2013, *85* (8), 1711–1713. https://doi.org/10.1351/PAC-REC-12-05-10.

(22) Minyaev, R. M.; Minkin, V. I. Theoretical Study of O-> X (S, Se, Te) Coordination in Organic Compounds. *Can. J. Chem.* 1998, *76* (6), 776–788. https://doi.org/10.1139/v98-080.

(23) Zahn, S.; Frank, R.; Hey-Hawkins, E.; Kirchner, B. Pnicogen Bonds: A New Molecular Linker? *Chem. – A Eur. J.* 2011, *17* (22), 6034–6038. https://doi.org/10.1002/chem.201002146.
(24) Scheiner, S. A New Noncovalent Force: Comparison of P···N Interaction with Hydrogen and Halogen Bonds. *J. Chem. Phys.* 2011, *134* (9), 094315. https://doi.org/10.1063/1.3562209.
(25) Bauzá, A.; Mooibroek, T. J.; Frontera, A. Tetrel-Bonding Interaction: Rediscovered Supramolecular Force? *Angew. Chemie Int. Ed.* 2013, *52* (47), 12317–12321. https://doi.org/10.1002/anie.201306501.
(26) Mani, D.; Arunan, E. The X–C···Y (X = O/F, Y = O/S/F/Cl/Br/N/P) 'Carbon Bond' and Hydrophobic Interactions. *Phys. Chem. Chem. Phys.* 2013, *15* (34), 14377. https://doi.org/10.1039/c3cp51658j.
(27) Cavallo, G.; Metrangolo, P.; Pilati, T.; Resnati, G.; Terraneo, G. Naming Interactions from the Electrophilic Site. *Cryst. Growth Des.* 2014, *14* (6), 2697–2702. https://doi.org/10.1021/cg5001717.
(28) Legon, A. C.; Walker, N. R. What's in a Name? 'Coinage-Metal' Non-Covalent Bonds and Their Definition. *Phys. Chem. Chem. Phys.* 2018, *20* (29), 19332–19338. https://doi.org/10.1039/C8CP03432J.
(29) Latimer, W. M.; Rodebush, W. H. Polarity And Ionization From The Standpoint Of The Lewis Theory Of Valence. *J. Am. Chem. Soc.* 1920, *42* (7), 1419–1433. https://doi.org/10.1021/JA01452A015.
(30) Pauling, L. *The Nature of the Chemical Bond*; CorneUUniv. Press, Ithsea: New York, 1939.
(31) Chand, A.; Sahoo, D. K.; Rana, A.; Jena, S.; Biswal, H. S. The Prodigious Hydrogen Bonds with Sulfur and Selenium in Molecular Assemblies, Structural Biology, and Functional Materials. *Acc. Chem. Res.* 2020, *53* (8), 1580–1592. https://doi.org/10.1021/ACS.ACCOUNTS.0C00289.
(32) Desiraju, G. R. Hydrogen Bridges in Crystal Engineering: Interactions without Borders. *Acc. Chem. Res.* 2002, *35* (7), 565–573.
(33) Dyke, T. R.; Mack, K. M.; Muenter, J. S. The Structure of Water Dimer from Molecular Beam Electric Resonance Spectroscopy. *J. Chem. Phys.* 1977, *66* (2), 498. https://doi.org/10.1063/1.433969.
(34) Odutola, J. A.; Dyke, T. R. Partially Deuterated Water Dimers: Microwave Spectra and Structure. *J. Chem. Phys.* 1980, *72* (9), 5062. https://doi.org/10.1063/1.439795.
(35) Pérez, C.; Muckle, M. T.; Zaleski, D. P.; Seifert, N. A.; Temelso, B.; Shields, G. C.; Kisiel, Z.; Pate, B. H. Structures of Cage, Prism, and Book Isomers of Water Hexamer from Broadband Rotational Spectroscopy. *Science (80-.).* 2012, *336* (6083), 897–901. https://doi.org/10.1126/SCIENCE.1220574.
(36) Pérez, C.; Zaleski, D. P.; Seifert, N. A.; Temelso, B.; Shields, G. C.; Kisiel, Z.; Pate, B. H. Hydrogen Bond Cooperativity and the Three-Dimensional Structures of Water Nonamers and Decamers. *Angew. Chemie Int. Ed.* 2014, *53* (52), 14368–14372. https://doi.org/10.1002/ANIE.201407447.
(37) Caminati, W.; Grabow, J.-U. J.-U. Advancements in Microwave Spectroscopy. In *Frontiers and Advancements in Microwave Spectroscopy*; Laane, J., Ed.; Elsevier: Amsterdam, 2018; pp 569–598. https://doi.org/10.1016/B978-0-12-811220-5.00018-6.
(38) Caminati, W.; Grabow, J.-U. Microwave Spectroscopy Molecular Systems. In *Frontiers of Molecular Spectroscopy*; Laane, J., Ed.; Elsevier Inc.: Amsterdam, 2008; pp 456–552.
(39) Biswal, H. S. Hydrogen Bonding Involving Sulfur: New Insights from Ab Initio Calculations and Gas Phase Laser Spectroscopy. In *Noncovalent Forces*; Scheiner, S., Ed.; Springer Int. Pub.: Switzerland, 2015.
(40) Biswal, H. S.; Shirhatti, P. R.; Wategaonkar, S. O–H···O versus O–H···S Hydrogen Bonding I: Experimental and Computational Studies on the p -Cresol·H2O and p -Cresol·H2S Complexes. *J. Phys. Chem. A* 2009, *113* (19), 5633–5643. https://doi.org/10.1021/jp9009355.
(41) Goebel, J. R.; Ault, B. S.; Del Bene, J. E. Matrix Isolation and Ab Initio Study of 1:1 Hydrogen-Bonded Complexes of H 2 O 2 with Phosphorus and Sulfur Bases. *J. Phys. Chem. A* 2001, *105* (50), 11365–11370. https://doi.org/10.1021/jp013262b.
(42) Wierzejewska, M. Infrared Matrix Isolation Studies of Complexes Formed between

Dimethylsulfide, Dimethyldisulfide and Nitrous Acid. *J. Mol. Struct.* 2000, *520* (1–3), 199–214. https://doi.org/10.1016/S0022-2860(99)00342-7.

(43) Wategaonkar, S.; Bhattacherjee, A. N–H···S Interaction Continues To Be an Enigma: Experimental and Computational Investigations of Hydrogen-Bonded Complexes of Benzimidazole with Thioethers. *J. Phys. Chem. A* 2018, *122* (17), 4313–4321. https://doi.org/10.1021/acs.jpca.8b01943.

(44) Biswal, H. S.; Wategaonkar, S. OH · · · X (X = O, S) Hydrogen Bonding in Thetrahydrofuran and Tetrahydrothiophene. *J. Chem. Phys.* 2011, *135* (13), 134306. https://doi.org/10.1063/1.3645107.

(45) Das, A.; Mandal, P. K.; Lovas, F. J.; Medcraft, C.; Walker, N. R.; Arunan, E. The H2S Dimer Is Hydrogen-Bonded: Direct Confirmation from Microwave Spectroscopy. *Angew. Chemie Int. Ed.* 2018, *57* (46), 15199–15203. https://doi.org/10.1002/anie.201808162.

(46) Sanz, M. E.; López, J. C.; Alonso, J. L.; Maris, A.; Favero, P. G.; Caminati, W. Conformation and Stability of Adducts of Sulfurated Cyclic Compounds with Water: Rotational Spectrum of Tetrahydrothiophene–Water. *J. Phys. Chem. A* 1999, *103* (27), 5285–5290. https://doi.org/10.1021/jp991002c.

(47) Lobo, I. A. A.; Robertson, P. A.; Villani, L.; Wilson, D. J. D.; Robertson, E. G.; A. Robertson, P.; Villani, L.; J. D. Wilson, D.; G. Robertson, E. Thiols as Hydrogen Bond Acceptors and Donors: Spectroscopy of 2-Phenylethanethiol Complexes. *J. Phys. Chem. A* 2018, *122* (36), 7171–7180. https://doi.org/10.1021/acs.jpca.8b06649.

(48) Martin, D. E.; Robertson, E. G.; Thompson, C. D.; Morrison, R. J. S. Resonant 2-Photon Ionization Study of the Conformation and the Binding of Water Molecules to 2-Phenylethanethiol (PhC H2 C H2 SH). *J. Chem. Phys.* 2008, *128* (16), 164301. https://doi.org/10.1063/1.2903477.

(49) Mishra, K. K.; Borish, K.; Singh, G.; Panwaria, P.; Metya, S.; Madhusudhan, M. S.; Das, A. Observation of an Unusually Large IR Red-Shift in an Unconventional S–H···S Hydrogen-Bond. *J. Phys. Chem. Lett.* 2021, *12* (4), 1228–1235. https://doi.org/10.1021/ACS.JPCLETT.0C03183.

(50) Bhattacharyya, S.; Wategaonkar, S. ZEKE Photoelectron Spectroscopy of p -Fluorophenol···H 2 S/H 2 O Complexes and Dissociation Energy Measurement Using the Birge–Sponer Extrapolation Method. *J. Phys. Chem. A* 2014, *118* (40), 9386–9396. https://doi.org/10.1021/jp505393p.

(51) Bhattacherjee, A.; Matsuda, Y.; Fujii, A.; Wategaonkar, S. Acid–Base Formalism in Dispersion-Stabilized S–H···Y (Y═O, S) Hydrogen-Bonding Interactions. *J. Phys. Chem. A* 2015, *119* (7), 1117–1126. https://doi.org/10.1021/jp511904a.

(52) Bhattacherjee, A.; Matsuda, Y.; Fujii, A.; Wategaonkar, S. The Intermolecular S-H···Y (Y=S,O) Hydrogen Bond in the H2S Dimer and the H 2 S-MeOH Complex. *ChemPhysChem* 2013, *14* (5), 905–914. https://doi.org/10.1002/cphc.201201012.

(53) Bhattacharyya, S.; Bhattacherjee, A.; Shirhatti, P. R.; Wategaonkar, S. O–H···S Hydrogen Bonds Conform to the Acid–Base Formalism. *J. Phys. Chem. A* 2013, *117* (34), 8238–8250. https://doi.org/10.1021/jp405414h.

(54) Cole, G. C.; Møllendal, H.; Guillemin, J.-C. Microwave Spectrum of 3-Butyne-1-Thiol: Evidence for Intramolecular S–H···π Hydrogen Bonding. *J. Phys. Chem. A* 2006, *110* (30), 9370–9376. https://doi.org/10.1021/jp062093y.

(55) Juanes, M.; Saragi, R. T.; Jin, Y.; Zingsheim, O.; Schlemmer, S.; Lesarri, A. Rotational Spectrum and Intramolecular Hydrogen Bonding in 1,2-Butanedithiol. *J. Mol. Struct.* 2020, *1211*. https://doi.org/10.1016/j.molstruc.2020.128080.

(56) Xu, L.-H.; Liu, Q.; Suenram, R. D.; Lovas, F. J.; Hight Walker, A. R.; Jensen, J. O.; Samuels, A. C. Rotational Spectra, Conformational Structures, and Dipole Moments of Thiodiglycol by Jet-Cooled FTMW and Ab Initio Calculations. *J. Mol. Spectrosc.* 2004, *228* (2), 243–250. https://doi.org/10.1016/j.jms.2004.04.004.

(57) Juanes, M.; Saragi, R. T.; Zingsheim, O.; Schlemmer, S.; Lesarri, A. Chirality, Structure and Hydrogen Bonding in Dithiols: Rotational Spectrum of the Chiral and Meso 2,3-Butanedithiol. *J. Mol. Struct.* 2021, *1246*, 131221. https://doi.org/10.1016/J.MOLSTRUC.2021.131221.

(58) Juanes, M.; Lesarri, A.; Pinacho, R.; Charro, E.; Rubio, J. E.; Enríquez, L.; Jaraíz, M. Sulfur

Hydrogen Bonding in Isolated Monohydrates: Furfuryl Mercaptan versus Furfuryl Alcohol. *Chem. – A Eur. J.* 2018, *24* (25), 6564–6571. https://doi.org/10.1002/CHEM.201705727.

(59) Juanes, M.; Saragi, R. T.; Pinacho, R.; Rubio, J. E.; Lesarri, A. Sulfur Hydrogen Bonding and Internal Dynamics in the Monohydrates of Thenyl Mercaptan and Thenyl Alcohol. *Phys. Chem. Chem. Phys.* 2020. https://doi.org/10.1039/D0CP01706J.

(60) Ghosh, S.; Bhattacharyya, S.; Wategaonkar, S. Dissociation Energies of Sulfur-Centered Hydrogen-Bonded Complexes. *J. Phys. Chem. A* 2015, *119* (44), 10863–10870. https://doi.org/10.1021/acs.jpca.5b08185.

(61) Cooke, S. A.; Corlett, G. K.; Legon, A. C. Comparisons of the Interactions of Benzene, Furan and Thiophene with Lewis Acids: The Rotational Spectrum of Thiophene···HF. *Chem. Phys. Lett.* 1998, *291* (3–4), 269–276. https://doi.org/10.1016/S0009-2614(98)00587-9.

(62) Cocinero, E. J.; Sánchez, R.; Blanco, S.; Lesarri, A.; López, J. C.; Alonso, J. L. Weak Hydrogen Bonds C–H···S and C–H···F–C in the Thiirane–Trifluoromethane Dimer. *Chem. Phys. Lett.* 2005, *402* (1–3), 4–10. https://doi.org/10.1016/j.cplett.2004.11.073.

(63) Tubergen, M. J.; Flad, J. E.; Del Bene, J. E. Microwave Spectroscopic and Ab Initio Studies of the Hydrogen-Bonded Trimethylamine–Hydrogen Sulfide Complex. *J. Chem. Phys.* 1997, *107* (7), 2227–2231. https://doi.org/10.1063/1.474619.

(64) Wang, D.; Chopra, P.; Wategaonkar, S.; Fujii, A. Electronic and Infrared Spectroscopy of Benzene-(H 2 S) n (n = 1 and 2): The Prototype of the SH-π Interaction. *J. Phys. Chem. A* 2019, *123* (33), 7255–7260. https://doi.org/10.1021/acs.jpca.9b02199.

(65) Burley, S.; Petsko, G. Aromatic-Aromatic Interaction: A Mechanism of Protein Structure Stabilization. *Science (80-.).* 1985, *229* (4708), 23–28. https://doi.org/10.1126/science.3892686.

(66) Mcgaughey, G. B.; Gagne, M.; Rappe, A. K. π-Stacking Interactions, Alive and Well in Proteins. *J. Biol. Chem.* 1998, *273* (25), 15458–15463.

(67) Kool, E. T. Hydrogen Bonding, Base Stacking, and Steric Effects in DNA Replication. *Annu. Rev. Biophys. Biomol. Struct.* 2001, *30* (October), 1–22.

(68) Schlosser, F.; Moos, M.; Lambert, C.; Würthner, F. Redox-Switchable Intramolecular π-π-Stacking of Perylene Bisimide Dyes in a Cyclophane. *Adv. Mater.* 2013, *25* (3), 410–414. https://doi.org/10.1002/adma.201201266.

(69) Maharramov, A. M.; Mahmudov, K. T.; Kopylovich, M. N.; Pombeiro, A. J. L. *Non-Covalent Interactions in the Synthesis and Design of New Compounds*; Maharramov, A. M., Mahmudov, K. T., Kopylovich, M. N., Pombeiro, A. J. L., Eds.; John Wiley & Sons, Inc: Hoboken, New Jersey, 2016. https://doi.org/10.1002/9781119113874.

(70) Stornaiuolo, M.; De Kloe, G. E.; Rucktooa, P.; Fish, A.; Van Elk, R.; Edink, E. S.; Bertrand, D.; Smit, A. B.; De Esch, I. J. P.; Sixma, T. K. Assembly of a π-π Stack of Ligands in the Binding Site of an Acetylcholine-Binding Protein. *Nat. Commun.* 2013, *4* (May). https://doi.org/10.1038/ncomms2900.

(71) Ma, S.; Zhao, W.; Zhou, J.; Wang, J.; Chu, S.; Liu, Z.; Xiang, G. A New Type of Noncovalent Surface–π Stacking Interaction Occurring on Peroxide-Modified Titania Nanosheets Driven by Vertical π-State Polarization. *Chem. Sci.* 2021, *12* (12), 4411–4417. https://doi.org/10.1039/D0SC06601J.

(72) Knowles, R. R.; Jacobsen, E. N. Attractive Noncovalent Interactions in Asymmetric Catalysis: Links between Enzymes and Small Molecule Catalysts. *Proc. Natl. Acad. Sci.* 2010, *107* (48), 20678–20685. https://doi.org/10.1073/PNAS.1006402107.

(73) Krenske, E. H.; Houk, K. N. Aromatic Interactions as Control Elements in Stereoselective Organic Reactions. *Acc. Chem. Res.* 2012, *46* (4), 979–989. https://doi.org/10.1021/AR3000794.

(74) Hunter, C. A.; Sanders, J. K. M. The Nature of π-π Interactions. *J. Am. Chem. Soc.* 1990, *112* (14), 5525–5534. https://doi.org/10.1021/ja00170a016.

(75) and, M. O. S.; Sherrill*, C. D. High-Accuracy Quantum Mechanical Studies of Π−π Interactions in Benzene Dimers. *J. Phys. Chem. A* 2006, *110* (37), 10656–10668. https://doi.org/10.1021/JP0610416.

(76) Wheeler, S. E. Unraveling the Origin of Substituents Effects in π-Stacking Interactions. In *Challenges and Advances in Computational Chemistry and Physics*; Springer, Cham, 2015; Vol. 19, pp 421–442. https://doi.org/10.1007/978-3-319-14163-3_14.
(77) Wheeler, S. E.; Houk, K. N. Substituent Effects in the Benzene Dimer Are Due to Direct Interactions of the Substituents with the Unsubstituted Benzene. *J. Am. Chem. Soc.* 2008, *130* (33), 10854–10855. https://doi.org/10.1021/ja802849j.
(78) Grimme, S. Do Special Noncovalent π-π Stacking Interactions Really Exist? *Angew. Chemie - Int. Ed.* 2008, *47* (18), 3430–3434. https://doi.org/10.1002/anie.200705157.
(79) Martinez, C. R.; Iverson, B. L. Rethinking the Term "π-Stacking." *Chem. Sci.* 2012, *3* (7), 2191–2201. https://doi.org/10.1039/c2sc20045g.
(80) Pauly, H. *Atom, Molecule, and Cluster Beams I*; Springer Series on Atomic, Optical, and Plasma Physics; Springer Berlin Heidelberg: Berlin, Heidelberg, 2000; Vol. 28. https://doi.org/10.1007/978-3-662-04213-7.
(81) Campargue, R. *Atomic and Molecular Beams*; Campargue, R., Ed.; Springer Berlin Heidelberg: Berlin, Heidelberg, 2001. https://doi.org/10.1007/978-3-642-56800-8.
(82) Shipman, S. T.; Pate, B. H. New Techniques in Microwave Spectroscopy. *Handb. High-resolution Spectrosc.* 2011. https://doi.org/10.1002/9780470749593.HRS036.
(83) Grabow, J.-U.; Caminati, W. Microwave Spectroscopy Experimental Techniques. In *Frontiers of Molecular Spectroscopy*; Laane, J., Ed.; Elsevier, 2009; pp 383–454. https://doi.org/10.1016/B978-0-444-53175-9.X0001-3.
(84) Gordy, W.; Cook, R. L. *Microwave Molecular Spectra*; John Wiley & Sons, Ltd: New York, 1984.
(85) Kroto, H. W. *Molecular Rotation Spectra*; Dover Publication Inc.: New York, 1992.
(86) Townes, C. H.; Schawlow, A. L. *Microwave Spectroscopy*; Dover Publication Inc.: New York, 1975.
(87) Jensen, F. *Introduction to Computational Chemistry*; John Wiley & Sons, Incorporated: Chichester, 2016.
(88) Cleeton, C. E.; Williams, N. H. Electromagnetic Waves of 1.1 Cm Wave-Length and the Absorption Spectrum of Ammonia. *Phys. Rev.* 1934, *45* (4), 234–237. https://doi.org/10.1103/PhysRev.45.234.
(89) Dicke, R. H.; Romer, R. H. Pulse Techniques in Microwave Spectroscopy. *Rev. Sci. Instrum.* 1955, *26* (10), 915–928. https://doi.org/10.1063/1.1715156.
(90) Ekkers, J.; Flygare, W. H. Pulsed Microwave Fourier Transform Spectrometer. *Rev. Sci. Instrum.* 1976, *47* (4), 448–454. https://doi.org/10.1063/1.1134647.
(91) Somers, R. M.; Poehler, T. O.; Wagner, P. E. Microwave Time Domain Fabry–Perot Emission Spectrometer. *Rev. Sci. Instrum.* 1975, *46* (6), 719–725. https://doi.org/10.1063/1.1134296.
(92) Legon, A. C. Isolation and Characterisation of Some Transient Complexes of Chemical Interest Using Pulsed-Nozzle, Fourier-Transform Microwave Spectroscopy. *J. Mol. Struct.* 1992, *266* (C), 21–37. https://doi.org/10.1016/0022-2860(92)80047-L.
(93) Balle, T. J.; Campbell, E. J.; Keenan, M. R.; Flygare, W. H. A New Method for Observing the Rotational Spectra of Weak Molecular Complexes: KrHCl. *J. Chem. Phys.* 1979, *71* (6), 2723–2724. https://doi.org/10.1063/1.438631.
(94) Balle, T. J.; Flygare, W. H. Fabry-Perot Cavity Pulsed Fourier Transform Microwave Spectrometer with a Pulsed Nozzle Particle Source. *Rev. Sci. Instrum.* 1981, *52* (1), 33–45. https://doi.org/10.1063/1.1136443.
(95) Grabow, J. U.; Stahl, W.; Dreizler, H. A Multioctave Coaxially Oriented Beam-Resonator Arrangement Fourier-Transform Microwave Spectrometer. *Rev. Sci. Instrum.* 1996, *67* (12), 4072–4084. https://doi.org/10.1063/1.1147553.
(96) Grubbs II, G.; Moon, N.; Persinger, T.; Gillcrist, D.; Marshall, F. A Chirped Pulse Fourier Transform Microwave (Cp-Ftmw) Spectrometer with Laser Ablation Source to Search for Actinide-Containing Molecules and Noble Metal Clusters. In *Proceedings of the 71st International Symposium on Molecular Spectroscopy*; University of Illinois at Urbana-Champaign: Urbana, Illinois, 2016; pp 1–1. https://doi.org/10.15278/isms.2016.MJ12.
(97) Patterson, D.; Schnell, M.; Doyle, J. M. Enantiomer-Specific Detection of Chiral Molecules via

Microwave Spectroscopy. *Nature* 2013, *497* (7450), 475–477. https://doi.org/10.1038/nature12150.

(98) Grabow, J.-U. Fourier Transform Microwave Spectroscopy Measurement and Instrumentation. In *Handbook of High-resolution Spectroscopy*; Quack, M., Merkt, F., Eds.; John Wiley & Sons, Ltd, 2011; pp 724–799.

(99) Pate, B. H.; Evangelisti, L.; Caminati, W.; Xu, Y.; Thomas, J.; Patterson, D.; Perez, C.; Schnell, M. Quantitative Chiral Analysis by Molecular Rotational Spectroscopy. In *Chiral Analysis: Advances in Spectroscopy, Chromatography and Emerging Methods: Second Edition*; Polavarapu, P. L., Ed.; Elsevier: Amsterdam, 2018; pp 679–729. https://doi.org/10.1016/B978-0-444-64027-7.00019-7.

(100) Watson, J. K. G. Simplification of the Molecular Vibration-Rotation Hamiltonian. *Mol. Phys.* 1968, *15* (5), 479–490. https://doi.org/10.1080/00268976800101381.

(101) Meyer, H. The Molecular Hamiltonian. *Annu. Rev. Phys. Chem.* 2002, *53* (1), 141–172. https://doi.org/10.1146/annurev.physchem.53.082201.124330.

(102) Watson, J. K. G. Aspects of Quartic and Sextic Centrifugal Effects on Rotational Energy Levels. In *Vibrational Spectra and Structure, vol. 6*; Durig, J. R., Ed.; Elsevier B.V.: Amsterdam, 1977; pp 1–89.

(103) Pickett, H. M. Vibration—Rotation Interactions and the Choice of Rotating Axes for Polyatomic Molecules. *J. Chem. Phys.* 1972, *56* (4), 1715. https://doi.org/10.1063/1.1677430.

(104) Saragi, R. T.; Juanes, M.; Caminati, W.; Lesarri, A.; Enríquez, L.; Jaraíz, M. Rotational Spectrum, Tunneling Motions, and Intramolecular Potential Barriers in Benzyl Mercaptan. *J. Phys. Chem. A* 2019, *123* (39). https://doi.org/10.1021/acs.jpca.9b06921.

(105) Evangelisti, L.; Caminati, W. Internal Dynamics in Complexes of Water with Organic Molecules. Details of the Internal Motions in Tert-Butylalcohol–Water. *Phys. Chem. Chem. Phys.* 2010, *12* (43), 14433–14441. https://doi.org/10.1039/C0CP01195A.

(106) Demaison, J. Accurate Structures of Non-Rigid Molecules by Microwave Spectroscopy. In *Structures and Conformations of Non-Rigid Molecules*; Laane, J., Dakkouri, M., van der Veken, B., Oberhammer, H., Eds.; Springer, Dordrecht, 1993; pp 239–256. https://doi.org/10.1007/978-94-011-2074-6_12.

(107) Ruoff, R. S.; Klots, T. D.; Emilsson, T.; Gutowsky, H. S. Relaxation of Conformers and Isomers in Seeded Supersonic Jets of Inert Gases. *J. Chem. Phys.* 1990, *93* (5), 3142–3150. https://doi.org/10.1063/1.458848.

(108) Grabow, J.-U.; Heineking, N.; Stahl, W. The Microwave Spectrum of Tert-Butyl Isocyanate. *J. Mol. Spectrosc.* 1992, *154* (1), 129–136. https://doi.org/10.1016/0022-2852(92)90034-L.

(109) Grabow, J. *Chemische Bindung Und Interne Dynamik in Großen Isolieren Molekülen: Rotationsspektroskopische Untersuchung*, HABILITATI.; Hannover, 2004.

(110) Neill, J. L.; Shipman, S. T.; Alvarez-Valtierra, L.; Lesarri, A.; Kisiel, Z.; Pate, B. H. Rotational Spectroscopy of Iodobenzene and Iodobenzene–Neon with a Direct Digital 2–8GHz Chirped-Pulse Fourier Transform Microwave Spectrometer. *J. Mol. Spectrosc.* 2011, *269* (1), 21–29. https://doi.org/10.1016/j.jms.2011.04.016.

(111) Brown, G. G.; Dian, B. C.; Douglass, K. O.; Geyer, S. M.; Shipman, S. T.; Pate, B. H. A Broadband Fourier Transform Microwave Spectrometer Based on Chirped Pulse Excitation. *Rev. Sci. Instrum.* 2008, *79* (5), 1–13. https://doi.org/10.1063/1.2919120.

(112) Saragi, R. T.; Juanes, M.; Abad, J. L.; Lesarri, A.; Pinacho, R.; Rubio, J. E. Rotational Spectroscopy of Organophosphorous Chemical Agents: Cresyl and Phenyl Saligenin Phosphates. *Phys. Chem. Chem. Phys.* 2019, *21* (30). https://doi.org/10.1039/c9cp03093j.

(113) Fokin, A. A.; Zhuk, T. S.; Blomeyer, S.; Pérez, C.; Chernish, L. V.; Pashenko, A. E.; Antony, J.; Vishnevskiy, Y. V.; Berger, R. J. F.; Grimme, S.; Logemann, C.; Schnell, M.; Mitzel, N. W.; Schreiner, P. R. Intramolecular London Dispersion Interaction Effects on Gas-Phase and Solid-State Structures of Diamondoid Dimers. *J. Am. Chem. Soc.* 2017, *139* (46), 16696–16707. https://doi.org/10.1021/JACS.7B07884.

(114) Halgren, T. A. Merck Molecular Force Field. I. Basis, Form, Scope, Parameterization, and Performance of MMFF94. *J. Comput. Chem.* 1996, *17* (5–6), 490–519.

https://doi.org/10.1002/(SICI)1096-987X(199604)17:5/6<490::AID-JCC1>3.0.CO;2-P.
(115) Kolossváry, I.; Keserü, G. M. Hessian-free Low-mode Conformational Search for Large-scale Protein Loop Optimization: Application to C-jun N-terminal Kinase JNK3. *J. Comput. Chem.* 2001, *22* (1), 21–30.
(116) Møller, C.; Plesset, M. S. Note on an Approximation Treatment for Many-Electron Systems. *Phys. Rev.* 1934, *46* (7), 618–622. https://doi.org/10.1103/PhysRev.46.618.
(117) Valatin, J. G. Generalized Hartree-Fock Method. *Phys. Rev.* 1961, *122* (4), 1012–1020. https://doi.org/10.1103/PhysRev.122.1012.
(118) Leininger, M. L.; Allen, W. D.; Schaefer, H. F.; Sherrill, C. D. Is Mo/Ller–Plesset Perturbation Theory a Convergent Ab Initio Method? *J. Chem. Phys.* 2000, *112* (21), 9213–9222. https://doi.org/10.1063/1.481764.
(119) Becke, A. D. Perspective: Fifty Years of Density-Functional Theory in Chemical Physics. *J. Chem. Phys.* 2014, *140* (18). https://doi.org/10.1063/1.4869598.
(120) Goerigk, L.; Hansen, A.; Bauer, C.; Ehrlich, S.; Najibi, A.; Grimme, S. A Look at the Density Functional Theory Zoo with the Advanced GMTKN55 Database for General Main Group Thermochemistry, Kinetics and Noncovalent Interactions. *Phys. Chem. Chem. Phys.* 2017, *19* (48), 32184–32215.
(121) Raghavachari, K. Perspective on "Density Functional Thermochemistry. III. The Role of Exact Exchange." *Theor. Chem. Accounts Theory, Comput. Model. (Theoretica Chim. Acta)* 2000, *103* (3–4), 361–363. https://doi.org/10.1007/s002149900065.
(122) Chai, J.-D. Da; Head-Gordon, M. Long-Range Corrected Hybrid Density Functionals with Damped Atom–Atom Dispersion Corrections. *Phys. Chem. Chem. Phys.* 2008, *10* (44).
(123) Grimme, S.; Neese, F. Double-Hybrid Density Functional Theory for Excited Electronic States of Molecules. *J. Chem. Phys.* 2007, *127* (15), 154116. https://doi.org/10.1063/1.2772854.
(124) Zhao, Y.; Truhlar, D. G. Density Functionals with Broad Applicability in Chemistry. *Acc. Chem. Res.* 2008, *41* (2), 157–167. https://doi.org/10.1021/ar700111a.
(125) Zhao, Y.; Truhlar, D. G. The M06 Suite of Density Functionals for Main Group Thermochemistry, Thermochemical Kinetics, Noncovalent Interactions, Excited States, and Transition Elements: Two New Functionals and Systematic Testing of Four M06-Class Functionals and 12 Other Function. *Theor. Chem. Acc.* 2008, *120* (1–3), 215–241. https://doi.org/10.1007/s00214-007-0310-x.
(126) Grimme, S.; Ehrlich, S.; Goerigk, L. Effect of the Damping Function in Dispersion Corrected Density Functional Theory. *J. Comput. Chem.* 2011, *32* (7), 1456–1465. https://doi.org/10.1002/jcc.21759.
(127) Johnson, E. R.; Becke, A. D. A Post-Hartree-Fock Model of Intermolecular Interactions: Inclusion of Higher-Order Corrections. *J. Chem. Phys.* 2006, *124* (17), 174104. https://doi.org/10.1063/1.2190220.
(128) Perdew, J. P.; Schmidt, K. Jacob's Ladder of Density Functional Approximations for the Exchange-Correlation Energy. *AIP Conf. Proc.* 2001, *577* (1), 1. https://doi.org/10.1063/1.1390175.
(129) Weigend, F.; Ahlrichs, R. Balanced Basis Sets of Split Valence, Triple Zeta Valence and Quadruple Zeta Valence Quality for H to Rn: Design and Assessment of Accuracy. *Phys. Chem. Chem. Phys.* 2005, *7* (18), 3297. https://doi.org/10.1039/b508541a.
(130) Frisch, M. J.; Pople, J. A.; Binkley, J. S. Self-consistent Molecular Orbital Methods 25. Supplementary Functions for Gaussian Basis Sets. *J. Chem. Phys.* 1984, *80* (7), 3265–3269. https://doi.org/10.1063/1.447079.
(131) Frisch, M. J.; Trucks, G. W.; Schlegel, H. B.; Scuseria, G. E.; Robb, M. A.; Cheeseman, J. R.; Scalmani, G.; Barone, V.; Petersson, G. A.; Nakatsuji, H.; Li, X.; Caricato, M.; Marenich, A. V.; Bloino, J.; Janesko, B. G.; Gomperts, R.; Mennucci, B.; Hratch, D. *Gaussian 16, Revision C.01*; J. Gaussian, Inc.: Wallingford CT, 2016.
(132) Boys, S. F.; Bernardi, F. The Calculation of Small Molecular Interactions by the Differences of Separate Total Energies. Some Procedures with Reduced Errors. *Mol. Phys.* 2002, *100* (1), 65–73. https://doi.org/10.1080/00268970110088901.

(133) Szalewicz, K. Symmetry-Adapted Perturbation Theory of Intermolecular Forces. *Wiley Interdiscip. Rev. Comput. Mol. Sci.* 2012, *2* (2), 254–272. https://doi.org/10.1002/wcms.86.

(134) Boto, R. A.; Peccati, F.; Laplaza, R.; Quan, C.; Carbone, A.; Piquemal, J.-P.; Maday, Y.; Contreras-García, J. NCIPLOT4: Fast, Robust, and Quantitative Analysis of Noncovalent Interactions. *J. Chem. Theory Comput.* 2020, *16* (7), 4150–4158. https://doi.org/10.1021/ACS.JCTC.0C00063.

(135) Contreras-García, J.; R. Johnson, E.; Keinan, S.; Chaudret, R.; Piquemal, J.-P.; N. Beratan, D.; Yang, W. NCIPLOT: A Program for Plotting Noncovalent Interaction Regions. *J. Chem. Theory Comput.* 2011, *7* (3), 625–632. https://doi.org/10.1021/ct100641a.

(136) Johnson, E. R.; Keinan, S.; Mori-Sánchez, P.; Contreras-García, J.; Cohen, A. J.; Yang, W. Revealing Noncovalent Interactions. *J. Am. Chem. Soc.* 2010, *132* (18), 6498–6506. https://doi.org/10.1021/ja100936w.

(137) Turney, J. M.; Simmonett, A. C.; Parrish, R. M.; Hohenstein, E. G.; Evangelista, F. A.; Fermann, J. T.; Mintz, B. J.; Burns, L. A.; Wilke, J. J.; Abrams, M. L.; Russ, N. J.; Leininger, M. L.; Janssen, C. L.; Seidl, E. T.; Allen, W. D.; Schaefer, H. F.; King, R. A.; Valeev, E. F.; Sherrill, C. D.; Crawford, T. D. Psi4: An Open-Source Ab Initio Electronic Structure Program. *Wiley Interdiscip. Rev. Comput. Mol. Sci.* 2012, *2* (4), 556–565. https://doi.org/10.1002/wcms.93.

(138) Parrish, R. M.; Burns, L. A.; Smith, D. G. A.; Simmonett, A. C.; DePrince, A. E.; Hohenstein, E. G.; Bozkaya, U.; Sokolov, A. Y.; Di Remigio, R.; Richard, R. M.; Gonthier, J. F.; James, A. M.; McAlexander, H. R.; Kumar, A.; Saitow, M.; Wang, X.; Pritchard, B. P.; Verma, P.; Schaefer, H. F.; Patkowski, K.; King, R. A.; Valeev, E. F.; Evangelista, F. A.; Turney, J. M.; Crawford, T. D.; Sherrill, C. D. Psi4 1.1: An Open-Source Electronic Structure Program Emphasizing Automation, Advanced Libraries, and Interoperability. *J. Chem. Theory Comput.* 2017, *13* (7), 3185–3197. https://doi.org/10.1021/acs.jctc.7b00174.

(139) Laplaza, R.; Peccati, F.; Boto, R. A.; Quan, C.; Carbone, A.; Piquemal, J.-P.; Maday, Y.; Contreras-García, J. NCIPLOT and the Analysis of Noncovalent Interactions Using the Reduced Density Gradient. *WIREs Comput. Mol. Sci.* 2021, *11* (2). https://doi.org/10.1002/wcms.1497.

Chapter 2.

The Thiophenol Dimer and Trimer

This chapter discusses the self-aggregation of thiophenol, the simplest thiol analog of phenol. We have observed a balance between sulfur hydrogen bonding and π–stacking interactions in the formation of the dimer and trimer of the molecule. The experiment used broadband chirped-pulse Fourier transform microwave spectroscopy in Valladolid and a COMPACT spectrometer in Hamburg as part of the work conducted during a research visit to DESY. Two different isomers were detected for the thiophenol dimer, while a symmetric-top was observed for the trimer. The results observed from the experiments are compared with DFT calculations to explore the relevance of substituent effects to modulate π–stacking geometries and the role of the sulfur-centered hydrogen bond. This chapter is adapted from the publication

- R.T. Saragi, M. Juanes, C. Pérez, P. Pinacho, D. Tikhonov, W. Caminati, M. Schnell, A. Lesarri, "Switching Hydrogen Bonding to π-Stacking: The Thiophenol Dimer and Trimer". *J. Phys. Chem. Lett.* 2021, 12, 5, 1367–1373.

2.1. Introduction

π–Stacking forces are fascinating interactions, but its own name is somehow misguiding, as one could incorrectly assume some overlap of the π–orbitals. For this reason, some scientists advocate to dismiss this term.[1,2] Non-covalent interactions between neutral closed-shell unsaturated organic groups were early recognized as decisive contributors to biochemical structures, as in DNA/RNA nucleobase stacking or protein folding.[3–5] In addition, the influence of π–π stacking forces extends to organic and organometallic synthesis,[6] protein and crystal design,[7] host-guest compounds,[8]

catalysis,[9] materials,[10] and supramolecular chemistry,[6] calling for a description at a molecular level.

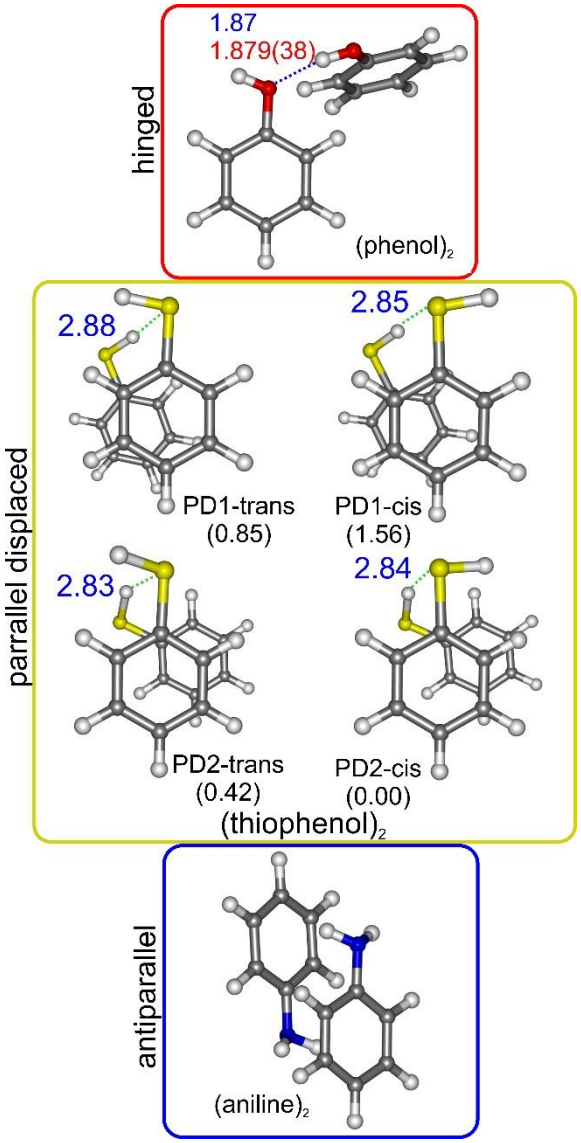

Figure 2.1. Parallel displaced isomers of the thiophenol dimer compared with the weakly-bound dimers of phenol and aniline. Relative electronic energy energies (ZPE corrected, energy in kJ mol^{-1}) and S–H···S hydrogen-bond distances (B2PLYP-D3(BJ)/def2-TZVP, Table 2.1) are given for the thiophenol dimer. The O–H···O hydrogen-bond distance for the phenol dimer is taken from reference [11].

The polar electrostatic or Hunter-Sanders[12] model initially ascribed π–stacking to quadrupole-quadrupole interactions ($1/r^7$ distance dependence). However, more recent computational analyses[1,2] using energy decomposition attribute the physical origin of π–π stacking stabilization to dispersion forces ($1/r^6$ dependence), promoted by the close near-parallel biplanar arrangement. The quadrupolar electrostatic potential of unsaturated rings actually favors stacking of saturated rings, but this factor is counterbalanced by a reduced Pauli exchange repulsion for arene-arene stacking. Other calculations have explored the balance between dispersion and electrostatic effects[13–15] and revealed the connection between dispersion and DNA helicity.[16] However, since the stabilizing electron correlations result from a positional effect and are not attributed to direct π–electron interactions, the concept of π–π stacking should be merely considered a positional descriptor.

Experiments on stacking are crucial to validate the increasingly complex theoretical models. In particular, gas-phase experiments are unbiased by perturbing matrix effects and directly comparable to the computational predictions. As an illustrative example, the rotational spectrum of the benzene dimer resolved the theoretical dispute between the observed T-shape[17–19] and the alternative parallel geometry.[20] Most gas-phase experiments have used double-resonance IR-UV spectroscopy,[21–25] but their vibrational signatures are usually of low resolution. Microwave spectroscopy provides accurate structural descriptions through the moments of inertia.[26,27] However, there are just a few rotational investigations of π-stacking clusters. For a single benzene ring, the serendipitous observation of the 1,2-difluorobenzene dimer[28] benefited from the changes in the molecular electrostatic potential due to strongly electronegative substituents but it took years to realize the correct geometry. For two fused rings, dibenzofuran[29] and 1-napthol[30] exhibit stacking, consistent with the increased stability of larger arene dimers.[1]

Apart from fluorination, other weaker substituent effects,[13,14] like fine-tuning of hydrogen bonding, can be explored to switch single-ring dimers from non-stacking into stacking. In the case of phenol, the dimer[11,31] is controlled by a moderately strong O-H···O hydrogen bond which results in a "hinged" structure intermediate between T or stacked geometries, very sensitive to dispersion contributions.[32] The dimer of aniline shows the opposite effect, with a (head-to-tail) apolar antiparallel stacking and no N-H···N hydrogen bond between the amino groups (Figure 2.1).[33] In this chapter, we explore the replacement of oxygen in phenol by a heavier less-electronegative chalcogen atom like sulfur, proving that it maintains S-H···S hydrogen bonding while simultaneously resulting in a π-stacking homodimer. The study is also extended to the thiophenol trimer, complementing our view on sulfur hydrogen bonding[34–37] and allowing comparisons with the phenol[11] and aniline[38] trimers.

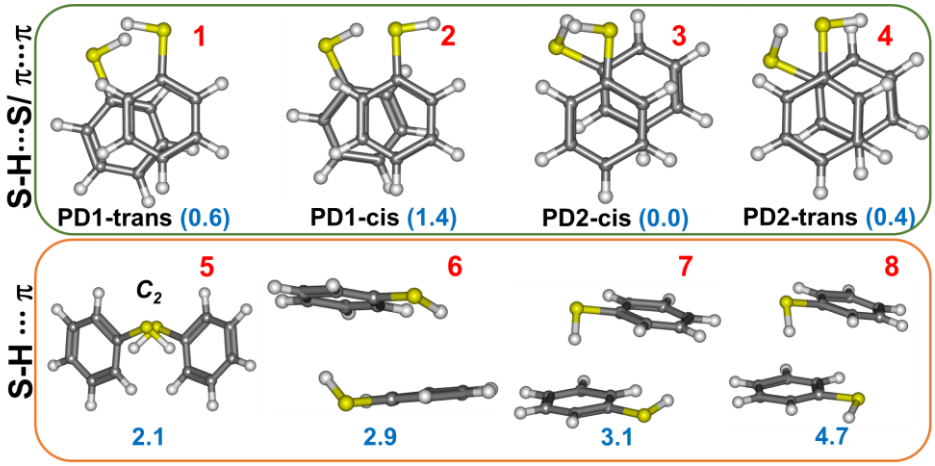

Figure 2.2. The structures of the eight most stable thiophenol dimers using B3LYP-D3(BJ)/def2-TZVP. The relative electronic energy values shown in blue are in kJ mol^{-1}.

2.2. Methods

The experimental investigation used supersonic-jet chirped-pulsed Fourier-transform microwave[39] (CP-FTMW) spectrometers in Valladolid and Hamburg, operating in the region 2-8 GHz. The sample of thiophenol is a liquid at room temperature (m.p. -15°C, b.p. 169°C) was heated in a reservoir nozzle (60-70°C) inside the vacuum chamber, and neon gas was used as a carrier gas with the backing pressure of 2 bar. The second experiment used argon as a carrier gas to confirm the conformational relaxation on one of the dimers.

Several computational models assisted the experiment. An initial set of starting structures was generated using Molecular Mechanics[40] and conformational searching routines implemented in Macromodel.[41] We present results based on hybrid (B3LYP, ωB97XD) and double-hybrid (B2PLYP) methods. The Becke functionals were supplemented with Grimme's D3(BJ) dispersion corrections, while ωB97XD includes D2 empirical dispersion.[42] The B3LYP-D3(BJ) dimer calculations converged to the eight structures illustrated in Figure 2.2, with four isomers at electronic energies below 1.4 kJ mol^{-1} and four additional species in the range 2-5 kJ mol^{-1}. The four most stable structures were reoptimized with B2PLYP-D3(BJ) (Table 2.1) to check the computational consistency. For the trimer, B3LYP-D3(BJ) predicted two practically isoenergetic isomers, while six other structures were found at electronic energies below 5 kJ mol^{-1}. The two most stable trimer isomers were similarly reoptimized with B2PLYP-D3(BJ) in Table 2.2. All reported species are local minima at their calculation level. The non-covalent interaction analysis was calculated using NCIPlot.[43,44] A binding energy

decomposition was obtained from a third-order symmetry-adapted perturbation theory (SAPT2+(3))[45,46] analysis implemented in PSI4[47] code using a double-ζ aug-cc-pVDZ[48] basis set. More detailed information may be found in the in Appendix (Table S2.1-S2.4).

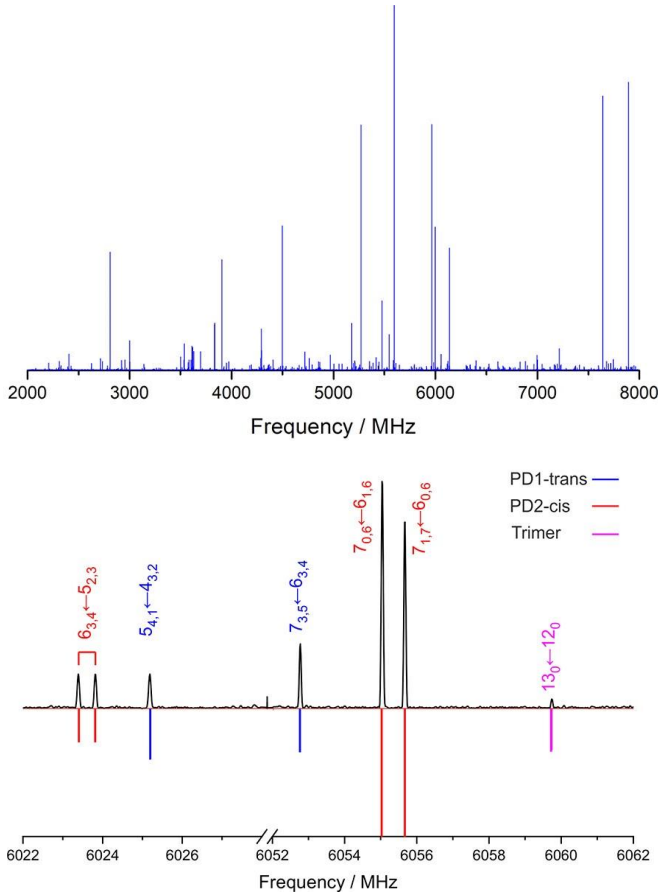

Figure 2.3. The microwave spectrum of thiophenol and its aggregates, showing the tunnelling splittings in isomer PD2-cis.

2.3. Results and Discussions

The observed rotational spectrum in Figure 2.3 is dominated by intense monomer transitions, previously reported.[49] Similarly to phenol, thiophenol tunnels between two equivalent planar structures connected by the internal rotation of the thiol group, splitting the ground vibrational state into two torsional-rotation sublevels (Table S2.5,

Appendix). However, the internal rotation barrier is much smaller than in phenol, i.e. 277.1(3) cm^{-1} versus 1213 cm^{-1}.[50]

For the thiophenol dimer, two different asymmetric rotors were assigned in the spectrum. Isomer I exhibits only μ_b transitions and behaves like a semi-rigid rotor, which could be fitted using Watson's Hamiltonian.[51] Isomer II presented μ_b transitions with small (<0.5 MHz) tunneling doublings, indicative of an internal large-amplitude motion (LAM) connecting two symmetry-equivalent structures. A second set of μ_c transitions showed larger tunnelling splitting (ca. 17 MHz), near independent of the angular momentum quantum number. This fact suggested a μ_c-inverting motion, so the experimental transitions were fitted to a two-state rovibrational Hamiltonian without Coriolis coupling terms. For the trimer, we found a set of transitions corresponding to the pattern of a symmetric rotor, but we could not resolve the *K* quantum number fine structure. The experimental rotational transitions are collected in Tables S2.6-S2.8 (Appendix).

The comparison between experiment and theory in Tables 2.1 and 2.2 allowed the identification of the spectral carriers. The dimer exhibits parallel displaced (PD) geometries, all sustained by an intermolecular hydrogen bond S-H···S. Two alternatives slipped structures are predicted depending on the relative orientation of the phenyl ring with respect to the linking thiol groups, denoted PD1 and PD2 in Figures 2.1 and 2.2. Moreover, for each ring geometry, two isomers arise, differing on the parallel (*cis*) or antiparallel (*trans*) orientation of the terminal thiol groups, so four isomers are finally predicted for the dimer. Isomer I was identified as PD1-*trans* based on the rotational constants and dominance of μ_b-dipole moment. Similarly, the presence of a μ_c spectrum led to the assignment of isomer II as PD2-*cis*.

The potential energy function describes the concerted internal rotation of the two thiol groups in isomer II (PD2-cis) of the thiophenol dimer, which exchange the proton donor and acceptor moieties. The inversion barrier was determined from the experimental tunnelling splitting ΔE_{01} = 8.8698(51) MHz using Meyer's flexible model.[52] The determination of two-fold internal rotation barriers using semi-rigid formalisms has been discussed elsewhere.[53,54] Meyer's flexible model, which has been extensively used to treat the MW data of molecular complexes,[55] is designed to numerically calculate energies and wavefunctions of vibrational and rotational states for 1- or 2-dimensional (1D, 2D) vibrational problems. This model can be applied to any type of internal motion of any non-linear molecule, with the advantages that it allows for structural relaxation, has no symmetry restrictions, and works efficiently for a few mesh points. In the case of a 1D problem, if we consider τ as the parameter to describe the motion (for example, the correlated SH internal rotation coordinate in isomer II), the relaxations of any

Table 2.1. Rotational parameters for the two isomers of the thiophenol dimer.

	Experiment			Theory[h]			
	Isomer I	Isomer II		PD1-trans	PD1-cis	PD2-cis	PD2-trans
		v=0	v=1				
A / MHz[a]	662.74850(27)[g]	626.72005(70)	626.71915(70)	693.6	690.4	628.4	629.7
B / MHz	499.49241(20)	511.48422(83)	511.48295(83)	496.3	496.9	527.6	530.3
C / MHz	338.59668(19)	422.94594(94)	422.90305(91)	347.3	348.9	435.8	435.6
κ	-0.01	-0.13		-0.14	-0.13	-0.05	-0.02
Δ_J / kHz[b]	0.1611(13)	0.1884(99)		0.355	0.329	0.077	0.094
Δ_{JK} / kHz	28.7175(37)	0.090(41)		-0.527	-0.402	0.297	0.225
Δ_K / kHz	-28.7008(36)	-0.199(38)		0.217	0.121	-0.312	-0.253
δ_J / kHz	0.05185(50)	-0.0276(47)		0.041	0.030	-0.024	-0.022
δ_K / kHz	14.1665(20)	0.330(28)		0.054	0.150	0.495	0.446
ΔE_{10} / MHz[c]		8.8698(51)					
N[d]	145	139					
σ / kHz	7.6	19.8					
$\lvert\mu_a\rvert$ / D[e]	Not detected	Not detected		0.1	0.5	0.0	0.8
$\lvert\mu_b\rvert$ / D	Detected	Detected		1.5	2.1	1.6	1.1
$\lvert\mu_c\rvert$ / D	Not detected	Detected		0.4	0.9	1.1	0.2
ΔE / kJ mol^{-1} [f]				0.85	1.56	0.00	0.42
$\Delta G_{100\,K}$ / kJ mol^{-1}				0.03	0.73	0.00	0.42
$\Delta G_{298\,K}$ / kJ mol^{-1}				0.00	0.54	1.87	2.42
ΔE_c / kJ mol^{-1}				-25.77	-25.02	-27.15	-27.28
r(S-H ··· S) / Å				2.879	2.846	2.843	2.830
∠(S-H···S) / deg				138.9	140.8	134.5	134.0

[a]Rotational constants (A, B, C) and Ray's asymmetry parameter (κ=(2B-A-C)/(A-C)).[b]Watson's A-reduction centrifugal distortion constants (Δ_J, Δ_{JK}, Δ_K, δ_J, δ_K). [c]Torsional energy difference (ΔE_{10}). [d]Number of transitions (N) and RMS deviation (σ) of the fit. [e]Electric dipole moments (μ_α, α = a, b, c). [f]Relative energies corrected with the zero-point energy (ZPE), Gibbs energy (ΔG) at 100 K and 298 K (1 atm) and complexation energy (ΔE_c). [g]Standard errors in units of the last digit. [h]B2PLYP-D3(BJ)/def2-TVZP predictions, see Appendix for B3LYP-D3(BJ) and ωB97XD values

structural parameter can be taken into account as a function of τ. We assumed the following double minimum potential energy function to be appropriate for our problem:

$$V(\tau) = B_2[1 - (\tau/\tau_0)^2]^2 \quad \textbf{(2.1)}$$

where B_2 is the barrier at $\tau = 0°$ and τ_0 is the equilibrium value of the inversion angle. Since the HS-CC dihedral angles at the energy minimum are slightly different for the two thiol groups, we fixed τ_0 to their average value (63°) and adjusted B_2 to reproduce the experimental ΔE_{10} splitting. We needed to take into account the structural relaxations of at least three structural parameters as a function of the leading parameter τ. Guided by the B3LYP-D3(BJ)/def2-TZVP ab initio structures at the minimum ($\tau = \tau_0$) and at the transition state ($\tau = 0°$) we have chosen the three structural relaxations expressed below (see Figure 2.4 for labelling), where R, $\angle$, and D denote atomic distances, bond angles, and dihedrals:

$$R_{S-S} \,/\, \text{Å} = 3.9696 - 0.0919\,(\tau/\tau_0)^2 \quad \textbf{(2.2)}$$

$$\angle(\text{C1} - \text{S1} - \text{S2}) \,/\, \text{deg} = 77.0 - 2.0\,(\tau/\tau_0)^2 - 1.0\,(\tau/\tau_0) \quad \textbf{(2.3)}$$

$$\angle(\text{C2} - \text{S2} - \text{S1}) \,/\, \text{deg} = 77.0 - 2.0\,(\tau/\tau_0)^2 + 1.0\,(\tau/\tau_0) \quad \textbf{(2.4)}$$

$$\angle(\text{C3} - \text{C1} - \text{S1}) / \text{deg} = 77.0 - 1.9\,(\tau/\tau_0) \quad \textbf{(2.5)}$$

$$\angle(\text{C4} - \text{C2} - \text{S2}) \,/\, \text{deg} = 77.0 + 1.9\,(\tau/\tau_0) \quad \textbf{(2.6)}$$

$$D(\text{C3C1} - \text{S1S2}) \,/\, \text{deg} = -71.5 + 7.8\,(\tau/\tau_0)^2 - 2.0\,(\tau/\tau_0) \quad \textbf{(2.7)}$$

$$D(\text{C4C2} - \text{S2S1}) \,/\, \text{deg} = -71.5 + 7.8\,(\tau/\tau_0)^2 + 2.0\,(\tau/\tau_0) \quad \textbf{(2.8)}$$

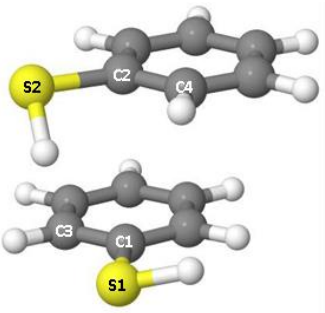

Figure 2.4. Definition of the structural parameters used in Meyer's flexible model to calculate the potential barrier of Equation 2.1.

With these structural conditions, we found that a barrier of B_2 = 250.3 cm^{-1} leads to a torsional splitting of ΔE_{10} = 8.88 MHz, i.e., it reproduces the experimental value. In the flexible model calculations, the τ coordinate has been considered in the ±110°

range and solved into 79 mesh points. A lack of double-minimum symmetry prevents tunnelling effects for isomer PD1.

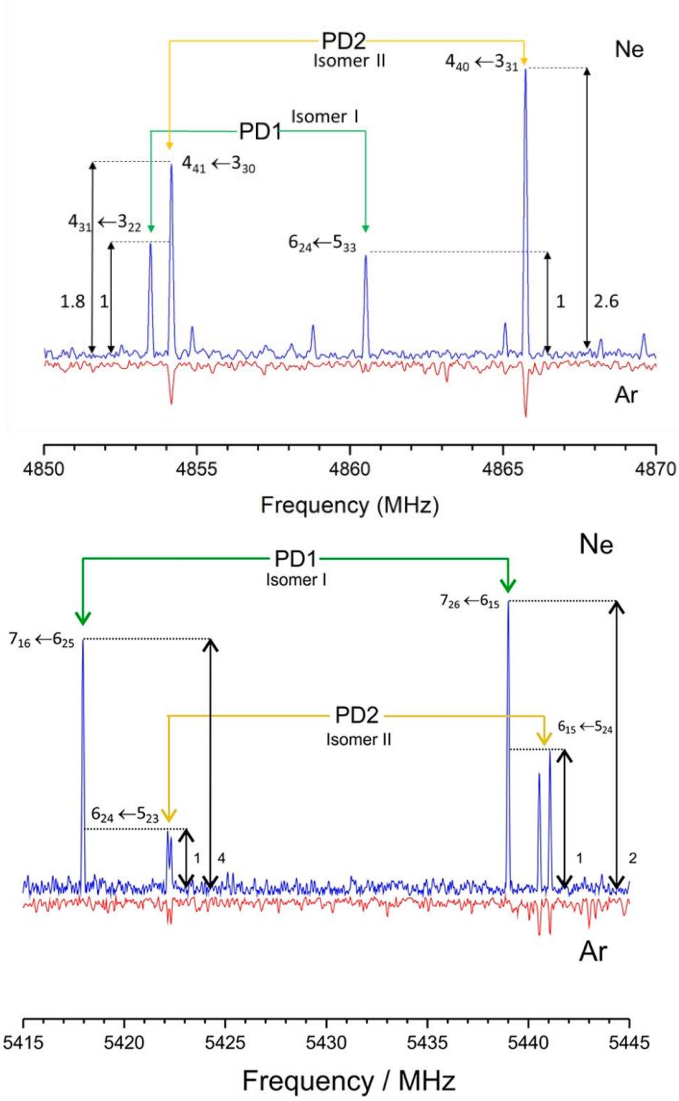

Figure 2.5. Two sections of 30 MHz (upper trace) and 20 MHz (lower trace) of the rotational spectrum of the thiophenol dimer, showing the disappearance of isomer I (PD1) when the neon carrier gas is replaced by argon, enforcing conformational relaxation to the global minimum PD2.

The dimer global minimum was identified with a second experiment using argon as the carrier gas, checking the possibility of conformational relaxation with more

energetic intermolecular jet collisions. The weaker argon spectrum, illustrated in Figure 2.5 revealed no signals from PD1 and confirmed PD2 as the global minimum. For the thiophenol trimer, the symmetric rotor UUU in Table 2.2 and Figure 2.6 characterized by three consecutive S-H···S hydrogen bonds, can be associated to the observed transitions. No other dimer or trimer species could be identified positively. However, the presence of other species is not excluded because of additional unidentified lines.

Table 2.2. Rotational Parameters for the Thiophenol Trimer

	Experiment	Theory	
	Isomer 1	1 UUU	2 UUD
A / MHz[a]		236.3	243.2
B / MHz	233.07124(18)	236.1	231.8
C / MHz		201.1	193.2
κ		0.99	0.54
D_J / kHz[b]	0.0123(45)	0.011	0.011
D_{JK} / kHz		0.049	0.017
D_K / kHz		-0.055	-0.021
d_1 / kHz		0.000	0.002
d_2 / kHz		-0.072	0.038
$\lvert\mu_a\rvert$ / D		0.0	0.5
$\lvert\mu_b\rvert$ / D		0.0	0.3
$\lvert\mu_c\rvert$ / D		3.1	0.8
N[b]	13		
σ / kHz	0.006		
ΔE/kJ mol^{-1} [c]		0.74	0
$\Delta G_{100\,K}$ / kJ mol^{-1}		0.06	0
$\Delta G_{298\,K}$ / kJ mol^{-1}		0.06	0
ΔE_c / kJ mol^{-1}		-68.07	-67.82
r(S-H ··· S) / Å		2.748	2.758
∠(S-H···S) / *deg*		155.6	157.8

[b]Watson's S-reduction centrifugal distortion constants (D_J, D_{JK}, D_K, d_1 d_2). The rest of parameters definitions as in Table 2.1.

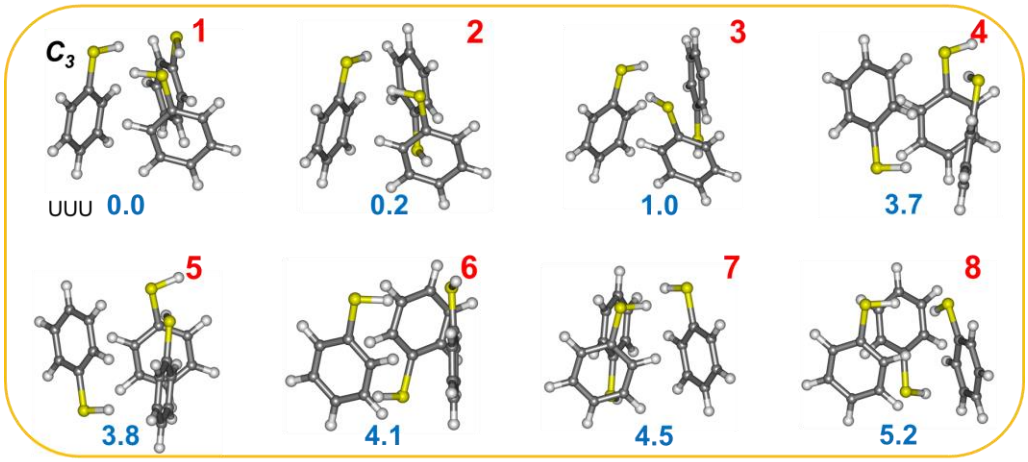

Figure 2.6. The structures of the eight most stable thiophenol trimers using B3LYP-D3(BJ)/def2-TZVP, the relative electronic energy values shown in blue ink are in kJ mol^{-1}. The global minimum of thiophenol trimer has C_3 symmetry; the UUU (up up up) notation describes the orientation of the thiol group, the rest of the trimers correspond to UUD (up up down).

A coherent picture emerges from the present experiment concerning the correlation between thiophenol aggregation and non-covalent interactions. For the thiophenol dimer, the calculations suggest two alternative clustering mechanisms, based either in S-H···S or S-H···π hydrogen bonds. While the relative energies for the first eight isomers are quite close, the preference for a combination of S-H···S hydrogen bond and π-stacking is notorious, offering insight into their structural, energetic, and physical properties. The parallel-displaced global minimum PD2-cis exhibits a long hydrogen bond (B2PLYP: *r*(S-H···S)=2.84 Å) with considerable non-linearity (∠(S-H···S)=134 .5°). Similar values are presented for PD1 in Figure 2.1. This bonding distance is slightly larger than the prototype of the hydrogen sulfide dimer[56] (*r*(S-H···S)=2.778(9) Å) and qualitatively reflects the gradation of hydrogen bond strength observed in the dimers of H_2S-H_2O[57] (*r*(O-H···S)=2.597(4) Å), H_2O-H_2S[57] (*r*(S-H···O)=2.195 Å) and $(H_2O)_2$[58] (*r*(O-H···O)=1.951 Å) in Table 2.3. Thiol-alcohol gas-phase hydrogen bonds were also reported for the monohydrates of furfuryl[36] and thenyl[37] mercaptan (*r*(S-H···O)=2.22-2.44 Å; *r*(O-H···S)=2.43-2.58 Å), but the experimental investigations of gas-phase hydrogen bonds between thiols are still scarce.[34,35] Protein crystal contacts between the cysteine thiol and the sulfur atom in methionine or cysteine have shorter average values of *r*(S-H···S)=2.55(47) Å.[59]

Table 2.3 Hydrogen bond distances for the dimers of hydrogen sulfide and water.

Dimer	HB	Method	r(X···Y) / Å[a]	r(X-H···Y) / Å	∠(X-H···Y) / deg
$(H_2O)_2$	O-H···O	MW[b]	2.980(10)		
		MW[c]	2.976		
		IR[d]	2.952		
		MP2[e]		1.951	171
$(H_2S)(H_2O)$	O-H···S	MW[f]	3.535(3)	2.597(4)	193.4(4)
		MW[g]	3.544(8)	2.590(6)	185.2(63)
		MP2[h]	3.480	2.52	187.8
$(H_2O)(H_2S)$	S-H···O	MW[i]	3.55	2.195	180
$(H_2S)_2$	S-H···S	Experiment[e]	4.112(1)	2.778(9)	175(7)
		MP2/aug-cc-pVDZ[e]	4.096	2.743	173

[a]X, Y denotes O or S atoms. [b]R. Dyke, J. S. Muenter, *J. Chem. Phys*. **1974**, *60*, 2929-2930. T. R. Dyke, K. M. Mack, J. S. Muenter, *J. Chem. Phys*. **1977**, *66*, 498-510. [c]J. A. Odutola, T.R. Dyke, *J. Chem. Phys*. **1980**, *72*, 5062-5070. [d]A. Mukhopadhyay, W. T.S. Cole, R. J. Saykally, *Chem. Phys. Lett*. **2015**, *633*, 13–26. [e]MP2/aug-cc-pVDZ: A. Das, P. K. Mandal, F. J. Lovas, C. Medcraft, N. R. Walker, E. Arunan, *Angew.Chem. Int. Ed*. **2018**, *57*, 15199-15203. [f]A_2 state: F. Lovas, private communication, 2020. [g]B_2 state: F. Lovas, private communication, 2020. [h]MP2/6- 311++G(3d1f,3p1d): Y.-B. Wang, F.-M. Tao, Y.-K. Pan, *Chem. Phys. Lett.* **1994**, *230*, 480-484. [i]F. Lovas, private communication, 2020.

The π-stacking geometry of the thiophenol dimers is characterized by the distance between centroids (d) and angle between aromatic planes (ϕ). The interplanar distances, shorter for PD2 (B2PLYP: d(PD2)=3.41-3.42 Å < d(PD1)=3.76-3.77 Å), and the ring orientations in the thiophenol dimer (B2PLYP: ϕ (PD2)=2.9°-4.4° < ϕ (PD1)=9.2°-10.2°) nicely match previous structural surveys of protein-ligand interactions between aromatic groups, confirming a common binding pattern.[60] For the trimer, the final geometry balances both S-H···S and C-H···π interactions, as in phenol and aniline, with a hydrogen bond distance of r(S-H···S)=2.75 Å (B2PLYP).

NCIPlots in Figures 2.7 and 2.8 indicate a confluence of the S-H···S hydrogen bond and delocalized interaction regions in between the aromatic rings, consistent with the observed geometries. A binding energy decomposition using Symmetry-Adapted Perturbation Theory SAPT 2+(3) in Figure 2.9 and Table 2.4 offers a comparison with phenol and aniline. The SAPT 2+(3) binding energy of the thiophenol dimer (PD1: -25.9 kJ mol^{-1}; PD2: -26.9 kJ mol^{-1}) is only 1-2 kJ mol^{-1} smaller than in the phenol dimer (-27.6 kJ mol^{-1}). However, it shows a much larger dispersion component than in phenol, accounting for 59.5% (PD1) or 60.6% (PD2) of the total attractive contribution, close to the contribution in the van der Waals dimer of pyridine-methane (74.7%). In parallel, the electrostatic contribution in thiophenol is reduced to 30.9% (PD1) and 29.8% (PD2) of the total attractive contribution, compared to 48.3% in the phenol dimer or 20.5% in pyridine-methane.

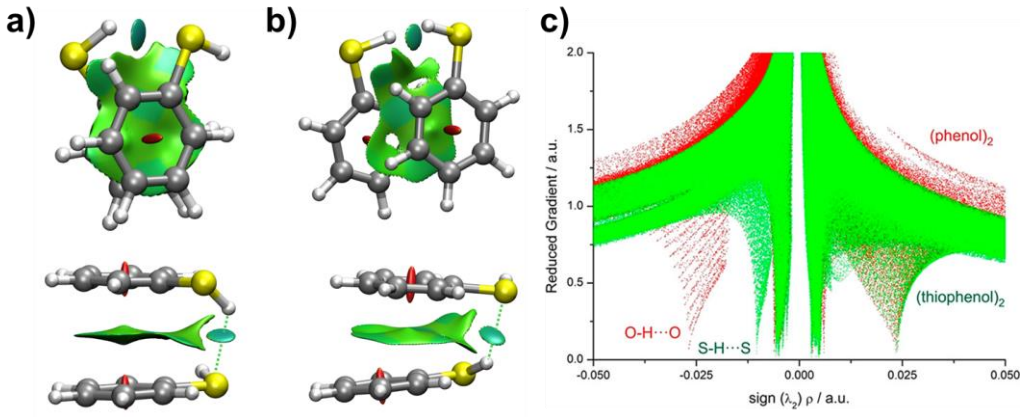

Figure 2.7. Mapping of non-covalent interactions in the observed dimer of PD2-cis (a) and PD1-trans (b), the color scaling: -2.0 to 2.0. In the NCIplot, blue shades indicate strong attractive interactions (associated to the hydrogen bond), green colors indicate weak attractive interactions (like S-H···S or S-H···π), and red represents repulsive interactions (ring critical points). Figure (c) shows the comparison of the reduced gradient of the isomer PD2-cis with the phenol dimer.

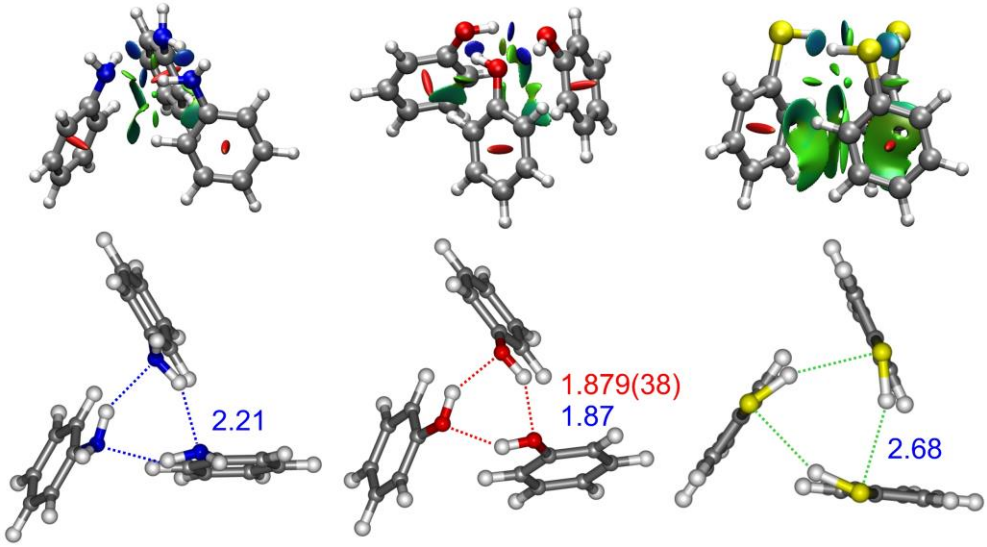

Figure 2.8. NCPlots for the C_3-symmetric structures of the trimers of aniline (left), phenol (center) and thiophenol (right, hydrogen bond distances according to B2PLYP-D3(BJ)), the color scaling: -2.0 to 2.0.

Table 2.4. Results from Symmetry-Adapted Perturbation Theory (SAPT2+(3)/aug-cc-PVDZ//B3LYP-D3(BJ)/def2-TZVP) binding energy decomposition of $(thiophenol)_2$ and related dimers (all values are in kJ mol^{-1}).

	$E_{Electrostatic.}$	$E_{Dispersion}$	$E_{Induction}$	$E_{Exchange}$	E_{Total}	ΔE_{S22}[g]
$(H_2O)_2$ [a]	-35.7[63.4%][h]	-9.5[16.9%]	-11.1[19.7%]	37.7	-18.6	-21.0
$(Phenol)_2$ [b]	-41.8[48.3%]	-28.8[33.3%]	-15.9[18.4%]	58.9	-27.6	-29.5
$(Aniline)_2$ [c]	-24.6[34.7%]	-39.3[55.5%]	-6.9[9.7%]	38.2	-32.6	
$(H_2S)_2$ [d]	-12.1[49.2%]	-7.8[31.7%]	-4.7[19.1%]	19.2	-5.4	
$(Thiophenol)_2$ PD1-trans [e]	-24.9[30.9%]	-47.9[59.5%]	-7.7[9.6%]	54.6	-25.9	
$(Thiophenol)_2$ PD2-cis [e]	-26.2[29.8%]	-53.3[60.6%]	-8.4[9.6%]	61.0	-26.9	
Pyridine-methane [f]	-3.0[20.5%]	-10.9[74.7%]	-0.7[4.8%]	9.4	-5.2	

[a]T. R. Dyke, K. M. Mack, J. S. Muenter, *J. Chem. Phys.*, **1977**, *66*, 498–510. [b]N. A. Seifert, A. L. Steber, J. L. Neill, C. Pérez, D. P. Zaleski, B. H. Pate, A. Lesarri, *Phys. Chem. Chem. Phys.* **2013**, *15*, 11468-11477. [c]C. Pérez, I. León, A. Lesarri, B.H. Pate, R. Martínez, J. Millán, J.A. Fernández, Angew. Chem, Int. Ed., 2018, 57, 15112-15116. [d]A. Das, P. K. Mandal, F. J. Lovas, C. Medcraft, N. R. Walker, E. Arunan, *Angew. Chem. Int. Ed.*, **2018**, *57*, 15199–15203. [e]This work. [f]Q. Gou, L. Spada, M. Vallejo-López, A. Lesarri, E. J. Cocinero, W. Caminati, *Phys. Chem. Chem. Phys.*, **2014**, *16*, 13041–13046. [g]Interaction energies in Hobza's S22 database, recalculated by Sherrill: T. Takatani, E. G. Hohenstein, M. Malagoli, M. S. Marshall, C. D. Sherrill, *J. Chem. Phys.*, **2010**, *132*, 144104. [h]Relative contribution to the attractive interactions (E_{elect}+E_{disp}+E_{ind}).

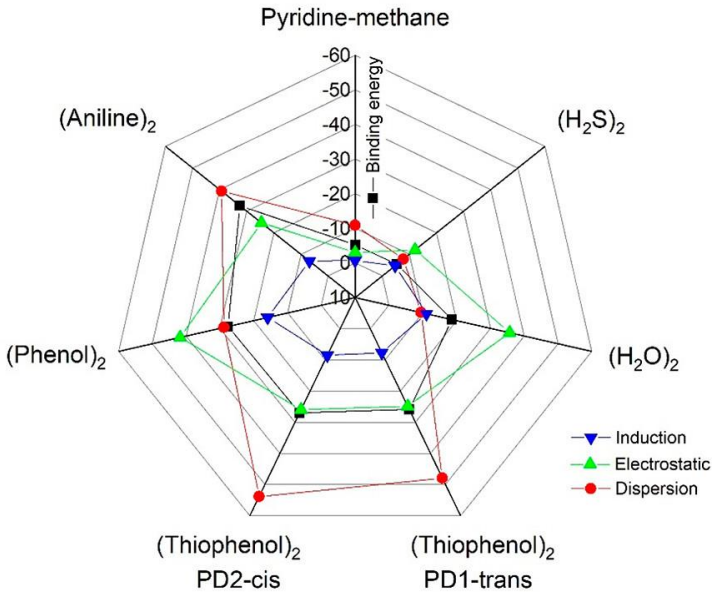

Figure 2.9. A radar chart illustrated the SAPT2+(3) binding energy decomposition for the thiophenol dimers (PD1-trans and PD2-cis) and compared the dimers of phenol, aniline, water, hydrogen sulfide, and pyridine-methane reported in **T**able 2.4.

2.4. Conclusions

In conclusion, chirped-pulse rotation spectroscopy pushes new avenues for investigating increasingly larger gas-phase adducts, simultaneously offering a striking comparison with low-resolution IR studies.[61] We observed two isomers of the thiophenol dimer, confirming two different π-stacking structures assisted by a long S-H···S hydrogen bond. The dimer geometries reveal flexible internal dynamics, as two different geometries are simultaneously detected, and one of the isomers exhibits an internal large-amplitude motion causing spectral doublings. The experiment also provided empirical evidence to contrast the computational models. The three DFT model predictions were comparable in structural terms, with relative deviations from the experimental rotational constants of 0.2-3.5% (ωB97XD), 0.2-4.0% (B3LYP-D3) and 0.3-4.4% (B2PLYP-D3). The ωB97XD/cc-PVTZ binding energies, previously reported to be similar to CCSD(T) for aromatic homodimers,[60] differ less than 1 kJ mol^{-1} from B2PLYP-D3, with B3LYP-D3 giving larger values by 3-4 kJ mol^{-1}. The moderate interaction energies and the energy decomposition balance evidence that the thiophenol dimer represents an interesting case of coexistence of electrostatic and dispersion interactions, with the primary S-H···S hydrogen bond acting as a molecular anchor for positioning of the phenyl rings. The geometry of the trimer maintains the preference for a cooperative hydrogen bond network as observed in phenol and aniline, but the C_3 symmetry reflects a delicate balance between the hydrogen bond and C-H···π interactions, which may disappear for weaker clusters. The results emphasize the role of substituents effects to modulate π-stacking geometries and the importance of sulfur-centered hydrogen bonds. The connection between gas-phase aggregation processes and the design of supramolecular architectures remains a challenge for future studies.

References

(1) Grimme, S. Do Special Noncovalent π-π Stacking Interactions Really Exist? *Angew. Chemie - Int. Ed.* **2008**, *47* (18), 3430–3434. https://doi.org/10.1002/anie.200705157.

(2) Martinez, C. R.; Iverson, B. L. Rethinking the Term "π-Stacking." *Chem. Sci.* **2012**, *3* (7), 2191–2201. https://doi.org/10.1039/c2sc20045g.

(3) Burley, S.; Petsko, G. Aromatic-Aromatic Interaction: A Mechanism of Protein Structure Stabilization. *Science (80-.).* **1985**, *229* (4708), 23–28. https://doi.org/10.1126/science.3892686.

(4) Mcgaughey, G. B.; Gagne, M.; Rappe, A. K. π-Stacking Interactions, Alive and Well in Proteins. *J. Biol. Chem.* **1998**, *273* (25), 15458–15463.

(5) Kool, E. T. Hydrogen Bonding, Base Stacking, and Steric Effects in DNA Replication. *Annu. Rev. Biophys. Biomol. Struct.* **2001**, *30* (October), 1–22.

(6) *Non-Covalent Interactions in the Synthesis and Design of New Compounds*; Maharramov, A. M., Mahmudov, K. T., Kopylovich, M. N., Pombeiro, A. J. L., Eds.; John Wiley & Sons, Inc: Hoboken,

NJ, 2016. https://doi.org/10.1002/9781119113874.

(7) Stornaiuolo, M.; De Kloe, G. E.; Rucktooa, P.; Fish, A.; Van Elk, R.; Edink, E. S.; Bertrand, D.; Smit, A. B.; De Esch, I. J. P.; Sixma, T. K. Assembly of a π-π Stack of Ligands in the Binding Site of an Acetylcholine-Binding Protein. *Nat. Commun.* **2013**, *4* (May). https://doi.org/10.1038/ncomms2900.

(8) Salonen, L. M.; Ellermann, M.; Diederich, F. Aromatic Rings in Chemical and Biological Recognition: Energetics and Structures. *Angew. Chemie - Int. Ed.* **2011**, *50* (21), 4808–4842. https://doi.org/10.1002/anie.201007560.

(9) Neel, A. J.; Hilton, M. J.; Sigman, M. S.; Toste, F. D. Exploiting Non-Covalent π Interactions for Catalyst Design. *Nature* **2017**, *543* (7647), 637–646. https://doi.org/10.1038/nature21701.

(10) Schlosser, F.; Moos, M.; Lambert, C.; Würthner, F. Redox-Switchable Intramolecular π-π-Stacking of Perylene Bisimide Dyes in a Cyclophane. *Adv. Mater.* **2013**, *25* (3), 410–414. https://doi.org/10.1002/adma.201201266.

(11) Seifert, N. A.; Steber, A. L.; Neill, J. L.; Pérez, C.; Zaleski, D. P.; Pate, B. H.; Lesarri, A. The Interplay of Hydrogen Bonding and Dispersion in Phenol Dimer and Trimer: Structures from Broadband Rotational Spectroscopy. *Phys. Chem. Chem. Phys.* **2013**, *15* (27), 11468–11477. https://doi.org/10.1039/c3cp51725j.

(12) Hunter, C. A.; Sanders, J. K. M. The Nature of π-π Interactions. *J. Am. Chem. Soc.* **1990**, *112* (14), 5525–5534. https://doi.org/10.1021/ja00170a016.

(13) Wheeler, S. E.; Houk, K. N. Substituent Effects in the Benzene Dimer Are Due to Direct Interactions of the Substituents with the Unsubstituted Benzene. *J. Am. Chem. Soc.* **2008**, *130* (33), 10854–10855. https://doi.org/10.1021/ja802849j.

(14) Riwar, L. J.; Trapp, N.; Kuhn, B.; Diederich, F. Substituent Effects in Parallel-Displaced π–π Stacking Interactions: Distance Matters. *Angew. Chemie - Int. Ed.* **2017**, *56* (37), 11252–11257. https://doi.org/10.1002/anie.201703744.

(15) Watt, M.; Hardebeck, L. K. E.; Kirkpatrick, C. C.; Lewis, M. Face-to-Face Arene-Arene Binding Energies: Dominated by Dispersion but Predicted by Electrostatic and Dispersion/Polarizability Substituent Constants. *J. Am. Chem. Soc.* **2011**, *133* (11), 3854–3862. https://doi.org/10.1021/ja105975a.

(16) Černý, J.; Kabeláč, M.; Hobza, P. Double-Helical → Ladder Structural Transition in the B-DNA Is Induced by a Loss of Dispersion Energy. *J. Am. Chem. Soc.* **2008**, *130* (47), 16055–16059. https://doi.org/10.1021/ja805428q.

(17) Arunan, E.; Gutowsky, H. S. The Rotational Spectrum, Structure and Dynamics of a Benzene Dimer. *J. Chem. Phys.* **1993**, *98* (5), 4294. https://doi.org/10.1063/1.465035.

(18) Schnell, M.; Erlekam, U.; Bunker, P. R.; Vonhelden, G.; Grabow, J. U.; Meijer, G.; Vanderavoird, A. Structure of the Benzene Dimer - Governed by Dynamics. *Angew. Chemie - Int. Ed.* **2013**, *52* (19), 5180–5183. https://doi.org/10.1002/anie.201300653.

(19) Schnell, M.; Erlekam, U.; Bunker, P. R.; Von Helden, G.; Grabow, J.-U.; Meijer, G.; Van Der Avoird, A. Unraveling the Internal Dynamics of the Benzene Dimer: A Combined Theoretical and Microwave Spectroscopy Study. *Phys. Chem. Chem. Phys.* **2013**, *15* (25), 10207–10223. https://doi.org/10.1039/c3cp51181b.

(20) Sinnokrot, M. O.; Sherrill, C. D. Highly Accurate Coupled Cluster Potential Energy Curves for the Benzene Dimer: Sandwich, T-Shaped, and Parallel-Displaced Configurations. *J. Phys. Chem. A* **2004**, *108* (46), 10200–10207. https://doi.org/10.1021/jp0469517.

(21) Busker, M.; Svartsov, Y. N.; Häber, T.; Kleinermanns, K. IR-UV Double Resonance Spectra of Pyrazine Dimers: Competition between CH ⋯ π, π ⋯ π and CH ⋯ N Interactions. *Chem. Phys. Lett.* **2009**, *467* (4–6), 255–259. https://doi.org/10.1016/j.cplett.2008.10.091.

(22) Pietraperzia, G.; Pasquini, M.; Schiccheri, N.; Piani, G.; Becucci, M.; Castellucci, E.; Biczysko, M.; Bloino, J.; Barone, V. The Gas Phase Anisole Dimer: A Combined High-Resolution Spectroscopy and Computational Study of a Stacked Molecular System. *J. Phys. Chem. A* **2009**, *113* (52), 14343–14351. https://doi.org/10.1021/jp903236z.

(23) Maity, S.; Patwari, G. N.; Sedlak, R.; Hobza, P. A π-Stacked Phenylacetylene Dimer. *Phys. Chem. Chem. Phys.* **2011**, *13* (37), 16706–16712. https://doi.org/10.1039/c1cp20677j.

(24) Kundu, A.; Sen, S.; Patwari, G. N. The Propargylbenzene Dimer: C-H···π Assisted π-π Stacking. *Phys. Chem. Chem. Phys.* **2015**, *17* (14), 9090–9097. https://doi.org/10.1039/c5cp00162e.

(25) Mondal, S. I.; Sen, S.; Hazra, A.; Patwari, G. N. π-Stacked Dimers of Fluorophenylacetylenes: Role of Dipole Moment. *J. Phys. Chem. A* **2017**, *121* (18), 3383–3391. https://doi.org/10.1021/acs.jpca.7b00209.

(26) Caminati, W.; Grabow, J.-U. J.-U. Advancements in Microwave Spectroscopy. In *Frontiers and Advancements in Microwave Spectroscopy*; Laane, J., Ed.; Elsevier: Amsterdam, 2018; pp 569–598. https://doi.org/10.1016/B978-0-12-811220-5.00018-6.

(27) Juanes, M.; Saragi, R. T.; Caminati, W.; Lesarri, A. *The Hydrogen Bond and Beyond: Perspectives for Rotational Investigations of Non-Covalent Interactions*; 2019; Vol. 25, pp 11402–11411.

(28) Goly, T.; Spoerel, U.; Stahl, W. The Microwave Spectrum of the 1,2-Difluorobenzene Dimer. *Chem. Phys.* **2002**, *283* (1–2), 289–296. https://doi.org/10.1016/S0301-0104(02)00500-1.

(29) Fatima, M.; Steber, A. L.; Poblotzki, A.; Pérez, C.; Zinn, S.; Schnell, M. Rotational Signatures of Dispersive Stacking in the Formation of Aromatic Dimers. *Angew. Chemie - Int. Ed.* **2019**, *58* (10), 3108–3113. https://doi.org/10.1002/anie.201812556.

(30) Seifert, N. A.; Hazrah, A. S.; Jäger, W. The 1-Naphthol Dimer and Its Surprising Preference for π-π Stacking over Hydrogen Bonding. *J. Phys. Chem. Lett.* **2019**, *10* (11), 2836–2841. https://doi.org/10.1021/acs.jpclett.9b00646.

(31) Schmitt, M.; Böhm, M.; Ratzer, C.; Krügler, D.; Kleinermanns, K.; Kalkman, I.; Berden, G.; Meerts, W. L. Determining the Intermolecular Structure in the S0 and S1 States of the Phenol Dimer by Rotationally Resolved Electronic Spectroscopy. *ChemPhysChem* **2006**, *7* (6), 1241–1249. https://doi.org/10.1002/cphc.200500670.

(32) Hobza, P.; Muller-Dethlefs, K. *Non-Covalent Interactions*; Hobza, P., Muller-Dethlefs, K., Eds.; Theoretical and Computational Chemistry Series; Royal Society of Chemistry: Cambridge, 2009. https://doi.org/10.1039/9781847559906.

(33) Sugawara, K. I.; Miyawaki, J.; Nakanaga, T.; Takeo, H.; Lembach, G.; Djafari, S.; Barth, H. D.; Brutschy, B. Infrared Depletion Spectroscopy of the Aniline Dimer. *J. Phys. Chem.* **1996**, *100* (43), 17145–17147. https://doi.org/10.1021/jp961901q.

(34) Biswal, H. S.; Bhattacharyya, S.; Bhattacherjee, A.; Wategaonkar, S. Nature and Strength of Sulfur-Centred Hydrogen Bonds: Laser Spectroscopic Investigations in the Gas Phase and Quantum-Chemical Calculations. *Int. Rev. Phys. Chem.* **2015**, *34* (1), 99–160. https://doi.org/10.1080/0144235X.2015.1022946.

(35) Juanes, M.; Saragi, R. T.; Jin, Y.; Zingsheim, O.; Schlemmer, S.; Lesarri, A. Rotational Spectrum and Intramolecular Hydrogen Bonding in 1,2-Butanedithiol. *J. Mol. Struct.* **2020**, *1211*. https://doi.org/10.1016/j.molstruc.2020.128080.

(36) Juanes, M.; Lesarri, A.; Pinacho, R.; Charro, E.; Rubio, J. E.; Enríquez, L.; Jaraíz, M. Sulfur Hydrogen Bonding in Isolated Monohydrates: Furfuryl Mercaptan versus Furfuryl Alcohol. *Chem. – A Eur. J.* **2018**, *24* (25), 6564–6571. https://doi.org/10.1002/CHEM.201705727.

(37) Juanes, M.; Saragi, R. T.; Pinacho, R.; Rubio, J. E.; Lesarri, A. Sulfur Hydrogen Bonding and Internal Dynamics in the Monohydrates of Thenyl Mercaptan and Thenyl Alcohol. *Phys. Chem. Chem. Phys.* **2020**. https://doi.org/10.1039/D0CP01706J.

(38) Pérez, C.; León, I.; Lesarri, A.; Pate, B. H.; Martínez, R.; Millán, J.; Fernández, J. A. Isomerism of the Aniline Trimer. *Angew. Chemie - Int. Ed.* **2018**, *57* (46), 15112–15116. https://doi.org/10.1002/anie.201808602.

(39) Shipman, S. T.; Pate, B. H. New Techniques in Microwave Spectroscopy. *Handb. High-resolution Spectrosc.* **2011**. https://doi.org/10.1002/9780470749593.HRS036.

(40) Halgren, T. A. Merck Molecular Force Field. II. MMFF94 van Der Waals and Electrostatic Parameters for Intermolecular Interactions - Wiley Online Library. *J. Comput. Chem.* **1996**, *17* (5–6), 520–522.

(41) Macromodel. Schrödinger, LLC: New York 2012.

(42) Grimme, S.; Ehrlich, S.; Goerigk, L. Effect of the Damping Function in Dispersion Corrected Density Functional Theory. *J. Comput. Chem.* **2011**, *32* (7), 1456–1465. https://doi.org/10.1002/jcc.21759.

(43) Johnson, E. R.; Keinan, S.; Mori-Sánchez, P.; Contreras-García, J.; Cohen, A. J.; Yang, W. Revealing Noncovalent Interactions. *J. Am. Chem. Soc.* **2010**, *132* (18), 6498–6506. https://doi.org/10.1021/ja100936w.

(44) Contreras-García, J.; R. Johnson, E.; Keinan, S.; Chaudret, R.; Piquemal, J.-P.; N. Beratan, D.; Yang, W. NCIPLOT: A Program for Plotting Noncovalent Interaction Regions. *J. Chem. Theory Comput.* **2011**, *7* (3), 625–632. https://doi.org/10.1021/ct100641a.

(45) Jeziorski, B.; Moszynski, R.; Szalewicz, K. Perturbation Theory Approach to Intermolecular Potential Energy Surfaces of van Der Waals Complexes. *Chem. Rev.* **1994**, *94* (7), 1887–1930. https://doi.org/10.1021/cr00031a008.

(46) Hohenstein, E. G.; Sherrill, C. D. Density Fitting of Intramonomer Correlation Effects in Symmetry-Adapted Perturbation Theory. *J. Chem. Phys.* **2010**, *133* (1), 014101. https://doi.org/10.1063/1.3451077.

(47) Parrish, R. M.; Burns, L. A.; Smith, D. G. A.; Simmonett, A. C.; DePrince, A. E.; Hohenstein, E. G.; Bozkaya, U.; Sokolov, A. Y.; Di Remigio, R.; Richard, R. M.; Gonthier, J. F.; James, A. M.; McAlexander, H. R.; Kumar, A.; Saitow, M.; Wang, X.; Pritchard, B. P.; Verma, P.; Schaefer, H. F.; Patkowski, K.; King, R. A.; Valeev, E. F.; Evangelista, F. A.; Turney, J. M.; Crawford, T. D.; Sherrill, C. D. Psi4 1.1: An Open-Source Electronic Structure Program Emphasizing Automation, Advanced Libraries, and Interoperability. *J. Chem. Theory Comput.* **2017**, *13* (7), 3185–3197. https://doi.org/10.1021/acs.jctc.7b00174.

(48) Wilson, A. K.; Van Mourik, T.; Dunning, T. H. Gaussian Basis Sets for Use in Correlated Molecular Calculations. VI. Sextuple Zeta Correlation Consistent Basis Sets for Boron through Neon. *J. Mol. Struct. THEOCHEM* **1996**, *388* (1–3), 339–349. https://doi.org/10.1016/S0166-1280(96)80048-0.

(49) Larsen, N. W.; Schulz, L. Internal Rotation and Structure of Thiophenol and 4-Fluorothiophenol Studied by Microwave Spectroscopy and Quantum Chemistry. *J. Mol. Struct.* **2009**, *920* (1–3), 30–39. https://doi.org/10.1016/j.molstruc.2008.10.015.

(50) Larsen, N. W.; Nicolaisen, F. M. Far-Infrared Gas Spectra of Phenol, 4-Fluorophenol, Thiophenol and Some Deuterated Species: Barrier to Internal Rotation. *J. Mol. Struct.* **1974**, *22* (1), 29–43. https://doi.org/10.1016/0022-2860(74)80065-7.

(51) Watson, J. K. G. Aspects of Quartic and Sextic Centrifugal Effects on Rotational Energy Levels. In *Vibrational Spectra and Structure, vol. 6*; Durig, J. R., Ed.; Elsevier B.V.: Amsterdam, 1977; pp 1–89.

(52) Meyer, R. Flexible Models for Intramolecular Motion, a Versatile Treatment and Its Application to Glyoxal. *J. Mol. Spectrosc.* **1979**, *76* (1–3), 266–300. https://doi.org/10.1016/0022-2852(79)90230-3.

(53) Sørensen, G. O. A New Approach to the Hamiltonian of Nonrigid Molecules. In *In Topics in Current Chemistry 82: Large Amplitude Motion in Molecules II*; Springer-Verlag: Berlin, Heidelberg, 1979; pp 97–175. https://doi.org/10.1007/BFB0048009.

(54) Bauder, A.; Mathier, E.; Meyer, R.; Ribeaud, M.; Günthard, H. H. Theory of Rotation and Torsion Spectra for a Semi-Rigid Model of Molecules with an Internal Rotor of C 2v Symmetry. *http://dx.doi.org/10.1080/00268976800101501* **1968**, *15* (6), 597–614. https://doi.org/10.1080/00268976800101501.

(55) Caminati, W. Microwave Spectroscopy of Large Molecules and Molecular Complexes. In *Handbook of High-resolution Spectroscopy*; Merkt, F., Quack, M., Eds.; John Wiley & Sons, Ltd: New York, 2011. https://doi.org/10.1002/9780470749593.HRS035.

(56) Das, A.; Mandal, P. K.; Lovas, F. J.; Medcraft, C.; Walker, N. R.; Arunan, E. The H2S Dimer Is Hydrogen-Bonded: Direct Confirmation from Microwave Spectroscopy. *Angew. Chemie Int. Ed.* **2018**, *57* (46), 15199–15203. https://doi.org/10.1002/anie.201808162.

(57) Lovas, F. J. *Private Communication*; 2020.

(58) Mukhopadhyay, A.; Cole, W. T. S.; Saykally, R. J. The Water Dimer I: Experimental Characterization. *Chem. Phys. Lett.* **2015**, *633*, 13–26. https://doi.org/10.1016/j.cplett.2015.04.016.

(59) Zhou, P.; Tian, F.; Lv, F.; Shang, Z. Geometric Characteristics of Hydrogen Bonds Involving Sulfur

Atoms in Proteins. *Proteins Struct. Funct. Bioinforma.* **2009**, *76* (1), 151–163. https://doi.org/10.1002/prot.22327.

(60) Huber, R. G.; Margreiter, M. A.; Fuchs, J. E.; Von Grafenstein, S.; Tautermann, C. S.; Liedl, K. R.; Fox, T. Heteroaromatic π-Stacking Energy Landscapes. *J. Chem. Inf. Model.* **2014**, *54* (5), 1371–1379. https://doi.org/10.1021/ci500183u.

(61) David, J. G.; Hallam, H. E. Hydrogen-Bonding Studies of Thiophenols. *Spectrochim. Acta* **1965**, *21* (4), 841–850. https://doi.org/10.1016/0371-1951(65)80041-8.

Chapter 3.
The Benzyl Mercaptan Dimer

In this chapter, we study the benzyl mercaptan dimer as an extension of the thiophenol aggregation studies of Chapter 2. By having the side chain enlarged by one methylene group, the degrees of conformational freedom of benzyl mercaptan increase, and the flexibility of the thiol group permits more interaction patterns on dimerization. Furthermore, the longer sidechain permits a discussion on transient chirality and the preferences for homochiral or heterochiral self-aggregation. Finally, the study of the benzyl mercaptan dimer may be compared with the benzyl alcohol dimer, previously examined also in our group, offering insight into the hydrogen bonds established by sulfur centers. In both dimers a single homochiral isomer was observed, with a similar hydrogen bond pattern. This chapter has been adapted from the references below:

- R.T. Saragi, M. Juanes, R. Pinacho, J.E. Rubio, J.A. Fernández, A. Lesarri, "Molecular Recognition, Transient Chirality and Sulfur Hydrogen Bonding in the Benzyl Mercaptan Dimer". *Symmetry* **2021**, 13, 2022,
- R.T. Saragi, M. Juanes, W. Caminati, A. Lesarri, L. Enríquez, and M. Jaraíz, "Rotational Spectrum, Tunnelling Motions, and Intramolecular Potential Barriers in Benzyl Mercaptan". *J. Phys. Chem. A,* **2019**, 123, 8435-8440 and
- R. Medel, A. Camiruaga, R. T. Saragi, P. Pinacho, C. Pérez, M. Schnell, A. Lesarri, M. A. Suhm, J. A. Fernandez, "Rovibronic signatures of molecular aggregation in the gas phase: subtle homochirality trends in the dimer, trimer and tetramer of benzyl alcohol" *Phys. Chem. Chem. Phys.,* **2021**, 23, 23610-23624.

3.1. Introduction

Molecular recognition is a subtle chemical process involving a combination of intermolecular interactions and intramolecular factors, largely dependent on the composition of the host and guest molecules. The consequences of molecular recognition, extending to large-scale chemical phenomena like supramolecular[1] and

technological applications,[2] justify the molecular investigation of the electronic and stereochemical features of the recognition process using high-resolution spectroscopy[3] and quantum mechanical methods.[4,5] In this context, the preparation of mass-selected intermolecular adducts in the gas phase is a well-known procedure for isolation and observation of specific weak interactions between target chemical groups, which otherwise would be blurred in the condensed media. This approach, when combined with rationalizing theoretical calculations, has led in the last decade to an explosion of new weak intermolecular interactions previously unnoticed.[6,7]

Molecular recognition is especially interesting between chiral species, as it may provide insight into biochemical docking, asymmetric synthesis, and chiral analysis. Among chiral molecules, those with very low (5-10 kJ mol^{-1}) torsional stereomutation barriers display transient chirality. Transient enantiomers interconvert in nanosecond time scales that would be undetectable with conventional techniques. However, transient chirality can be revealed by the formation of diastereomeric dimers in the gas phase, simultaneously freezing stereomutation and providing information on the structural and energetic factors controlling homo- or heterochiral aggregation.[8,9] The process of chirality synchronization was first observed with electronic and vibrational spectroscopy,[10–12] but these techniques require computational support for spectral interpretation. Alternatively, rotational spectroscopy[7,13] offers an unequivocal structural identification which complements molecular orbital calculations and may contribute to validate the computational models, which in turn are critical for the determination of the weak chirodiastaltic energies[14–16] between homo- and heterochiral aggregates.

Rotational experiments on homodimer synchronization have been mostly restricted to alcohols (ethanol,[17,18] 2-propanol,[19] 2-butanol,[20] glycidol,[21] cyclohexanol[22]) and fluoroalcohols (2-fluoroethanol,[23] trifluoroethanol,[24] hexafluoroisopropanol[25]), which benefit of the stronger O-H···O hydrogen bonds. Conversely, molecular studies of thiol aggregation are much scarcer.[5] The experiments available have mostly probed thiols as proton acceptors, in particular in O-H···S [26–31], N-H···S [32] and C-H···S [33,34] hydrogen bonds. Thiol dimerization studies particularly contribute to the description of thiol as proton donors in S-H···S[35–37] and other weak sulfur interactions (S-H···O[38], S-H···π[39], etc.), far less investigated[40] and consequently needed of molecular studies.

In this chapter, we selected benzyl mercaptan as a dimerization target. Benzyl mercaptan represents an extension of our previous work on thiophenol dimerization,[36] and will establish if the two rings maintain the π-stacking thiophenol arrangement or tilted geometries similar to the benzyl alcohol dimer,[41] recently revisited.[42] Additionally, it will discern whether the homochiral aggregation of benzyl alcohol is respected in the

mercaptan and the structural and physical differences in the S-H···S hydrogen bond compared to the canonical O-H···O hydrogen bond.

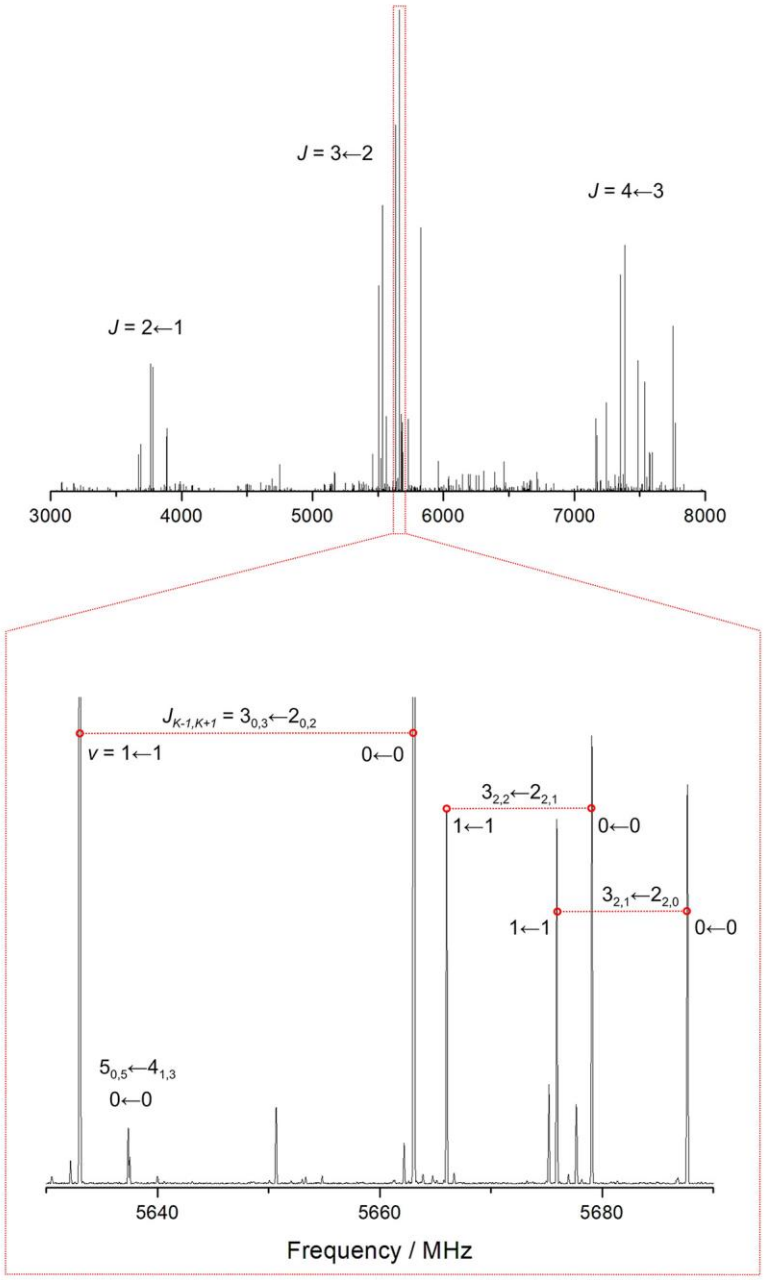

Figure 3.1. A section of the microwave spectrum of benzyl mercaptan (3–8 GHz) showing tunnelling splittings in the μ_a transitions of the monomer.

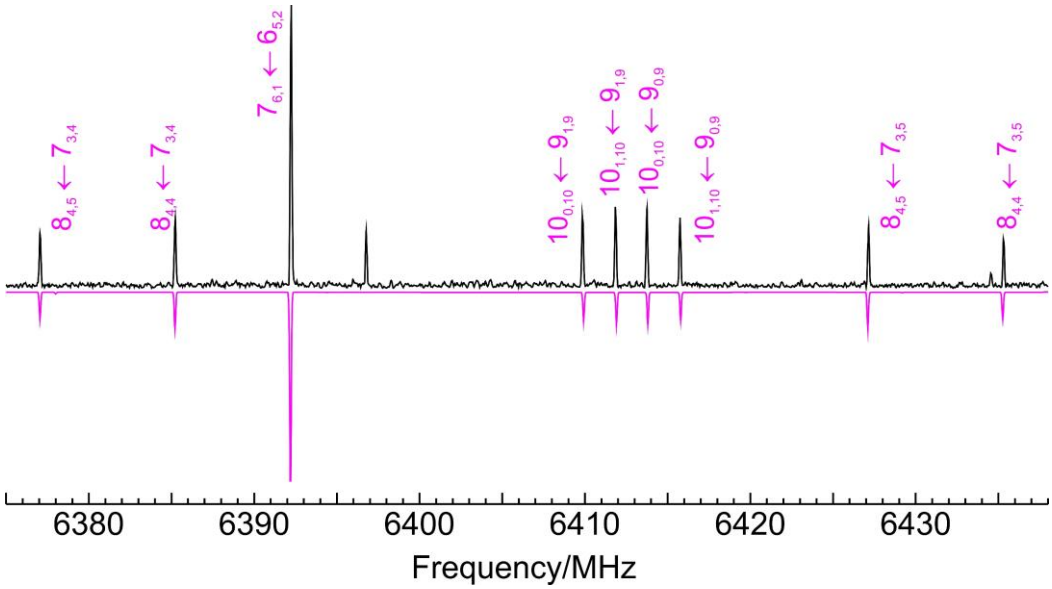

Figure 3.2. A short 60 MHz section of the microwave spectrum of benzyl mercaptan, showing typical rotational transitions of the homochiral dimer 1 (GG-GG-Lp-).

3.2. Methods

The sample of benzyl mercaptan (>96%, bp 195°C) was obtained commercially and required no further purification. The sample was vaporized inside the heating reservoir (45-55°C) of a pulsed solenoid injector and expanded near adiabatically through a 0.8 mm nozzle to form a supersonic jet within an expansion chamber. Neon at stagnation pressures of 0.2 MPa was used as a carrier gas, with typical molecular pulses of 800-900 μs. The expanding jet was probed in the 2-8 GHz cm-wave region with a direct-digital chirped-pulse Fourier transform microwave (CP-FTMW) spectrometer, following Pate's design.[43] The operation sequence is based on short (4 μs, 20 W) chirped pulses that are broadcasted perpendicularly to the jet. The MW radiation produces a fast-passage broadband transient excitation,[44,45] simultaneously covering the full spectral bandwidth. Following the excitation, the molecular ensemble emits a free-induction decay, which is detected in the time-domain (ca. 40 μs) and acquired using a (25 GSamples/s) digital oscilloscope. A Fourier transformation with a Kaiser-Bessel window results in FWHM linewidths of ca. 100 kHz. In this experiment, ca. 1 M averages were acquired at a repetition rate of 5 Hz. The uncertainty of the frequency measurements was estimated below 20 kHz.

Several computational calculations complemented the experimental study. Following an initial conformational screening with molecular mechanics (MMFFs[46]), all further

calculations used density-functional theory (DFT) molecular orbital calculations. Two density-functional methods were selected here, including the hybrid B3LYP[47] and double-hybrid B2PLYP[48] methods, combined with Ahlrichs' polarized triple-zeta basis def2-TZVP [49]. Both methods were supplemented with D3[50] dispersion corrections and Becke-Johnson damping.[51] Frequency calculations were performed at the same level of theory, using the harmonic approximation. The calculation of complexation energies considered the basis set superposition errors (BSSE) with the counterpoise approximation.[52] All DFT calculations were conducted with Gaussian 16.[53] The physical contributions to the binding potential of the water clusters were estimated by energy decomposition analysis using second-order symmetry adapted perturbation theory[54,55] (SAPT), implemented in PSI4.[56] Finally, the presence of non-covalent interactions was analysed with the NCIPlot methodology, based on a reduced gradient of the electronic density.[57] Detailed information is provided in the Tables S3.1-S3.9 in the Appendix.

3.3. Results and Discussions

3.3.1. Benzyl mercaptan monomer

Benzyl mercaptan displays a bidimensional potential energy surface, qualitatively similar to benzyl alcohol.[58] The two torsional degrees of freedom are associated to the elevation and orientation of the terminal thiol group, given by dihedrals τ_1(SC_α-$C_{ipso}C_{ortho}$) and τ_2(HS-$C_\alpha C_{ipso}$). In this conformation, the sulfur atom is synclinal to the ring plane ($\tau_1 \sim \pm 74°$ vs ±55° in benzyl alcohol) and the thiol hydrogen is synchronously oriented towards the π ring ($\tau_2 \sim \pm 74°$ vs ±53° in benzyl alcohol), denoted *gauche-gauch*e or GG. The rotational parameters including the torsional energy are summarized in Table 3.1, and the complete list of rotational transitions of monomer can be found in Table S3.5 (Appendix).

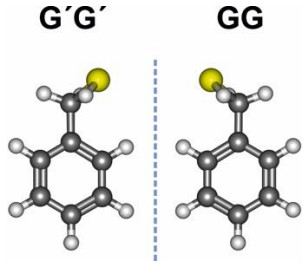

Figure 3.3. The most stable GG conformer of benzyl mercaptan and its enantiomer G´G´.

Table 3.1 Rotational parameters of the benzyl mercaptan monomer.

	Conformer GG		
	Experiment		Theory [a]
	v=0	v=1	
A / MHz [b]	4167.4584(15) [f]	4167.7017(15)	4185.0
B / MHz	1001.61056(41)	1001.59720(36)	1000.6
C / MHz	891.69084(39)	891.65660(37)	891.0
D_J / kHz	0.1550(41)		0.127
D_{JK} / kHz [c]	2.506(22)		1.809
D_K / kHz	0.288(77)		1.726
d_1 / kHz	[0.0] [g]		0.0038
d_2 / kHz	[0.0]		0.0048
ΔE_{01} / MHz [d]	2180.4879(35)		
F_{ab} / MHz	96.3332(14)		
F_{bc} / kHz	17.88461(23)		
σ / kHz	11.5		
N	102		
μ_a / D	Detected		1.2
μ_b / D	Detected		0.6
μ_c / D	Detected		0.4
μ_{TOTAL} / D			2.0
ΔE_{ZPE}/ kJ mol^{-1} [e]			0.0
ΔG / kJ mol^{-1}			0.0
HS–$C_\alpha C_{ipso}$ / deg			53.7
SC_α–$C_{ipso}C_{ortho}$ / deg			75.3

[a]B3LYP-D3(BJ)/def2-TZVP. [b]Rotational constants (A, B, C) for the two torsional sub-states (v=0, 1). [c]Watson's S-reduction centrifugal distortion constants (D_J, D_{JK}, D_K, d_1, d_2). [d]Energy difference between the first torsional substates (ΔE_{01}), Coriolis coupling parameters (F_{ab}, F_{bc}), standard error of the fit (σ) and number of measured transitions (N). [e]Electronic energies, Gibbs energy (298 K, 1 atm) and structural parameters. [f]Standard errors in parentheses in units of the last digit. [g]Fixed to zero.

The global minimum is four-fold degenerate since the thiol group may tunnel between symmetry equivalent conformations either by reflection on the ring plane or a perpendicular plane bisecting the phenyl ring through carbons C_{ipso} and C_{para}. Inversion through the perpendicular plane creates a detectable barrier (B_2 = 248 cm^{-1} = 2.97 kJ mol^{-1}), which produces characteristic tunnelling doublings in the rotational spectrum of Figures 3.1 and 3.2, strongly perturbed by Coriolis interactions.[59] The inversion barrier in benzyl mercaptan is ca. 11% lower than in the alcohol (B_2 = 280 cm^{-1} = 3.35 kJ mol^{-1}). The molecule thus changes chirality by inverting between the two *gauche-gauche* enantiomers GG and G´G´ of Figure 3.3 (primes denote negative dihedrals).

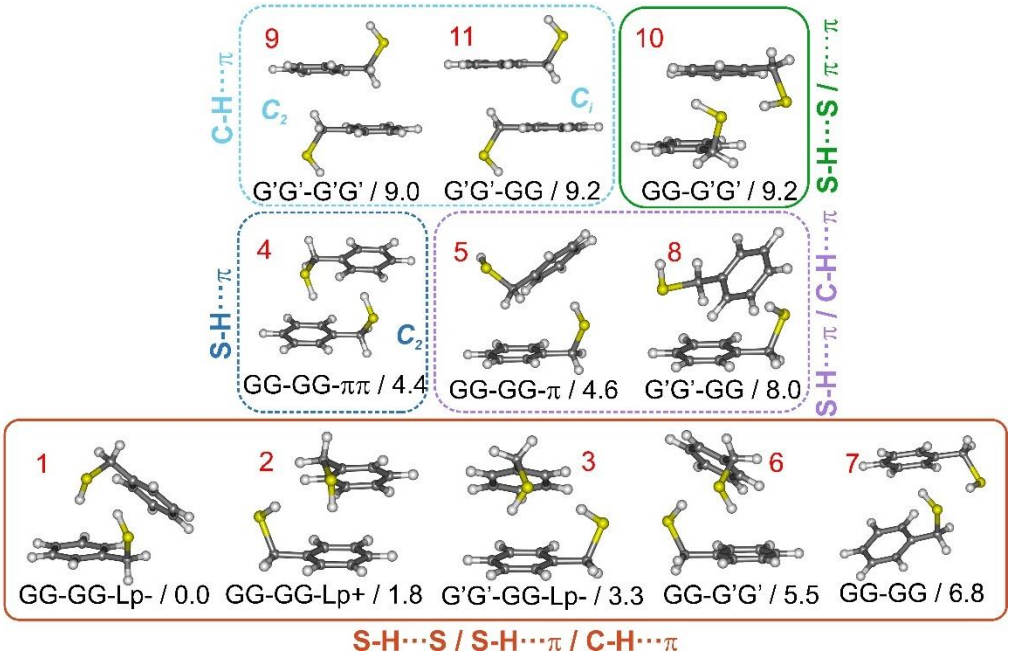

Figure 3.4. The most stable isomers of the benzyl mercaptan dimer, classified by their intermolecular interactions and ordered by the relative electronic energy (ΔE_{ZPE}, kJ mol^{-1}) calculated at the B3LYP-D3(BJ)/def2-TZVP level. Isomers in the dashed rectangle exhibit a sulfur S-H···S hydrogen bond. The only symmetric isomers are 5 (C_2), 9 (C_2) and 11 (C_i).

3.3.2. Benzyl mercaptan homodimer

For benzyl mercaptan, the dimerization from a single *gauche-gauche* conformation may in principle produce only homochiral (GG-GG = G′G′-G′G′) or heterochiral (GG- G′G′= G′G′-GG) diastereoisomers (proton donor denoted first). The most stable isomers are expected to balance several intermolecular interactions, mainly involving the S-H and C-H groups as proton donors and the sulfur lone pairs and π electrons as acceptors. However, the two diastereotopic acceptor lone pairs (Lp+/-) and the multiple possibilities for interaction between the polar thiol groups and the two ring molecules are expected to produce multiple isomers. The results of a DFT (B3LYP-D3(BJ)) conformational search are summarized in Figures 3.4 and 3.5 (Table S3.6 in Appendix), suggesting 11 isomers within complexation energies below 10 kJ mol^{-1}.

The five most stable isomers are compared to the benzyl alcohol dimer[41] in Figure 3.6. The two most stable dimers 1 (= GG-GG-Lp-) and 2 (= GG-GG-Lp+) are homochiral and controlled by the two thiol groups, which engage in two successive S-H···S and S-H···π interactions. The two rings adopt tilted (C_1) unsymmetric orientations to permit

further interaction via C(sp^2)-H··· π weak hydrogen bonds, with the alternative use of the two sulfur lone-pairs at the acceptor molecule producing two different ring orientations Lp+ and Lp- (Figure 3.5 a), well separated in energy (ΔE_{ZPE}= 1.9 kJ mol^{-1}, ΔE_c= 3.1 kJ mol^{-1}). The third isomer (=G´G-GG-Lp-) is the heterochiral equivalent to isomer 1 (Figure 3.5 b), predicted at ΔE_{ZPE}= 3.3 kJ mol^{-1} (ΔE_c= 4.6 kJ mol^{-1}). The fourth (=GG-GG-ππ) and fifth (=GG-GG-π) isomers reveal different homochiral S-H···π interactions, either alone or combined with a C(sp^3)-H···π link, which are destabilized ca. 4-5 kJ mol^{-1} with respect to the thiol S-H···S hydrogen bonding. Isomer GG-GG-ππ uses two identical S-H···π interactions to produce the lowest-lying C_2-symmetric dimer, characterized by two tilted rings which avoid π-stacking. Only for the higher energy isomers (>10 kJ mol^{-1}) near-parallel π···π or C-H···π interactions are predicted, as in the (C_2) homochiral isomer 9 (=GG-GG) and the (C_i) heterochiral isomer 11 (=GG-G´G´). The preference for C_2-symmetric heterochiral S-H···π dimers observed in the crystallographic structure[60] must thus be attributed to matrix effects and does not represent the isolated molecule. The three most stable isomers of the benzyl mercaptan dimer were reoptimized at B2PLYP-D3(BJ) level in Table 3.2, offering a prediction of the rotational parameters.

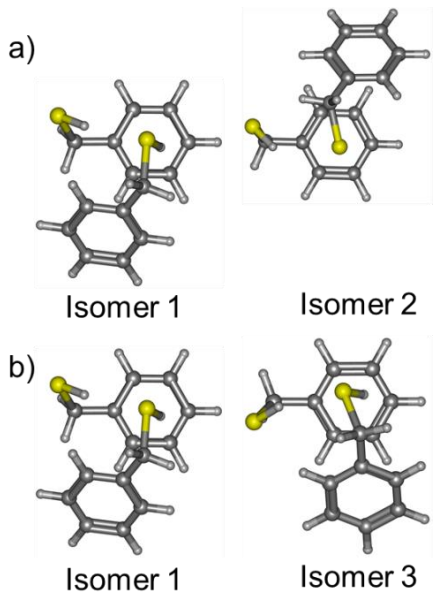

Figure 3.5. A comparison of the three asymmetric (C_1) most stable isomers of the benzyl mercaptan dimer. a) Isomers 1 (G´G´-G´G´-Lp+ = GG-GG-Lp-, left) and 2 (G´G´-G´G´-Lp- = GG-GG-Lp+, right) are both homochiral but differ in the acceptor lone pair position of sulfur (the dihedral formed by the lone pair or τ(LpS-$C_\alpha C_{ipso}$) have different signs for isomer 1 and isomer 2), producing a change of relative orientation between the rings. b) Isomers 1 (G´G´-G´G´-Lp+ = GG-GG-Lp-, left) and 3 (GG-G´G´-Lp+ = G´G´-GG-Lp-, right) differ in the stereochemistry of the donor group, either homochiral in isomer 1 or heterochiral in isomer 3.

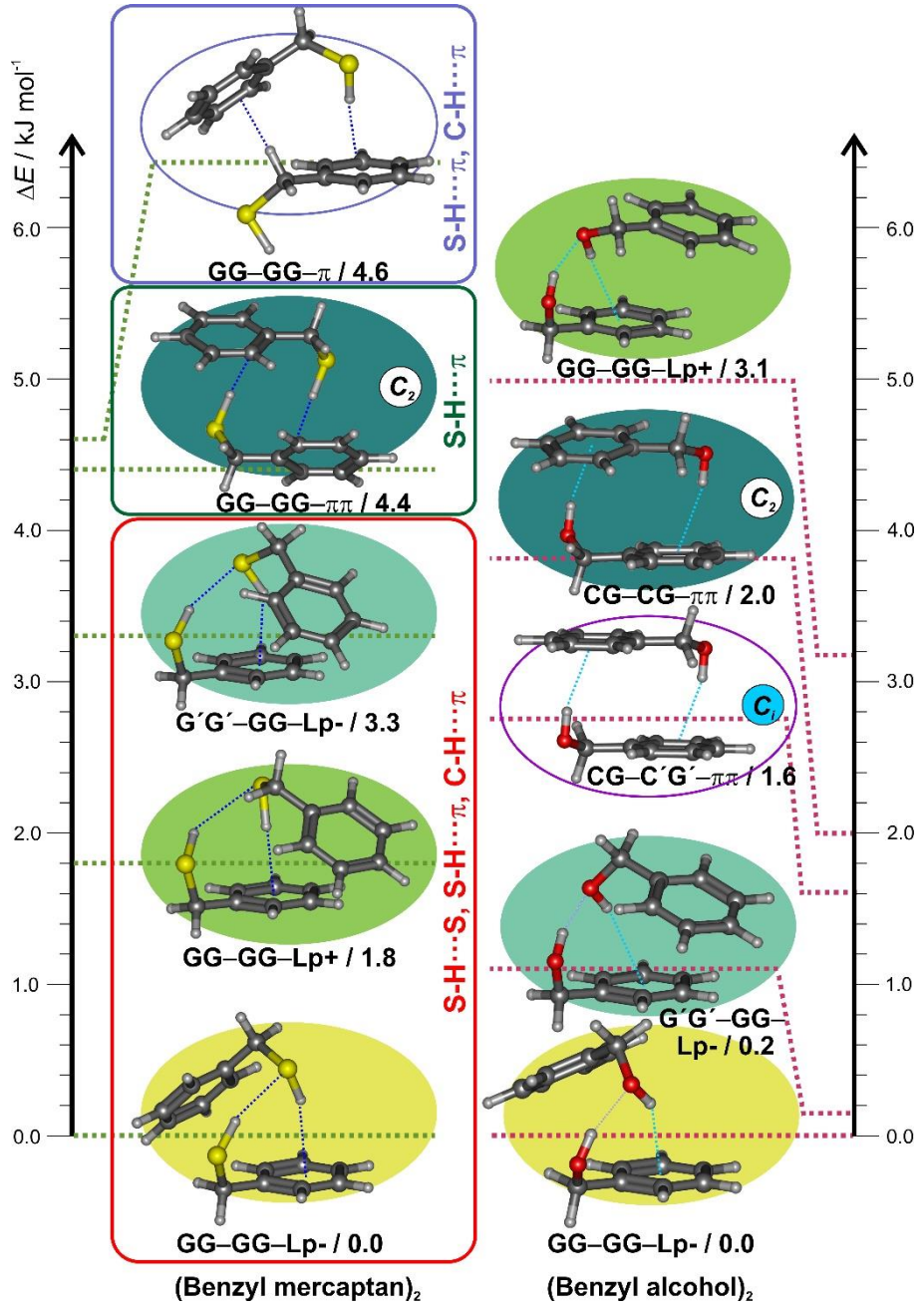

Figure 3.4. Conformational search for the benzyl mercaptan dimer (left column), representing the electronic energies (ΔE) of the five most stable isomers (see Figure 3.4 for a larger energy window and Figure 3.5 for isomers 1-3) using B3LYP-D3(BJ)/def2TZVP. The right column represents the most stable isomers of the benzyl alcohol dimer, the complete listing of rotational parameters can be found in Table S3.7 in Appendix.

Table 3.2. Rotational parameters of the benzyl mercaptan dimer.

	Experiment	Theory		
Isomer		1 (GG-GG-Lp-)	2 (GG-GG-Lp+)	3 (GG-G´G´-Lp+)
A / MHz [a]	490.79216(17) [f]	498.41[g] / 496.24 [h]	535.19 / 538.12	510.98 / 509.23
B / MHz	344.12732(12)	352.92 / 352.51	332.27 / 328.24	340.02 / 338.05
C / MHz	317.21115(11)	325.95 / 324.58	302.16 / 299.94	320.98 / 319.40
D_J / kHz [b]	0.03861(51)	0.0323 / 0.0326	0.0667 / 0.0596	0.0471 / 0.0507
D_{JK} / kHz	0.0642(18)	0.0584 / 0.0608	-0.1183 / -0.0984	-0.0064 / -0.0040
D_K / kHz	-0.0718(20)	-0.0662 / -0.0675	0.2012 / 0.1748	0.0411 / 0.0420
d_1 / kHz	-0.00375(33)	-0.0026 / -0.0026	-0.0002 / -0.0004	-0.0028 / -0.0031
d_2 / kHz	0.00089(13)	0.0007 / 0.0008	-0.0007 / -0.0005	0.0007 / 0.0008
$\lvert\mu_a\rvert$ / D	Detected	1.5 / 1.6	0.4 / 0.4	1.1 / 1.0
$\lvert\mu_b\rvert$ / D	Detected	1.7 / 1.7	1.3 / 1.3	1.6 / 1.6
$\lvert\mu_c\rvert$ / D	Detected	1.3 / 1.4	0.8 / 0.8	0.5 / 0.7
HBond donor [c]				
HS–CαCβ / deg		-39.6 / -41.3	-49.9 / -50.6	40.2 / 42.8
SCα–CβC1 / deg		-57.4 / -56.6	-70.2 / -70.0	64.9 / 63.3
HBond acceptor				
HS–CαCβ / deg		-53.1 / -54.1	-45.0 / -46.3	-44.5 / -45.8
SCα–CβC1 / deg		-67.6 / -65.7	-56.8 / -56.1	-70.9 / -68.9
r(S···H) / Å		2.684 / 2.748	2.879 / 2.941	2.728 / 2.803
∠(S–H···S) / deg		164.8 / 162.9	138.5 / 137.5	160.9 / 158.6
r(S–H···centroid) / Å		2.527 / 2.515	2.408 / 2.398	2.558 / 2.553
ΔE_{ZPE}/ kJ mol^{-1} [d]		0.0 / 0.0	1.8 / 1.7	3.3 / 3.4
ΔG / kJ mol^{-1}		0.7 / 0.4	0.0 / 0.0	1.8 / 1.4
E_c / kJ mol^{-1}		-41.3 / -35.6	-38.2 / -33.1	-36.7 / -31.3
ΔE_c / kJ mol^{-1}		0.0 / 0.0	3.1 / 2.6	4.6 / 4.3
N [e]	337			
σ / kHz	8.5			

[a]Rotational constants (A, B, C). [b]Watson's S-reduction centrifugal distortion constants (D_J, D_{JK}, D_K, d_1, d_2). [c]Structural parameters of the dimer. [d]Relative electronic energies including the ZPE correction, Gibbs energy (298 K, 1 atm), complexation energies (E_c) and relative complexation energies (ΔE_c). [e]Number of measured transitions (N) and standard error of the fit (σ). [f]Standard errors in parentheses in units of the last digit. [g]B3LYP-D3(BJ)/def2-TZVP. [h]B2PLYP-D3(BJ)/def2-TZVP.

The jet-cooled microwave spectrum provided experimental evidence on the nature of the dimerization adduct. Figure 3.2 shows spectral sections with typical rotational transitions. Noticeably, a single isomer was observed for the dimer of benzyl mercaptan. The spectrum was quite dense and more than 300 rotational transitions were measured experimentally, with all three (μ_a, μ_b, μ_c) selection rules active. The wide range of angular momentum quantum numbers (J=3-15 and K_{-1}<12) and the diversity of R-branch (J+1←J) and some Q-branch (J←J) transitions assured a good determination of the rotational parameters. There was no indication of tunnelling effects in the spectra, which were reproduced satisfactorily with a Watson's (S-reduced) semirigid rotor

Hamiltonian[61] and quartic centrifugal distortion terms. The experimental rotational parameters are compared with B2PLYP-D3(BJ) theoretical predictions in Table 3.2, with the full listing of observed transitions in Table S3.8 (Appendix). Since several low-lying isomers were predicted at small relative energies (< 3-5 kJ mol^{-1}), the observation of a single dimer species cannot be uniquely attributed to a pre-expansion thermal depopulation and probably suggests a conformational relaxation through low interconversion barriers, previously observed in jet experiments[62,63] and kinetically affecting the jet populations.[64]

The identification of the benzyl mercaptan dimer was unequivocal. We confirmed the detection of the predicted global minimum, identified as the homochiral GG-GG-Lp-. The predictions for the equilibrium rotational constants slightly exceed the experimental ground-state values by 6-8 MHz, but the relative differences are below 1.6%-2.8%, ensuring a positive identification. The agreement of the (harmonic) centrifugal distortion constants with the experiment values is consistent with the conformational assignment.

3.3.3. Non-covalent interactions

The intermolecular interactions associated to the benzyl mercaptan dimerization were explored using structural, energetic, and electronic density information. Unlike the parallel-displaced hydrogen-bonded dimer of thiophenol,[36] the aggregation of benzyl mercaptan follows a pattern of non-stacked cooperative hydrogen bonding. A primary S-H···S hydrogen bond is formed in which the thiol acts as proton donor to a second sulfur atom, followed by a secondary S-H···π hydrogen bond to the opposed π ring. Weak C-H···π or C-H···S hydrogen bonds are minor necessary contributors to the most stable isomers. The benzyl mercaptan dimers exhibit characteristically long S-H···S hydrogen bonds (B2PLYP: r(S-H···S) = 2.75 Å), relatively close to linearity (B2PLYP: ∠(S-H···S) = 163°). These values compare satisfactorily with the few rotational studies of thiol-thiol hydrogen bonding in the dimers of thiophenol[36] (B2PLYP: r(S-H···S) = 2.84 Å, ∠(S-H···S) = 135°) and hydrogen sulfide[35] (experiment: r(S-H···S) = 2.778(9) Å; B2PLYP: r(S-H···S) = 2.79 Å, ∠(S-H···S) = 172°). Crystallographic surveys of cysteine-methionine contacts have yielded shorter average values of r(S-H···S) = 2.55(47) Å[65] and r(S-H···S) = 2.5-2.7 Å[37]. The secondary hydrogen bond interactions between the thiol group and the π ring in Table 1 show distances to the ring centroid of r(S-H···centroid) = 2.52 Å (B2PLYP).

Binding energies are collected in Tables 3.2 and 3.3, comparing B2PLYP and a second-order 2+(3) symmetry-adapted perturbation theory (SAPT) energy decomposition. The interaction energy is decomposed into electrostatic (E_{elec}), inductive (multipole interactions/charge transfer, E_{ind}), exchange repulsion (E_{exch}) and dispersion (E_{disp})

energy terms. Not unexpectedly, the predicted binding energy of the benzyl mercaptan dimer (SAPT: -35.3 kJ mol^{-1}) is larger than in thiophenol (-25.9 to -27 kJ mol^{-1})[36] but remains ca. 84% smaller than in the benzyl alcohol dimer (-42.1 kJ mol^{-1})[42], reflecting the weaker thiol H-bond. Additional insight into the nature of the thiol hydrogen bond is obtained from the attractive contributions to the energy decomposition. The largest attractive contributor in the benzyl mercaptan dimer is dispersive (54%) but in smaller proportion than in the thiophenol dimer (60%) and with larger electrostatic participation (34% vs 29-31% in thiophenol). This result reverts the calculation for the benzyl alcohol dimer, where the electrostatic component (45%) is larger but nearly matched by dispersion (41%). A comparison with the dispersive pyridine-methane dimer and the water and hydrogen sulfide dimers is also given in Table 3.3. Similar trends of decreasing strength and dispersion have been observed in other thiol clusters and monohydrates.[30,31] To our knowledge, there are no comparable experimental binding energies involving thiol dimers except for hydrogen sulfide clusters.[26,27]

Table 3.3. Binding energy decomposition for (benzyl mercaptan)$_2$ and related dimers using SAPT(2)+3/aug-cc-pVDZ//B3LYP-D3(BJ)/def2-TZVP (all values in kJ mol^{-1}).

Cluster	E_{elect}	E_{disp}	E_{ind}	E_{exch}	E_{total}
(Benzyl mercaptan)$_2$ [a]	-39.3[34.4%] [h]	-61.1[53.6%]	-13.6[12.0%]	78.7	-35.3
(Thiophenol)$_2$ PD1-trans [b]	-24.9[31.0%]	-47.9[59.5%]	-7.7[9.5%]	54.6	-25.9
(Thiophenol)$_2$ PD2-cis	-26.0[29.4%]	-53.8[60.9%]	-8.4[9.6%]	61.3	-27.0
(H_2S)$_2$ [c]	-12.1[49.0%]	-7.8[31.7%]	-4.7[19.3%]	19.2	-5.4
(Benzyl alcohol)$_2$ [d]	-58.7[44.5%]	-54.6[41.4%]	-18.6[14.1%]	89.8	-42.1
(Phenol)$_2$ [e]	-41.8[48.3%]	-28.8[33.3%]	-15.9[18.4%]	58.9	-27.6
(H_2O)$_2$ [f]	-35.7[63.5%]	-9.5[16.8%]	-11.1[19.8%]	37.7	-18.6
Pyridine-methane [g]	-3.0[20.6%]	-10.9[74.6%]	-0.7[4.8%]	9.4	-5.2

[a]This work. [b]Ref. [36] [c]Ref. [35]. [d]Ref. [42]. [e]Seifert, N.A.; Steber, A.L.; Neill, J.L.; Pérez, C.; Zaleski, D.P.; Pate, B.H.; Lesarri, A. *Phys. Chem. Chem. Phys.* **2013**, *15*, 11468–11477. [f]Mukhopadhyay, A.; Cole, W.T.S.; Saykally, R.J. *Chem. Phys. Lett.* **2015**, *633*, 13–26. [g]Gou, Q.; Spada, L.; Vallejo-López, M.; Lesarri, A.; Cocinero, E.J.; Caminati, W. *Phys. Chem. Chem. Phys.* **2014**, *16*, 13041–13046. [h]Relative contribution to the attractive interactions (E_{elect}+E_{disp}+E_{ind}).

Non-covalent interactions can also be analysed using the topological properties of the electron density ($\rho(r)$) with the NCIPlot method [57]. Figure 3.7 represents a reduced electronic density gradient s $\left(=\frac{1}{2(3\pi^2)^{1/3}}\frac{|\nabla\rho|}{\rho^{4/3}}\right)$ versus the signed electronic density $(\text{sign}\,(\lambda_2)\,\rho)$ using the second eigenvalue (λ_2) of the electron density Hessian, comparing the global minimum of the benzyl mercaptan and benzyl alcohol dimers. This representation qualitatively identifies the stronger O-H···O hydrogen bond interactions in the alcohol (at more negative abscissas), simultaneously providing a 3D visualization

of the most relevant interaction surfaces. Furthermore, the 3D plot clearly identifies the S-H···S hydrogen bond and broad interaction regions between the two rings mainly associated to the S-H···π contact. The reduced electronic density calculations thus confirm the cooperative scheme of intermolecular interactions present in the benzyl mercaptan dimer, complementing the structural and energetic description in Table 3.2 and 3.3.

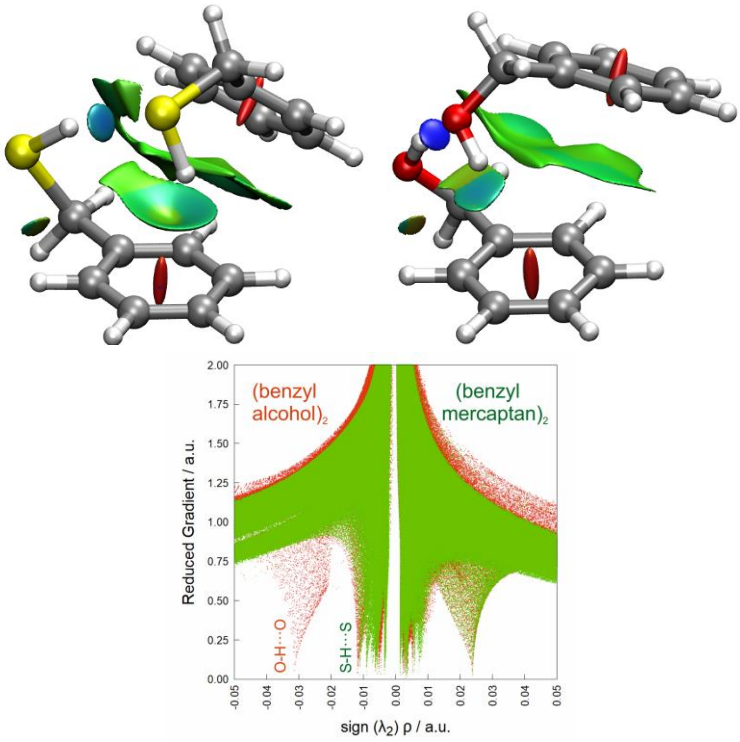

Figure 3.5. NCIplot (upper panel) and reduced electronic density gradient (lower panel). The color scaling used in VMD program is from -2.0 to 2.0, the benzyl mercaptan (left) and benzyl alcohol (right). The reduced electronic density shows the attractive (negative minima) and repulsive (positive minima) interactions in the dimers of benzyl mercaptan (green) and benzyl alcohol (red), with a stronger O-H···O interaction.

The benzyl mercaptan dimer is a model cluster with a primary amphoteric thiol group and a combination of aliphatic proton donors and a π ring acceptor. The methylene pivot between the thiol and the aromatic ring permits some conformational flexibility and a variety of intermolecular forces, generally balancing two cooperative interactions. The rotational spectrum confirmed a single isomer in the gas phase, providing data for comparison between experiment and theory. The observed global

minimum (GG-GG-Lp-) is homochiral and characterized by a leading thiol-thiol (S-H···S) hydrogen bond, in cooperation with a secondary thiol-aromatic (S-H···π) hydrogen bond. Characteristically, this interaction pattern and stereochemistry are coincident with the most stable (hom-O^{g}π-I) benzyl alcohol dimer, stabilized by stronger O-H···O and O-H···π alcohol hydrogen bonds.[41,42] In consequence, the expected reduction in hydrogen bond strength of the thiol group does not affect the conformational equilibrium observed in the alcohol, and the π ring acceptor maintains its secondary role in both dimers. The smaller, more rigid phenol and thiophenol dimers, also observed in the gas phase,[36,66] similarly depend on the S-H···S or O-H···O hydrogen bonds but adopt different hinged or stacked orientations which reflect a different balance with the ring interactions. Since the number of experimental observations is limited additional thiol-alcohol comparisons are presently possible only for a few other aromatic dimers like 2-phenylethanethiol,[29,67] also showing similar thiol-thiol interactions in the global minimum.

The second isomer of the mercaptan dimer (GG-GG-Lp+), separated about 1.9 kJ mol^{-1}, differs in the use of a different sulfur lone-pair in the acceptor molecule but maintains its homochiral character. The equivalent isomer in the alcohol (hom-O^{t}π-V: 3.2 kJ mol^{-1}) is much higher in energy. Consequently, the benzyl mercaptan dimer shows a reinforced preference for homochirality compared to the alcohol, where the heterochiral isomer (het-O^{g}π-II) is nearly isoenergetic (0.2 kJ mol^{-1}) with the (hom-O^{g}π-I) global minimum. Conversely, in the benzyl mercaptan dimer, the heterochiral isomer (G´G´-GG-Lp- ≡ het-O^{g}π-II) is third in energy and more separated (3.3 kJ mol^{-1}) from the homochiral partner.

The fourth and fifth isomers of the benzyl mercaptan dimer do not show thiol-thiol hydrogen bonds, which are replaced by separate thiol interactions to different proton acceptors. These isomers introduce the discussion on the strength of the thiol or alcohol groups as proton acceptors in the presence of competing groups, which has been mostly studied for alcohol dimers with two acceptor groups. In those cases, the observed alcohol-alcohol hydrogen bonding of (benzyl alcohol)$_2$ is confirmed with related aromatic acceptors, as in (indanol)$_2$[68] or (propargyl alcohol)$_2$.[69] However, ethers,[21,70] carbonyl groups[71] or carboxylic acids[72] show preference as primary proton acceptors, more intense in amino[73] or cyano[74] groups. Additionally, when the two thiol/alcohol groups bind separately to secondary acceptors, both homo and heterochiral symmetric geometries become possible. In the benzyl mercaptan dimer, the fourth isomer (GG-GG-ππ, 4.4 kJ mol^{-1}) shows a homochiral C_2 antiparallel geometry stabilized by two S-H···π hydrogen bonds, higher in energy than the equivalent C_2 benzyl alcohol dimer (homππ-IV, 2.0 kJ mol^{-1}) and reminiscent of the antiparallel aniline dimer.[75] However, the

heterochiral C_i benzyl alcohol dimer (hetππ-III, 1.6 kJ mol^{-1}) does not appear among the preferred geometries of the benzyl mercaptan dimer, where the fifth unsymmetric isomer (GG-GG-π, 4.6 kJ mol^{-1}) instead shows a combination of S-H···π and C-H···π interactions.

Differences in the physical forces operating in the benzyl mercaptan and alcohol dimers are notorious in the topological analysis of the electronic density and the SAPT energy decomposition of Table 3.3 and Figure 3.7. The weaker, dispersive character of the thiol dimer thus contributes to a better description of non-covalent forces involving low-electronegativity atoms.

3.4. Conclusions

The conformation landscape of benzyl mercaptan dimer shows that the self-aggregation has a preference on the homodimer, a result which is coincident with the benzyl alcohol dimer. The observation of a single homodimer of benzyl mercaptan using rotational spectroscopy is also supported by the computational calculations, including additional an NCIplot analysis and SAPT calculation. Interaction within the benzyl mercaptan dimer is stabilized not only by S-H···S-H hydrogen bond but also between the S-H to the π orbital from the aromatic ring. Future advances in the understanding of intermolecular forces are expected to extend to different chemical groups, incorporating a synergic combination of empirical data and computational models. In this work, rotational spectroscopy has an increasingly important role thanks to the development of chirped-pulsed broadband techniques.

References

(1) Liu, M.; Zhang, L.; Wang, T. Supramolecular Chirality in Self-Assembled Systems. *Chem. Rev.* **2015**, *115* (15), 7304–7397. https://doi.org/10.1021/cr500671p.

(2) Brandt, J. R.; Salerno, F.; Fuchter, M. J. The Added Value of Small-Molecule Chirality in Technological Applications. *Nat. Rev. Chem.* **2017**, *1*. https://doi.org/10.1038/s41570-017-0045.

(3) Schermann, J.-P. *Spectroscopy and Modeling of Biomolecular Building Blocks*; Elsevier, 2008. https://doi.org/10.1016/B978-0-444-52708-0.X5001-1.

(4) Hobza, P.; Muller-Dethlefs, K. *Non-Covalent Interactions*; Hobza, P., Muller-Dethlefs, K., Eds.; Theoretical and Computational Chemistry Series; Royal Society of Chemistry: Cambridge, 2009. https://doi.org/10.1039/9781847559906.

(5) *Noncovalent Forces*; Scheiner, S., Ed.; Challenges and Advances in Computational Chemistry and Physics; Springer International Publishing: Cham, Switzerland, 2015; Vol. 19. https://doi.org/10.1007/978-3-319-14163-3.

(6) Alkorta, I.; Elguero, J.; Frontera, A. Not Only Hydrogen Bonds: Other Noncovalent Interactions. *Crystals* **2020**, *10* (3). https://doi.org/10.3390/cryst10030180.

(7) Juanes, M.; Saragi, R. T.; Caminati, W.; Lesarri, A. *The Hydrogen Bond and Beyond: Perspectives*

for Rotational Investigations of Non-Covalent Interactions; 2019; Vol. 25, pp 11402–11411. https://doi.org/10.1002/chem.201901113.

(8) Zehnacker, A.; Suhm, M. A. Chirality Recognition between Neutral Molecules in the Gas Phase. *Angew. Chemie Int. Ed.* **2008**, *47* (37), 6970–6992. https://doi.org/10.1002/anie.200800957.

(9) *Chiral Recognition in the Gas Phase*; Zehnacker, A., Ed.; CRC Press: Boca Raton, Florida, 2010.

(10) Pierini, M.; Troiani, A.; Speranza, M.; Piccirillo, S.; Bosman, C.; Toja, D.; Giardini-Guidoni, A. Gas-Phase Enantiodifferentiation of Chiral Molecules: Chiral Recognition of 1-Phenyl-1-Propanol/2-Butanol Clusters by Resonance Enhanced Multiphoton Ionization Spectroscopy. *Angew. Chemie - Int. Ed.* **1997**, *36* (16), 1729–1731. https://doi.org/10.1002/anie.199717291.

(11) Le Barbu, K.; Brenner, V.; Millié, P.; Lahmani, F.; Zehnacker-Rentien, A. An Experimental and Theoretical Study of Jet-Cooled Complexes of Chiral Molecules: The Role of Dispersive Forces in Chiral Discrimination. *J. Phys. Chem. A* **1998**, *102* (1), 128–137. https://doi.org/10.1021/jp972465q.

(12) Borho, N.; Häber, T.; Suhm, M. A. Chiral Self-Recognition in the Gas Phase: The Case of Glycidol Dimers. *Phys. Chem. Chem. Phys.* **2001**, *3* (11), 1945–1948. https://doi.org/10.1039/b102382a.

(13) Caminati, W.; Grabow, J.-U. J.-U. Advancements in Microwave Spectroscopy. In *Frontiers and Advancements in Microwave Spectroscopy*; Laane, J., Ed.; Elsevier: Amsterdam, 2018; pp 569–598. https://doi.org/10.1016/B978-0-12-811220-5.00018-6.

(14) Portmann, S.; Inauen, A.; Lüthi, H. P.; Leutwyler, S. Chiral Discrimination in Hydrogen-Bonded Complexes. *J. Chem. Phys.* **2000**, *113* (21), 9577–9585. https://doi.org/10.1063/1.1321315.

(15) Alkorta, I.; Elguero, J. Discrimination of Hydrogen-Bonded Complexes with Axial Chirality. *J. Chem. Phys.* **2002**, *117* (14), 6463–6468. https://doi.org/10.1063/1.1504710.

(16) Borho, N.; Xu, Y. Tailoring the Key in a Molecular Lock-and-Key Model System: The Propylene Oxide···2-Fluoroethanol Complex. *J. Am. Chem. Soc.* **2008**, *130* (18), 5916–5921. https://doi.org/10.1021/ja0783411.

(17) Hearn, J. P. I.; Cobley, R. V.; Howard, B. J. High-Resolution Spectroscopy of Induced Chiral Dimers: A Study of the Dimers of Ethanol by Fourier Transform Microwave Spectroscopy. *J. Chem. Phys.* **2005**, *123* (13), 1–7. https://doi.org/10.1063/1.2049267.

(18) Loru, D.; Peña, I.; Sanz, M. E. Ethanol Dimer: Observation of Three New Conformers by Broadband Rotational Spectroscopy. *J. Mol. Spectrosc.* **2017**, *335*, 93–101. https://doi.org/10.1016/j.jms.2017.03.007.

(19) Snow, M. S.; Howard, B. J.; Evangelisti, L.; Caminati, W. From Transient to Induced Permanent Chirality in 2-Propanol upon Dimerization: A Rotational Study. *J. Phys. Chem. A* **2011**, *115* (1), 47–51. https://doi.org/10.1021/jp1107944.

(20) King, A. K.; Howard, B. J. A Microwave Study of the Hetero-Chiral Dimer of Butan-2-Ol. *Chem. Phys. Lett.* **2001**, *348* (3–4), 343–349. https://doi.org/10.1016/S0009-2614(01)01121-6.

(21) Maris, A.; Giuliano, B. M.; Bonazzi, D.; Caminati, W. Molecular Recognition of Chiral Conformers: A Rotational Study of the Dimers of Glycidol. *J. Am. Chem. Soc.* **2008**, *130* (42), 13860–13861. https://doi.org/10.1021/ja8057887.

(22) Juanes, M.; Usabiaga, I.; León, I.; Evangelisti, L.; Fernández, J. A.; Lesarri, A. The Six Isomers of the Cyclohexanol Dimer: A Delicate Test for Dispersion Models. *Angew. Chemie Int. Ed.* **2020**, *59* (33), anie.202005063. https://doi.org/10.1002/anie.202005063.

(23) Liu, X.; Borho, N.; Xu, Y. Molecular Self-Recognition: Rotational Spectra of the Dimeric 2-Fluoroethanol Conformers. *Chem. - A Eur. J.* **2009**, *15* (1), 270–277. https://doi.org/10.1002/chem.200802028.

(24) Thomas, J.; Xu, Y. Chirality Synchronization in Trifluoroethanol Dimer Revisited: The Missing Heterochiral Dimer. *J. Phys. Chem. Lett.* **2014**, *5* (11), 1850–1855.

(25) Oswald, S.; Seifert, N. A.; Bohle, F.; Gawrilow, M.; Grimme, S.; Jäger, W.; Xu, Y.; Suhm, M. A. The Chiral Trimer and a Metastable Chiral Dimer of Achiral Hexafluoroisopropanol: A Multi-Messenger Study. *Angew. Chemie - Int. Ed.* **2019**, *58* (15), 5080–5084. https://doi.org/10.1002/anie.201813881.

(26) Bhattacharyya, S.; Wategaonkar, S. ZEKE Photoelectron Spectroscopy of P-

Fluorophenol···H2S/H2O Complexes and Dissociation Energy Measurement Using the Birge-Sponer Extrapolation Method. *J. Phys. Chem. A* **2014**, *118* (40), 9386–9396. https://doi.org/10.1021/jp505393p.

(27) Ghosh, S.; Bhattacharyya, S.; Wategaonkar, S. Dissociation Energies of Sulfur-Centered Hydrogen-Bonded Complexes. *J. Phys. Chem. A* **2015**, *119* (44), 10863–10870. https://doi.org/10.1021/acs.jpca.5b08185.

(28) Martin, D. E.; Robertson, E. G.; Thompson, C. D.; Morrison, R. J. S. Resonant 2-Photon Ionization Study of the Conformation and the Binding of Water Molecules to 2-Phenylethanethiol (PhC H2 C H2 SH). *J. Chem. Phys.* **2008**, *128* (16), 164301. https://doi.org/10.1063/1.2903477.

(29) Lobo, I. A. A.; Robertson, P. A.; Villani, L.; Wilson, D. J. D.; Robertson, E. G.; A. Robertson, P.; Villani, L.; J. D. Wilson, D.; G. Robertson, E. Thiols as Hydrogen Bond Acceptors and Donors: Spectroscopy of 2-Phenylethanethiol Complexes. *J. Phys. Chem. A* **2018**, *122* (36), 7171–7180. https://doi.org/10.1021/acs.jpca.8b06649.

(30) Juanes, M.; Lesarri, A.; Pinacho, R.; Charro, E.; Rubio, J. E.; Enríquez, L.; Jaraíz, M. Sulfur Hydrogen Bonding in Isolated Monohydrates: Furfuryl Mercaptan versus Furfuryl Alcohol. *Chem. – A Eur. J.* **2018**, *24* (25), 6564–6571. https://doi.org/10.1002/CHEM.201705727.

(31) Juanes, M.; Saragi, R. T.; Pinacho, R.; Rubio, J. E.; Lesarri, A. Sulfur Hydrogen Bonding and Internal Dynamics in the Monohydrates of Thenyl Mercaptan and Thenyl Alcohol. *Phys. Chem. Chem. Phys.* **2020**. https://doi.org/10.1039/D0CP01706J.

(32) Wategaonkar, S.; Bhattacherjee, A. N–H···S Interaction Continues To Be an Enigma: Experimental and Computational Investigations of Hydrogen-Bonded Complexes of Benzimidazole with Thioethers. *J. Phys. Chem. A* **2018**, *122* (17), 4313–4321. https://doi.org/10.1021/acs.jpca.8b01943.

(33) Cocinero, E. J.; Sánchez, R.; Blanco, S.; Lesarri, A.; López, J. C.; Alonso, J. L. Weak Hydrogen Bonds C–H···S and C–H···F–C in the Thiirane–Trifluoromethane Dimer. *Chem. Phys. Lett.* **2005**, *402* (1–3), 4–10. https://doi.org/10.1016/j.cplett.2004.11.073.

(34) Ghosh, S.; Chopra, P.; Wategaonkar, S. C-H···S Interaction Exhibits All the Characteristics of Conventional Hydrogen Bonds. *Phys. Chem. Chem. Phys.* **2020**, *22* (31), 17482–17493. https://doi.org/10.1039/d0cp01508c.

(35) Das, A.; Mandal, P. K.; Lovas, F. J.; Medcraft, C.; Walker, N. R.; Arunan, E. The H2S Dimer Is Hydrogen-Bonded: Direct Confirmation from Microwave Spectroscopy. *Angew. Chemie Int. Ed.* **2018**, *57* (46), 15199–15203. https://doi.org/10.1002/anie.201808162.

(36) Saragi, R. T.; Juanes, M.; Pérez, C.; Pinacho, P.; Tikhonov, D. S.; Caminati, W.; Schnell, M.; Lesarri, A.; S. Tikhonov, D.; Caminati, W.; Schnell, M.; Lesarri, A. Switching Hydrogen Bonding to π-Stacking: The Thiophenol Dimer and Trimer. *J. Phys. Chem. Lett.* **2021**, *12* (5), 1367–1373. https://doi.org/10.1021/acs.jpclett.0c03797.

(37) Mishra, K. K.; Borish, K.; Singh, G.; Panwaria, P.; Metya, S.; Madhusudhan, M. S.; Das, A. Observation of an Unusually Large IR Red-Shift in an Unconventional S–H···S Hydrogen-Bond. *J. Phys. Chem. Lett.* **2021**, *12* (4), 1228–1235. https://doi.org/10.1021/ACS.JPCLETT.0C03183.

(38) Bhattacherjee, A.; Matsuda, Y.; Fujii, A.; Wategaonkar, S. Acid-Base Formalism in Dispersion-Stabilized S-H···Y (Y=O, S) Hydrogen-Bonding Interactions. *J. Phys. Chem. A* **2015**, *119* (7), 1117–1126. https://doi.org/10.1021/jp511904a.

(39) Wang, D.; Chopra, P.; Wategaonkar, S.; Fujii, A. Electronic and Infrared Spectroscopy of Benzene-(H2S) n (n = 1 and 2): The Prototype of the SH-ΠInteraction. *J. Phys. Chem. A* **2019**, *123* (33), 7255–7260. https://doi.org/10.1021/acs.jpca.9b02199.

(40) Biswal, H. S.; Bhattacharyya, S.; Bhattacherjee, A.; Wategaonkar, S. Nature and Strength of Sulfur-Centred Hydrogen Bonds: Laser Spectroscopic Investigations in the Gas Phase and Quantum-Chemical Calculations. *Int. Rev. Phys. Chem.* **2015**, *34* (1), 99–160. https://doi.org/10.1080/0144235X.2015.1022946.

(41) Medel, R.; Suhm, M. A. Understanding Benzyl Alcohol Aggregation by Chiral Modification: The Pairing Step. *Phys. Chem. Chem. Phys.* **2020**, *22* (44), 25538–25551. https://doi.org/10.1039/d0cp04825a.

(42) Medel, R.; Camiruaga, A.; Saragi, R. T.; Pinacho, P.; Pérez, C.; Lesarri, A.; Suhm, M. A.; Fernández,

J. A. Rovibronic Signatures of Molecular Aggregation in the Gas Phase: Subtle Homochirality Trends in the Dimer, Trimer and Tetramer of Benzyl Alcohol. *Phys. Chem. Chem. Phys.* **2021**, *submitted*.

(43) Neill, J. L.; Shipman, S. T.; Alvarez-Valtierra, L.; Lesarri, A.; Kisiel, Z.; Pate, B. H. Rotational Spectroscopy of Iodobenzene and Iodobenzene-Neon with a Direct Digital 2-8 GHz Chirped-Pulse Fourier Transform Microwave Spectrometer. *J. Mol. Spectrosc.* **2011**, *269* (1), 21–29. https://doi.org/10.1016/j.jms.2011.04.016.

(44) Shipman, S. T.; Pate, B. H. New Techniques in Microwave Spectroscopy. *Handb. High-resolution Spectrosc.* **2011**. https://doi.org/10.1002/9780470749593.HRS036.

(45) Grabow, J.-U. Fourier Transform Microwave Spectroscopy Measurement and Instrumentation. In *Handbook of High-resolution Spectroscopy*; Quack, M., Merkt, F., Eds.; John Wiley & Sons, Ltd, 2011; pp 724–799.

(46) Halgren, T. A. MMFF VI. MMFF94s Option for Energy Minimization Studies. *J. Comput. Chem.* **1999**, *20* (7), 720–729. https://doi.org/10.1002/(SICI)1096-987X(199905)20:7<720::AID-JCC7>3.0.CO;2-X.

(47) Becke, A. D. Density-Functional Thermochemistry. III. The Role of Exact Exchange. *J. Chem. Phys.* **1993**, *98* (7), 5648–5652. https://doi.org/10.1063/1.464913.

(48) Grimme, S. Semiempirical Hybrid Density Functional with Perturbative Second-Order Correlation. *J. Chem. Phys.* **2006**, *124* (3), 034108. https://doi.org/10.1063/1.2148954.

(49) Weigend, F.; Ahlrichs, R. Balanced Basis Sets of Split Valence, Triple Zeta Valence and Quadruple Zeta Valence Quality for H to Rn: Design and Assessment of Accuracy. *Phys. Chem. Chem. Phys.* **2005**, *7* (18), 3297. https://doi.org/10.1039/b508541a.

(50) Grimme, S.; Ehrlich, S.; Goerigk, L. Effect of the Damping Function in Dispersion Corrected Density Functional Theory. *J. Comput. Chem.* **2011**, *32* (7), 1456–1465. https://doi.org/10.1002/jcc.21759.

(51) Johnson, E. R.; Becke, A. D. A Post-Hartree-Fock Model of Intermolecular Interactions: Inclusion of Higher-Order Corrections. *J. Chem. Phys.* **2006**, *124* (17), 174104. https://doi.org/10.1063/1.2190220.

(52) Boys, S. F.; Bernardi, F. The Calculation of Small Molecular Interactions by the Differences of Separate Total Energies. Some Procedures with Reduced Errors. *Mol. Phys.* **2002**, *100* (1), 65–73. https://doi.org/10.1080/00268970110088901.

(53) Frisch, M. J.; Trucks, G. W.; Schlegel, H. B.; Scuseria, G. E.; Robb, M. A.; Cheeseman, J. R.; Scalmani, G.; Barone, V.; Petersson, G. A.; Nakatsuji, H.; Li, X.; Caricato, M.; Marenich, A. V.; Bloino, J.; Janesko, B. G.; Gomperts, R.; Mennucci, B.; Hratchian, H. P.; Ortiz, J. V.; Izmaylov, A. F.; Sonnenberg, J. L.; Williams; Ding, F.; Lipparini, F.; Egidi, F.; Goings, J.; Peng, B.; Petrone, A.; Henderson, T.; Ranasinghe, D.; Zakrzewski, V. G.; Gao, J.; Rega, N.; Zheng, G.; Liang, W.; Hada, M.; Ehara, M.; Toyota, K.; Fukuda, R.; Hasegawa, J.; Ishida, M.; Nakajima, T.; Honda, Y.; Kitao, O.; Nakai, H.; Vreven, T.; Throssell, K.; Montgomery Jr., J. A.; Peralta, J. E.; Ogliaro, F.; Bearpark, M. J.; Heyd, J. J.; Brothers, E. N.; Kudin, K. N.; Staroverov, V. N.; Keith, T. A.; Kobayashi, R.; Normand, J.; Raghavachari, K.; Rendell, A. P.; Burant, J. C.; Iyengar, S. S.; Tomasi, J.; Cossi, M.; Millam, J. M.; Klene, M.; Adamo, C.; Cammi, R.; Ochterski, J. W.; Martin, R. L.; Morokuma, K.; Farkas, O.; Foresman, J. B.; Fox, D. J. Gaussian 16, Rev. C.01. Gaussian, Inc: Wallingford CT 2016.

(54) Jeziorski, B.; Moszynski, R.; Szalewicz, K. Perturbation Theory Approach to Intermolecular Potential Energy Surfaces of van Der Waals Complexes. *Chem. Rev.* **1994**, *94* (7), 1887–1930. https://doi.org/10.1021/cr00031a008.

(55) Scheiner, S. *Hydrogen Bonding. A Theoretical Perspective*; Oxford University Press: Oxford, 1997.

(56) Parrish, R. M.; Burns, L. A.; Smith, D. G. A.; Simmonett, A. C.; DePrince, A. E.; Hohenstein, E. G.; Bozkaya, U.; Sokolov, A. Y.; Di Remigio, R.; Richard, R. M.; Gonthier, J. F.; James, A. M.; McAlexander, H. R.; Kumar, A.; Saitow, M.; Wang, X.; Pritchard, B. P.; Verma, P.; Schaefer, H. F.; Patkowski, K.; King, R. A.; Valeev, E. F.; Evangelista, F. A.; Turney, J. M.; Crawford, T. D.; Sherrill, C. D. Psi4 1.1: An Open-Source Electronic Structure Program Emphasizing Automation, Advanced Libraries, and Interoperability. *J. Chem. Theory Comput.* **2017**, *13* (7), 3185–3197.

https://doi.org/10.1021/acs.jctc.7b00174.

(57) Johnson, E. R.; Keinan, S.; Mori-Sánchez, P.; Contreras-García, J.; Cohen, A. J.; Yang, W. Revealing Noncovalent Interactions. *J. Am. Chem. Soc.* **2010**, *132* (18), 6498–6506. https://doi.org/10.1021/ja100936w.

(58) Utzat, K. A.; Bohn, R. K.; Montgomery, J. A.; Michels, H. H.; Caminati, W. Rotational Spectrum, Tunneling Motions, and Potential Barriers of Benzyl Alcohol. *J. Phys. Chem. A* **2010**, *114* (25), 6913–6916. https://doi.org/10.1021/jp102903p.

(59) Papousek, D.; Aliev, M. R. *Molecular Vibrational-Rotational Spectra - Studies in Physical and Theoretical Chemistry 17*; Elsevier: Amsterdam, 1982.

(60) Nayak, S. K.; Sathishkumar, R.; Row, T. N. G. Directing Role of Functional Groups in Selective Generation of C-H···π Interactions: In Situ Cryo-Crystallographic Studies on Benzyl Derivatives. *CrystEngComm* **2010**, *12* (10), 3112–3118. https://doi.org/10.1039/c001190h.

(61) Watson, J. K. G. Aspects of Quartic and Sextic Centrifugal Effects on Rotational Energy Levels. In *Vibrational Spectra and Structure, vol. 6*; Durig, J. R., Ed.; Elsevier B.V.: Amsterdam, 1977; pp 1–89.

(62) Godfrey, P. D.; Brown, R. D. Proportions of Species Observed in Jet Spectroscopy-Vibrational-Energy Effects: Histamine Tautomers and Conformers. *J. Am. Chem. Soc.* **1998**, *120* (41), 10724–10732. https://doi.org/10.1021/ja980560m.

(63) Florio, G. M.; Christie, R. A.; Jordan, K. D.; Zwier, T. S. Conformational Preferences of Jet-Cooled Melatonin: Probing Trans- and Cis-Amide Regions of the Potential Energy Surface. *J. Am. Chem. Soc.* **2002**, *124* (34), 10236–10247. https://doi.org/10.1021/ja0265916.

(64) Lesarri, A.; Pinacho, R.; Enríquez, L.; Rubio, J. E.; Jaraíz, M.; Abad, J. L.; Gigosos, M. A. Rotational Spectra of Tetracyclic Quinolizidine Alkaloids: Does a Water Molecule Flip Sparteine? *Phys. Chem. Chem. Phys.* **2017**, *19* (27), 17553–17559. https://doi.org/10.1039/c7cp01432e.

(65) Zhou, P.; Tian, F.; Lv, F.; Shang, Z. Geometric Characteristics of Hydrogen Bonds Involving Sulfur Atoms in Proteins. *Proteins Struct. Funct. Bioinforma.* **2009**, *76* (1), 151–163. https://doi.org/10.1002/prot.22327.

(66) Seifert, N. A.; Steber, A. L.; Neill, J. L.; Pérez, C.; Zaleski, D. P.; Pate, B. H.; Lesarri, A. The Interplay of Hydrogen Bonding and Dispersion in Phenol Dimer and Trimer: Structures from Broadband Rotational Spectroscopy. *Phys. Chem. Chem. Phys.* **2013**, *15* (27), 11468–11477. https://doi.org/10.1039/c3cp51725j.

(67) Mons, M.; Robertson, E. G.; Simons, J. P. Intra- and Intermolecular π-Type Hydrogen Bonding in Aryl Alcohols: UV and IR–UV Ion Dip Spectroscopy. *J. Phys. Chem. A* **2000**, *104* (7), 1430–1437. https://doi.org/10.1021/jp993178k.

(68) Altnöder, J.; Bouchet, A.; Lee, J. J.; Otto, K. E.; Suhm, M. A.; Zehnacker-Rentien, A. Chirality-Dependent Balance between Hydrogen Bonding and London Dispersion in Isolated (±)-1-Indanol Clusters. *Phys. Chem. Chem. Phys.* **2013**, *15* (25), 10167–10180. https://doi.org/10.1039/c3cp50708d.

(69) Mani, D.; Arunan, E. Rotational Spectra of Propargyl Alcohol Dimer: A Dimer Bound with Three Different Types of Hydrogen Bonds. *J. Chem. Phys.* **2014**, *141* (16), 164311. https://doi.org/10.1063/1.4898378.

(70) Longarte, A.; Redondo, C.; Fernández, J. A.; Castaño, F. IR/UV and UV/UV Double-Resonance Study of Guaiacol and Eugenol Dimers. *J. Chem. Phys.* **2005**, *122* (16), 164304. https://doi.org/10.1063/1.1881232.

(71) Altnöder, J.; Lee, J. J.; Otto, K. E.; Suhm, M. A. Molecular Recognition in Glycolaldehyde, the Simplest Sugar: Two Isolated Hydrogen Bonds Win Over One Cooperative Pair. *ChemistryOpen* **2012**, *1* (6), 269–275. https://doi.org/10.1002/open.201200031.

(72) Evangelisti, L.; Spada, L.; Li, W.; Vazart, F.; Barone, V.; Caminati, W. The Borderline between Reactivity and Pre-Reactivity of Binary Mixtures of Gaseous Carboxylic Acids and Alcohols. *Angew. Chemie - Int. Ed.* **2017**, *56* (14), 3872–3875. https://doi.org/10.1002/anie.201612231.

(73) Asselin, P.; Madebène, B.; Soulard, P.; Georges, R.; Goubet, M.; Huet, T. R.; Pirali, O.; Zehnacker-Rentien, A. Competition between Inter- and Intra-Molecular Hydrogen Bonding: An Infrared Spectroscopic Study of Jet-Cooled Amino-Ethanol and Its Dimer. *J. Chem. Phys.* **2016**, *145* (22),

224313. https://doi.org/10.1063/1.4972016.
(74) Seurre, N.; Le Barbu-Debus, K.; Lahmani, F.; Zehnacker-Rentien, A.; Sepioł, J. Electronic and Vibrational Spectroscopy of Jet-Cooled m-Cyanophenol and Its Dimer: Laser-Induced Fluorescence and Fluorescence-Dip IR Spectra in the S0 and S1 States. *Chem. Phys.* **2003**, *295* (1), 21–33. https://doi.org/10.1016/j.chemphys.2003.07.009.
(75) Pérez, C.; León, I.; Lesarri, A.; Pate, B. H.; Martínez, R.; Millán, J.; Fernández, J. A. Isomerism of the Aniline Trimer. *Angew. Chemie - Int. Ed.* **2018**, *57* (46), 15112–15116. https://doi.org/10.1002/anie.201808602.

Chapter 4.
The 2-Phenethyl Mercaptan Dimer

In this chapter, we present a structural analysis of the dimers of 2-phenethyl mercaptan and 2-phenethyl alcohol. This investigation extends the previous studies of Chapters 2 and 3, adding a two-carbon aliphatic spacer in between the aromatic group and the thiol or alcohol groups. The larger spacer produces more complicated conformational landscapes for the dimer. The contents of this chapter are presently in publication.

4.1. Introduction

Microwave spectroscopy has successfully been applied to the structural investigation of a large number of polar molecules in the gas phase.[1–3] In combination with supersonic jet expansions and computational methods, it provides an efficient method for the generation and characterization of intermolecular complexes, informing on the conformational landscapes, molecular geometries, relative energies, and nature of the intra- and intermolecular interactions. The studies on non-covalent interactions have mostly addressed microsolvation adducts, often stabilized by hydroxyl O-H···O hydrogen bonds,[4] and a smaller number of aggregates, normally in molecular sizes between dimers and tetramers. In order to extend both the range of molecular sizes and hydrogen bonds analysed rotationally we have examined in this thesis a series of progressively larger thiol homodimers, which have been compared to their alcohol counterparts. One of the most relevant series is the aromatic thiol aggregates, where the π-electron system may engage in several competing non-covalent interactions. At the same time, the capacity of the aromatic ring to act as an electronic chromophore permits comparative studies with electronic and vibrational spectroscopy. Following the previous studies of the dimers of thiophenol and benzyl mercaptan we decided to analyse aromatic molecules with a 2-carbon aliphatic skeleton, specifically 2-phenethyl mercaptan and 2-phenethyl alcohol. Previous spectroscopy studies were available for

both compounds, but only concerning the monomer and the monohydrates. 2-Phenethyl alcohol[5–9] has been studied using laser-induced fluorescence, resonance-enhanced two-photon ionization,[5] UV-UV and IR-UV double-resonance,[10] and millimeter-wave spectroscopy.[6,7] These experiments confirmed the observation of two conformations of the monomer and a single alcohol monohydrate, with water preferentially acting as a proton acceptor, as in phenol-water.[11] 2-Phenethyl mercaptan was studied only with laser spectroscopy techniques,[12,13] reporting two isomers for the monomer and a single water dimer, where water adopts a different proton donor behavior to the thiol group. This observation is consistent with previous experiments, where sulfur is generally observed to be a much better hydrogen bond acceptor than donor.[14,15]The need to study sulfur-centered hydrogen bonds is also obvious from a biochemical point of view, since sulfur is an essential element in many biomolecules and biochemical processes.

In this chapter, we explore the role of the thiol and alcohol groups in the dimerization process of 2-phenethyl mercaptan and 2-phenethyl alcohol, the influence of the length of the alkyl chain, and the balance of intermolecular interactions involving the aromatic ring. This study is justified to examine if the larger aliphatic spacer produces changes in the hydrogen bonds at the oxygen and sulfur centers and, in particular, at which point the proton donor character of phenol-water could be reverted to proton acceptor by a larger carbon chain, as observed in aliphatic alcohols. At the same time, we were interested to check whether a longer aliphatic chain may increase the number of observable isomers of the dimer.

4.2. Methods

The rotational spectra were collected using a chirped-pulse Fourier transform microwave (CP-FTMW) spectrometer working in the frequency region 2-8 GHz. The sample of 2-phenethyl mercaptan was vaporized at 45-50°C, while a higher temperature of 100°C was required for 2-phenethyl alcohol. The sample vapor was pressurized with an inert carrier gas (neon, 2 bar) and expanded supersonically through a circular nozzle (ϕ =0.8 mm), forming a pulsed molecular jet inside a high-vacuum chamber (ultimate pressure 10^{-7} mbar). The time-domain transient experiment recorded the free-induction decay following a short (1 μs) broadband chirped-pulse excitation. A Fourier transformation produced the frequency domain spectrum. The uncertainty of the frequency measurements was estimated to be better than 20 kHz. The samples were purchased commercially and used without any further purification.

The experiment was supported with several computational calculations. A conformational search is initially done using a molecular mechanics method (MMFFs[16]), in order to obtain a large number of starting structures. Geometry optimization was then

performed on each conformer using DFT (B3LYP, B2PLYP) and ab-initio (MP2). The density functional theory method was tested using B3LYP,[17] supplemented with D3 dispersion corrections and Becke-Johnson damping.[18,19] The computational models used def2-TZVP as the basis set.[20] Frequency calculations were performed using the harmonic approximation at the same level of theory. The interaction energies were calculated considering the basis set superposition errors (BSSE).[21] All calculations were performed using Gaussian 16.[22] The presence of non-covalent interaction was analysed using the NCIplot method, based on a reduced gradient of electronic density.[23,24] The physical contributions to the binding potential of the water clusters were estimated by energy decomposition analysis using second-order symmetry adapted perturbation theory[25,26] (SAPT), implemented in PSI4.[27] More information could be found in the Appendix (Table S4.1-S4.14).

4.3. Results and Discussions

4.3.1. Mercaptan and alcohol monomers

The internal rotors of 2-phenethyl mercaptan and 2-phenethyl alcohol generate a three-dimensional (3D) potential energy surface. In previous studies, five isomers have been predicted for both monomers using various computational methods, ranging from B3LYP to the CCSD level of theory.[5–9,12,13] All stable conformations share a nearly perpendicular orientation of the C_β atom ($\tau_1(C_{ortho}C_{ipso}\text{-}C_\alpha C_\beta)\sim90°$). This situation is similar to ethylbenzene,[28–30] while benzyl mercaptan[31] and benzyl alcohol[32] exhibit large-amplitude torsional motions more deviated from perpendicularity. The isomers are then divided into two groups, either *gauche* (G) or *anti* (A), depending on the position of the thiol/alcohol group with respect to the aromatic ring, i.e., the dihedral $\tau_2(C_{ipso}C_\alpha\text{-}C_\beta\mathbf{X}$, **X**= O, S). A second g/t indicator specifies the orientation of the terminal thiol/alcohol hydrogen atom, i.e., $\tau_3(C_\alpha C_\beta\text{-}\mathbf{X}H$, **X**= O, S). Following the previous notation,[9,12,13] the two non-equivalent *gauche-gauche* conformations are denoted as Ggπ or Gg, depending on whether the thiol/alcohol atom points towards or outside the ring, respectively. Conversely, the two Ag *anti-gauche* conformations are degenerate. The additional consideration of the *gauche-anti* and *anti-anti* cases produces the five most stable isomers of Figure 4.1.

The global minimum for the alcohol and the thiol is the Ggπ conformer, which may benefit from an intramolecular **X**-H···π (**X**= O, S) hydrogen bond to the ring. However, the conformational landscape of the two molecules is not the same. In the alcohol,[5] the calculated relative energies (B3LYP-D3(BJ)/def2-TZVP, ZPE corrected) point to the Ag conformer (5.3 kJ mol^{-1}) as the second more stable, followed by At (5.4 kJ mol^{-1}, C_s symmetry), Gt (6.7 kJ mol^{-1}), and Gg (8.0 kJ mol^{-1}). This calculation contrasts with the

experimental observations from the rotational spectrum of the alcohol, which detected two conformers, Ggπ and At.[8,9]

For phenethyl mercaptan the global minimum is still predicted to be Ggπ at the B3LYP-D3(BJ)/def2-TZVP level (ZPE corrected), with conformer Ag (2.8 kJ mol^{-1}) closer in energy than in the alcohol. The next conformers have a different ordering, and Gg (5.0 kJ mol^{-1}) becomes more stable than At (5.7 kJ mol^{-1}) and Gt (7.4 kJ mol^{-1}). A comparative NCIPlot analysis of benzyl mercaptan and 2-phenethyl mercaptan in Figure 4.2 confirmed that the larger sidechain of the latter permits an S-H···π interaction in isomer GGπ, as expected from chemical arguments.

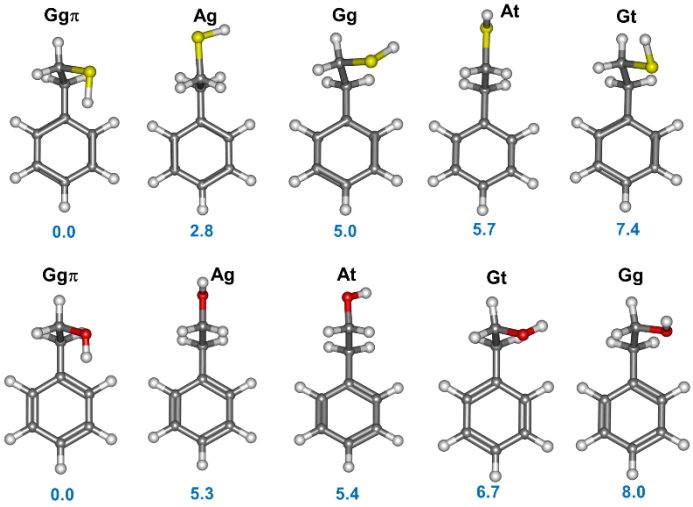

Figure 4.1. The conformations of 2-phenethyl mercaptan monomers with their relative energy values (ZPE-corrected) in kJ mol^{-1} (B3LYP-D3(BJ)/def2TZVP).

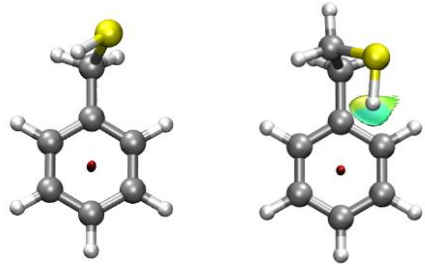

Figure 4.2. The comparison of NCIplot of the most stable conformation of benzyl mercaptan GG (left) and 2-phenethyl mercaptan Ggπ (right), computed at B3LYP-D3(BJ)/def2TZVP. 2-Phenetyl mercarptan Ggπ shows the SH···π interaction.

There were no previous studies of the rotational spectrum for 2-phenethyl mercaptan, so the monomer was first investigated. Figure 4.3 shows the microwave spectrum of the thiol in the 2-8 GHz frequency range, for which two isomers were soon identified. A set of intense μ_a- and μ_b-type transitions, together with a smaller set of weaker μ_c-type lines were assigned as isomer Ggπ. All ^{13}C and ^{34}S monosubstituted isotopologues were detected in natural abundance (1% and 4%) so that a structural analysis was possible using the effective (r_0) and substitution (r_s) methods, Figure S4.1 (Appendix).

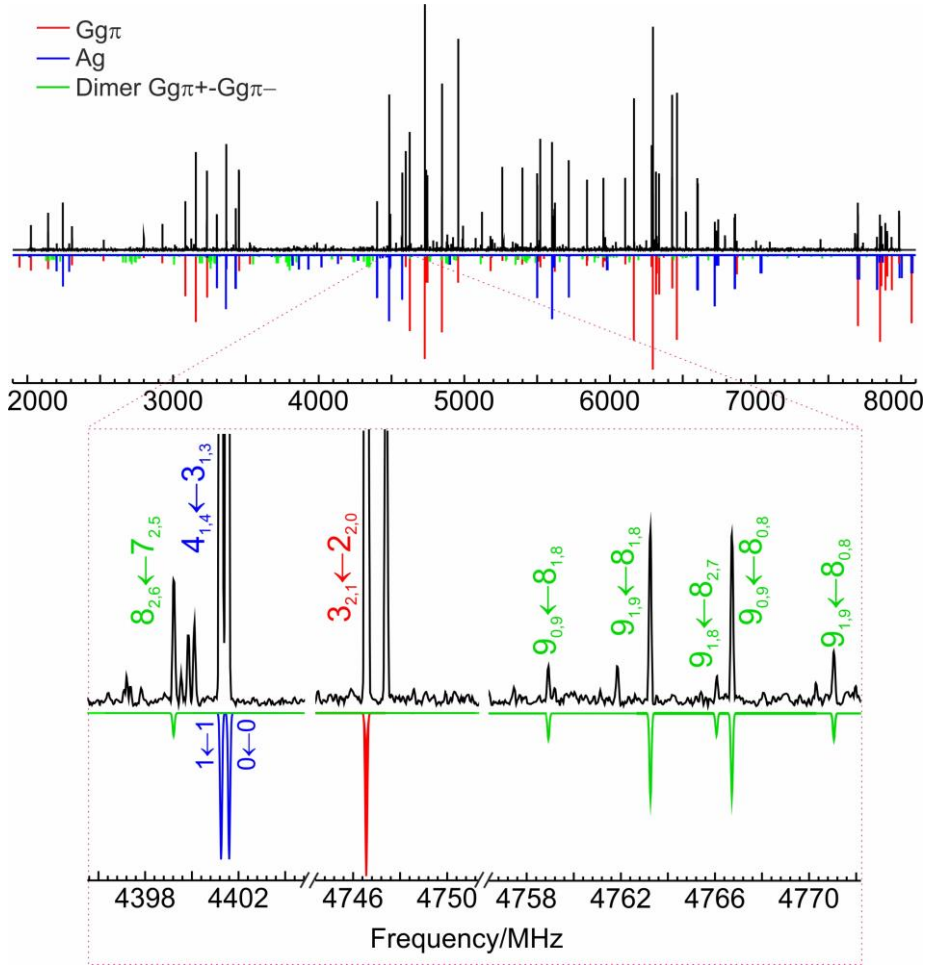

Figure 4.3. The rotational spectrum of 2-phenethyl mercaptan in 2-8 GHz frequency region (upper panel). The positive traces show the experimental spectrum; the negative traces are the simulation of fitted rotational constants of the monomers and the Ggπ+ Ggπ- dimer, based on the fit of Tables 4.1 and 4.2. The lower panel also illustrates the doublets in the Ag monomer due to the tunnelling motion of the thiol group.

A second isomer was later assigned in the spectrum. In this isomer, the μ_a- and μ_b-type transitions occur as doublets due to the tunnelling motion of the thiol group, consistent with the assignment of isomer Ag. The spectra of the two isomers were fitted to a Watson's (S-reduced) semi-rigid-rotor Hamiltonian,[33] implemented in Pickett's SPFIT program. For isomer Ag, the transitions were fitted independently for each state. The comparison between the experimental and theoretical results for the observed monomers of 2-phenethyl mercaptan is presented in Table 4.1. No other species were detected, which may be attributed to a conformational relaxation of the higher energy species to the global minimum through small potential barriers. The potential for the torsion around the $C_{ipso}C_\alpha$-$C_\beta X$ dihedral is presented in Figure S4.2-S4.3 (Appendix).[6]

Table 4.1. Rotational parameters of the 2-phenethyl mercaptan monomer.

	Experiment			Theory [h]	
	Isomer 1	Isomer 2		Ggπ	Ag
		v=0	v=1		
A / MHz [a]	2700.35422(56) [f]	4349.4(24)	4361.3(23)	2712.2	4389.1
B / MHz	826.62097(11)	582.7995(18)	582.8054(15)	830.8	582.0
C / MHz	752.72166(12)	539.3987(19)	539.3954(14)	750.4	539.3
D_J / kHz	0.2056(11)	0.080(14)	0.080(14)	0.169	0.022
D_{JK} / kHz [b]	-0.0340(70)	0.931(59)	0.931(59)	2.194	1.158
D_K / kHz	1.560(88)	[0.] [g]	[0.]	-0.912	0.639
d_1 / kHz	0.00360(18)	[0.]	[0.]	-0.024	-0.002
d_2 / kHz	-0.009760(72)	[0.]	[0.]	0.018	0.002
σ / kHz [c]	3.8	18.7	19.3		
N	93	38	38		
μ_a / D [d]				1.0	1.4
μ_b / D				1.2	0.6
μ_c / D				0.2	0.1
ΔE_{ZPE} / kJ mol^{-1} [e]				0	2.8
ΔG / kJ mol^{-1}				0	1.1

[a]Rotational constants for the first two torsional sub-states (A, B, C). [b]Watson's S-reduction centrifugal distortion constants (D_J, D_{JK}, D_K, d_1, d_2). [c]Standard error of the fit (σ) and number of measured transitions (N). [d]Electric dipole moments. [e]Electronic and Gibbs energy (298 K, 1 atm). [f]Standard errors in parentheses in units of the last digit. [g]Fixed to zero. [h]B3LYP-D3(BJ)/def2-TZVP.

4.3.2. 2-Phenethyl mercaptan dimer

Compared to benzyl mercaptan, 2-phenethyl mercaptan has one extra methylene group and one additional degree of freedom, making the 3D PES much different *a priori*. However, we can also expect that despite the larger number of possible orientations for the ethanethiol chain, the most stable dimers may contain preferentially the observed monomers Ggπ and Ag. Both structures display transient chirality, i.e., the monomers interconvert between two equivalent mirror images by relatively low stereomutation

barriers (B3LYP-D3(BJ): 30.4 kJ mol^{-1} and 45.1 kJ mol^{-1} for the alcohol and thiol, respectively). While this unimolecular process has short (nsec) lifetimes which make them indistinguishable, the formation of the homodimers will freeze the diastereoisomers in either homochiral or heterochiral forms. Figure 4.4 shows the two enantiomers of conformer Ggπ, denoted Ggπ– or Ggπ+ attending to the thiol dihedral τ_3($C_\beta C_\alpha$-SH). A lower barrier is expected for the interconversion between Ag– and Ag+, which proceeds by a single alcohol/thiol torsion

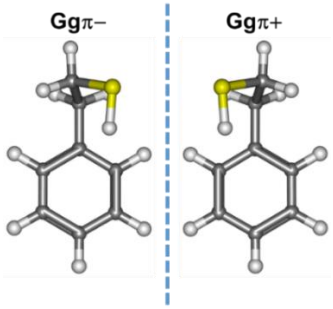

Figure 4.4. The most stable Ggπ– isomer of 2-PEM and its enantiomer Ggπ+.

Following a preliminary structural screening using molecular mechanics, a DFT conformational search (B3LYP-D3(BJ)/def2-TZVP) found eight isomers of the 2-phenethyl mercaptan dimer below 10 kJ mol^{-1}. The predicted structures are classified according to their intermolecular interactions in Figure 4.5. The adopted notation is based on the structure of the subunits, starting with the proton donor, proton acceptor, and the acceptor lone pair (Lp+/- depending on the dihedral LpS-$C_\alpha C_\beta$).

Characteristically, six of the eight most stable structures are based on Ggπ+ conformations for both monomers. For the two remaining isomers, one of the components is in the Ag conformation. The most stable heterochiral isomer (Ggπ+ Ggπ–Lp-) displays an S-H···S hydrogen bond, which is the primary interaction for most of the dimers. However, the isomers differ in the secondary interactions. For the global minimum, the S-H···S link is assisted by S-H···π, C(sp^2)-H···π and C(sp^3)-H···S interactions. The second and third isomers are nearly isoenergetic (ΔE_{ZPE} = 3.8-3.9 kJ mol^{-1}) but present quite different interaction patterns. The second isomer is a C_2-symmetric GGπ–GGπ– homodimer, where the two subunits are facing each other, avoiding the S-H···S interaction. This structure is stabilized by S-H···π and C(sp^3)-H···S interactions. Conversely, the third isomer GGπ+GGπ–Lp– is quite similar to the global minimum, mostly differing in a reorientation of the aromatic ring and the use of S-H···S, S-H···π, and C(sp^2)-H··· π interactions. Isomers 4, 5, and 7 (3.8-7.7 kJ mol^{-1}) represent different variations of the main S-H···S pattern. In particular, isomer 4 is the homodimer

equivalent to isomer 3. Finally, isomers 6 (5.4 kJ mol^{-1}) and 8 (9.6 kJ mol^{-1}) differ in the use of one Ag subunit as a proton donor. Isomer 6 is controlled by S-H···S, C-H···S, and C-H···π interactions, avoiding an S-H···π contact. The S-H···π interaction is also absent in isomer 8, based in C(sp^2)-H···π and C(sp^3)-H···π interactions.

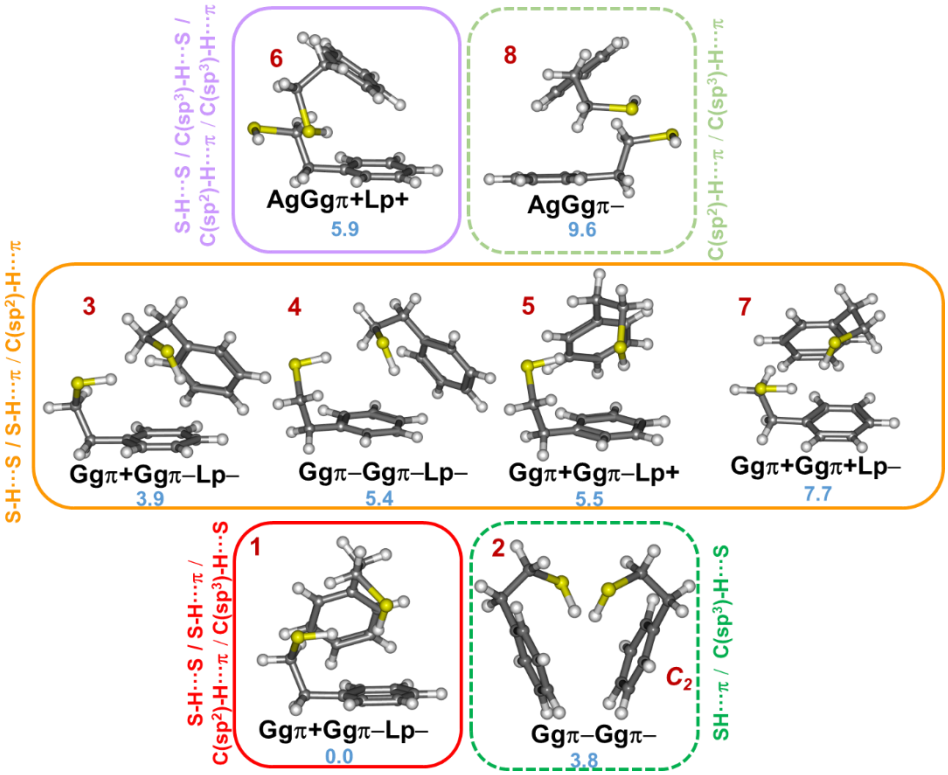

Figure 4.5 The most stable isomers of the 2-phenethyl mercaptan dimer, classified by their intermolecular interactions. The numbers in red show the stability order according to the electronic energies (ΔE_{ZPE}, kJ mol^{-1}, in blue) calculated at B3LYP-D3(BJ)/def2-TZVP level. Isomers in the dashed rectangle do not exhibit a sulfur S-H···S hydrogen bond. The only symmetric isomer is isomer 2 (C_2).

The predictions for the thiol dimer were compared to the experimental microwave spectrum in Figure 4.3. This spectral analysis revealed a single isomer for the phenethyl mercaptan dimer, characterized by a semi-rigid rotor behaviour and absence of tunnelling effects. The wide range of angular momentum quantum numbers (J=3-15 and K_{-1}<12) and large dataset of more than 280 μ_a-, μ_b-, and μ_c-type transitions ensured an unambiguous and satisfactory fit to experimental accuracy. The results of the fit to a Watson's (S-reduced) semi-rigid rotor Hamiltonian[33] up to quartic centrifugal distortion

terms are presented in Table 4.2 and Table S4.1 (Appendix). Rotational parameters using B2PLYP-D3(BJ) and MP2 methods can be found in Table S4.2-S4.3 (Appendix).

Table 4.2. Rotational parameters of the 2-phenethyl mercaptan dimer.

	Experiment	Theory		
Isomer		1 (GGπ+GGπ–Lp–)	2 (C_2) (GGπ–GGπ–)	3 (GGπ+GGπ–Lp–)
A / MHz [a]	390.86720(30)	394.9[e]	403.5	481.9
B / MHz	279.72785(19)	288.2	289.4	244.4
C / MHz	262.05574(21)	267.0	269.5	214.1
D_J / kHz [d]	0.02677(61)	0.017	0.024	0.034
D_{JK} / kHz	0.1007(20)	0.076	0.143	-0.152
D_K / kHz	-0.1020(32)	-0.077	-0.137	0.409
d_1 / kHz	0.00434(49)	0.002	-0.003	-0.003
d_2 / kHz	-0.00142(22)	-0.002	-0.001	0.000
$\lvert\mu_a\rvert$ / D	Detected	1.8	0.0	1.7
$\lvert\mu_b\rvert$ / D	Detected	0.9	0.2	0.9
$\lvert\mu_c\rvert$ / D	Detected	1.1	0.1	1.8
HBond donor [b]				
HS–$C_\beta C_\alpha$ / deg		-69.5	71.2	-67.4
SC_β–$C_\alpha C_{ipso}$ / deg		67.3	-61.1	67.0
$C_\beta C_\alpha$-$C_{ipso}C_{ortho}$ / deg		74.4	86.0	-77.7
HBond acceptor				
HS–$C_\beta C_\alpha$ / deg		67.0	65.3	69.4
SC_β–$C_\alpha C_{ipso}$ / deg		-59.7	-58.7	-74.2
$C_\beta C_\alpha$-$C_{ipso}C_{ortho}$ / deg		-81.3	74.6	84.2
r(S···H) / Å		2.668	-	2.621
∠(S–H···S) / deg		151.1	-	157.0
r(S–H···centroid) / Å		2.596	2.695 3.157	2.612
r(C–H···centroid) / Å		2.994	-	2.693
r(C-H···S) / Å		2.957	-	-
ΔE_{ZPE}/ kJ mol^{-1} [c]		0.0	3.8	3.9
ΔG / kJ mol^{-1}		0.0	0.6	2.2
E_c / kJ mol^{-1} [j]		-45.1	-37.7	-38.6
ΔE_c / kJ mol^{-1}		0.0	7.4	6.4
N [d]	289			
σ / kHz	11.6			

[a]Parameter definition as in Table 4.1. [b]Structural parameters of the dimer. [c]Relative electronic energy (ΔE_{ZPE}), Gibbs energy (ΔG), complexation energy (E_c), and relative complexation energies (ΔE_c). [d]Number of fitted transitions (N) and standard deviation of the fit (σ). [e]B3LYP-D3(BJ)/def2-TZVP.

The comparison of experiment and theory in Table 4.2 clearly pointed to the identification of the heterodimer isomer GGπ+-GGπ–Lp– of the 2-phenethyl mercaptan dimer, predicted as the global minimum. Isomers 2 and 3 are not far in energy (<3.9 kJ mol^{-1}), but they could be affected by low dipole moments in case of isomer 2 (μ_b<0.2 D) or by plausible relaxation mechanisms to the global minimum in case of isomer 3.

4.3.3. 2-Phenethyl alcohol dimer

A similar procedure was followed for the investigation of the 2-phenethyl alcohol dimer, but it was anticipated that the different nature and strength of the alcohol-to-alcohol and alcohol-to-ring interactions could change the PES considerably. The results of the B3LYP-D3(BJ) conformational search are shown in Figure 4.6 and Table S4.4 (Appendix), with isomers denoted I to X. The most stable dimers contain possible combinations of the most stable Ggπ monomer conformation. For the higher-energy species, other Gg or Gt *gauche* species are predicted, while the At conformation only appears at the highest electronic energies (> 10 kJ mol^{-1}). The three lowest-lying dimers (I, II, III) are stabilized by a combination of O-H···O and O-H···π hydrogen bonds, assisted by weaker C(sp^2)-H···π interactions. However, the three structures differ only in the chirality of the monomers or the position of the acceptor lone pair and show small

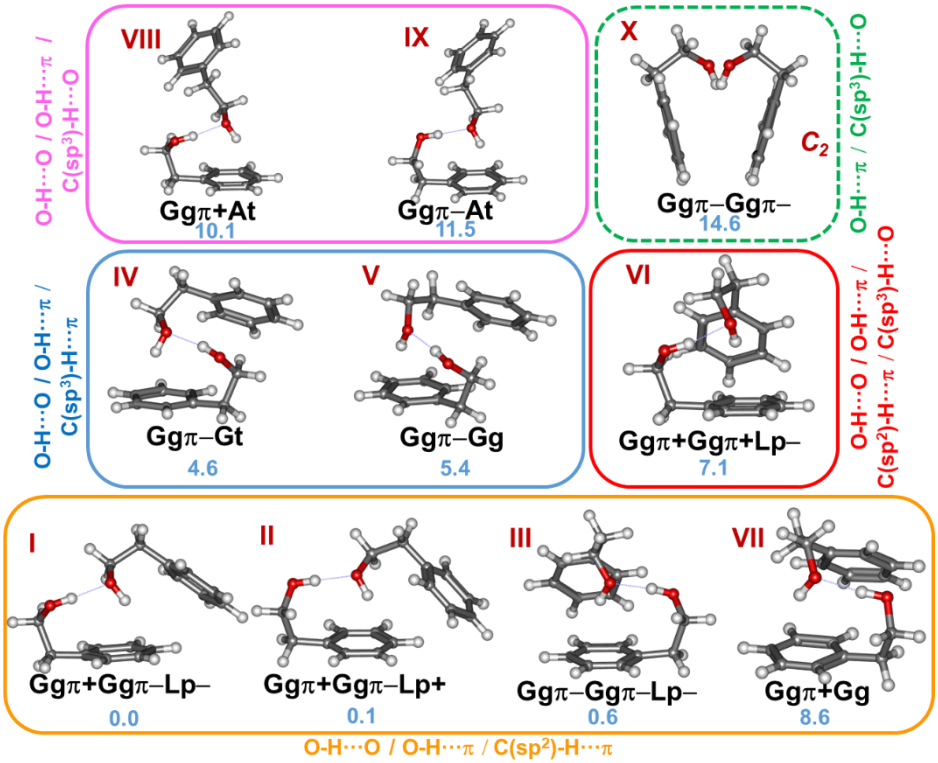

Figure 4.6. The most stable isomers of the 2-phenethyl alcohol dimer, ordered by their relative electronic energy (ΔE_{ZPE}, kJ mol^{-1}, in blue) calculated at the B3LYP-D3(BJ)/def2-TZVP level. The only symmetric isomer is isomer X (C_2), which does not exhibit an O-H···O hydrogen bond.

energy differences well below the estimated calculation errors (ΔE_{ZPE} = 0.1-0.6 kJ mol^{-1}). In these conditions, the identification as the global minimum of the heterochiral Ggπ+Ggπ–Lp– isomer I or its close variants Ggπ+Ggπ–Lp+ (II) or Ggπ–Ggπ–Lp– (III) is ambiguous, and the experiment is required to indicate the conformational stability of the dimer. Other families of dimers (IV, V, VI: 4.6-7.1 kJ mol^{-1}) maintain the O-H···O and O-H···π hydrogen bonds but supported by C(sp^3)-H···π interactions. The two isomers based on At monomers (VIII-IX: 10.1-11.5 kJ mol^{-1}) and the only C_2-symmetric structure are predicted quite higher in energy (14.6 kJ mol^{-1}).

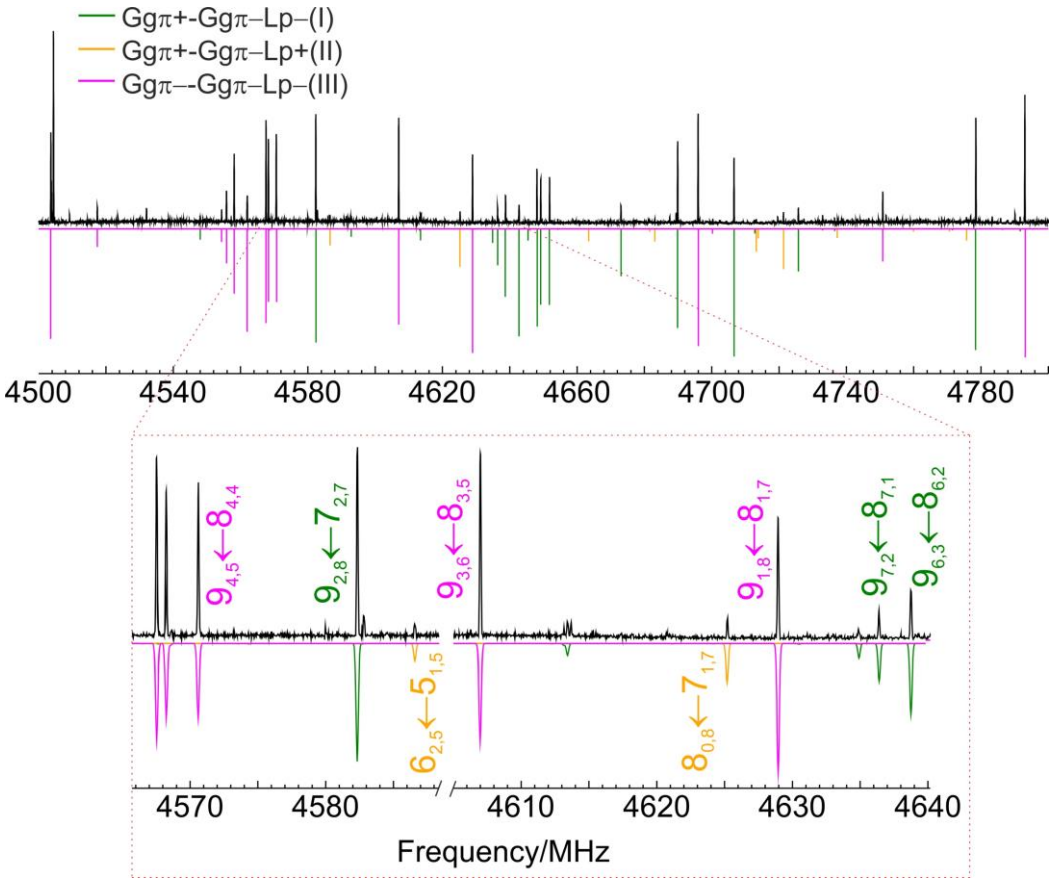

Figure 4.7. Two short sections of 300 MHz (upper panel) and 70 MHz (lower panel) of the rotational spectrum of 2-phenethyl alcohol, showing isomers I, II, and III. The positive trace is the experimental spectra, the negative trace presents a simulation based on the fits of Table 4.3.

The three most stable isomers of the alcohol were recalculated using B2PLYP/def2TZVP (Table S4.5, Appendix), but the structural parameters are comparable to B3LYP results. The energy difference using B2PLYP/def2TZVP is also consistent with the B3LYP method, where isomers I, II, and III are isoenergetic with ΔE=0.1-0.6 kJ mol^{-1}. An optimization test of the dimers using MP2/def2TZVP (Table S4.6, Appendix) gave a different energy ordering between isomers I-III, with isomers I and III isoenergetic (ΔE=0.3 kJ mol^{-1}) and isomer II at relative energy of ΔE=0.7 kJ mol^{-1}.

The investigation of the microwave spectrum of Figure 4.7 permitted the validation of the computational predictions for the alcohol dimer. Three different species were detected in the dense spectrum. For two of these isomers, all three (μ_a, μ_b, μ_c) selection

Table 4.3. Rotational parameters of the 2-phenethyl alcohol dimer.

	Experiment			Theory[e]		
Isomer	A	B	C	I	II	III
A / MHz [a]	708.07951(20)	563.05177(29)	713.30267(39)	717.6	563.9	724.8
B / MHz	276.410756(99)	313.31209(20)	271.81195(16)	280.8	317.8	274.6
C / MHz	237.62572(10)	286.68383(24)	233.31321(16)	242.0	288.7	236.5
D_J / kHz	0.02024(26)	0.0415(11)	0.01339(37)	0.019	0.034	0.011
D_{JK} / kHz	-0.04231(88)	[0.]	-0.0068(14)	-0.045	0.006	-0.006
D_K / kHz	0.1948(29)	0.0187(30)	0.1498(84)	0.195	0.013	0.121
d_1 / kHz	-0.00434(16)	[0.]	-0.00212(29)	-0.004	0.001	-0.002
d_2 / kHz	[0.]	[0.]	[0.]	0.0	-0.001	0.0
$\lvert\mu_a\rvert$ / D	Detected	Detected	Detected	2.3	0.7	2.3
$\lvert\mu_b\rvert$ / D	Detected	Detected	Detected	1.0	1.4	1.3
$\lvert\mu_c\rvert$ / D	Detected	Detected	Not detected	2.0	1.3	0.1
HBond donor [a]						
HO–$C_\beta C_\alpha$/deg				77.6	83.8	-80.2
OC_β–$C_\alpha C_{ipso}$/deg				-63.2	-61.5	59.6
$C_\beta C_\alpha$-$C_{ipso}C_{ortho}$/deg				-80.5	-82.6	76.2
HBond acceptor						
HO–$C_\beta C_\alpha$/deg				-73.5	-78.4	-74.3
OC_β–$C_\alpha C_{ipso}$/deg				63.3	62.2	64.7
$C_\beta C_\alpha$-$C_{ipso}C_{ortho}$/deg				85.3	72.5	88.2
r(O···H)/Å				1.879	1.856	1.881
∠(O–H···O)/deg				173.7	174.4	179.0
r(O–H···centroid)/Å				2.411	2.380	2.357
r(C–H···centroid)/Å				2.890	2.932	2.785
ΔE_{ZPE}/ kJ mol^{-1} [c]				0.0	0.1	0.6
ΔG / kJ mol^{-1}				0.0	0.9	1.4
E_c / kJ mol^{-1} [j]				-53.2	-55.5	-53.9
ΔE_c / kJ mol^{-1}				2.3	0.0	1.6
N [d]	438	193	310			
σ / kHz	9.8	10.6	12.6			

[a]Parameter definition as in Table 4.1. [b]Structural parameters of the dimer. [c]Relative electronic energy (ΔE_{ZPE}), Gibbs energy (ΔG), complexation energy (E_c) and relative complexation energies (ΔE_c). [d]Number of fitted transitions (N) and standard deviation of the fit (σ). [e]B3LYP-D3(BJ)/def2-TZVP.

rules are active, and a large number of 438 and 193 transitions were collected. Meanwhile, a set of 310 μ_a- and μ_b-type transitions were observed in the third isomer. A comparison of experiment and theory in Table 4.3 unambiguously confirmed the detection of isomers I (GGπ+GGπ–Lp–), II (GGπ+GGπ–Lp+), and III (GGπ–GGπ–Lp–). All spectra showed a semi-rigid rotor behaviour, and similarly to the mercaptan dimer, no tunnelling effects were detected. The spectral fits used a Watson's (S-reduced) semi-rigid rotor Hamiltonian[33] and quartic centrifugal distortion terms.

Based on the intensities of the observed species in the experimental rotational spectrum, isomer II corresponds to the weakest species. However, additional experiments with different carrier gas would be necessary. The theoretical rotational constants for each isomer are in a good agreement with the experimental rotational constants, with relative differences of 0.1-1.8% Table S4.7 (Appendix). The theoretical centrifugal distortion constants are also consistent with the experimental values. List of observed transitions can be found in Table S4.8-S4.14 (Appendix).

4.3.4. Alcohol-thiol comparison

The experimental observation of only one isomer for the 2-phenethyl mercaptan dimer, but three isomers for the dimer of 2-phenethyl alcohol is directly related to the differences in their PES and aggregation properties.

The conformational landscapes of the dimers of 2-phenethyl mercaptan and 2-phenethyl alcohol are compared in Figure 4.8. Both systems share a preference for an arrangement made of two consecutive **X**-H···**X**-H···π (**X**=O, S) hydrogen bonds. However, both dimers are very sensitive to the chirality, orientation of the aromatic rings, and secondary interactions, and the two global minima exhibit different geometries. A notorious difference is the presence of three nearly isoenergetic isomers in the alcohol, while the second isomer is much higher in the mercaptan. Anyhow, it is possible to correlate the species of both dimers. In particular, isomers I, II, and III of the 2-phenethyl alcohol dimer are equivalent to isomers 3, 5, and 4 of the 2-phenethyl mercaptan dimer. The global minimum of the mercaptan correlates with isomer VI in the alcohol dimer, where it is much less destabilized (Ggπ+Ggπ+Lp–). The only symmetric structure is much higher in energy in the alcohol (14.6 kJ mol^{-1}) than in the thiol (3.8 kJ mol^{-1}), where it appears as the second most stable.

The different characters of the hydrogen bonds in the thiol and the alcohol can be observed in several structural and energetic properties. The complexation energy (B3LYP-D3(BJ), BSSE-corrected) between the thiol dimer and the alcohol dimer differ by ΔE_c = 10 kJ mol^{-1} and are larger for the 2-phenethyl alcohol. This is in agreement with the total binding energy calculated by SAPT2+(3) where the ΔBE_{Total} = 12.4-14.7 kJ mol^{-1}.

Moreover, the binding components are different since the dispersion contribution in the thiol dimer (54.9% of total attractive contribution) is larger than in the alcohol dimer (38.8-40.8%), as summarized in Table 4.4.

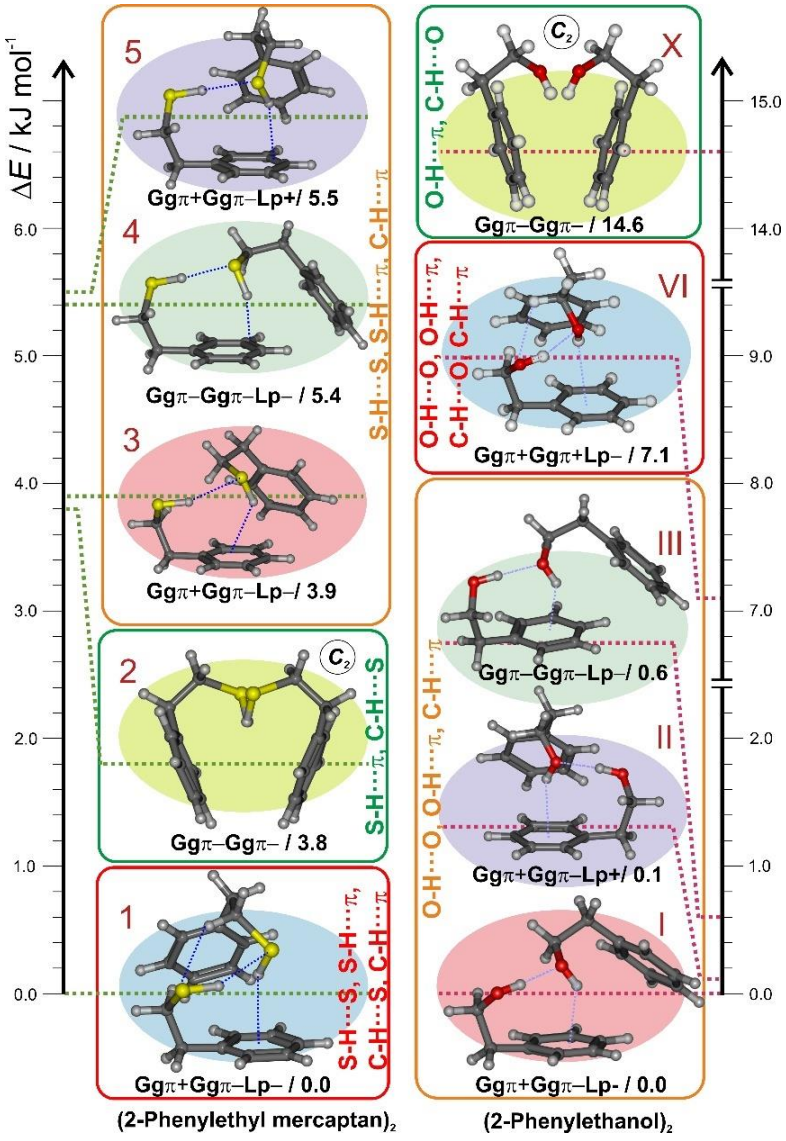

Figure 4.8. Comparison of the conformational predictions for the dimers of 2-phenethyl mercaptan (left column) and 2-phenethyl alcohol (right column). The calculations used B3LYP-D3(BJ)/def2TZVP.

Table 4.4. Binding energy decomposition for (benzyl mercaptan)$_2$ and related dimers using SAPT2+(3)/aug-cc-pVDZ//B3LYP-D3(BJ)/def2-TZVP (all values in kJ mol^{-1}).

Cluster	E_{elect}	E_{disp}	E_{ind}	E_{exch}	E_{total}	E_c [g]
(2-PEM)$_2$ [a]	-39.5[33.4%][f]	-65.0[54.9%]	-13.9[11.7%]	84.2	-34.2	-45.1
(Benzyl mercaptan)$_2$ [b]	-39.3[34.4%]	-61.1[53.6%]	-13.6[12.0%]	78.7	-35.3	-41.3
(Thiophenol)$_2$ [c]	-26.0[29.4%]	-53.8[60.9%]	-8.4[9.6%]	61.3	-27	-31.3
(2-PEAL)$_2$-2 [a]	-63.4[43.6%]	-59.3[40.8%]	-22.7[15.6%]	98.8	-46.6	-53.2
(2-PEAL)$_2$-3 [a]	-68.4[44.4%]	-59.8[38.8%]	-25.8[16.7%]	105.1	-48.9	-55.5
(2-PEAL)$_2$-1 [a]	-63.5[44.0%]	-58.1[40.3%]	-22.7[15.7%]	96.7	-47.6	-53.9
(Benzyl alcohol)$_2$ [d]	-58.7[44.5%]	-54.6[41.4%]	-18.6[14.1%]	89.8	-42.1	-48.0
(Phenol)$_2$ [e]	-41.8[48.3%]	-28.8[33.3%]	-15.9[18.4%]	58.9	-27.6	-29.8

[a]This work. [b]Ref.[15] [c]Ref. [14]. [d]Ref. [34]. [e]Seifert, N.A.; Steber, A.L.; Neill, J.L.; Pérez, C.; Zaleski, D.P.; Pate, B.H.; Lesarri, A. *Phys. Chem. Chem. Phys.* **2013**, *15*, 11468–11477. [f]Relative contribution to the attractive interactions (E_{elect}+E_{disp}+E_{ind}). [g]Complexation energy (BSSE-corrected) calculated using B3LYP-D3(BJ)/def2TZVP in Gaussian16.

In Table 4.4, we compare the binding energy decomposition not only for the three most stable dimers of 2-phenethyl alcohol and 2-phenethyl mercaptan, but also for other aromatic alcohols and thiols explored in the previous chapters. The relative total binding energy for all 2-phenethyl alcohol dimers gives similar values, ranging from 0-2.2 kJ mol^{-1}. The energy decomposition ratios also provide a similar proportion for each component: 44% for electrostatic, 16-17% for induction, and 39-41% for dispersion (relative to total attractive contribution). Interestingly, the energy decomposition for 2-phenethyl alcohol dimers is similar to the phenol dimer, where the induction contribution is slightly larger than that in the phenol dimer (14%). However, the total binding energy of the 2-phenethyl alcohol dimer is lower than in the phenol dimer (21.3 kJ mol^{-1}) and the benzyl alcohol dimer (6.8 kJ mol^{-1}).

Conversely, the dispersive contribution of the 2-phenethyl alcohol dimer is smaller than in the benzyl alcohol dimer (55%). In aromatic alcohol dimers, the conclusion is that the longer the aliphatic group connects the OH group to the aromatic ring, the smaller the total binding energy of the dimer. This trend also agrees with the values of complexation energy of the dimers (BSSE-corrected), where the energy differences are 7.5 and 25.7 kJ mol^{-1}, respectively, for the benzyl alcohol dimer and the phenol dimer, relative to 2-phenethyl alcohol dimer.

In aromatic thiols, the 2-phenethyl mercaptan dimer has a similar dispersive contribution than the benzyl mercaptan dimer (54%), although the total binding energy is about 1.1 kJ mol^{-1} higher than in the benzyl mercaptan dimer. However, the dispersion contribution in the 2-phenethyl mercaptan dimer is 7% lower than that in the thiophenol dimer. This is because the structure of thiophenol dimers is dominated by S-H···S interaction, which has a weak interaction of dispersive character, and the π-π stacking. On the other hand, the aliphatic chain plus thiol group controls the stability of the dimer. The complexation energy of 2-phenethyl mercaptan dimer is -45.1 kJ mol^{-1},

lower than in the benzyl mercaptan dimer by 3.8 kJ mol^{-1}, and 13.7 kJ mol^{-1} lower than thiophenol dimer. Moreover, the additional C-H···S interactions give more electrostatic contribution to the 2-phenethyl mercaptan dimer.

Table 4.5. Structural parameters for hydrogen bond in aromatic thiols/alcohols.

	B3LYP/def2TZVP		B2PLYP/def2TZVP	
	r(**X**···H)/Å	∠(**X**–H···**X**)/deg	r(**X**···H)/Å	∠(**X**–H···**X**)/deg
X=S				
(2-PEM)$_2$ [a]	2.668	151.1	2.715	150.8
(Benzyl mercaptan)$_2$ [b]	2.684	164.8	2.748	162.9
(Thiophenol)$_2$ PD2-cis [c]	2.787	136.7	2.843	134.5
(Thiophenol)$_2$ PD1-trans [c]	2.838	138.8	2.879	138.9
X=O				
(2-PEAL)$_2$-2 [a]	1.879	173.7	1.881	173.9
(2-PEAL)$_2$-3 [a]	1.856	174.4	1.860	174.5
(2-PEAL)$_2$-1 [a]	1.881	179.0	1.883	179.3
(Benzyl alcohol)$_2$ [d]	1.951	163.3	1.955	163.1
(Phenol)$_2$	1.894	169.1	1.901	168.1
	r0, M06-2X/6-311++g(d,p) [e]		r0, MP2/cc-pVTZ-cp [e]	
(Phenol)$_2$ [e]	1.837(23)	170.5(21)	1.879(38)	166.2(37)

[a]This work. [b]Ref.[15] [c]Ref. [14]. [d]Ref. [34]. [e]Seifert, N.A.; Steber, A.L.; Neill, J.L.; Pérez, C.; Zaleski, D.P.; Pate, B.H.; Lesarri, A. *Phys. Chem. Chem. Phys.* **2013**, *15*, 11468–11477. [f]Relative contribution to the attractive interactions (E_{elect}+E_{disp}+E_{ind}). [g]Complexation energy (BSSE-corrected) calculated using B3LYP-D3(BJ)/def2TZVP in Gaussian16.

In Table 4.5, we compare the structural parameters of the hydrogen bonds in the 2-phenethyl dimers with some related thiols and alcohols. In the 2-phenethyl mercaptan or alcohol dimers the SH or OH groups are not directly attached to the aromatic ring, like in benzyl mercaptan/alcohol. Therefore, the aliphatic chain could reduce the delocalization effects from the aromatic cloud. At the same time, the aromatic ring may collaborate in binding through secondary interactions. The flexibility of the aliphatic separator in the 2-phenethyl dimers allows us to assess the impact of the additional degrees of freedom on the aggregation process. In the thiophenol dimer, the dispersion effect is the main contribution of the stabilization, not only due to the weak dispersive character of the S-H···S hydrogen bond but also to the π···π stacking interaction.[14]

As we explored in Chapter 3, the dimer of benzyl mercaptan is mainly stabilized by S-H···S, S-H···π, and C(sp^2)-H···π interactions. In the 2-phenethyl mercaptan dimer, the previous hydrogen bonds are supplemented with an additional C(sp^3)-H···S weak interaction with r(C-H···S)=2.957 Å, ∠(C-H···S)=137.6° (B3LYP-D3(BJ)).[15] This binding pattern produces a long (r(S-H···S)=2.668 Å), not-linear (∠(S-H···S)=151.1°) primary hydrogen bond, in line with previous observations in sulfur centers. In comparison, the observed isomers of the 2-phenethyl alcohol dimer show a shorter and more linear O-

H···O hydrogen bond with a range of distances of r(O-H···O) = 1.856-1.881 Å and linearities of ∠(O-H···O)=173.7-179.0°.

In aromatic thiols, the longer the aliphatic separator, the shorter the S-H···S bond. However, for the angle of S-H···O, it depends on the structure of the dimer. In thiophenol, since the structures display the π-π stacking interaction, the S-H···S became much bent. In the benzyl mercaptan dimer, this angle is much closer to linearity compared to the 2-phenethyl mercaptan dimer (164.8° vs. 151.1°). In aromatic alcohols, the reported effective structure of phenol depends on the initial structures (M06-2X: 1.837(23); MP2: Å1.879(38) but is the shortest among related aromatic alcohol.[35] In 2-phenethyl alcohol, the O···H distance is shorter than that in the benzyl alcohol dimer and also much closer to linearity.

The description of non-covalent interactions in the 2-phenethyl dimers used an NCIplot analysis, shown in Figure 4.9. This figure shows similar features as in the previous chapter for the benzyl mercaptan dimer. The blue lentils represent regions with strong attractive interactions typical of the O-H···O hydrogen bonds, weaker for the S-H···S hydrogen bond. The figure also shows the O-H···π/ S-H···π interactions between the OH/SH groups to the aromatic ring. The green surfaces show the weak interactions for all dimers, as shown for the C(sp^2)-H···π interactions.

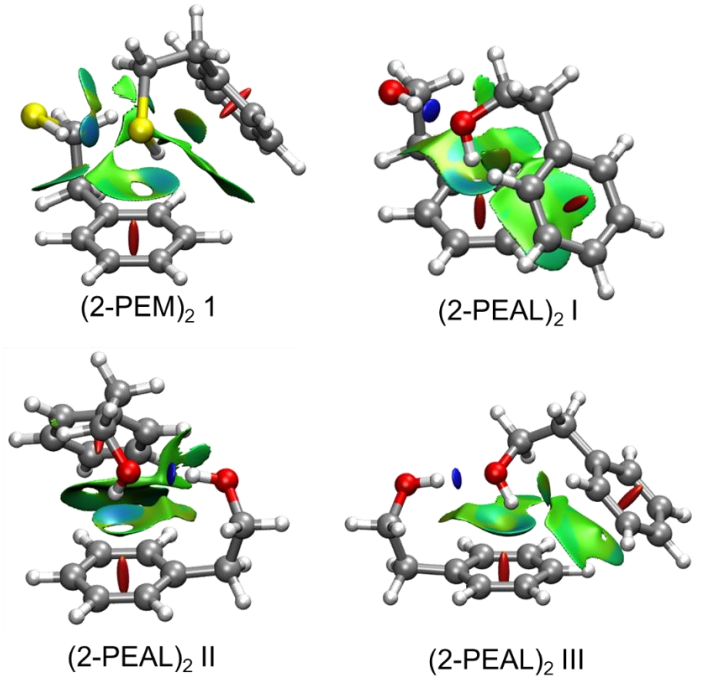

Figure 4.9. NCIplots for the observed dimer of the dimers of 2-phenethyl mercaptan and alcohol (color scaling from -2.0 to 2.0 a.u.).

4.4. Conclusions

The dimerization of 2-phenethyl mercaptan and 2-phenethyl alcohol produces quite different results, directly associated to their PES. The mercaptan dimer gives only one (GGπ+GGπ–Lp–) heterochiral isomer, which contrasts with two heterodimers (GGπ+GGπ–Lp–, and GGπ–GGπ–Lp+) and one homodimer (GGπ–GGπ–Lp–) for the alcohol. The primary binding pattern formed by two thiol-thiol and thiol-ring interactions is replicated in the alcohol, but the weaker, more dispersive character associated to the low electronegativity and larger polarizability of sulfur results in the different number of minima in the two dimers. The observations based on rotational spectroscopy are supported by several computational calculations, which included an NCIplot analysis and the SAPT energy decomposition. This information provides an accurate description of the electronic and structural properties of the dimers. In consequence, the present study will contribute to a better understanding of the intermolecular interactions of sulfur centers.

References

(1) Shipman, S. T.; Pate, B. H. New Techniques in Microwave Spectroscopy. *Handb. High-resolution Spectrosc.* **2011**. https://doi.org/10.1002/9780470749593.HRS036.

(2) Grabow, J.-U.; Caminati, W. Microwave Spectroscopy Experimental Techniques. In *Frontiers of Molecular Spectroscopy*; Laane, J., Ed.; Elsevier, 2009; pp 383–454. https://doi.org/10.1016/B978-0-444-53175-9.X0001-3.

(3) Caminati, W.; Grabow, J.-U. Microwave Spectroscopy Molecular Systems. In *Frontiers of Molecular Spectroscopy*; Laane, J., Ed.; Elsevier Inc.: Amsterdam, 2008; pp 456–552.

(4) León, I.; Millán, J.; Cocinero, E. J.; Lesarri, A.; Fernández, J. A. Shaping Micelles: The Interplay Between Hydrogen Bonds and Dispersive Interactions. *Angew. Chemie Int. Ed.* **2013**, *52* (30), 7772–7775. https://doi.org/10.1002/ANIE.201303245.

(5) Dickinson, J. A.; Hockridge, M. R.; Kroemer, R. T.; Robertson, E. G.; Simons, J. P.; McCombie, J.; Walker, M. Conformational Choice, Hydrogen Bonding, and Rotation of the S1 ← S0 Electronic Transition Moment in 2-Phenylethyl Alcohol, 2-Phenylethylamine, and Their Water Clusters. *J. Am. Chem. Soc.* **1998**, *120* (11), 2622–2632. https://doi.org/10.1021/JA972104O.

(6) Godfrey, P. D. Shapes of Molecules by Millimeter-Wave Spectroscopy: 2-Phenylethanol. *J. Phys. Chem. A* **1999**, *103* (38), 7621–7626. https://doi.org/10.1021/JP990419F/SUPPL_FILE/JP990419F_S.PDF.

(7) Brown, R. D.; Godfrey, P. D. Detection of a Higher Energy Conformer of 2-Phenylethanol by Millimeter-Wave Spectroscopy. *J. Phys. Chem. A* **2000**, *104* (24), 5742–5746. https://doi.org/10.1021/JP0003252/SUPPL_FILE/JP0003252_S.PDF.

(8) Mons, M.; Robertson, E. G.; Simons, J. P. Intra- and Intermolecular π-Type Hydrogen Bonding in Aryl Alcohols: UV and IR–UV Ion Dip Spectroscopy. *J. Phys. Chem. A* **2000**, *104* (7), 1430–1437. https://doi.org/10.1021/jp993178k.

(9) Mons, M.; Robertson, E. G.; Snoek, L. C.; Simons, J. P. Conformations of 2-Phenylethanol and Its Singly Hydrated Complexes: UV–UV and IR–UV Ion-Dip Spectroscopy. *Chem. Phys. Lett.* **1999**, *310* (5–6), 423–432. https://doi.org/10.1016/S0009-2614(99)00814-3.

(10) Guchhait, N.; Ebata, T.; Mikami, N. Discrimination of Rotamers of Aryl Alcohol Homologues by

Infrared–Ultraviolet Double-Resonance Spectroscopy in a Supersonic Jet. *J. Am. Chem. Soc.* **1999**, *121* (24), 5705–5711. https://doi.org/10.1021/JA9829618.

(11) Melandri, S.; Maris, A.; Favero, P. G.; Caminati, W. Free Jet Absorption Millimetre-Wave Spectrum and Model Calculations of Phenol–Water. *Chem. Phys.* **2002**, *283* (1–2), 185–192. https://doi.org/10.1016/S0301-0104(02)00600-6.

(12) Martin, D. E.; Robertson, E. G.; Thompson, C. D.; Morrison, R. J. S. Resonant 2-Photon Ionization Study of the Conformation and the Binding of Water Molecules to 2-Phenylethanethiol (PhC H2 C H2 SH). *J. Chem. Phys.* **2008**, *128* (16), 164301. https://doi.org/10.1063/1.2903477.

(13) Lobo, I. A. A.; Robertson, P. A.; Villani, L.; Wilson, D. J. D.; Robertson, E. G.; A. Robertson, P.; Villani, L.; J. D. Wilson, D.; G. Robertson, E. Thiols as Hydrogen Bond Acceptors and Donors: Spectroscopy of 2-Phenylethanethiol Complexes. *J. Phys. Chem. A* **2018**, *122* (36), 7171–7180. https://doi.org/10.1021/acs.jpca.8b06649.

(14) Saragi, R. T.; Juanes, M.; Pérez, C.; Pinacho, P.; Tikhonov, D. S.; Caminati, W.; Schnell, M.; Lesarri, A.; S. Tikhonov, D.; Caminati, W.; Schnell, M.; Lesarri, A. Switching Hydrogen Bonding to π-Stacking: The Thiophenol Dimer and Trimer. *J. Phys. Chem. Lett.* **2021**, *12* (5), 1367–1373. https://doi.org/10.1021/acs.jpclett.0c03797.

(15) Saragi, R. T.; Juanes, M.; Pinacho, R.; Rubio, J. E.; Fernández, J. A.; Lesarri, A. Molecular Recognition, Transient Chirality and Sulfur Hydrogen Bonding in the Benzyl Mercaptan Dimer. *Symmetry 2021, Vol. 13, Page 2022* **2021**, *13* (11), 2022. https://doi.org/10.3390/SYM13112022.

(16) Halgren, T. A. MMFF VI. MMFF94s Option for Energy Minimization Studies. *J. Comput. Chem.* **1999**, *20* (7), 720–729. https://doi.org/10.1002/(SICI)1096-987X(199905)20:7<720::AID-JCC7>3.0.CO;2-X.

(17) Becke, A. D. Density-Functional Thermochemistry. III. The Role of Exact Exchange. *J. Chem. Phys.* **1993**, *98* (7), 5648–5652. https://doi.org/10.1063/1.464913.

(18) Johnson, E. R.; Becke, A. D. A Post-Hartree-Fock Model of Intermolecular Interactions: Inclusion of Higher-Order Corrections. *J. Chem. Phys.* **2006**, *124* (17), 174104. https://doi.org/10.1063/1.2190220.

(19) Grimme, S.; Ehrlich, S.; Goerigk, L. Effect of the Damping Function in Dispersion Corrected Density Functional Theory. *J. Comput. Chem.* **2011**, *32* (7), 1456–1465. https://doi.org/10.1002/jcc.21759.

(20) Weigend, F.; Ahlrichs, R. Balanced Basis Sets of Split Valence, Triple Zeta Valence and Quadruple Zeta Valence Quality for H to Rn: Design and Assessment of Accuracy. *Phys. Chem. Chem. Phys.* **2005**, *7* (18), 3297. https://doi.org/10.1039/b508541a.

(21) Boys, S. F.; Bernardi, F. The Calculation of Small Molecular Interactions by the Differences of Separate Total Energies. Some Procedures with Reduced Errors. *Mol. Phys.* **2002**, *100* (1), 65–73. https://doi.org/10.1080/00268970110088901.

(22) Frisch, M. J.; Trucks, G. W.; Schlegel, H. B.; Scuseria, G. E.; Robb, M. A.; Cheeseman, J. R.; Scalmani, G.; Barone, V.; Petersson, G. A.; Nakatsuji, H.; Li, X.; Caricato, M.; Marenich, A. V.; Bloino, J.; Janesko, B. G.; Gomperts, R.; Mennucci, B.; Hratchian, H. P.; Ortiz, J. V.; Izmaylov, A. F.; Sonnenberg, J. L.; Williams; Ding, F.; Lipparini, F.; Egidi, F.; Goings, J.; Peng, B.; Petrone, A.; Henderson, T.; Ranasinghe, D.; Zakrzewski, V. G.; Gao, J.; Rega, N.; Zheng, G.; Liang, W.; Hada, M.; Ehara, M.; Toyota, K.; Fukuda, R.; Hasegawa, J.; Ishida, M.; Nakajima, T.; Honda, Y.; Kitao, O.; Nakai, H.; Vreven, T.; Throssell, K.; Montgomery Jr., J. A.; Peralta, J. E.; Ogliaro, F.; Bearpark, M. J.; Heyd, J. J.; Brothers, E. N.; Kudin, K. N.; Staroverov, V. N.; Keith, T. A.; Kobayashi, R.; Normand, J.; Raghavachari, K.; Rendell, A. P.; Burant, J. C.; Iyengar, S. S.; Tomasi, J.; Cossi, M.; Millam, J. M.; Klene, M.; Adamo, C.; Cammi, R.; Ochterski, J. W.; Martin, R. L.; Morokuma, K.; Farkas, O.; Foresman, J. B.; Fox, D. J. Gaussian 16, Rev. C.01. Gaussian, Inc: Wallingford CT 2016.

(23) Johnson, E. R.; Keinan, S.; Mori-Sánchez, P.; Contreras-García, J.; Cohen, A. J.; Yang, W. Revealing Noncovalent Interactions. *J. Am. Chem. Soc.* **2010**, *132* (18), 6498–6506. https://doi.org/10.1021/ja100936w.

(24) Contreras-García, J.; R. Johnson, E.; Keinan, S.; Chaudret, R.; Piquemal, J.-P.; N. Beratan, D.; Yang, W. NCIPLOT: A Program for Plotting Noncovalent Interaction Regions. *J. Chem. Theory Comput.*

2011, *7* (3), 625–632. https://doi.org/10.1021/ct100641a.

(25) Jeziorski, B.; Moszynski, R.; Szalewicz, K. Perturbation Theory Approach to Intermolecular Potential Energy Surfaces of van Der Waals Complexes. *Chem. Rev.* **1994**, *94* (7), 1887–1930. https://doi.org/10.1021/cr00031a008.

(26) Scheiner, S. *Hydrogen Bonding. A Theoretical Perspective*; Oxford University Press: Oxford, 1997.

(27) Parrish, R. M.; Burns, L. A.; Smith, D. G. A.; Simmonett, A. C.; DePrince, A. E.; Hohenstein, E. G.; Bozkaya, U.; Sokolov, A. Y.; Di Remigio, R.; Richard, R. M.; Gonthier, J. F.; James, A. M.; McAlexander, H. R.; Kumar, A.; Saitow, M.; Wang, X.; Pritchard, B. P.; Verma, P.; Schaefer, H. F.; Patkowski, K.; King, R. A.; Valeev, E. F.; Evangelista, F. A.; Turney, J. M.; Crawford, T. D.; Sherrill, C. D. Psi4 1.1: An Open-Source Electronic Structure Program Emphasizing Automation, Advanced Libraries, and Interoperability. *J. Chem. Theory Comput.* **2017**, *13* (7), 3185–3197. https://doi.org/10.1021/acs.jctc.7b00174.

(28) True, N. S.; Farag, M. S.; Bohn, R. K.; MacGregor, M. A.; Radhakrishnan, J. Low-Resolution Microwave Studies of Substituted Ethyl- and Isopropylbenzenes. *J. Phys. Chem.* **1983**, *87* (23), 4622–4627. https://doi.org/10.1021/J100246A018/SUPPL_FILE/J100246A018_SI_001.PDF.

(29) Caminati, W.; Damiani, D.; Corbelli, G.; Velino, B.; Bock, B. W. Microwave Spectrum and Ab Initio Calculations of Ethylbenzene: Potential Energy Surface of the Ethyl Group Torsion. *http://dx.doi.org/10.1080/00268979100102661* **2006**, *74* (4), 885–895. https://doi.org/10.1080/00268979100102661.

(30) Brunvoll, J.; Kolonits, M.; Bohn, R. K.; ván Hargittai, I. Molecular Structure of P-Ethylbenzaldehyde and p-Isopropyl Benzaldehyde from Electron Diffraction. *J. Mol. Struct.* **1985**, *131* (1–2), 177–181. https://doi.org/10.1016/0022-2860(85)85112-7.

(31) Saragi, R. T.; Juanes, M.; Caminati, W.; Lesarri, A.; Enríquez, L.; Jaraíz, M. Rotational Spectrum, Tunneling Motions, and Intramolecular Potential Barriers in Benzyl Mercaptan. *J. Phys. Chem. A* **2019**, *123* (39). https://doi.org/10.1021/acs.jpca.9b06921.

(32) Utzat, K. A.; Bohn, R. K.; Montgomery, J. A.; Michels, H. H.; Caminati, W. Rotational Spectrum, Tunneling Motions, and Potential Barriers of Benzyl Alcohol. *J. Phys. Chem. A* **2010**, *114* (25), 6913–6916. https://doi.org/10.1021/jp102903p.

(33) Watson, J. K. G. Aspects of Quartic and Sextic Centrifugal Effects on Rotational Energy Levels. In *Vibrational Spectra and Structure, vol. 6*; Durig, J. R., Ed.; Elsevier B.V.: Amsterdam, 1977; pp 1–89.

(34) Medel, R.; Camiruaga, A.; Saragi, R. T.; Pinacho, P.; Pérez, C.; Lesarri, A.; Suhm, M. A.; Fernández, J. A. Rovibronic Signatures of Molecular Aggregation in the Gas Phase: Subtle Homochirality Trends in the Dimer, Trimer and Tetramer of Benzyl Alcohol. *Phys. Chem. Chem. Phys.* **2021**, *submitted*.

(35) Seifert, N. A.; Steber, A. L.; Neill, J. L.; Pérez, C.; Zaleski, D. P.; Pate, B. H.; Lesarri, A. The Interplay of Hydrogen Bonding and Dispersion in Phenol Dimer and Trimer: Structures from Broadband Rotational Spectroscopy. *Phys. Chem. Chem. Phys.* **2013**, *15* (27), 11468–11477. https://doi.org/10.1039/c3cp51725j.

Chapter 5.
The 2-Naphthalenethiol Dimers

In previous chapters, we have explored the interaction between thiol groups in aromatic molecules, observing the balance between S-H···S hydrogen bonding and the π electron interaction as the aliphatic spacer between the ring and the thiol group increased in size from zero to two carbon atoms. In this chapter, we study the π-stacking interactions in the 2-naphthalenethiol dimer, adopting a different approach in which we extend the ring size for a single thiol group. This investigation offers comparison with the thiophenol dimer, which simultaneously permitted a π-stacking aggregation controlled by a S-H···S hydrogen bond. Conversely, in the 2-naphthalenethiol dimer we observed an absence of sulfur hydrogen bonding, allowing a comparison with other aromatic complexes. The results of this chapter are presently submitted for publication.

5.1. Introduction

Hydrogen bonds play a key role as stabilizing factors in biological and chemical processes. As an example, hydrogen bonds determine solvation, the stabilization of second-order protein structures, the construction or large biological macromolecules like DNA or host-guest recognition and information transfer. The hydrogen bonds in aromatic compounds are very intriguing because of the involvement of the π electron system of the aromatic ring, which may be competitive with weak hydrogen bonds, like those associated to sulfur centers. In this context, high-resolution chirped-pulse microwave spectroscopy has proved to be a reliable method to extend the size and scope of the molecular systems examined rotationally, offering an experimental route to enlarge our knowledge on hydrogen bonding and self-aggregation. This effort has produced an increase in molecular information concerning gas-phase dimerization, complementing other experimental techniques. As an example, the 1-naphthol dimer was detected by UV-IR ion-dip double-resonance laser spectroscopy,[1] which concluded

that the dimer was stabilized by π–stacking and an additional O-H···O hydrogen bond. This result was argued by microwave spectroscopy,[2] confirming that the dimer is instead mainly controlled by π–stacking with no canonical hydrogen bond. This observation was termed "a surprising preference", somehow ignoring the increment in dispersion interactions associated to a larger number of aromatic rings.[3] Here we report the observation of the 2-naphthalenethiol dimer by microwave spectroscopy and supporting quantum chemical calculations.

The effect of chemical substitutions in aromatic rings is very interesting to understand their self-aggregation process. In Chapter 2, we explored this effect on the thiophenol dimer with comparison to the phenol dimer and aniline dimer. Thiol S-H···S hydrogen bonding in the thiophenol dimer and trimer was the primary force to stabilize the cluster. However, unlike in the phenol and aniline dimers, the π–π interactions control the orientation between the two rings and produce a near-parallel orientation of the ring despite the notorious large-amplitude motions within the thiol groups. The observation of the thiol dimer properties calls for the investigation of other substitution effects in aromatic thiols and alcohols. The objective of this chapter is to answer if a larger biaromatic compound like 2-naphthalenethiol (Figure 5.1) will render a dimer stabilized by hydrogen bond or π-stacking, offering direct comparison with the 1-naphthol and thiophenol dimers. The dimer of 2-naphthalenethiol will permit to compare the influence of sulfur, an atom of smaller electronegativity but larger size and polarizability than oxygen, and the plausible inductive effects from the rings, offering information on the more dispersive physical nature of the intermolecular interactions to sulfur centers.

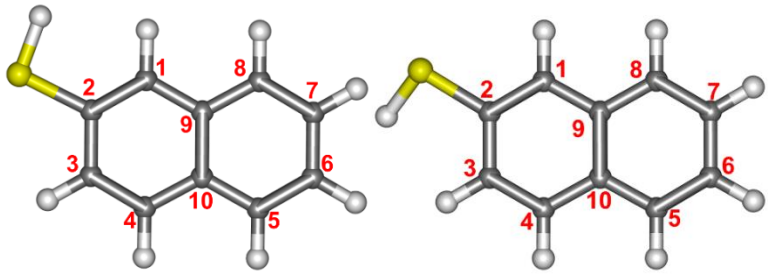

Figure 5.1. Isomers of the 2-naphthalenethiol monomer: *cis* (left) and *trans* (right).

A priori, the naphthalene dimer structure may use sandwich, parallel-displaced or T-shaped geometries similar to the naphthalene or benzene dimers.[4–6] The parallel-displaced forms may present different relative orientations depending on the shift

between the two subunits of naphthalene, either symmetrically or unsymmetrically arranged. The symmetric dimers include the crossed (C_2) or slipped (C_i) structures, which admit different D_{2d}, C_{2h}, or D_{2h} point-group geometries.[5] As proposed by Seifert,[2] the term V-shape may be use to distinguish the dimers in parallel-displaced form.

5.2. Methods

The rotational spectrum of 2-naphtalenethiol was recorded in the region 2-8 GHz using chirped-pulse Fourier transform microwave spectroscopy. The sample of 2-naphthalenethiol (m.p. 80-81°C, b.p. 92-94°C) was obtained commercially (TCI Chemicals) and heated at 110°C. Neon was used as carrier gas at backing pressures of 3.5 bar, forming a supersonic jet by pulsed near-adiabatic expansion inside a high vacuum chamber. The gas injection used typical pulses of 900 μs, followed by a perpendicular 20 W broadband chirped excitation. The free-induction decay was recorded in intervals of 40 μs and Fourier transformed to the frequency domain. The use of an apodization Kaiser-Besel window resulted in linewidths below 150 kHz. The frequency measurements have an estimated accuracy better than 10 kHz.

Several computational methods complemented the experimental results. The initial conformational search used molecular mechanics and the MMFFs force field.[7] The dimers then were fully reoptimized with the B3LYP[8] and ωB97XD[9] density-functional theory (DFT) hybrid methods and the Alrichs' def2-TZVP basis set.[10] The ten most stable isomers are distributed within an energy window of only 2.2 kJ mol^{-1}. The five most stable isomers were reoptimized by B2PLYP and MP2 level of theory to check the consistency of the calculations.[11–13] Harmonic vibrational frequency calculations, limited to the DFT methods, confirmed that all stationary points are minima of the potential energy surface. The B3LYP and B2PLYP methods were supplemented with D3 empirical dispersion corrections and a Becke-Johnson damping function.[14,15] The complexation energies were calculated taking into account the basis set superposition error (BSSE), corrected with the counterpoise method.[16] The quantum mechanical calculations used Gaussian16. The non-covalent interactions were analysed using the topology of the electron density with the NCIplot method.[17,18] A binding energy decomposition was calculated using symmetry-adapted perturbation theory at the SAPT2+(3) level with the aug/cc-PVDZ basis set, implemented in PSI4.[19] Detailed results can be found in the Appendix (Tables S5.1-S5.4).

5.3. Results and Discussions

5.3.1. Monomers

2-Naphthalenethiol is a monosubstituted derivative of naphthalene, a C_s planar molecule with a thiol group attached in position C(2). This molecule has two conformers, *cis* and *trans*, depending on the orientation of the thiol group. The *cis* form is the global minimum, with an energy difference between the two conformers is about 0.6 kJ mol^{-1} (B3LYP-D3(BJ)). The interconversion barrier between the *cis* and *trans* conformers was calculated in Figure 5.2 from a monodimensional scan of the HS-C2C3 dihedral. The resulting barrier of 4.6 kJ mol^{-1} (B3LYP-D3(BJ)) indicates that the two conformers may be populated. Assuming the planarity of the molecule the spectral contributions will come from μ_a- and μ_b-type transitions for both conformers.

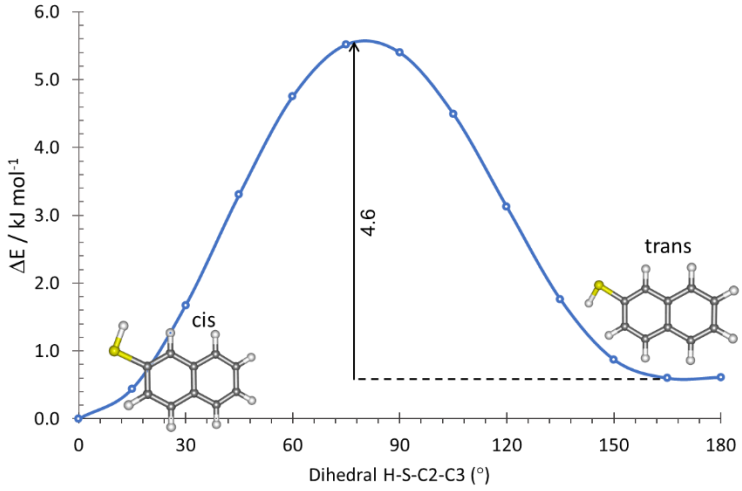

Figure 5.2. Interconversion barrier between the *cis*- and *trans*-2-naphthalenethiol monomer, calculated using B3LYP-D3(BJ)/def2TZVP.

The experimental spectrum is shown in Figure 5.3. A dataset of more than two hundred eighty transitions were assigned for the 2-naphthalenethiol monomer (Tables S5.5-S5.6 in Appendix) and the dimer of 2-naphthalenethiol···Ne (Tables S5.7-S5.9 in Appendix). The monomer transitions appeared as two independent series, identified as the *cis* and *trans* conformers from comparison with the computational predictions. Both μ_a- and μ_b-transitions were detected for isomer *cis* and *trans*. The spectrum was reproduced with a semi-rigid rotor model, using the S-reduced Watson Hamiltonian. The centrifugal distortion effects were very small and only one distortion parameter was

determinable from the present experiment. The fitted rotational parameters for the thiol monomer are presented in Table 5.1. The small negative values of the inertial defect[20] for both *cis* and *trans* species (Δ= -0.0056 u Å^2) confirmed the molecule as effectively planar in its ground state, with minor out-of-plane vibrations due to the thiol group. The calculations predicted equilibrium out-of-plane angles of 0.03° and 13.5° for the *cis* and *trans* conformers, respectively. The experimental values are in a good agreement with the B3LYP-D3(BJ) predictions.

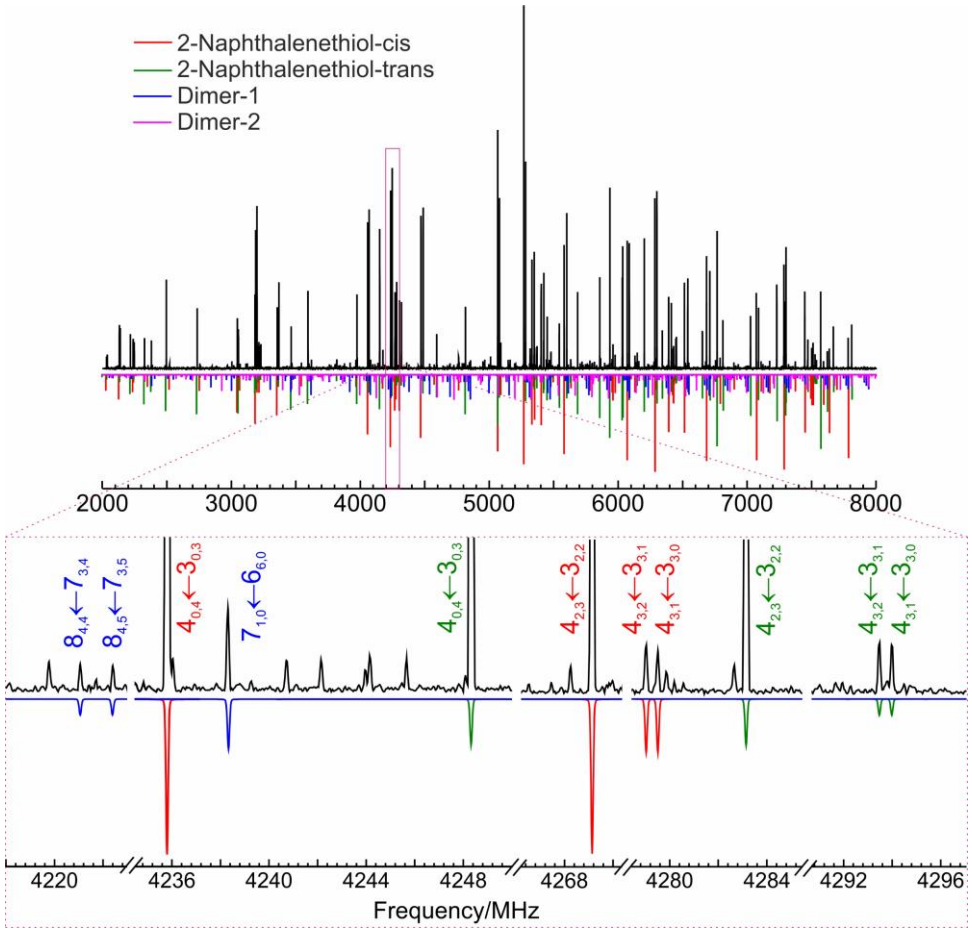

Figure 5.3. Rotational spectrum of 2-naphthalenethiol (upper trace) and simulated spectra using the fitted parameters of Table 5.1 (lower trace). The red and green traces correspond to the monomer, while the weaker blue and purple transitions originate from the dimer.

All monosubstituted ^{13}C and ^{34}S isotopologues in natural abundance (1% and 4%, respectively) could be assigned for the *cis* and *trans* form in the rotational spectrum.

However, since the focus of this chapter is centered in the 2-naphtalenethiol dimer, a description of the spectra of the isotopic species is not presented here and will be reported separately.

Table 5.1. Rotational parameters of the 2-naphthalenethiol monomer.

	Experiment		Theory [h]	
Isomer	*cis*	*trans*	*cis*	*trans*
A / MHz [a]	2729.29259(58) [f]	2701.15089(61)	2751.22	2723.99
B / MHz	585.644787(95)	588.203036(88)	587.71	590.14
C / MHz	482.347817(99)	483.322880(97)	484.26	485.14
Δ / u Å^2	-0.00560	-0.00555	-0.00565	-0.00560
D_J / kHz [b]	[0.] [g]	[0.]	0.005	0.005
D_{JK} / kHz	[0.]	[0.]	0.026	0.001
D_K / kHz	[0.]	0.248(31)	0.353	0.270
d_1 / kHz	[0.]	[0.]	-0.001	0.001
d_2 / kHz	[0.]	[0.]	-0.026	0.024
$\lvert\mu_a\rvert$ / D [c]	+++	++	0.8	0.6
$\lvert\mu_b\rvert$ / D	++	+++	0.5	-1.0
$\lvert\mu_c\rvert$ / D	-	-	0.0	-0.2
N [d]	7.5	7.6		
σ / kHz	93	117		
ΔE_{ZPE}/ kJ mol^{-1} [e]			0.0	0.6
ΔG / kJ mol^{-1}			1.6	0.0

[a]Rotational constants (A, B, C) and inertial defect (Δ=I_c-I_a-I_b). [b]Watson's S-reduction centrifugal distortion constants (D_J, D_{JK}, D_K, d_1, d_2). [c]Dipole moments. [d]Number of measured transitions (N) and standard error of the fit (σ). [e]Electronic energies (zero point-corrected) and Gibbs energy (298 K, 1 atm). [f]Standard errors in parentheses in units of the last digit. [g]Fixed to zero. [h]B3LYP-D3(BJ)/def2-TZVP.

5.3.2. Homodimers

Fifteen structures of the 2-naphthalenethiol dimer were optimized using B3LYP-D3(BJ) within a window energy of 4.3 kJ mol^{-1} (Figure S5.1 in Appendix). Characteristically, all structures showed near-parallel configurations. From these structures, the dimer conformations can be classified based on the interactions between the two moieties, such as the existence of a thiol S-H···S hydrogen bond between the monomers and/or the stacking orientation and symmetry of the dimer. Seven out of the fifteen dimer structures exhibit the thiol hydrogen bond. Noticeably, the three most stable dimers showed no thiol hydrogen bond, as illustrated in Figure 5.4.

Since the *cis* monomer is more stable than the *trans*, the dimer most likely contains a *cis* monomer at least in one of the subunits. For the fifteen calculated dimers, there are only four dimers that consist of *trans-trans* (TT) monomers (dimers 8, 10, 12, and 14) with electronic energies in the range ΔE = 1.8-3.9 kJ mol^{-1}. For the dimers with energies below 1.5 kJ mol^{-1}, dimers 1, 2, and 5 are *cis-cis* (CC) homodimers, where both subunits have identical conformation. The three most stable dimers (dimers 1, 2, and 3) are

practically isoenergetic at the B3LYP level of theory, with energy separations of ΔE=0.2-0.5 kJ mol^{-1}, The first three dimers are controlled by parallel displaced π–stacking interactions, with a global minimum characterized by a C_2-symmetric CC structure. Dimers 4, 5, and 6 combine S-H···S hydrogen bonds and π stacking interaction in CT or CC orientations. Dimers 4 and 6 displayed a sandwich-like structure, placing one 2-naphthalenthiol molecule nearly on top of the other. The other C_2-symmetric dimers are dimers 8 and 14. Unlike in the naphthalene dimer, the T-shaped structure for 2-naphthalenethiol dimer is not found within the energy window of 4.3 kJ mol^{-1}.

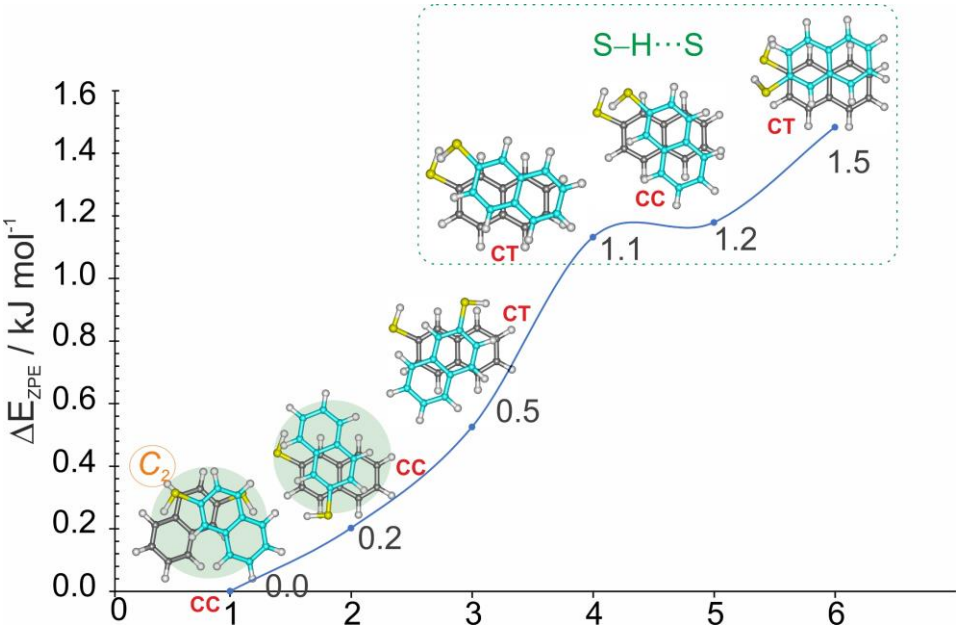

Figure 5.2. The conformational landscape of 2-napthalenethiol dimer.

Since the three most stable structures of 2-naphthalenthiol dimer lack a S-H···S hydrogen bond their structural characterization depends on the ring orientations. The closest distance between the two 2-naphtalenethiol planes ranges between 3.281-3.296 Å, but in the dimers 4-6 these distances increase about 2% to 3.322-3.387 Å (B3LYP-D3(BJ) level). For the optimization using B2PLYP-D3(BJ) these values range in 3.264-3.279 Å for dimers 1-3 and 3.335-3.367 Å for dimers 4-6 (Figure S5.2). Some of these structures indeed resemble the structure of the thiophenol dimer. In thiophenol dimer, the closest distance between the planes is in a range of 3.359-3.376 Å. When a S-H···S sulfur hydrogen bond is present in the 2-naphthalenethiol or thiophenol dimers it serves as anchor point, but there is a margin for different distances and orientations between the biaromatic rings.

The investigation of the rotational spectra of the 2-naphthalenthiol dimer started once all monomer signals were identified. Following several spectral surveys two isomers denoted 1 and 2 were observed in the spectrum, as illustrated in Figure 5.5.

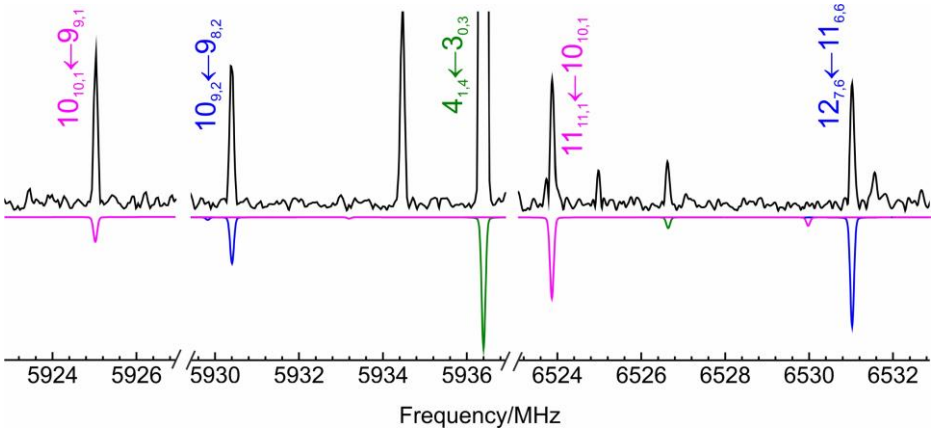

Figure 5.3. Spectral section showing the assigned species of the 2-naphthalenethiol dimer. The green trace corresponds to the trans monomer, while the blue and purple transitions originate from the dimer.

Table 5.2. Rotational parameters of the 2-naphthalenethiol dimer.

	Experiment		Theory [c]		
Rotational parameters	Isomer 1	Isomer 2	CC-1 (C_2)	CC-2 (C_1)	CT-3 (C_1)
A / MHz [a]	308.38853(21) [d]	299.45856(51)	318.10	304.23	294.60
B / MHz	231.75029(16)	246.9652(12)	233.40	250.65	245.68
C / MHz	226.78483(18)	221.5793(15)	231.34	225.72	240.89
D_J / kHz	0.01761(44)	0.1328(56)	0.016	0.012	0.024
D_{JK} / kHz	[0.] [e]	-0.242(14)	-0.003	0.028	-0.037
D_K / kHz	0.0234(12)	0.164(10)	0.023	0.005	0.055
d_1 / kHz	[0.]	0.0434(28)	-0.002	0.000	-0.007
d_2 / kHz	[0.]	[0.]	0.001	-0.001	0.002
$\lvert\mu_a\rvert$ / D	-	-	0.0	0.2	1.0
$\lvert\mu_b\rvert$ / D	-	++	0.0	0.6	1.1
$\lvert\mu_c\rvert$ / D	+++	++	1.3	0.6	0.6
ΔE_{ZPE}/ kJ mol^{-1}			0.0	0.2	0.5
ΔG / kJ mol^{-1}			1.4	1.8	0.0
E_c / kJ mol^{-1} [b]			-48.7	-47.4	-47.2
ΔE_c / kJ mol^{-1}			0.0	1.3	1.5
N	173	86			
σ / kHz	10.6	10.6			

[a]Rotational parameters as defined in Table 5.1 [b]Complexation energies (E_c) and relative complexation energies (ΔE_c). [c]B3LYP-D3(BJ)/def2-TZVP.

The spectra of the two dimers were reproduced with a semirigid-rotor model implemented in the Watson S-reduced Hamiltonian, including quartic centrifugal distortion. No tunnelling splitting was observed, unlike in the thiophenol dimer. The spectral measurements comprised more than 250 rotational transitions for the two isomers, which were fitted to spectral accuracy in Table 5.2. The complete lists of transitions are presented in the Table S5.10-S5.11 (Appendix).

Table 5.3. Rotational constants of the observed dimers of 2-naphtalenethiol compared to four theoretical predictions with B3LYP-D3(BJ), ωB97XD, B2PLYP-D3(BJ), and MP2, and their relative differences.

Isomer 1	Experiment	B3LYP-D3(BJ) [c]	ωB97XD [c]	B2PLYP-D3(BJ) [c]	MP2 [c]
A / MHz	308.38853(21)[a]	318.1[3.1%][b]	314.9[2.1%]	317.7[3.0%]	329.0[6.7%]
B / MHz	231.75029(16)	233.4[0.7%]	235.6[1.7%]	233.0[0.5%]	243.9[5.2%]
C / MHz	226.78483(18)	231.3[2.0%]	230.4[1.6%]	231.9[2.3%]	235.2[3.7%]
B-C	5	2.1	5.2	1.1	8.7
B+C	458.5	464.7	466	464.8	479.1
Isomer 2	Experiment	B3LYP-D3(BJ)	ωB97XD	B2PLYP-D3(BJ)	MP2
A / MHz	299.45856(51)	304.2[1.6%]	299.1[0.1%]	305.6[2.0%]	329.5[10.0%]
B / MHz	246.9652(12)	250.7[1.5%]	251.5[1.9%]	250.8[1.6%]	252.2[2.1%]
C / MHz	221.5793(15)	225.7[1.9%]	226.1[2.0%]	225.1[1.6%]	230.1[3.9%]
B-C	25.4	24.9	25.5	25.7	22.1
B+C	468.5	476.4	477.6	475.9	482.3

[a]Standard errors in parentheses in units of the last digit. [b]Relative percentage differences in square brackets, calculated as (theory − exp.)/exp. [c]Basis sets def2-TZVP.

The conformational assignment was apparently difficult because the rotational constants are very similar for the two isomers. However, the consideration of the values of (*B-C*) and (*B+C*), the electric dipole moments and the centrifugal distortions constants produced an unequivocal identification. In particular, the spectrum of isomer 1 had only R-branch μ_c-type transitions, indicative of a C_2 symmetry cancelling the μ_a and μ_b dipole moment components, which matches isomer CC-1. Conversely, isomer 2 displayed both R-branch μ_b- and μ_c-type transitions, as expected for isomer CC-2. Although in this case the μ_a (=0.2 D) component is not zero, the small magnitude prevented the observation of these transitions. The comparison between experiment and theory is presented in Table 5.3. The B3LYP-D3(BJ), ωB97XD, and B2PLYP-D3(BJ) methods give an excellent agreement to the experimental values. Interestingly, the double-hybrid B2PLYP did not offer improvements over B3PLYP in structural terms. The centrifugal distortion constants are also consistent with the assigned isomers. As mentioned before the two observed dimers do not display any sulfur hydrogen bond, but these results are comparable with the observation of a V-shaped TT unsymmetric 1-naphthol dimer by rotational spectroscopy. No other dimer species were detected. However, the positive

identification of two dimers does not rule out the presence of other isomers, in particular the hydrogen bonded ones.

The binding energy (*BE*) of the 2-naphtalenethiol dimers was calculated by subtracting the electronic energy of the dimer with the energy of the monomers in the cluster. In the case of dimers 1, 2 and 5 the monomers are only in the *cis-cis* configuration, but for dimers 2, 4, and 6 the binding energy corresponds to *cis* and *trans* monomers. These binding energies included the ZPE and BSSE corrections and are presented in Table 5.4. For comparison, we also report the binding energy from the energy decomposition at the SAPT2+(3) level (aug-cc-pVDZ basis set) for 2-naphthalethiol dimer, thiophenol dimer, and H_2S dimer.

In general, the SAPT decomposition predicted similar contributions for all six dimers. The dispersion contributions in 2-napthathelenthiol dimers are 64-67% of all attractive energy. Grimme and Martinez concluded that the dispersion effect occurred only in a larger aromatic system which contain more than 10 carbon atoms.[3,21] In the case of 2-naphtalenthiol dimer, the dispersion effect increases about 3.7-6.6% compared to that in thiophenol dimer which also has π–stacking interaction, and increase more than 30% compared to the H_2S dimer. Since dimers 1-3 do not exhibit the sulfur hydrogen bonds, we expect that the electrostatic contribution is smaller than that in dimers 4-6, where each dimer has one sulfur hydrogen bond. However, the electrostatic contributions between two groups are somewhat similar and the average of electrostatic contributions is 26.3%. These similar values are probably due to the interactions between the thiol group and the π electrons are also present in the dimers 1-3. The electrostatic contributions in the 2-naphtahlenthiol dimers are about half than in the H_2S dimer, even considering the S-H···S sulfur hydrogen bond. For the induction energy contribution, the values somewhat similar, since all dimers show the π-stacking interaction. It is noteworthy that dimers 4 and 6 have slightly higher values compared to the other dimers, probably because dimers 4 and 6 have almost a sandwich-like structure where each subunit facing each other with.

The analysis of the electron density topology permits describing the non-covalent interactions within the 2-naphthalenthiol dimer. The NCIplot in Figure 5.6 confirmed that the dimers are stabilized by weakly attractive π–stacking interactions, shown as green regions between the rings. The representation of the reduced density gradient vs the signed product of the electron density times the second eigenvalue of the electron density Hessian ($\mathrm{sign}(\lambda_2)\rho$), also in Figure 5.6, additionally offers comparison between the dimers of 2-naphthalenthiol, thiophenol, and H_2S. This figure shows a tail at coordinates -0.01 a.u. for the dimers of H_2S and thiophenol, associated to the S-H···S hydrogen bond. For the 2-naphthalenthiol dimer, the plot minima are denser close to the origin of abscissas, reflecting the delocalized weak π–stacking interaction.

Table 5.4. Binding energy decomposition for (2-naphtahelenethil)$_2$ and related dimers using SAPT2+(3)/aug-cc-pVDZ//B3LYP-D3(BJ)/def2-TZVP (all values in kJ mol^{-1}).

Dimer	*BE*	E_{elect}	E_{disp}	E_{ind}	E_{exch}	E_{total}	E_c
1	-42.82	-34.1[26.7%]	-84.7[66.4%]	-8.8[6.9%]	80.1	-47.5	-11.64
2	-42.88	-33.8[26.1%]	-86.6[67.0%]	-8.9[6.9%]	82.9	-46.5	-11.33
3	-42.57	-32.9[25.5%]	-87.2[67.5%]	-9.0[7.0%]	82.7	-46.5	-11.27
4	-41.83	-35.4[27.2%]	-84.1[64.6%]	-10.6[8.2%]	85.0	-45.1	-11.21
5	-41.77	-32.8[26.2%]	-83.9[66.8%]	-8.8[7.0%]	80.2	-45.3	-11.11
6	-41.67	-34.2[26.3%]	-85.9[66.1%]	-9.8[7.6%]	85.2	-44.7	-11.16
(Thiophenol)$_2$ PD2-cis [b]	-22.90	-26.0[29.4%]	-53.8[60.9%]	-8.4[9.6%]	61.3	-27.0	-6.49
(H$_2$S)$_2$ [c]	-4.62	-12.1[49.0%]	-7.8[31.7%]	-4.7[19.3%]	19.2	-5.4	-2.12

[a]This work. [b]Ref. [22] [c]Ref. [23].

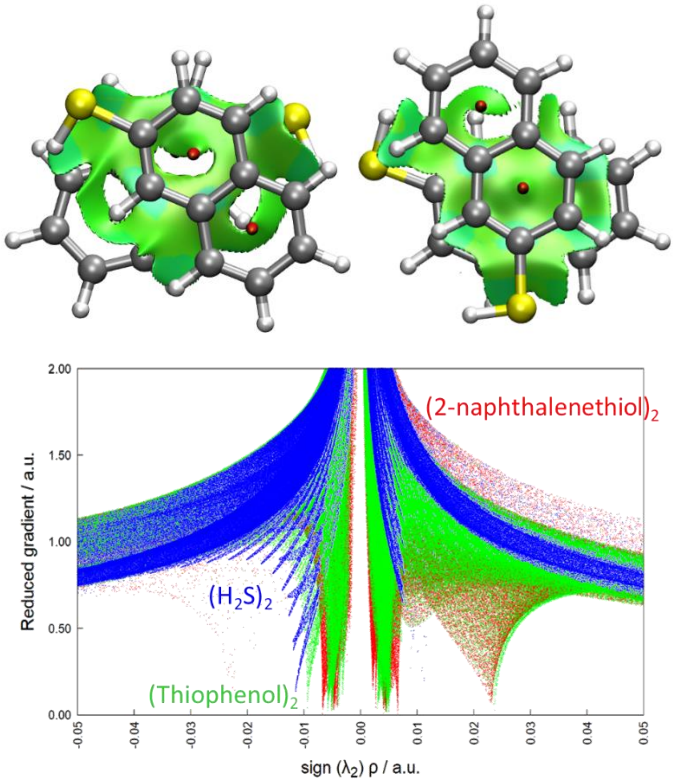

Figure 5.4. Upper panel: Three-dimensional NCI plot of CC-1 (left) and CC-2 (right, color scaling: -2.0 to 2.0, isovalue s = 0.5). Lower panel: Reduced electronic density gradient for the most stable dimer of 2-napthalenethiol (red), compared to the dimers of thiophenol (green) and H$_2$S (blue). Attractive/repulsive interactions appear as minima at negative/positive coordinates.

The results obtained in this chapter are comparable with the observation of the 1-naphthol dimer by Seifert *et. al.*, adopting an unsymmetric V-shaped trans-trans geometry. The observed dimers in both cases do not display any canonical hydrogen bond. It is worth to recall that the energy difference between the *cis* and *trans* monomers in 1-naphthol is much larger (ΔE= 5.3 kJ mol^{-1}) than in the 2-naphthalenthiol dimer, where the energy difference is just 0.6 kJ mol^{-1}. For this reason, there is a higher possibility to observe the cis-trans heterodimer in 2-naphthalenethiol. Experiments using other naphthalene derivatives and lighter carrier gas could be done in the future to improve the conformational landscape of fused biaryl compounds and the role of π-stacking.

5.4. Conclusions

The self-aggregation in 2-naphthalenethiol dimer is an interesting case of study. One could expect that self-aggregation in all thiol/alcohol molecules are stabilized by alcohol or thiol hydrogen bonds. However, due to the dispersion effect of the naphthalene aromatic frame, the dimer depends primarily on π-stacking interactions, balancing the forces between the monomers in two distinct isomer geometries. In particular the monomer presents an axially-symmetric C_2 parallel-displaced geometry. Different DFT and MP2 computational methods confirmed rationalized the experimental results, producing a good synergy between the microwave spectroscopy data and the theoretical values.

References

(1) Saeki, M.; Ishiuchi, S. I.; Sakai, M.; Fujii, M. Structure of the Jet-Cooled 1-Naphthol Dimer Studied by IR Dip Spectroscopy: Cooperation between the Π−π Interaction and the Hydrogen Bonding. *J. Phys. Chem. A* **2007**, *111* (6), 1001–1005. https://doi.org/10.1021/JP0668910.

(2) Seifert, N. A.; Hazrah, A. S.; Jäger, W. The 1-Naphthol Dimer and Its Surprising Preference for π-π Stacking over Hydrogen Bonding. *J. Phys. Chem. Lett.* **2019**, *10* (11), 2836–2841. https://doi.org/10.1021/acs.jpclett.9b00646.

(3) Grimme, S. Do Special Noncovalent π-π Stacking Interactions Really Exist? *Angew. Chemie - Int. Ed.* **2008**, *47* (18), 3430–3434. https://doi.org/10.1002/anie.200705157.

(4) Dubinets, N. O.; Safonov, A. A.; Bagaturyants, A. A. Structures and Binding Energies of the Naphthalene Dimer in Its Ground and Excited States. *J. Phys. Chem. A* **2016**, *120* (17), 2779–2782. https://doi.org/10.1021/ACS.JPCA.6B03761.

(5) Chen, Y.; Wang, Y. B.; Zhang, Y.; Wang, W. Accurate Calculations of the Noncovalent Systems with Flat Potential Energy Surfaces: Naphthalene Dimer and Azulene Dimer. *Comput. Theor. Chem.* **2017**, *1112*, 52–60. https://doi.org/10.1016/J.COMPTC.2017.04.021.

(6) Lemmens, A. K.; Chopra, P.; Garg, D.; Steber, A. L.; Schnell, M.; Buma, W. J.; Rijs, A. M. High-Resolution Infrared Spectroscopy of Naphthalene and Acenaphthene Dimers. *Mol. Phys.* **2021**, *119*(1–2).

https://doi.org/10.1080/00268976.2020.1811908/SUPPL_FILE/TMPH_A_1811908_SM9261.DOC.

(7) Halgren, T. A. MMFF VI. MMFF94s Option for Energy Minimization Studies. *J. Comput. Chem.* **1999**, *20* (7), 720–729. https://doi.org/10.1002/(SICI)1096-987X(199905)20:7<720::AID-JCC7>3.0.CO;2-X.

(8) Becke, A. D. Density-Functional Thermochemistry. III. The Role of Exact Exchange. *J. Chem. Phys.* **1993**, *98* (7), 5648–5652. https://doi.org/10.1063/1.464913.

(9) Chai, J.-D. Da; Head-Gordon, M. Long-Range Corrected Hybrid Density Functionals with Damped Atom–Atom Dispersion Corrections. *Phys. Chem. Chem. Phys.* **2008**, *10* (44).

(10) Weigend, F.; Ahlrichs, R. Balanced Basis Sets of Split Valence, Triple Zeta Valence and Quadruple Zeta Valence Quality for H to Rn: Design and Assessment of Accuracy. *Phys. Chem. Chem. Phys.* **2005**, *7* (18), 3297. https://doi.org/10.1039/b508541a.

(11) Grimme, S. Semiempirical Hybrid Density Functional with Perturbative Second-Order Correlation. *J. Chem. Phys.* **2006**, *124* (3), 034108. https://doi.org/10.1063/1.2148954.

(12) Frisch, M. J.; Head-Gordon, M.; Pople, J. A. Semi-Direct Algorithms for the MP2 Energy and Gradient. *Chem. Phys. Lett.* **1990**, *166* (3), 281–289. https://doi.org/10.1016/0009-2614(90)80030-H.

(13) Frisch, M. J.; Head-Gordon, M.; Pople, J. A. A Direct MP2 Gradient Method. *Chem. Phys. Lett.* **1990**, *166* (3), 275–280. https://doi.org/10.1016/0009-2614(90)80029-D.

(14) Johnson, E. R.; Becke, A. D. A Post-Hartree-Fock Model of Intermolecular Interactions: Inclusion of Higher-Order Corrections. *J. Chem. Phys.* **2006**, *124* (17), 174104. https://doi.org/10.1063/1.2190220.

(15) Grimme, S.; Ehrlich, S.; Goerigk, L. Effect of the Damping Function in Dispersion Corrected Density Functional Theory. *J. Comput. Chem.* **2011**, *32* (7), 1456–1465. https://doi.org/10.1002/jcc.21759.

(16) Boys, S. F.; Bernardi, F. The Calculation of Small Molecular Interactions by the Differences of Separate Total Energies. Some Procedures with Reduced Errors. *Mol. Phys.* **2002**, *100* (1), 65–73. https://doi.org/10.1080/00268970110088901.

(17) Contreras-García, J.; R. Johnson, E.; Keinan, S.; Chaudret, R.; Piquemal, J.-P.; N. Beratan, D.; Yang, W. NCIPLOT: A Program for Plotting Noncovalent Interaction Regions. *J. Chem. Theory Comput.* **2011**, *7* (3), 625–632. https://doi.org/10.1021/ct100641a.

(18) Johnson, E. R.; Keinan, S.; Mori-Sánchez, P.; Contreras-García, J.; Cohen, A. J.; Yang, W. Revealing Noncovalent Interactions. *J. Am. Chem. Soc.* **2010**, *132* (18), 6498–6506. https://doi.org/10.1021/ja100936w.

(19) Parrish, R. M.; Burns, L. A.; Smith, D. G. A.; Simmonett, A. C.; DePrince, A. E.; Hohenstein, E. G.; Bozkaya, U.; Sokolov, A. Y.; Di Remigio, R.; Richard, R. M.; Gonthier, J. F.; James, A. M.; McAlexander, H. R.; Kumar, A.; Saitow, M.; Wang, X.; Pritchard, B. P.; Verma, P.; Schaefer, H. F.; Patkowski, K.; King, R. A.; Valeev, E. F.; Evangelista, F. A.; Turney, J. M.; Crawford, T. D.; Sherrill, C. D. Psi4 1.1: An Open-Source Electronic Structure Program Emphasizing Automation, Advanced Libraries, and Interoperability. *J. Chem. Theory Comput.* **2017**, *13* (7), 3185–3197. https://doi.org/10.1021/acs.jctc.7b00174.

(20) Watson, J. K. G. Approximations for the Inertial Defects of Planar Molecules. *J. Chem. Phys.* **1993**, *98* (7), 5302. https://doi.org/10.1063/1.464929.

(21) Martinez, C. R.; Iverson, B. L. Rethinking the Term "π-Stacking." *Chem. Sci.* **2012**, *3* (7), 2191–2201. https://doi.org/10.1039/c2sc20045g.

(22) Saragi, R. T.; Juanes, M.; Pérez, C.; Pinacho, P.; Tikhonov, D. S.; Caminati, W.; Schnell, M.; Lesarri, A.; S. Tikhonov, D.; Caminati, W.; Schnell, M.; Lesarri, A. Switching Hydrogen Bonding to π-Stacking: The Thiophenol Dimer and Trimer. *J. Phys. Chem. Lett.* **2021**, *12* (5), 1367–1373. https://doi.org/10.1021/acs.jpclett.0c03797.

(23) Das, A.; Mandal, P. K.; Lovas, F. J.; Medcraft, C.; Walker, N. R.; Arunan, E. The H2S Dimer Is Hydrogen-Bonded: Direct Confirmation from Microwave Spectroscopy. *Angew. Chemie Int. Ed.* **2018**, *57* (46), 15199–15203. https://doi.org/10.1002/anie.201808162.

Chapter 6.
Complexation of Nucleosides and Amino Acids

In this chapter, we extend the work on non-covalent interactions to large biologically relevant molecules like the complexes of nucleoside dimers and amino acids. This research constitutes a preliminary step for investigating the interactions between DNA molecules and proteins and is intended to examine the capabilities and computational efficiency of density-functional methods. Unlike in previous chapters, the larger molecular size of these systems does not permit a comparison with experimental data, so this chapter is fully based on computational results. The results of this chapter are in publication.

6.1. Introduction

Non-covalent interactions are significant for determining the structure of biological macromolecules, including hydrogen bonding, π–stacking, donor-acceptor, or charge-transfer interactions.[1–3] As an example, the formation and stability of the DNA double helix rely on the hydrogen-bonding and stacking interactions between the nucleobase pairs.[4,5] Another examples are the secondary and tertiary structures of proteins, where the interactions between the amino acids depend on hydrogen-bonding and hydrophobic interactions.[6]

Deoxyribose nucleic acids (DNA) and proteins are well-known building blocks of life. Both play a vital role in biological processes, such as synthesizing a particular protein in a cell. Since proteins are produced by extracting information from the DNA, the connection between DNA and proteins in the cell is extensive. The interactions between DNA and proteins play a significant role in almost every cellular process, such as DNA replication and transcription, methylation, repair, gene expression, etc.[6–8]

Protein-DNA interactions have been probed at the atomic level by X-ray crystallography[9,10] and NMR.[11] However, computational chemistry is also a useful tool for studying the molecular structure and the influence of non-covalent

interactions. Additionally, calculations can provide information about individual interactions, while it is often difficult to separate the total stability of biological complexes into discrete interactions using experimental approaches. Thus, the nature of interactions within DNA and proteins has been the subject of several computational chemistry studies.[12–14] However, the macromolecular structures of proteins or protein-DNA complexes like histones, nucleosomes, chromatins, etc., are very large. For example, as illustrated in Figure 6.1, the nucleosome core structure is composed of an octameric complex of the core histone proteins, forming a coil to wrap 145 to 147 bp of DNA.[15] In order to reveal the information regarding the interaction in such a large structure, an expensive computational cost is needed, and one of the effective methods is using a reductionist approach.

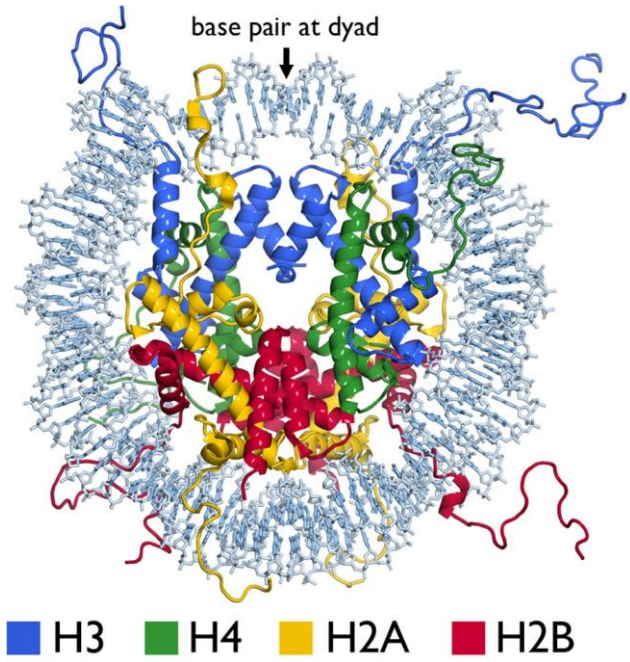

Figure 6.1. Nucleosome core particle structure and the histone-fold heterodimers. (a) Nucleosome core particle structure (PDB ID 1KX5). Histones (H3, H4, H2A, and H2B) and DNA are depicted in cartoon and sticks representations, respectively, and colored as indicated. The picture is taken from reference 15.

Employing a reductionist approach, it is possible to divide the histone-DNA interactions into amino acid-DNA base pairs, which may be investigated in detail using high-level quantum chemistry methods. Non-covalent interactions, such as

hydrogen bonds, van der Waals or dispersion forces, dominate all the interactions between the individual amino acid and the base pairs of DNA. Moreover, if this reductionist approach can link the magnitude and structure of the individual interactions with the statistical observations, it would demonstrate that the driving forces behind the aggregations of the superstructures have their origin precisely in such individual pairs and determine the large-scale coupling between two structures. The interaction within a supramolecular structure like histones has been tried before with this approach to study the epigenetic marks in biological systems.[16] In that case, a simplified model was composed of a DNA segment containing three base pairs and three amino acids in the N-terminal side of the H3 histone.

More recently, another study on protein-DNA interactions was reported by our group, modelling the interactions between one or two DNA nucleobases and one amino acid. In this initial simplified model, the DNA or RNA sugar was replaced with a methyl group or a hydrogen atom.[17–20] The amino acids were proved to interact with the nucleobases in various locations, showing strong interactions assisted by various types of bonding.[17–19] In the work carried during this thesis, we enlarged this system introducing deoxyribose sugar molecules to each nucleic base in order to improve the initial model and to examine in more detail the interactions between proteins and DNA. Following this work, we have also compared this new model with the simplified calculations where the deoxyribose molecules were absent.[19]

6.2. Computational Methods

6.2.1. Conformational search

An initial conformational search was performed to obtain the relevant structures for each complex within an energy window of 30 kJ mol^{-1}, using the Merck molecular mechanics force field (MMFFs).[21] In previous experiments, this method has shown to be reliable for groups of similar sizes to the amino acid-nucleoside dimer.[19] The conformational landscape was explored by combining the Monte Carlo method and the "large-scales low-mode" method based on a vibrational normal-mode analysis, implemented in Macromodel.[22] The conformers were then clustered into structural families based on molecular similarity criteria using the XCluster tool.[22]

6.2.2. Quantum-mechanical calculations

Geometry optimization was performed for each complex using the M06-2X DFT functional, which is applicable for systems where dispersion interactions are relevant.[23] The computational model used Pople's triple-ζ as the basis set with

polarization and diffuse orbitals (6-311++G(d,p)). All the optimizations were accompanied by normal-mode analysis, implemented in Gaussian16,[24] to verify that the resulting structures were true minima. The relative energy values given in the present work are zero-point energy (ZPE) corrected.

6.2.3. NCI analysis

A non-covalent interaction (NCI) analysis was carried out for the most stable structure of each cluster. The NCI approach calculates the intermolecular interactions based on the behaviour of the dimensionless reduced electron density, *s*, defined as:

$$s(\rho) = \frac{|\nabla\rho|}{2(3\pi^2)^{1/3}\rho^{4/3}} \quad (1)$$

The NCI approach localizes the non-covalent interactions between atoms, which appear as minima of the reduced electronic density and are then classified according to the sign of the electron-density Hessian (second derivative) eigenvalues.[25,26] The limiting cases include attractive (i.e., hydrogen bonds), weakly attractive (van der Waals), or repulsive interactions, which are displayed with a (blue, green, red) coloring scheme. The NCIplots were created using the NCIPLOT program[25,27] and were visualized with the Visual Molecular Dynamic (VMD) program.[28]

6.2.4. Cremer-Pople analysis

Deoxyribose is a flexible five-membered ring sugar, adopting non-planar conformations. Ring-puckering conformations are thus significant to stabilize the interaction between the protein and the base pair. In order to analyse the conformation quantitatively, the Cartesian coordinates of each deoxyribose ring were examined with a Cremer-Pople analysis.[29] In this section, the basic concepts of the Cremer-Pople analysis will be briefly reviewed.

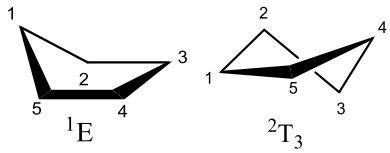

Figure 6.2. Example of an envelope and twist conformation for a cyclopentane.

The atoms of an *n*-membered ring are arranged in different conformations to reduce the ring strain. A set of *n*-3 generalized parameters are necessary to specify the out-of-plane coordinates, called Cremer-Pople coordinates. In a five-membered ring (*n*=5), there are two independent parameters: the puckering amplitude (*q*) and

the phase angle (φ). A five-membered ring adopts two limiting conformations: envelope (E) and twist (T) (Figure 6.2). When the ring adopts an E form, four atoms lie in the same plane, and the fifth stands either above or below that plane. The nomenclature is ${}^{x}E$ or E_x, where x is the atom located either above (superscript) or below (subscript) the plane formed by the other four. The ${}^{x}E$ and E_x conformations are sometimes referred as *endo* and *exo* configuration. For a T conformation, there are three atoms in the same plane, while the fourth and fifth atoms are located above and below, respectively. In this case, the nomenclature is ${}^{x}T_y$ (x is the atom above and y is the atom below).

The angle φ indicates what kind of E or T conformation the molecule adopts (e.g., E_3, ${}^{4}E$, ${}^{4}T_3$, ${}^{1}T_2$, etc., …). Meanwhile, the amplitude q represents how far the atom(s) stands out of the average plane of the ring. The visual representation of the Cremer-Pople analysis for a five-membered ring is a disc, shown in Figure 6.3.

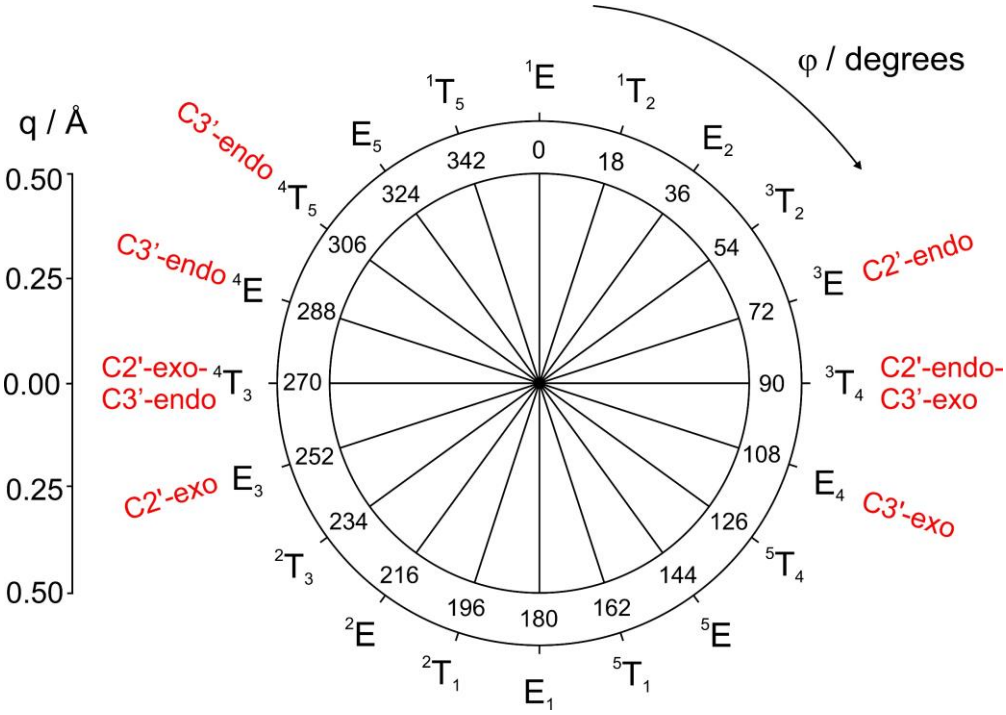

Figure 6.3. Cremer-Pople disc for a five-membered ring. The figure is adapted from ref. 30.

6.3. Results and Discussions

6.3.1. DNA base pairs

In order to study the interaction between proteins and DNA, we explored in this work the intermolecular clusters formed between a pair of weakly-bound nucleosides and one amino acid. The nucleosides consist of a nucleobase (cytosine or guanine) and a five-carbon sugar (2'-deoxyribose), linked through a glycosidic bond to the N1 atom of cytosine or the N9 of guanine (Figure 6.4).

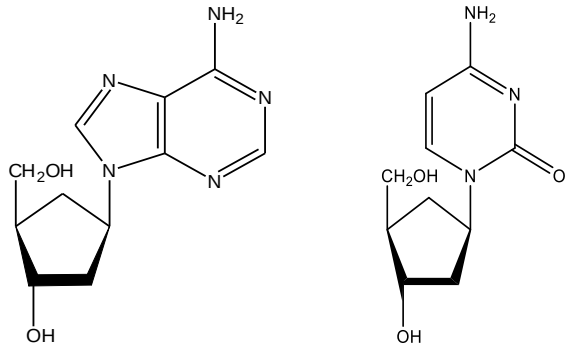

Figure 6.4. Structure of deoxycytidine (left) and deoxyguanosine (right).

6.3.2. Amino acids

For this research, a set of amino acids were selected according to their side chain, either non-polar, polar, or aromatic. Alanine (A) was chosen as non-polar amino acid, while asparagine (N) and phenylalanine (F) in Figure 6.5 were chosen as polar and aromatic amino acids. As the amino acid groups are engaged in the protein, the terminal carboxylic and amino groups are not available for interaction. Therefore, to resemble this situation, the amino acid groups were capped by an amide group at both ends of the molecule as shown also in Figure 6.5. The capped amino acids are denoted aA, aN, and aF.

Each amino acid was then complexed to a nucleoside dimer, like in Figure 6.6. The complexes were named by their nucleosides (i.e., dCdG refers to deoxycytidine and deoxyguanosine) and the associated capped amino acids (aA, aN, and aF). Following the conformational search, ca. 1000 structures were found for each complex within the specified energy window of 30 kJ mol^{-1}. A large number of structures reflects the complexity of the aggregation process and the flexibility of the amino acids and the sugar puckering. Therefore, the clustering process reducing the initial geometries to

independent structural families is key to reducing the number of initial structures to a more manageable dataset without losing important information.

However, even when a large number of structures were grouped into families, presenting all the structures is not practical. Therefore, only the global minimum and an additional structure of each complex are presented in this chapter. The rest of the complexes will be presented in the Appendix. Several structural restrictions were applied in this study. The aromatic rings of the nucleosides dimer were frozen to impose the Watson-Crick pair structure. The hydrogen bond conditions considered in this study were limited to bond lengths shorter than 2.300 Å and bond angles between 180°-140°. Angles lower than 140° were considered dispersive forces.

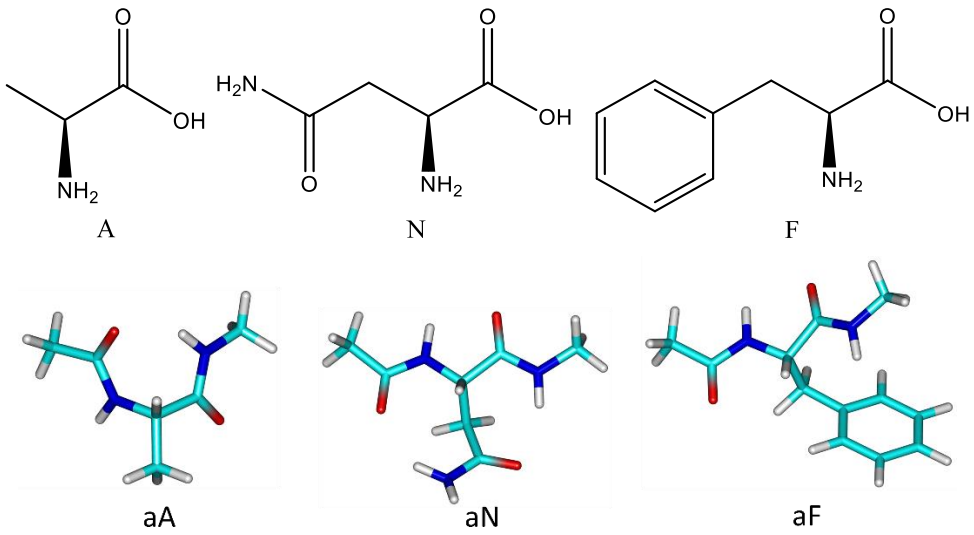

Figure 6.5. Structures of alanine (A), asparagine (N), and phenylalanine (F), and the capped amino acids.[31]

6.3.3. Binding energies

The binding energies were estimated by subtracting the energy of the complex by the energies of the optimized nucleoside dimer and the amino acid, taken from a previous study.[19,20,31] A set of 22 nucleoside dimers (deoxycytidine··· deoxyguanosine or dCdG) have been calculated, with the aromatic rings frozen to the Watson-Crick structures. Therefore, each structure has three hydrogen bonds and is also stabilized by the hydrogen bonds between the bases and the OH group of the deoxyribose molecules. The ten most stable structures are presented in Figure S6.1 (in Appendix). The most stable structure of the dCdG dimer is shown in Figure 6.6.

Both deoxyribose molecules attached to the base pair adopt a ^{3}E (C2'-endo) form configuration and display two hydrogen bonds. The binding energies were calculated by correcting the Basis Set Superposition Error correction with the Boys-Bernardi counterpoise method.[32]

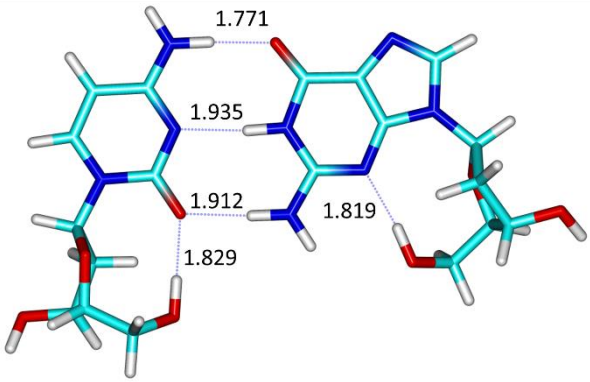

Figure 6.6. The most stable deoxycytidine···deoxyguanosine (dCdG) dimer. The hydrogen bonds (in black) are marked with a blue dashed line.

6.3.4. Nucleoside dimer and amino acid interactions

6.3.4.1. aA···dCdG

A set of 10 conformers were optimized for the alanine complexes (Figure S6.2 in Appendix), freezing the aromatic rings of the nucleoside dimer to the values of Figure 6.6. The conformational distribution (ZPE-corrected) is depicted in Figure 6.7. The number of hydrogen bonds (HB) varies, as shown in the figure. In general, the aA···dCdG complexes displayed a high number of hydrogen bonds between aA and the deoxyribose molecules. These kinds of interactions are observed in ca. half of all aA···dCdG complexes. We verified that the global minima for all the investigated systems have positive frequencies.

One of the OH groups in the deoxyribose molecule behaves as a proton donor to the bases and as a proton acceptor from the amino groups of alanine. Meanwhile, the hydrogen bond connecting alanine and the deoxyribose attached to guanine in the aA···dCdG-2 complex is getting weaker (2.024 Å vs 1.868 Å), and we considered it of dispersive character (red dashed lines in Figure 6.8). In addition, aA···dCdG-1 is the only isomer with a hydrogen bond between the OH group of deoxyribose and the O atom of cytosine, which makes this complex the most stable because of the higher number of hydrogen bonds (9 HBs). There are two hydrogen bonds less in the

complex aA···dCdG-2, disconnecting the OH groups of deoxyribose and the O atom of cytosine (O-H···O bond) or the -NH groups of aA (O···H-N). The N-H···O hydrogen bond is the most common interaction in these complexes. The hydrogen bonds parameters are summarized in Table 6.1.

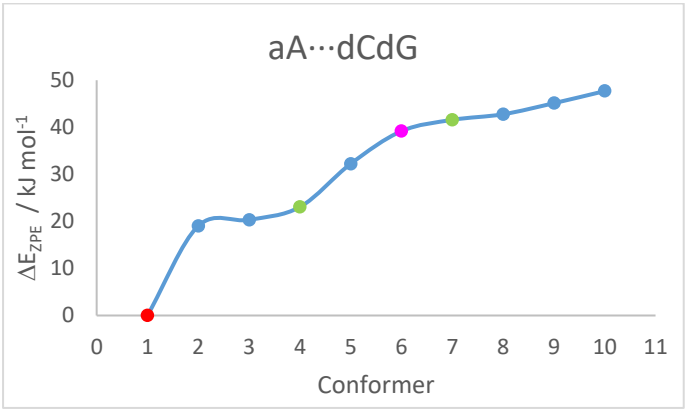

Figure 6.7. Conformational distribution of the most relevant interactions found for the first 10 complexes of aN···dCdG, aF···dCdG, and aA···dCdG (green = 6 HBs, blue = 7 HBs, purple = 8 HBs, and red = 9 HBs).

The sugar puckering analysis in Table 6.2 was done to quantitatively identify the form of deoxyribose molecules. The deoxyribose molecules in the complexes aA···dCdG-1 and aA···dCdG-2 showed a twist form (similar to C3'-endo), while aA···dCdG-3 has an envelope form (similar to C2'-endo).

Table 6.1. Distance (Å) and angles (°) of the hydrogen bonds observed in aA···dCdG-1, aA···dCdG-2 and aA···dCdG-3.

		aA···dCdG-1	aA···dCdG-2	aA···dCdG-3
deoxyribose-C	O-H···O	1.849/152.7		
deoxyribose-G	O-H···N	1.868/158.9	2.024/159.2	1.888/160.1
deoxyribose(C)-aA	O-H···O	1.966/151.1	1.851/171.6	1.875/165.1
	O···H-N	2.053/154.8		
deoxyribose(G)-aA	O-H···O	1.968/153.7	1.882/153.4	1.825/163.7
	O···H-N	1.981/152.9	2.024/159.2	1.916/156.8
intramolecular aA	N-H···O		2.138/146.0	

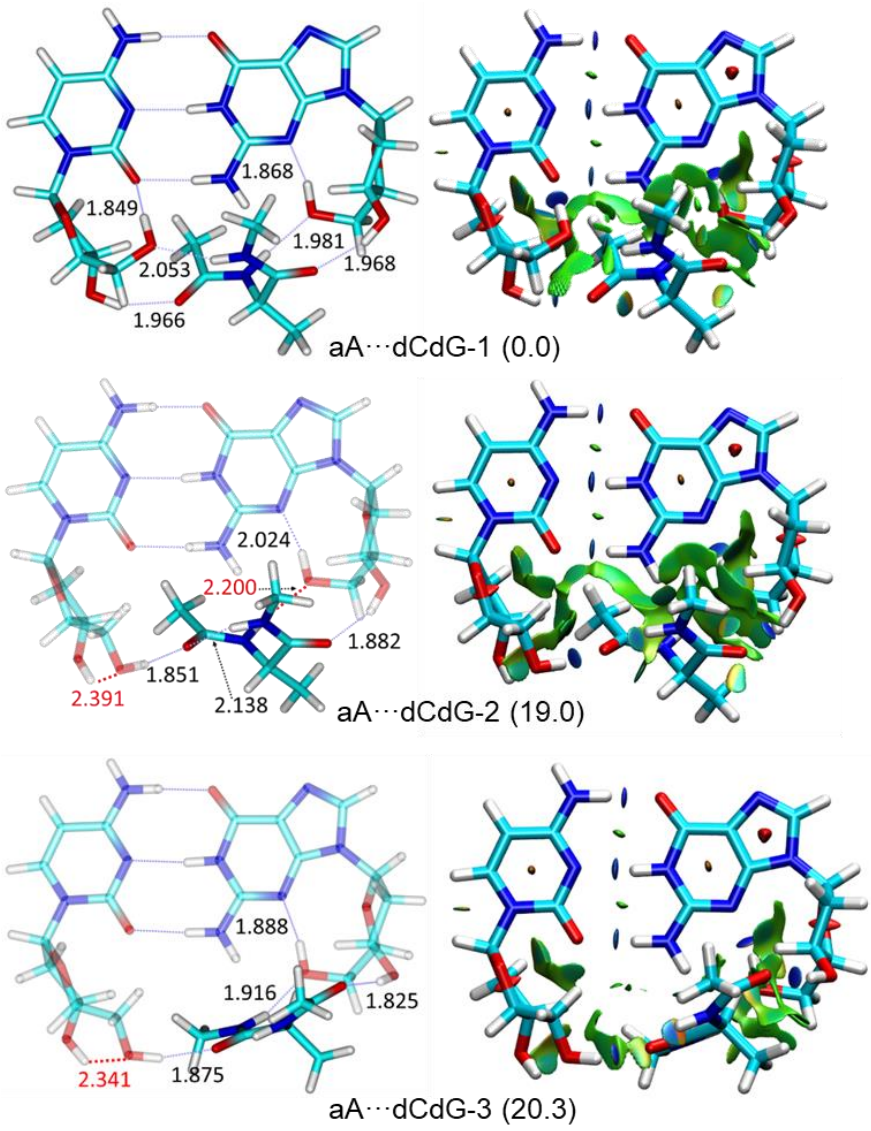

Figure 6.8. The three most stable structures for the aA···dCdG complexes (relative energies in kJ mol^{-1}) and their NCIplots (red = strong repulsive, blue = strong attractive, green = delocalized weak interactions; color scaling from -3.0 to 3.0, isovalue *s* = 0.5). The hydrogen bonds are marked with blue dashed lines (black distances), and the dispersive interactions are depicted in red dashed lines.

Table 6.2. The sugar puckering forms of deoxyribose attached to nucleobase.

	aA···dCdG-1	aA···dCdG-2	aA···dCdG-3
C-attached	$^4T_5$	$^4T_5$	^4E
G-attached	$^4T_5$	$^4T_5$	^4E

6.3.4.2. aN···dCdG

A set of 10 conformers were optimized for the complex with asparagine (Figure S6.3 in Appendix). The conformational distribution (ZPE-corrected) for aN···dCdG is displayed in Figure 6.9. In these complexes, the aN located above the base pair limited the interaction between aN and the deoxyribose molecules. Several hydrogen bonds in these complexes are due to the intramolecular interactions within the aN molecule.

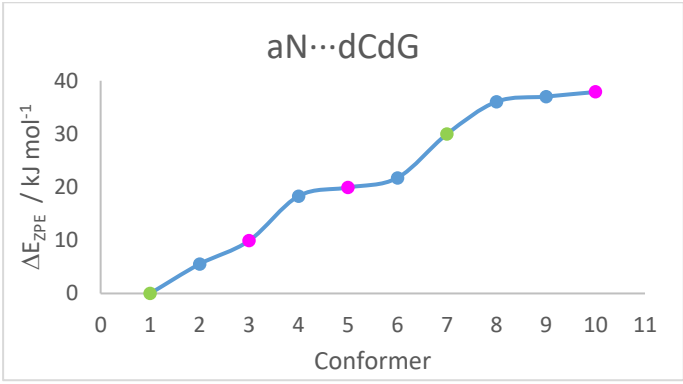

Figure 6.9. Conformational distribution of the most relevant interactions found for the first 10 complexes of aN···dCdG (green = 6 HBs, blue = 7 HBs, and purple = 8 HBs).

The global minimum in Figure 6.10 shows the interaction between the aN located on top of the base pair (in β_L conformation[33,34]) and the weak interaction between the amino acid and the base pair (broad green layer). However, there is no strong interaction between aN and the deoxyribose molecules. The nucleoside dimer of the second and the third most stable complex exhibited a similar configuration, with the energy difference to the global minimum being 5.5 and 9.9 kJ mol^{-1}, respectively.

The numbers of hydrogen bonds for aN···dCdG-1, aN···dCdG-2, and aN···dCdG-3 are 6, 7, and 8, respectively. The hydrogen bonds in aN···dCdG are collected in Table 6.3, for aN···dCdG-2 and aN···dCdG-3 there are two hydrogen bonds between the deoxyribose molecules and the bases. However, in the global minimum aN···dCdG-1, there is only one hydrogen bond connecting the deoxyribose molecule and the base

of guanine. The aN also displays different interactions for each complex. In aN···dCdG-1 there are two intramolecular N-H···O bonds, one intramolecular N-H···O bond in aN···dCdG-3, and no intramolecular hydrogen bonds in aN···dCdG-2 complex. In aN···dCdG-2 and aN···dCdG-3, the complex is also stabilized by the interaction between aN (β_L conformation) and the deoxyribose attached to guanine (O-H···O and N-H···O).

Table 6.3. Distance (Å) and angles (°) of the hydrogen bonds observed in aN···dCdG-1 (global minimum), aN···dCdG-2, and aN···dCdG-3.

		aN···dCdG-1	aN···dCdG-2	aN···dCdG-3
deoxyribose-C	O-H···O		1.823/165.9	1.801/167.9
deoxyribose-G	O-H···N	1.802/170.6	1.820/158.4	1.753/159.0
deoxyribose-aN	O-H···O		1.853/164.4	1.942/147.0
	O···N-H		1.966/158.7	2.087/142.1
aN	N-H···O	2.026/157.9		1.946/158.7
(Intramolecular)	N-H···O	2.283/145.8		

As mentioned before, the deoxyribose molecules in the complexes aN···dCdG-2 and aN···dCdG-3 showed a similar configuration. The sugar puckering was analysed by the Cremer-Pople coordinates as summarized in Table 6.4. The deoxyribose attached to guanine showed an envelope form for the three complexes, where the global minimum has a ^{3}E (C2'-endo) configuration while aN···dCdG-2 and aN···dCdG-3 have a ^{4}E (C3'-endo) configuration. The OH groups of deoxyribose attached to cytosine act as proton donors to the O atom of cytosine and force deoxyribose to display a ^{3}E envelope (C2'-endo) configuration in the aN···dCdG-2 and aN···dCdG-3 complexes. The absence of this hydrogen bond in the global minimum caused deoxyribose to have a $^4T_3$ form.

Table 6.4. The sugar puckering form of the deoxyribose group in the nucleobase.

	aN···dCdG-1	aN···dCdG-2	aN···dCdG-3
C-attached	$^4T_3$	^{3}E	^{3}E
G-attached	^{3}E	^{4}E	^{4}E

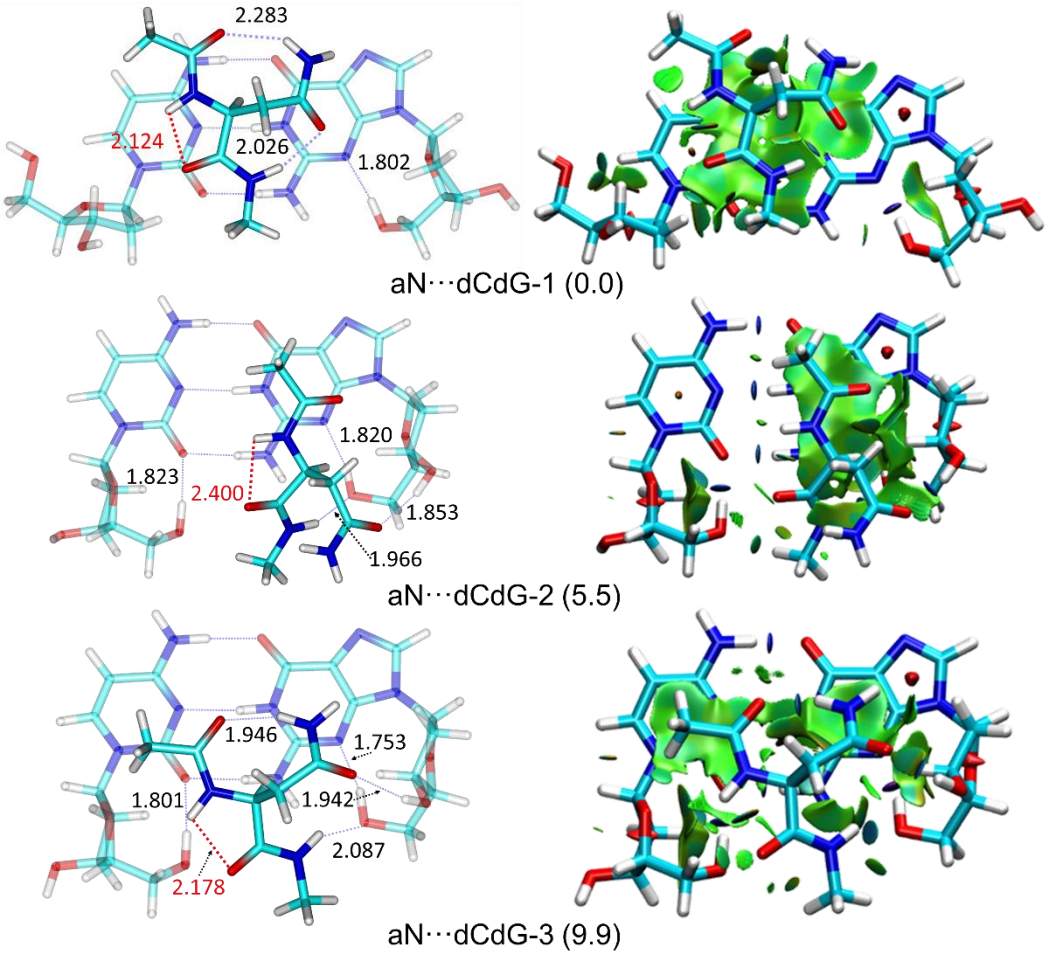

Figure 6.10. The three most stable structures for the aN···dCdG complexes (relative energies in kJ mol^{-1}) and their NCIplots (red = strong repulsive, blue = strong attractive, and green = delocalized weak interactions; color scaling from -3.0 to 3.0, isovalue *s* = 0.5). The hydrogen bonds are marked with blue dashed lines (black distances), and the dispersive interactions are depicted in red dashed lines.

6.3.4.3. aF···dCdG

A set of 10 structures were calculated for the phenylalanine complexes (Figure S6.4 in Appendix). The conformational landscape is depicted in Figure 6.11. Compared to other amino acids, the aF···dCdG complexes displayed fewer hydrogen bonds. The interactions between aF and the nucleoside dimer are mainly stabilized by π–stacking (~60% of all aF···dCdG complexes). The three most stable complexes of aF···dCdG are shown in Figure 6.12. For the global minimum aF···dCdG-1, aF shows γD conformation, but a βL conformation in aF···dCdG-2 and aF···dCdG-3. The energy difference between the global minimum to the other complexes are 1.2 and 2.1 kJ mol^{-1} (ZPE-corrected), respectively for aF···dCdG-2 and aF···dCdG-3. Since the relative energy values for the three most stable complexes are at a reasonable energetic distance, it is difficult to assess the global minimum. Moreover, these energy differences are at the limit of error of the calculation, so some alterations of the stability order could be produced by increasing the calculation level. However, the conclusion achieved in the present work would still be valid.

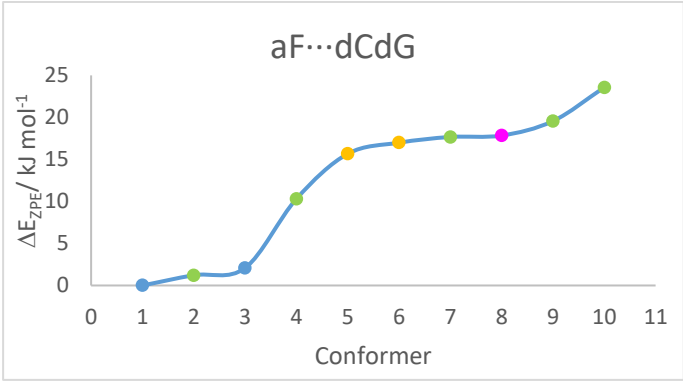

Figure 6.11. Conformational distribution of the most relevant interactions found for the first 10 complexes of aF···dCdG (yellow = 5 HBs, green = 6 HBs, blue = 7 HBs, and purple = 8 HBs).

The structural parameters are summarized in Table 6.5 and Figures 6.11 and 6.12. For the three most stable complexes, there are 7 hydrogen bonds for aF···dCdG-1 and aF···dCdG-3 and 6 hydrogen bonds for aF···dCdG-2. The side chain of the aF amino acid are parallel to the aromatic ring of the nucleobase dimer, showing π–stacking, both in aF···dCdG-1 and aF···dCdG-2. In the global minimum (aF···dCdG-1), the complex is additionally stabilized by the hydrogen bond between aF and guanine, aF and guanine deoxyribose, deoxyribose to cytosine, and the intramolecular hydrogen bond within aF. Meanwhile, in aF···dCdG-2, the complex

presents two hydrogen bonds between the lateral chain to the bases and between the deoxyribose and guanine. In the aF···dCdG-3 complex, the side chain of the aF amino acid displays a T-shaped form to the purine base of guanine. In addition, the lateral chain of aF interacted with the deoxyribose attached to guanine. Also, there are two hydrogen bonds formed between the deoxyribose molecules and the bases.

Table 6.5. Distance (Å) and angles (°) of the hydrogen bonds observed in aF···dCdG-1 (global minimum), aF···dCdG-2 and aF···dCdG-3.

		aF···dCdG-1	aF···dCdG-2	aF···dCdG-3
deoxyribose-C	O-H···O	1.825/166.2		1.830/166.0
deoxyribose-G	O-H···N		1.822/170.1	1.822/171.8
deoxyribose-aF	O-H···O	1.755/175.2		1.883/162.6
	N-H···O			1.957/167.3
C-aF	N-H···O		1.904/157.2	
	N···H-N			
G-aF	N-H···O	2.073/142.0	2.060/162.1	
intramolecular aF	N-H···O	1.926/151.0		

The deoxyribose molecules aF···dCdG-1 showed an envelope form as summarized in Table 6.6. The OH group of deoxyribose attached to cytosine acts as a proton donor to the O atom of cytosine with a ^{3}E (C2'endo) form. The OH group of deoxyribose attached to guanine acts as a proton donor but to the O atom of aF amino acid (E_4 or C3'-exo form). The absence of these interactions in complex aF···dCdG-2 is replaced by the interaction between the OH group of deoxyribose attached to guanine to the N atom of guanine. The OH group of deoxyribose attached to cytosine remains free and forces the sugar puckering to adopt a $^{3}T_4$ twist form (C2'endo-C3'exo). In the complex aF···dCdG-3, the OH group of deoxyribose attached to guanine acts as a proton donor to the O atom of the aF amino acid.

Table 6.6. The sugar puckering form of deoxyribose attached to nucleobase.

	aF···dCdG-1	aF···dCdG-2	aF···dCdG-3
C-attached	^{3}E	$^{3}T_4$	^{3}E
G-attached	E_4	^{3}E	$^{3}T_4$

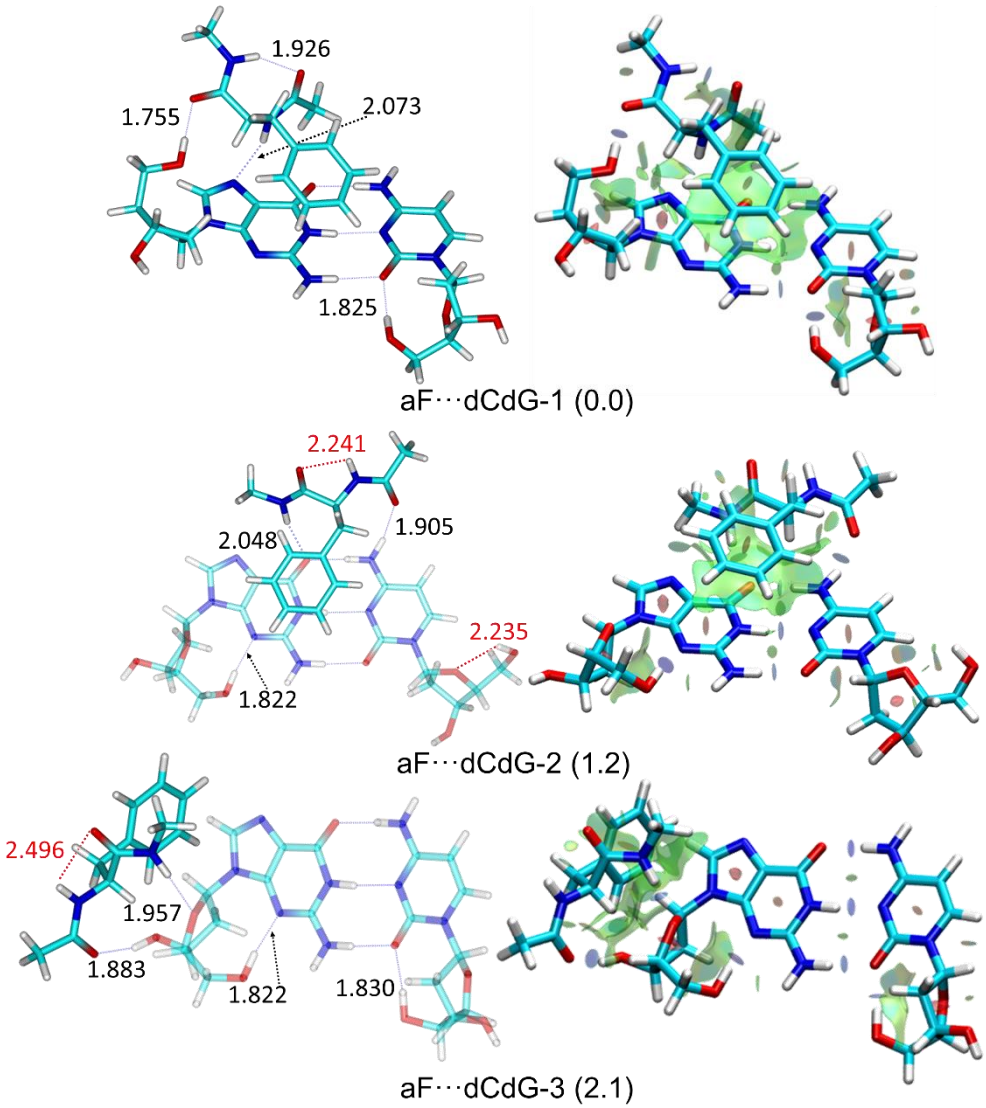

Figure 6.12. The three most stable structures for aF···dCdG complexes (relative energies in kJ mol^{-1}) and their NCIplots (red = strong repulsive, blue = strong attractive, and green = delocalized weak interactions; color scaling from -3.0 to 3.0, isovalue *s* = 0.5). The hydrogen bonds are marked with blue dashed lines (black distances), and the dispersive interactions are depicted in red dashed lines.

The comparison for the three amino acids shows that, in general, alanine complexes have a higher number of hydrogen bonds, with the most stable having 9 hydrogen bonds. The hydrogen bonds in alanine complexes are attributed to the interaction between the OH groups of deoxyribose and the alanine molecules. On the other hand, asparagine complexes have the smallest number of hydrogen bond intermolecular interactions between the asparagine and bases or deoxyribose. However, the lack of these interactions in asparagine complexes is compensated by the high intermolecular hydrogen bond within the asparagine molecule. Meanwhile, the phenylalanine complexes have fewer hydrogen bonds compared to the other amino acids, but in some of these complexes, there are additional π–stacking interactions between the aromatic ring of phenylalanine and the bases.

Table 6.7. The binding energy of the dCdG complexes with selected amino acids. The binding energies are calculated by subtracting from the complex the energy of the most stable dCdG and the most stable amino acid.

Complex	Binding energy (kJ mol^{-1})
aA⋯dCdG-1	-99.5
aN⋯dCdG-1	-68.6
aF⋯dCdG-1	-69.9

The comparison of the binding energy for the most stable isomer for each complex is summarized in Table 6.7. The interaction of the nucleoside dimer with the non-polar alanine has the lowest value (-99.5 kJ mol^{-1}), followed by the aromatic phenylalanine (-69.9 kJ mol^{-1}) and the polar asparagine amino acid (-68.6 kJ mol^{-1}). However, the structure of the amino acids in the complexes may have a different configuration to the most stable monomers, so the binding energy values could require a deformation correction.

6.3.5. Comparison to the non-sugar model

As mentioned initially, a simpler simplified model of DNA-protein interaction was previously built using only the bases and amino acids, without insertion of the sugars.[20] This model was enlarged here by adding deoxyribose molecules attached to the bases. This extension was intended to better reproduce the situation in histone-DNA interaction. However, some interaction patterns observed in the simplified model, such as between the lateral chain and the canonical base pairs, are

still present in the interaction in the sugar-base model. For instance, most of the complexes are mainly stabilized by the N-H···O or O-H···N hydrogen bonds.

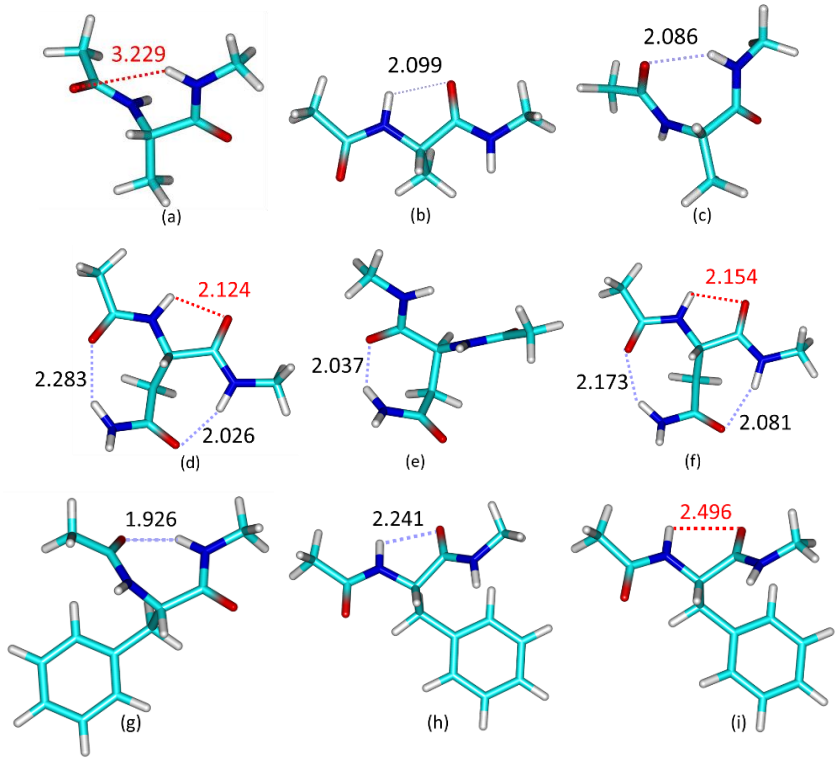

Figure 6.13. The structure of the selected amino acids in the studied complexes (all the nucleoside dimers were removed for clarity): aA···dCdG-1 (a), aA···dCdG-2 (b), aA···dCdG-3 (c), aN···dCdG-1 (d), aN···dCdG-2 (e), aN···dCdG-3 (f), aF···dCdG-1 (g), aF···dCdG-2 (h), and aF···dCdG-3 (i).

The insertion of sugar molecules in the complexes changed the orientation of the amino acid. Each sugar molecule has two OH groups, one of the OH groups typically interacts with the base pair, while the other OH group could interact with the amino acid. The interaction then also depends on the polarity of the related amino acid. The most stable conformations for an amino acid are γ_L and β_L, where γ_L is a 7-member ring and β_L is a 5-member ring.[31] In the aN···dCdG complexes, all aN structures have β_L conformation.

Meanwhile, in the aA···dCdG complexes, the aA structures mainly adopt γ_L and β_L conformations, but the global minimum of aA···dCdG has δ_L conformation.[33,34] In aF···dCdG complexes, the aF structures also mostly take on β_L, γ_L, and γ_D

conformations. The global minimum of aF···dCdG-1 has γ_D conformation. Figure 6.13 illustrates the related amino acid conformations; the blue dashed lines show the hydrogen bonds, and the black dashed lines indicate dispersive forces.

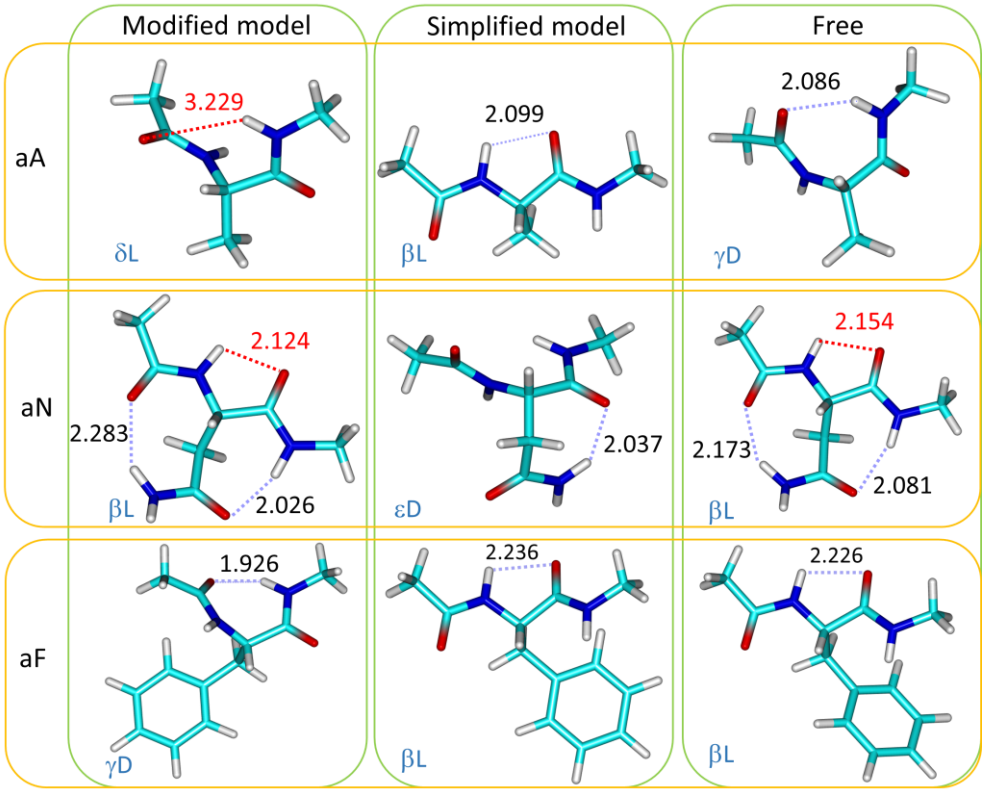

Figure 6.14. The comparison between the amino acid configurations for the modified sugar model, the simplified non-sugar model,[19,20] and the most stable free capped amino acid[31]. All nucleoside dimers of the sugar model and the base pairs of the simplified model were removed for clarity.

The comparison with the simplified non-sugar model where the deoxyribose molecules are absent in the complexes will be discussed in this section. The non-polar amino acid (alanine) displays strong attractive interactions with the deoxyribose molecules. The alanine located between the deoxyribose molecules makes four hydrogen bonds to all OH groups of the deoxyribose molecules. In the complex where the deoxyribose molecules are absent, alanine is located above the base pairs, making two hydrogen bonds to the base pairs. This type of interaction between the base pair and alanine was also found in one of our complexes (aA···dCdG-6) with a relatively very high energy difference of 43.0 kJ mol^{-1}

(Appendix). The other difference between the two models is the alanine conformation of β_L in aAmCmG and δ_L in aA···dCdG-1. However, the side chain in both complexes does not interact with either the base pair or the sugar molecules. The comparison between the simplified non-sugar model and modified sugar model is illustrated in Figure 6.15, displaying the number of contact points, which increases in the modified model of aA···dCdG-1. The green surfaces from the NCIplot show the weak interactions between alanine and deoxyribose molecules in the sugar model. In the simplified model, these interactions existed between the alanine and the bases.

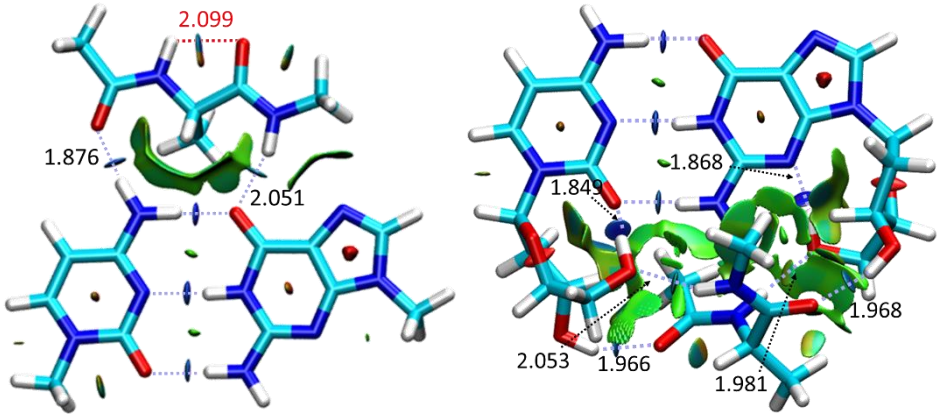

Figure 6.15. NCIPlots of aAmCmG (left) and aA···dCdG-1 (right).

Figure 6.16 presents the 2-dimensional NCI plots, divided into three ranges corresponding to attractive interactions ($sign(\lambda_2)\rho$: -0.05 to -0.01 a.u.), van der Waals or weak interactions (-0.01 to 0.01 a.u.) and repulsive or steric clashes (0.01-0.05 a.u.). The weak interactions are shown by the green plot in $sign(\lambda_2)\rho$: -0.01 to 0.01, and the hydrogen bonds are shown by the blue plot in the range of -0.05 to -0.01. In general, there are a denser number of interactions for the sugar model of aA···dCdG-1 (right panel) than the simplified model (left panel) as a consequence of the presence of sugar molecules. Thus, these denser interactions are also applied for the other amino acid. The rest of the 2D NCI plots for the other complexes can be found in Figure S6.5-S6.14 in Appendix.

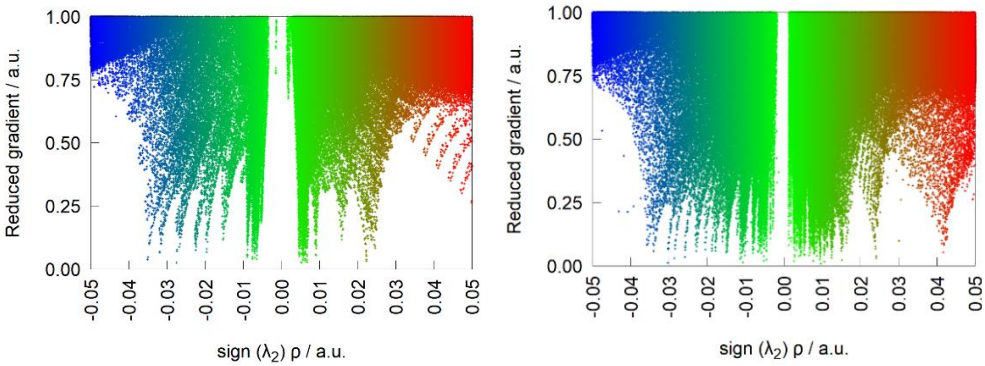

Figure 6.16. The 2-dimensional NCIplot of the aAmCmG non-sugar model (left) and aA···dCdG-1 modified model (right).

The interaction between the nucleoside dimer and polar amino acid asparagine is illustrated in Figure 6.17, compared to the non-sugar model. In the simplified model, the complex is stabilized by three hydrogen bonds between the asparagine and the base pair. Similar to the simplified model of alanine complex (aAmCmG, Figure 6.15), the asparagine is located above the bases for the non-sugar model, where the -CO group of the side chain weakly interacts with cytosine. In the sugar model of aN···dCdG-1, the side chain does not take part in the interaction with the nucleoside dimer. But it makes two intramolecular hydrogen bonds within the asparagine, which has β_L conformation. Compared to the aA···dCdG-1 complex, asparagine has no hydrogen bond either to the deoxyribose molecules or the base pair.

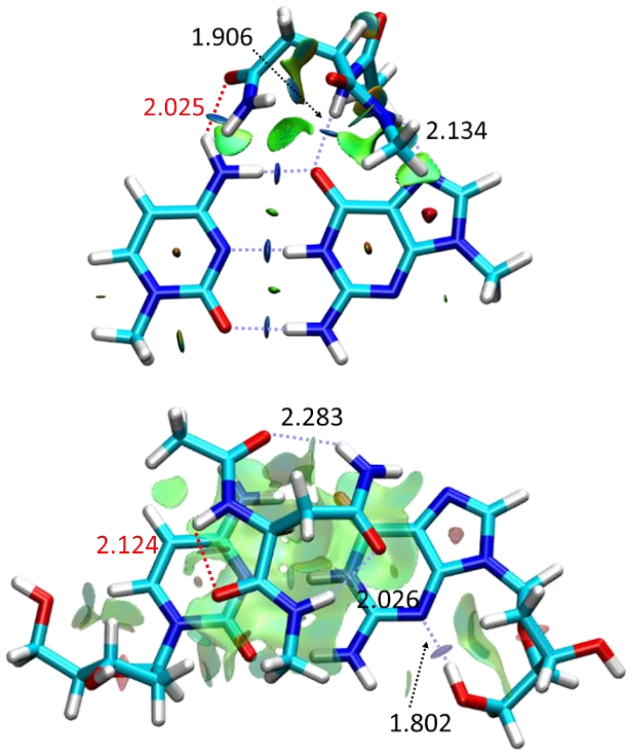

Figure 6.17. NCIPlots of aNmCmG (upper trace) and aN···dCdG-1 (lower trace).

A statistical structure analysis from 139 protein-DNA complexes from the Protein Data Bank (PDB) shows that all polar amino acids investigated are mostly in contact with the phosphate groups and interact with the base edges through hydrogen bonding.[9] Because we did not include the phosphate groups in the present model, asparagine displays the weak interaction to the aromatic rings of the base pair, as illustrated by the broad green surface in the NCIplot figures. However, some higher-energy conformers show interactions between the side chain of polar amino acids to the deoxyribose molecules. For the global minimum, the hydrogen bonds were only between the sugar molecules to the base pair. Other structures where the asparagine is "locked" between the deoxyribose molecules exist as higher energy conformers, for example, aN···dCdG-5 (19.9 kJ mol^{-1}) and aN···dCdG-7(30 kJ mol^{-1}), which are shown in Figure 6.18.

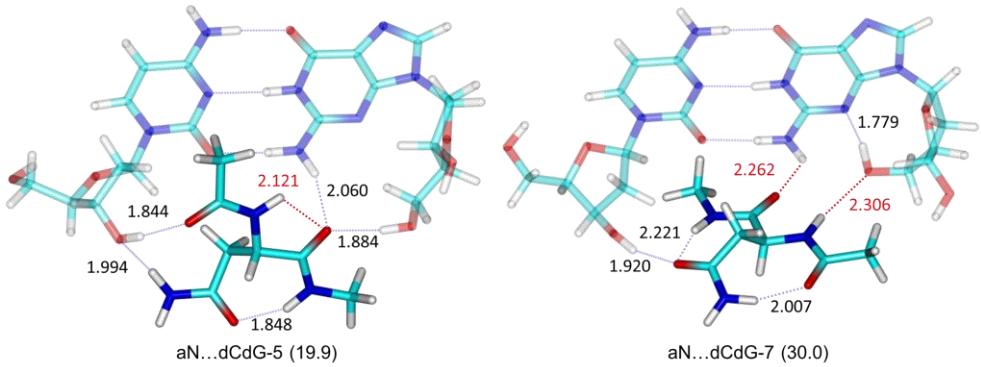

Figure 6.18. Higher energy conformers of aN···dCdG-5(left) and aN···dCdG-7(right) complexes where asparagine is located between the deoxyribose molecule.

There are many studies regarding the stability and interface concerning the interaction between the nucleobases, specifically the aromatic amino acids.[35–37] Cytosine dimers observed by IR/UV spectroscopy in the gas phase show planar structures, connected by hydrogen bonds of N-H···N and N-H···O.[38] In the gas phase, the dimers of simple aromatic compounds such as benzene,[39] thiophenol,[40] or dibenzofuran,[41] are also observed in parallel-displaced structures using rotational spectroscopy. In other DNA-related complexes, the parallel displacement structures between the nucleobases are somewhat enforced by the double helix structure. However, the arrangement between nucleobase and aromatic residues is found as T-shaped and π–stacking structures. The arrangement between adenine bases and aromatic residues (phenylalanine, tyrosine, and tryptophan) in proteins shows no preference for one configuration over the other.[42]

In the dCdG complexes investigated for the aromatic amino acid phenylalanine, the π–stacking between the side chain and the base pair became the primary interaction as a dispersive contribution. In addition, the -NH group from phenylalanine becomes a proton donor to the N atom of guanine, and the -CO group becomes a proton acceptor from the OH group of the deoxyribose attached to guanine. The comparison between the non-sugar and sugar-containing models is highlighted in Figure 6.19. The difference to the simplified model is the phenylalanine conformation, which in aF···dCdG-1 has γ_D conformation and β_L in the simplified one. Moreover, in the simplified model, the π–stacking structure is also stabilized by the two hydrogen bonds of the functional groups and the base pair. These interactions also found in the modified complex of aF···dCdG-2 are depicted in Figure 6.20 with the additional interaction of deoxyribose and guanine. The energy

difference of aF···dCdG-2 to the global minimum is about 1.2 kJ mol^{-1}, which can be considered as a possible competitor of the global minimum. However, both in the simplified and modified model, the aromatic side chain is in close contact with the aromatic ring of nucleoside dimer with the preference for the puric base of deoxyguanosine.

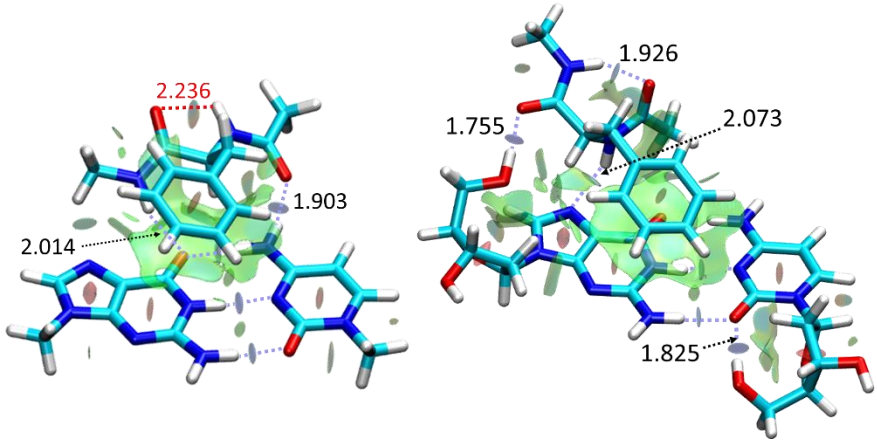

Figure 6.19. NCIPlots of aFmCmG (left) and aF···dCdG-1 (right).

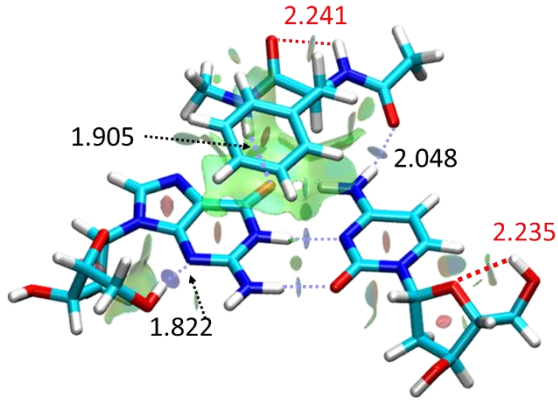

Figure 6.20. NCIplot of aF···dCdG-2.

6.4. Conclusions

We presented here some improvements over a previously tested reductionist model to investigate protein-DNA interactions, based on isolated clusters of amino acids and DNA base pairs. The model investigated in this work included the deoxyribose sugar molecules attached to the two nucleic bases, in order to improve the similarities with the biological system. To have a better understanding of the

protein-DNA interactions, we studied the clusters between the deoxycytidine-deoxyguanosine dimer (dCdG) and three amino acids with a different character of the lateral chain: alanine (non-polar), asparagine (polar) and phenylalanine (aromatic).

The presence of sugar molecules in the model changes the orientation of the amino acids in the complexes aA···dCdG, aN···dCdG and aF···dCdG because of the influence of the sugar puckering in the amino acid conformation. For both models (non-sugar and sugar-containing), the complexes were mainly stabilized by hydrogen bonds when the amino acids were introduced. The non-covalent interactions in alanine complexes are stabilized by the hydrogen bonds between the sugar molecules and the amino acid, while for the asparagine complexes the structures are additionally controlled by the intramolecular hydrogen bonds within the amino acid. For the phenylalanine complexes, some complexes show π–stacking structures as a dispersive contribution.

The study of non-covalent interactions between amino acids and nucleoside dimers would require further extensions to obtain more general conclusions. In particular, additional comparisons would need to examine more complex amino acids (as valine and isoleucine for non-polar side chains, glutamine for polar lateral chains and tryptophan and tyrosine, for instance) but also other nucleoside dimers (like deoxyadenosine-deoxythymidine (dAdT)). In addition, the introduction of the phosphate group should be considered. In any case, the present investigation represents a preliminary effort extending quantum mechanical methods to biologically related models.

References:

(1) Meyer, E. A.; Castellano, R. K.; Diederich, F. Interactions with Aromatic Rings in Chemical and Biological Recognition. *Angewandte Chemie - International Edition*. John Wiley & Sons, Ltd March 17, 2003, pp 1210–1250. https://doi.org/10.1002/anie.200390319.

(2) Müller-Dethlefs, K.; Hobza, P. Noncovalent Interactions: A Challenge for Experiment and Theory. *Chem. Rev.* **2000**, *100* (1), 143–167. https://doi.org/10.1021/cr9900331.

(3) Juanes, M.; Saragi, R. T.; Caminati, W.; Lesarri, A. *The Hydrogen Bond and Beyond: Perspectives for Rotational Investigations of Non-Covalent Interactions*; 2019; Vol. 25, pp 11402–11411. https://doi.org/10.1002/chem.201901113.

(4) Matta, C. F.; Castillo, N.; Boyd, R. J. Extended Weak Bonding Interactions in DNA: π-Stacking (Base-Base), Base-Backbone, and Backbone-Backbone Interactions. *J. Phys. Chem. B* **2006**, *110* (1), 563–578. https://doi.org/10.1021/jp054986g.

(5) Černý, J.; Kabeláč, M.; Hobza, P. Double-Helical → Ladder Structural Transition in the B-DNA Is Induced by a Loss of Dispersion Energy. *J. Am. Chem. Soc.* **2008**, *130* (47), 16055–16059. https://doi.org/10.1021/ja805428q.

(6) Dill, K. A. Dominant Forces in Protein Folding. *Biochemistry* **1990**, *29* (31), 7133–7155.

https://doi.org/10.1021/bi00483a001.
(7) Ptashne, M. Specific Binding of the λ Phage Repressor to λ DNA. *Nature* **1967**, *214* (5085), 232–234. https://doi.org/10.1038/214232a0.
(8) Höglund, A.; Kohlbacher, O. From Sequence to Structure and Back Again: Approaches for Predicting Protein-DNA Binding. *Proteome Science*. BioMed Central June 17, 2004, pp 1–7. https://doi.org/10.1186/1477-5956-2-3.
(9) Lejeune, D.; Delsaux, N.; Charloteaux, B.; Thomas, A.; Brasseur, R. Protein-Nucleic Acid Recognition: Statistical Analysis of Atomic Interactions and Influence of DNA Structure. *Proteins Struct. Funct. Genet.* **2005**, *61* (2), 258–271. https://doi.org/10.1002/prot.20607.
(10) Itsathitphaisarn, O.; Wing, R. A.; Eliason, W. K.; Wang, J.; Steitz, T. A. The Hexameric Helicase DnaB Adopts a Nonplanar Conformation during Translocation. *Cell* **2012**, *151* (2), 267–277. https://doi.org/10.1016/j.cell.2012.09.014.
(11) Lacabanne, D.; Boudet, J.; Malär, A. A.; Wu, P.; Cadalbert, R.; Salmon, L.; Allain, F. H. T.; Meier, B. H.; Wiegand, T. Protein Side-Chain-DNA Contacts Probed by Fast Magic-Angle Spinning NMR. *J. Phys. Chem. B* **2020**, *124* (49), 11089–11097. https://doi.org/10.1021/acs.jpcb.0c08150.
(12) Poddar, S.; Chakravarty, D.; Chakrabarti, P. Structural Changes in DNA-Binding Proteins on Complexation. *Nucleic Acids Res.* **2018**, *46* (7), 3298–3308. https://doi.org/10.1093/nar/gky170.
(13) Sagendorf, J. M.; Berman, H. M.; Rohs, R. DNAproDB: An Interactive Tool for Structural Analysis of DNA-Protein Complexes. *Nucleic Acids Res.* **2017**, *45* (W1), W89–W97. https://doi.org/10.1093/nar/gkx272.
(14) Biswas, S.; Guharoy, M.; Chakrabarti, P. Dissection, Residue Conservation, and Structural Classification of Protein-DNA Interfaces. *Proteins Struct. Funct. Bioinforma.* **2009**, *74* (3), 643–654. https://doi.org/10.1002/prot.22180.
(15) McGinty, R. K.; Tan, S. Nucleosome Structure and Function. *Chem. Rev.* **2014**, *115* (6), 2255–2273. https://doi.org/10.1021/CR500373H.
(16) Millan, J.; Lesarri, A.; Fernández, J. A.; Martínez, R. Exploring Epigenetic Marks by Analysis of Noncovalent Interactions. *ChemBioChem* **2021**, *22* (2), 408–415. https://doi.org/10.1002/CBIC.202000380.
(17) Copeland, K. L.; Pellock, S. J.; Cox, J. R.; Cafiero, M. L.; Tschumper, G. S. Examination of Tyrosine/Adenine Stacking Interactions in Protein Complexes. *J. Phys. Chem. B* **2013**, *117* (45), 14001–14008. https://doi.org/10.1021/jp408027j.
(18) Wilson, K. A.; Wells, R. A.; Abendong, M. N.; Anderson, C. B.; Kung, R. W.; Wetmore, S. D. Landscape of π-π And Sugar-π Contacts in DNA-Protein Interactions. *J. Biomol. Struct. Dyn.* **2016**, *34* (1), 184–197. https://doi.org/10.1080/07391102.2015.1013157.
(19) González, J.; Baños, I.; León, I.; Contreras-García, J.; J. Cocinero, E.; Lesarri, A.; A. Fernández, J.; Millán, J. Unravelling Protein–DNA Interactions at Molecular Level: A DFT and NCI Study. *J. Chem. Theory Comput.* **2016**, *12* (2), 523–534. https://doi.org/10.1021/acs.jctc.5b00330.
(20) González, J. Aggregation Of Biological Building Blocks: A Theoretical And Spectroscopic Study, Universidad del País Vasco, 2017.
(21) Halgren, T. A. Supplementary Material for: MMFF VII. Characterization of MMFF94, MMFF94s, and Other Widely Available Force Fields for Conformational Energies and for Intermolecular-Interaction Energies and Geometries. *J. Comput. Chem.* **1999**, *20* (7), 730–748.
(22) Macromodel. Schrödinger, LLC: New York 2012.
(23) Zhao, Y.; Truhlar, D. G. Density Functionals with Broad Applicability in Chemistry. *Acc. Chem. Res.* **2008**, *41* (2), 157–167. https://doi.org/10.1021/ar700111a.
(24) Frisch, M. J.; Trucks, G. W.; Schlegel, H. B.; Scuseria, G. E.; Robb, M. A.; Cheeseman, J. R.; Scalmani G.; Barone, V.; Petersson, G. A.; Nakatsuji, H.; Li, X.; Caricato, M.; Marenich, A. V.; Bloino, J.; Janesko, B. G.; Gomperts, R.; Mennucci, B.; Hratchian, H. P.; Ortiz, J. V.; Izmaylov, A. F.; Sonnenberg, J. L.; Williams-Young, D.; Ding, F.; Lipparini, F.; Egidi, F.; Goings, J.; Peng,

B.; Petrone, A.; Henderson, T.; Ranasinghe, D.; Zakrzewski, V. G.; Gao, J.; Rega, N.; Zheng, G.; Liang, W.; Hada, M.; Ehara, M.; Toyota, K.; Fukuda, R.; Hasegawa, J.; Ishida, M.; Nakajima, T.; Honda, Y.; Kitao, O.; Nakai, H.; Vreven, T.; Throssell, K.; Montgomery, J. A. . J.; Peralta, J. E.; Ogliaro, F.; Bearpark, M. J.; Heyd, J. J.; Brothers, E. N.; Kudin, K. N.; Staroverov, V. N.; Keith, T. A.; Kobayashi, R.; Normand, J.; Raghavachari, K.; Rendell, A. P.; Burant, J. C.; Iyengar, S. S.; Tomasi, J.; Cossi, M.; Millam, J. M.; Klene, M.; Adamo, C.; Cammi, R.; Ochterski, J. W.; Martin, R. L.; Morokuma, K.; Farkas, O.; Foresman, J. B.; Fox, D. J. Gaussian16. Gaussian, Inc.: Wallingford CT 2016.

(25) Contreras-García, J.; R. Johnson, E.; Keinan, S.; Chaudret, R.; Piquemal, J.-P.; N. Beratan, D.; Yang, W. NCIPLOT: A Program for Plotting Noncovalent Interaction Regions. *J. Chem. Theory Comput.* **2011**, *7* (3), 625–632. https://doi.org/10.1021/ct100641a.

(26) Johnson, E. R.; Keinan, S.; Mori-Sánchez, P.; Contreras-García, J.; Cohen, A. J.; Yang, W. Revealing Noncovalent Interactions. *J. Am. Chem. Soc.* **2010**, *132* (18), 6498–6506. https://doi.org/10.1021/ja100936w.

(27) Boto, R. A.; Peccati, F.; Laplaza, R.; Quan, C.; Carbone, A.; Piquemal, J.-P.; Maday, Y.; Contreras-García, J. NCIPLOT4: Fast, Robust, and Quantitative Analysis of Noncovalent Interactions. *J. Chem. Theory Comput.* **2020**, *16* (7), 4150–4158. https://doi.org/10.1021/ACS.JCTC.0C00063.

(28) Humphrey, W.; Dalke, A.; Schulten, K. VMD: Visual Molecular Dynamics. *J. Mol. Graph.* **1996**, *14* (1), 33–38. https://doi.org/10.1016/0263-7855(96)00018-5.

(29) Cremer, D.; A. Pople, J. General Definition of Ring Puckering Coordinates. *J. Am. Chem. Soc.* **1975**, *97* (6), 1354–1358. https://doi.org/10.1021/ja00839a011.

(30) Écija, P.; Uriarte, I.; Spada, L.; Davis, B. G.; Caminati, W.; Basterretxea, F. J.; Lesarri, A.; Cocinero, E. J. Furanosic Forms of Sugars: Conformational Equilibrium of Methyl b-D-Ribofuranoside † ChemComm COMMUNICATION. *Chem. Commun* **2016**, *52*, 6241. https://doi.org/10.1039/c6cc01180b.

(31) González, J.; Martínez, R.; Fernández, J. A.; Millan, J. THE EUROPEAN PHYSICAL JOURNAL D Conformational Landscape of Isolated Capped Amino Acids: On the Nature of Non-Covalent Interactions. *Eur. Phys. J. D* **2017**, *71*, 203. https://doi.org/10.1140/epjd/e2017-80187-5.

(32) Boys, S. F.; Bernardi, F. The Calculation of Small Molecular Interactions by the Differences of Separate Total Energies. Some Procedures with Reduced Errors. *Mol. Phys.* **2002**, *100* (1), 65–73. https://doi.org/10.1080/00268970110088901.

(33) Chass, G. A.; Sahai, M. A.; Law, J. M. S.; Lovas, S.; Farkas, Ö.; Perczel, A.; Rivail, J.-L.; Csizmadia, I. G. Toward a Computed Peptide Structure Database: The Role of a Universal Atomic Numbering System of Amino Acids in Peptides and Internal Hierarchy of Database. *Int. J. Quantum Chem.* **2002**, *90*, 933–968. https://doi.org/10.1002/qua.947.

(34) Schwing, K.; Gerhards, M. Investigations on Isolated Peptides by Combined IR/UV Spectroscopy in a Molecular Beam – Structure, Aggregation, Solvation and Molecular Recognition. *Int. Rev. Phys. Chem.* **2016**, *35* (4), 569–677. https://doi.org/10.1080/0144235X.2016.1229331.

(35) Poater, J.; Swart, M.; Bickelhaupt, F. M.; Fonseca Guerra, C. B-DNA Structure and Stability: The Role of Hydrogen Bonding, π-π Stacking Interactions, Twist-Angle, and Solvation. *Org. Biomol. Chem.* **2014**, *12* (26), 4691–4700. https://doi.org/10.1039/c4ob00427b.

(36) Churchill, C. D. M.; Rutledge, L. R.; Wetmore, S. D. Effects of the Biological Backbone on Stacking Interactions at DNA-Protein Interfaces: The Interplay between the Backbone···π and Π···π Components. *Phys. Chem. Chem. Phys.* **2010**, *12* (43), 14515–14526. https://doi.org/10.1039/c0cp00550a.

(37) Wilson, K. A.; Kellie, J. L.; Wetmore, S. D. DNA-Protein π-Interactions in Nature: Abundance, Structure, Composition and Strength of Contacts between Aromatic Amino Acids and DNA Nucleobases or Deoxyribose Sugar. *Nucleic Acids Res.* **2014**, *42* (10), 6726–6741. https://doi.org/10.1093/nar/gku269.

(38) González, J.; Usabiaga, I.; Arnaiz, P. F.; León, I.; Martínez, R.; Millán, J.; Fernández, J. A.

Competition between Stacked and Hydrogen Bonded Structures of Cytosine Aggregates. *Phys. Chem. Chem. Phys.* **2017**, *19* (13), 8826–8834. https://doi.org/10.1039/c6cp08476a.

(39) Schnell, M.; Erlekam, U.; Bunker, P. R.; Vonhelden, G.; Grabow, J. U.; Meijer, G.; Vanderavoird, A. Structure of the Benzene Dimer - Governed by Dynamics. *Angew. Chemie - Int. Ed.* **2013**, *52* (19), 5180–5183. https://doi.org/10.1002/anie.201300653.

(40) Saragi, R. T.; Juanes, M.; Pérez, C.; Pinacho, P.; Tikhonov, D. S.; Caminati, W.; Schnell, M.; Lesarri, A.; S. Tikhonov, D.; Caminati, W.; Schnell, M.; Lesarri, A. Switching Hydrogen Bonding to π-Stacking: The Thiophenol Dimer and Trimer. *J. Phys. Chem. Lett.* **2021**, *12* (5), 1367–1373. https://doi.org/10.1021/acs.jpclett.0c03797.

(41) Fatima, M.; Steber, A. L.; Poblotzki, A.; Pérez, C.; Zinn, S.; Schnell, M. Rotational Signatures of Dispersive Stacking in the Formation of Aromatic Dimers. *Angew. Chemie - Int. Ed.* **2019**, *58* (10), 3108–3113. https://doi.org/10.1002/anie.201812556.

(42) Mao, L.; Wang, Y.; Liu, Y.; Hu, X. Molecular Determinants for ATP-Binding in Proteins: A Data Mining and Quantum Chemical Analysis. *J. Mol. Biol.* **2004**, *336* (3), 787–807. https://doi.org/10.1016/j.jmb.2003.12.056.

Chapter 7.
Conclusions

Specific conclusions for each model dimer are presented in the corresponding chapters in this thesis. In addition, there are some general conclusions that can be obtained by comparing the molecular characteristics of the observed intermolecular clusters.

- The use of broadband rotational spectroscopy has proven to be a reliable method for describing the structural parameters of weakly-bound intermolecular clusters. We extended the scope and molecular size of previous cluster studies, analysing several thiol dimers of increasing size and complexity never studied before in the gas phase. As a result, we provide for the first time a description of molecular aggregation controlled by thiol groups, previously analysed only with vibrational laser spectroscopy. The higher structural resolution of the microwave studies will contribute to a better understanding of the weak interactions involving sulfur in the gas-phase, complementing other experimental and theoretical investigations.

- Most of the thiol aggregation processes in this Thesis were detected in homodimers, which were compared to the corresponding alcohols. The dimerization process is normally controlled by long S-H···S sulfur hydrogen bonds, cooperatively stabilized by other weak non-covalent interactions. In thiophenol dimers, the clusters exhibit a π-stacking interaction, a surprising preference compared to phenol and aniline. A single symmetric-top isomer of the thiophenol trimer was also observed, characterized by a C_3 symmetry topologically equivalent to that observed in the phenol and aniline trimers. The trimer structure combines S-H···S hydrogen bonds and C-H···π interactions.

- An additional methylene spacer in benzyl mercaptan and an ethylene spacer in 2-phenethyl mercaptan give more degrees of freedom for pivoting the thiol groups around the aromatic ring. Instead of being stabilized by π-stacking, these dimers display additional combinations of S-H···S, S-H···π, C-H···π and, in the case of 2-phenethyl mercaptan dimer, aliphatic-to-sulfur C-H···S hydrogen bond interactions, seldom characterized in the gas phase. Moreover, both compounds show transient chirality which generates two easily interconverting enantiomers. The dimerization process freezes stereomutation and produces aggregates that will display either homo or heterochiral preferences. The observed energy differences are quite small and different for each dimer. Benzyl mercaptan displays a homochiral character while we observed an heterochiral 2-phenethyl mercaptan dimer. The comparison with the alcohols shows similar binding patterns possibilities but with different energy orderings, confirming delicate conformational equilibria and small changes associated to the replacement of oxygen by sulfur. Interestingly C_2 or C_i symmetric dimers are relatively higher in energy than the global minimum and not observed.

- Unlike the monoaromatic thiol dimers, the 2-naphtahlenethiol dimers show no canonical hydrogen bonds. The dimers are mainly stabilized by a π-stacking interaction with additional S-H···π interactions, reflecting the increase in dispersion forces with the introduction of the second fused ring. The alcohol counterpart shows also a π-stacking geometry, but with a different orientation between the two rings.

- The synergy between theoretical calculations and rotational spectroscopy is noticeable. The experimental studies are supported by reliable density-functional theoretical predictions, but also contribute to the development of new theoretical models needed of benchmarks from experimentally obtained molecular structures. We have seen this interaction between theory and experiment all along this thesis.

- The binding energies and the nature of intermolecular forces in aromatic thiol dimers have been evaluated with SAPT energy decomposition. In general, the largest contributor to dimer binding comes from dispersion components (54-67%), followed by electrostatic (26-34%) and induction energies (7-12%). In the dimers showing π–stacking interactions like thiophenol and 2-naphthalenethiol the dispersion contribution increases around 6-12% compared to those without those interactions.

- The presence of attractive interactions in the dimer was explored using the topology of the reduced electronic density. This method provided a useful qualitative comparison tool and a graphic mapping of the regions showing intermolecular interactions.

- Non-covalent interactions are also very important to describe large biologically relevant systems. In this thesis, we investigated the DNA-protein interaction through a reductionist approach using complementary computational methods which included molecular mechanics, DFT calculations, and NCI analysis. The models improve previous studies by formation of clusters between nucleoside dimers and several capped amino acids. The presence of sugar molecules affected the conformation of the selected amino acids, simultaneously establishing the combination of hydrogen bonds and weak van der Waals dispersive forces.

- To conclude, the results of the thesis offer an experimental-computational perspective of intermolecular interactions, in particular those involving sulfur centers, providing information on their structural aspects, electronic structure, energy contributions and origin of the intermolecular forces.

Chapter 8.
Complementary Studies

During the Ph.D. program, I participated in other rotational spectroscopy studies which have not been included in this thesis, but that offer information on other molecular aspects of intermolecular interactions. Some results of these investigation have been published and some others are still in progress.

These investigations include also the work carried out during a research visit to the group of Prof. Melanie Schnell at the *Deutsches Elektronen-Synchrotron* (DESY), Hamburg, which were focused on the study of hydrogen sulfide and other five-membered ring clusters. This investigation has permitted the assignment of several large clusters.

Work was also initiated in our group concerning selenium compounds. In particular, I participated in the study of benzeneselenol and its interaction with water and hydrogen sulfide. This work will shed light on the intermolecular interactions associated to this chalcogen atom and its comparison with sulfur. Our preliminary results show that the selenol group behaves as proton acceptor in both monohydrated cluster and in the complex with hydrogen sulfide.

We also studied the hydrogen bonding competition between water and hydrogen sulfide through their solvated clusters of benzyl alcohol and benzyl mercaptan. In the benzyl alcohol monosolvates, the aromatic alcohol acts as a proton donor, opposing the benzyl mercaptan dimers, where the thiol group acts as a proton acceptor. For the bisolvated trimers, we observed two H_2O or H_2S molecules binding to benzyl alcohol and two water molecules attaching to benzyl mercaptan, always stabilized by cooperative hydrogen bonding. The clusters additionally involved secondary interactions between the solvents and the π ring system.

Other published works are briefly described here.

The S–S Bridge: A Mixed Experimental-Computational Estimation of the Equilibrium Structure of Diphenyl Disulfide

Jean Demaison, Natalja Vogt, Rizalina Tama Saragi, Marcos Juanes, Heinz Dieter Rudolph, and Alberto Lesarri

ChemPhysChem, 2019, 20, 366 –373

We measured diphenyl disulfide, $C_6H_5–S–S–C_6H_5$, using microwave spectroscopy. The disulfide bridge (–S–S–) is an important structural motif in organic and protein chemistry, but only a few accurate equilibrium structures are documented. A single conformation of C_2 symmetry was observed in the gas phase. The spectral assignment was done not only for the parent but also all ^{13}C and ^{34}S monosubstituted isotopologues. The equilibrium structure then determined by the mixed-estimation (ME) method. The structure were defined by 34 degree of freedom which make it a challenging case. Moreover, ab initio calculations revealed the presence of three low-frequency vibrations (<50 cm^{-1}) associated to phenyl torsions which would prevent the calculation of an accurate force field. As a consequence, we used the mass-dependent (rm) method to fit the structural parameters concurrently to moments of inertia and predicate parameters, affected with appropriate uncertainties. The predicates were obtained by high-level quantum-chemical computations. A careful analysis of the results of different fits and a comparison with the ab initio optimizations confirms the validity of the used methods, providing detailed structural information on the title compound and the disulfide bridge.

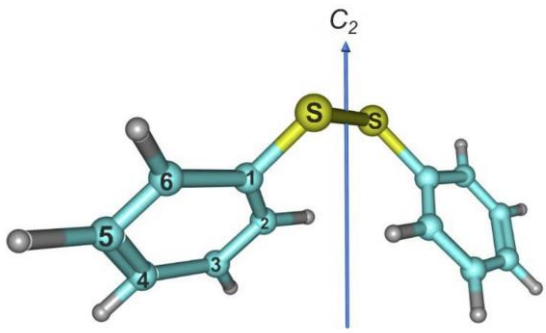

Figure 8.1. The experimentally observed C_2-symmetry conformation of diphenyl disulfide.

How flexible is the disulfide linker? A combined rotational–computational investigation of diallyl disulfide

Jean Demaison, Natalja Vogt, Rizalina Tama Saragi, Marcos Juanes, Heinz Dieter Rudolph, and Alberto Lesarri

Phys. Chem. Chem. Phys., 2019, 21, 19732-19736

In this work, we probed the rotational spectroscopy combining supersonic jets technique and supplemented with high-level ab-initio calculations to define different disulfide bridge. Diallyl disulfide, CH_2=CH−CH_2−S−S−CH_2−CH=CH_2, is a symmetrically substituted structure, which adopts a non-symmetric conformation in gas phase as observed with rotational spectroscopy. The calculations were done through the application of a predicate mixed estimation and the mass-dependent method. There is a satisfactory synergy between experiment and theory for moderate-size molecule like diallyl disulfide.

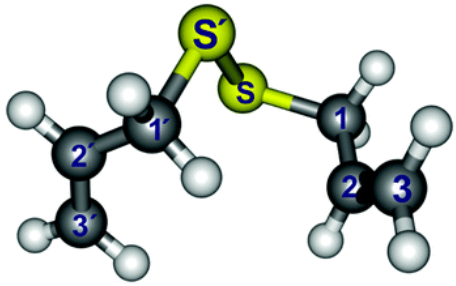

Figure 8.2. The observed (C_1) asymmetric conformation of DADS

Rotational spectroscopy of organophosphorous chemical agents: cresyl and phenyl saligenin phosphates

Rizalina Tama Saragi, Marcos Juanes, Jose L. Abad, Alberto Lesarri, Ruth Pinacho, and Jose E. Rubio

Phys. Chem. Chem. Phys., 2019, 21, 16418-16422

Cresyl and phenyl saligenin phosphates were specifically synthesized for this work. 2-(2-Cresyl)-4H-1,3,2-benzodioxaphosphorin-2-oxide (CBDP) and phenyl saligenin phosphate (PSP) differ only by one methyl group. The experiment in a jet expansion by broadband chirp-excitation microwave spectroscopy revealed that this method can be applied for large molecule where CBDP contains 19 heavy atom (276 u) and PSP contains 18 heavy atoms (262 u). Both compounds are observed as their most stable conformations. The rotational parameters also offer a high-resolution univocal route for characterization of organophosphorous agents and a testbed for computational models.

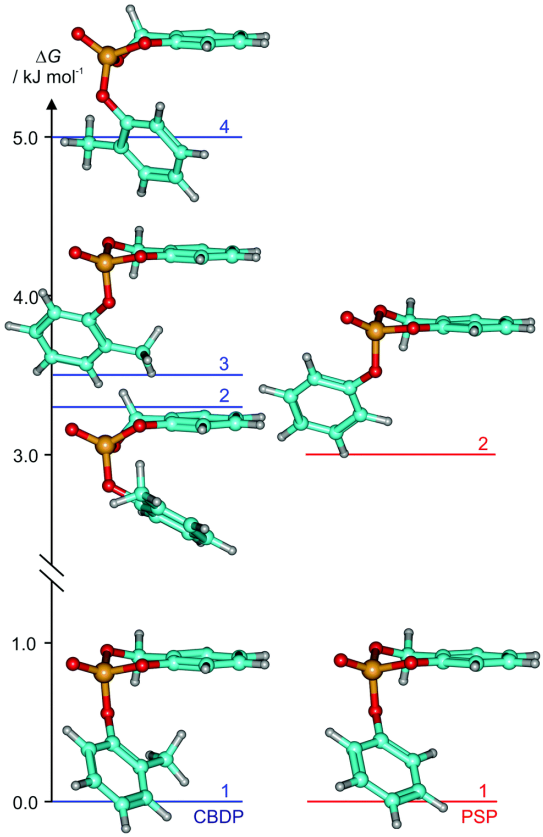

Figure 8.3. Conformational stability of CBDP and PSP according to B3LYP-D3(BJ).

Chirality-Puckering correlation and intermolecular interactions in Sphingosines: Rotational spectroscopy of jaspine B3 and its monohydrate

Rizalina Tama Saragi, Marcos Juanes, Jose L. Abad, Ruth Pinacho, Jose E. Rubio, and Alberto Lesarri

Spectrochimica Acta Part A: Molecular and Biomolecular Spectroscopy, 2022, 267, 120531

Chirality is determinant for sphingosine biofunctions and pharmacological activity, yet the reasons for the biological chiral selection are not well understood. Here, we characterized the intra- and intermolecular interactions at the headgroup of the cytotoxic anhydrophytosphingosine jaspine B, revealing chirality-dependent correlations between the puckering of the ring core and the formation of amino-alcohol hydrogen bond networks, both in the monomer and the monohydrate. Following the specific synthesis of a shortened 3-carbon side-chain molecule, denoted jaspine B3, six different isomers were observed in a jet expansion using broadband (chirped-pulsed) rotational spectroscopy. Additionally, a single isomer of the jaspine B3 monohydrate was observed, revealing the insertion of water in between the hydroxy and amino groups and the formation of a network of O-H···N-H···Oring hydrogen bonds. The specific jaspine B3 stereochemistry thus creates a double-faced molecule where the exposed lone-pair electrons may easily catalyze the formation of intermolecular aggregates and determine the sphingosine biological properties.

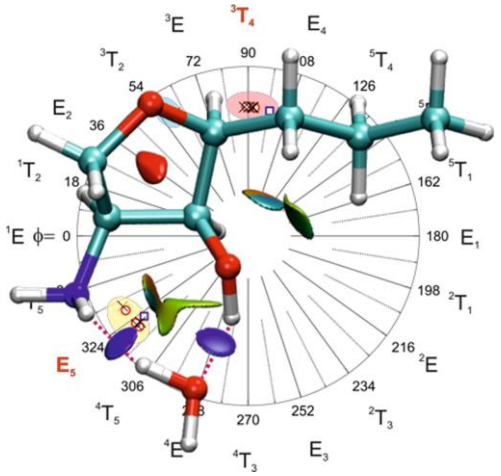

Figure 8.4. NCI plot mapping the inter- and intramolecular interactions in the observed monohydrate of jaspine B3.